# Multi-Scale Chemistry Modeling of the Thermochemical Conversion of Biomass in a Fluidized Bed Gasifier

by

Addison Killean Stark

B.S., Mathematics & B.A., Chemistry
University of Iowa (2007)
S.M., Technology and Policy & S.M., Mechanical Engineering
Massachusetts Institute of Technology (2010)

Submitted to the Department of Mechanical Engineering
in partial fulfillment of the requirements for the degree of

Doctor of Philosophy in Mechanical Engineering

at the

MASSACHUSETTS INSTITUTE OF TECHNOLOGY

February 2015



Author .....
Department of Mechanical Engineering
January 6, 2015

Certified by .....
Ahmed F. Ghoniem
Ronald C. Crane (1972) Professor of Mechanical Engineering
Thesis Supervisor

Accepted by .....
David E. Hardt
Chairman, Department Committee on Graduate Students

# Multi-Scale Chemistry Modeling of the Thermochemical Conversion of Biomass in a Fluidized Bed Gasifier

by

Addison Killean Stark

Submitted to the Department of Mechanical Engineering
on January 6, 2015, in partial fulfillment of the
requirements for the degree of
Doctor of Philosophy in Mechanical Engineering

## Abstract

The thermochemical conversion of biomass to fuels via syn-gas offers a promising approach to producing fungible substitutes for petroleum derived fuels and chemicals. In order for these fuels to be adopted, they must be produced in a cost-competitive way. Unfortunately, there exist a number of challenges in the chemical conversion of solid fuels to the gaseous intermediate syn-gas at an industrially relevant scale due to the complex interplay of chemical kinetics and transport processes which must be addressed to improve the feasibility of this conversion. In this thesis the multiple scales of the chemical conversion of solid biomass in a fluidized bed biomass gasifier (FBBG) as well as the influence of transport processes are analyzed and detailed models are developed capable of predicting reactor performance over a wide range of operating conditions on industrially relevant (fast) computational timescales.

First, the particle scale conversion, devolatilization, is considered and a model is developed capturing the interactions of external and internal heat transfer with primary devolatilization chemistry. It is shown that the particle diameter, via internal heat transfer, plays a controlling in the conversion kinetics which is manifested in both the particle conversion time as well as the product gas distribution. This is later shown to play an important role in the gas-phase conversion of the devolatilization products, and a direct correlation is shown between particle diameter and polycyclic aromatic hydrocarbon (PAH) production in a pyrolysis reactor.

Next, a reactor network model (RNM) is developed for FBBGs utilizing a detailed chemical kinetic modelling frame-work. The influence of reactor conditions (temperature, air-fuel ratio and residence times) on tar and PAH formation is elucidated, and improved kinetics are proposed that capture catalytic effects of solids on the gas conversion. This RNM is also extended to a reactor operated under pyrolytic conditions yielding good agreement with experimental results.

Finally, the influence of solids-solids mixing and bubble growth in the bed on the chemical conversion in the reactor is analyzed with reactive 3D computational fluid dynamic (CFD) simulations, and an improved RNM is developed capable of capturing inhomogeneity in the bed-zone. It is shown that both non-uniform devolatilization

zones and oxidant by-pass in the bubble phase lead to relatively rich zones in the emulsion which are suitable for PAH formation and growth. Operational strategies are proposed for the minimization of these inhomogeneities, in order to maximize the carbon conversion efficiency to syn-gas.

Thesis Supervisor: Ahmed F. Ghoniem
Title: Ronald C. Crane (1972) Professor of Mechanical Engineering

# Acknowledgments

There are many people who have influenced the development of this work in large and small ways. I am grateful for you all.

This work was funded by BP.

The Doctoral Thesis Committee consisted of the following members,
to whom A.K. Stark is forever grateful:

Professor Ahmed F. Ghoniem .....
Thesis Supervisor
Ronald C. Crane (1972) Professor of Mechanical Engineering

Professor Cullen R. Buie .....
Member, Doctoral Thesis Committee
Assistant Professor of Mechanical Engineering

Professor William H. Green .....
Member, Doctoral Thesis Committee
Hoyt C. Hottel Professor of Chemical Engineering

Professor Yuriy Román .....
Member, Doctoral Thesis Committee
Assistant Professor of Chemical Engineering

# Contents

# List of Figures

# List of Tables

# Chapter 1

# Introduction

Much consideration has been paid to the investigation of the conversion of biomass to fuels and chemicals since the oil crises of the 1970s; and current existential and economic conditions, such as global warming and volatile global oil prices, have fueled a resurgent interest in research focusing on novel conversion pathways from biomass to liquid petroleum substitutes. The most noticeable activities have been in the development of biological conversion routes for the production of ethanol from agricultural crops and lignocellulosic materials. There is a growing interest; however, in thermochemical conversion pathways such as slow-pyrolysis, flash-pyrolysis and gasification as independent conversion processes and/or for use with biological conversion in integrated bio-refineries in order to produce drop-in ready petroleum substitutes and chemical feedstocks [25]. Additionally, the use of biomass combustion and biomass/-coal co-firing is being expanded for heat and power systems due to its lower $CO_2$ intensity and resource abundance in certain regions [115].

The above-mentioned thermochemical conversions pyrolysis, gasification and combustion share many of the same physical and chemical sub-processes that characterize the overall conversion process from solid fuel to combustible gaseous intermediates and ultimately to gasification and combustion products ($CO_2$, $H_2O$, etc.). These processes are simply separated by the availability of oxygen in the system [2, 3, 39].

In this chapter biomass is introduced as a potential fixed carbon and energy feedstock, with particular focus on its potential for employ in thermochemical conver-

sion technologies. Further, pyrolysis, gasification and combustion technologies are discussed within context of their market applications. Fluidized Bed Biomass Gasification technology is identified as being of particular interest in this thesis and the technology is further elucidated. Next, the multi-scale analytical framework employed in consideration of and modeling the chemical conversion pathways of biomass in a fluidized bed biomass gasifier is described. Finally, the scope, layout and contributions from this thesis are highlighted.

## 1.1 Biomass Conversion to Fuels and Chemicals

The biological materials of plants and plant-derived materials, animal waste, and municipal wastes are often categorized collectively as biomass when referenced as potential feedstocks in the production of energy, fuels and/or chemicals. In the US alone it has been estimated that more than one billion dry tons of biomass could be sustainably harvested for use as an energy feedstock [110]. Previous work has estimated the potential biofuel production from this resource to be on the order of 60 billion gallons of gasoline equivalent (GGE) per year, or 45$ of the 134 billion gallons of gasoline consumed in the US in 2013 [133]. While, the overall environmental impact of such large harvests of biomass for use as an energy feedstock has been an issue of intense debate, though it is widely agreed that biomass will play a major role in any renewable energy future [129].

The most abundant type of biomass being considered for use as an energy feedstock is plant and plant derived materials and is therefore the focus of this thesis. This category can be further divided into subcategories: (1) Sugars and starchy biomass, (2) Lignocellulosic biomass, and (3) bio-oils. Currently, sugars and starchy biomass are the dominant feedstock used in bio-energy production, namely in the production of ethanol, where corn (maize) is the primary feedstock in the US and sugarcane is that in Brazil, the world's second largest biofuel producer by volume and largest by percentage of fuel consumed. For the US agricultural sector, the production of biofuels has become such an important industry that, in fact, corns use as a feedstock

for biofuel production is now becoming its primary market destination [47]. Bio-oils, such as soybean oil and canola (rapeseed), also play a major role in the current bio-energy industry since they are used in the production of biodiesel, though the overall production and utilization of biodiesel is much lower than that of ethanol from sugary feedstocks and fundamentally limited due to the challenges of integrating the oxygenated fuel into modern compression ignition engines [133].

Lignocellulosic biomass is seen as the ideal biomass-feedstock for energy production because it, unlike the starches, sugars and oils, does not face the so called food-versus-fuel trade-off [136]. Rather it can be sourced from agricultural residiues, such as corn stover (the stalk, husk and cob), cereal grain straw and wood waste as well as dedicated energy crops such as switchgrass, miscanthus or fast-growing woods such as willow.

### 1.1.1 Lignocellulosic Biomass as a Fixed Carbon Source

As the name lignocellulosic (or cellulosic) biomass suggests, it is made up of the primary constituents: lignin, cellulose and hemicellulose, with smaller concentrations of lipids, proteins, simple sugars, starches, water, hydrocarbons, ash, and other compounds. In Figure 1-1 the representative chemical structures of these three main biopolymers are illustrated. Lignocellulosic biomasss level of oxidation is much higher than that of coal; typically oxygen makes up 30-40% by weight of the dry matter [74]. This high degree of oxidation results in lower per mass heating values of biomass as compared to coal. Of the main constituents, lignin has a lower oxidation level (O:C ratio) and a lower H:C ratio, giving it a higher heating value, while cellulose and hemicellulose, being polysaccharides, have much higher O:C ratios, decreasing their heating values, but their higher H:C ratio somewhat dampens this effect [74]. These trends can be observed in Figure 1-2 where typical values of coals, peat and lignocellulosic biomasses are plotted on in a van Krevelen diagram.

Lignocellulosic biomass can be further divided into two broad subcategories: (1) woody biomass and (2) herbaceous biomass. Woody biomass is higher in lignin due to the greater development of cell walls, and as such has a higher heating value than

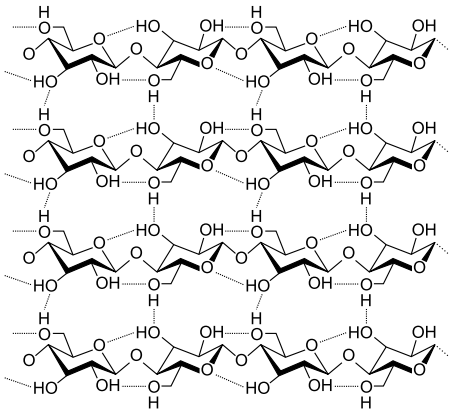

Cellulose

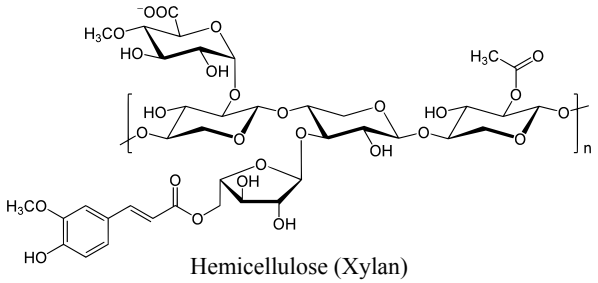

Hemicellulose (Xylan)

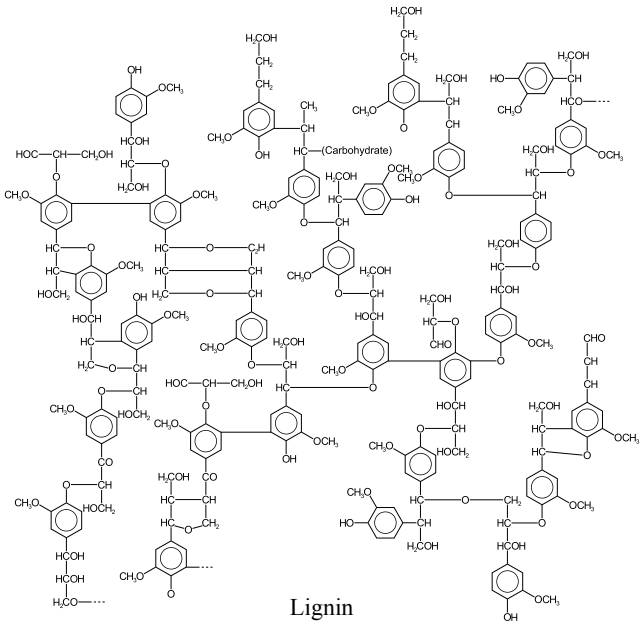

Lignin

Figure 1-1: Representative chemical structures of the three main biopolymers of biomass. Cellulose is a long straight-chained structural polysaccharide of $\beta(1 \rightarrow 4)$ linked D-glucose units, Hemicellulose is a short highly-branched heteropolymer of a mixture of sugars, and lignin is an amorphous heteropolymer of monolignols. Adapted from [60, 84]

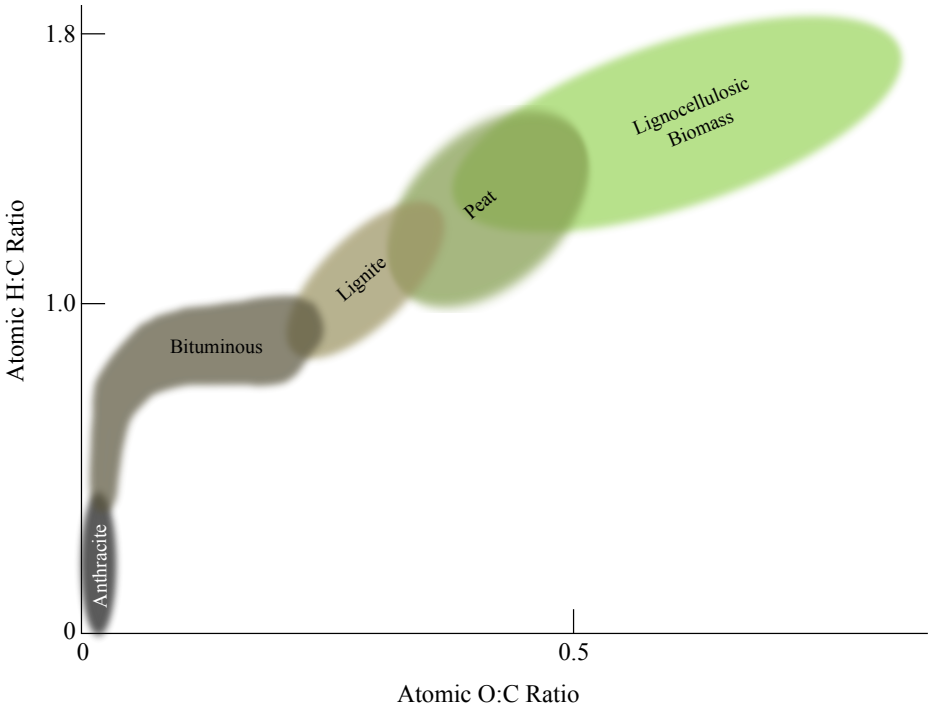


Figure 1-2: Comparison of atomic ratios of different classes of biomasses and coals. The heating value [Energy/Mass] increases in the north-west direction, with increasing H:C ratio and decreasing O:C ratio. Adapted from Jenkins (1998) [74].

herbaceous biomass as well as having a higher mass density due to the denser cellular structure [126,131]. Herbaceous biomass, sourced from grasses, has a higher H:C ratio than woody biomass, but often has higher amounts of less desirable elements such as sulfur, nitrogen and phosphorous which can cause down-stream clean-up challenges in a biomass conversion plant although biomass does have a lower ash content on average [36].

Biomass is composed primarily of three macro biomolecules: cellulose, hemicellulose and lignin; the characteristics of these three compounds are tabulated in Table 1.1. Hemicellulose and cellulose share many characteristics because they both are polysaccharides - polymers of sugars. Whereas cellulose is composed of long, straight chains ( $10,000DP$) of glucose, hemicellulose is composed of highly branched chains of a variety of different sugar monomers depending on the type of plant. Further, they both evolve similar pyrolysis products, including anhydrosugars and other monomeric derivatives [2].

Table 1.1: Characteristics of Cellulose, Hemicellulose and Lignin [29, 57]

| | Cellulose | Hemicellulose | Lignin |
|---|---|---|---|
| Chemical Composition and Biological Purpose | Composed of linear, semicrystalline anhydro beta glucopyranoside chains. | Mixture of polysaccharides that form an integral part of the cell wall | Phenolic polymer which encases the polysaccharides of the cell wall |
| Types | Xylans, Glucomannans, Arabinogalactans | | Gynosperm (softwood), Angiosperm (hardwood), Grass lignins |
| Decomposition Temperature | $200 - 300^{\circ}$ | $275 - 350^{\circ}$ | $200 - 600^{\circ}$ |

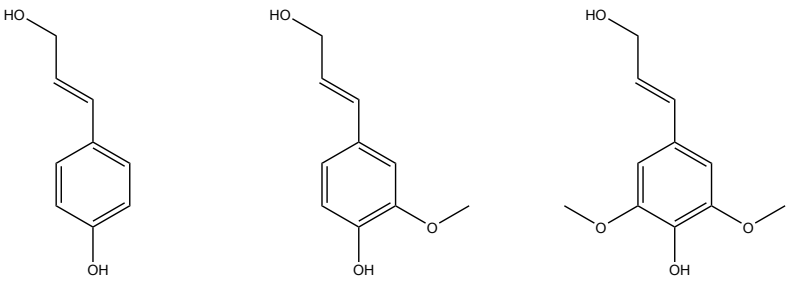


Figure 1-3: Representative Lignin Monomers, adapted from Nag (2009) [104].

Lignin, on the other hand, is not a regular long-chain polymer but instead a heavily branched amalgamation of phenylpropanoids [10, 79, 111]. There are three primary phenylpropanoids present in lignocellulosic biomass - p-hydroxyphenyl, guaiacyl and syringal - the ratios of which depend on the type of plant. Additionally, a small number of isomeric variations on these phenylpropanoids are present, as well as other types configurations and cross-linkages. Figure 1-3 shows a representative structure of these phenylpropanoids and the different functional groups defining the three primary types.

### 1.1.2 Conversion Pathways of Biomass to Fuels and Chemicals

Due to its chemical diversity and ubiquity, biomass is utilized as a feedstock in a number of conversion pathways for the production of energy, heat, fuels and chemicals, as previously mentioned. In Figure 1-4 the commercial and potential conversion technologies of bio-oils (oil crops), sugary & starchy crops (cereal grains, corn, sugar cane) and lignocellulosic biomass are shown. The dominant pathways commercially are transesterification of oil crops to biodiesel and fermentation of sugary & starchy crops to ethanol.

A variety of conversion pathways are currently under development for lignocellulosic biomass. Because of the large fraction of polysaccharides (cellulose and hemicellulose) there has been a strong focus on the development of pre-treatment steps

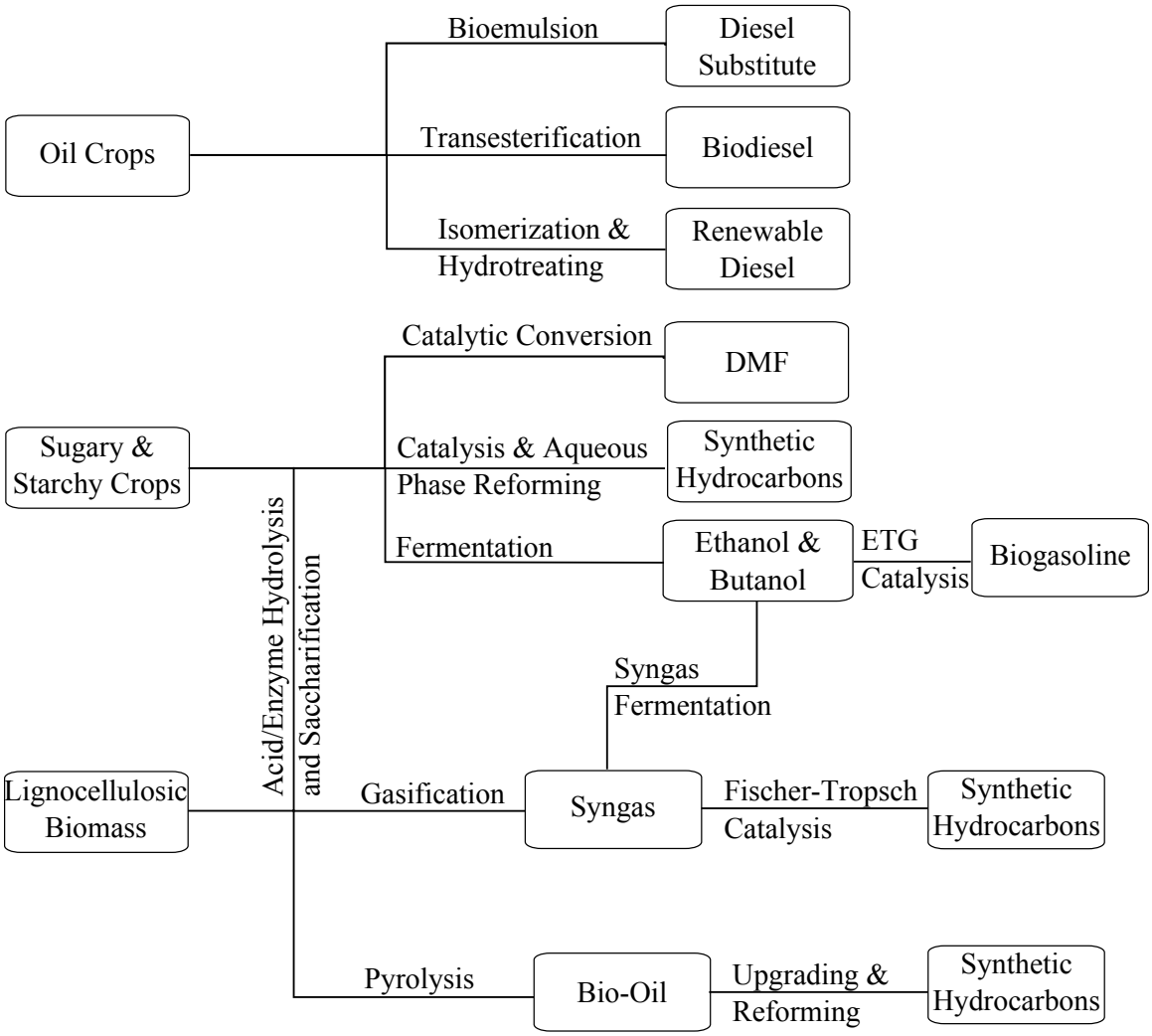


Figure 1-4: Major conversion pathways from biomass to fuels. Adapted from the Advanced Biofuels Association (ABFA).

to liberate the sugar monomers for fermentation as is done with sugar and starch crops. This conversion technology, however does not utilize the lignin fraction of the feedstock, which contains much of the fixed carbon and heating value.

The thermochemical conversion pathways, gasification and pyrolysis, have the potential to utilize the entire amount of biomass in autothermal conversion processes. Pyrolysis produces a highly oxygenated liquid bio-crude which can then be upgraded via catalytic hydrogenation to diesel and gasoline substitutes. Gasification, on the other hand produces a homogenous reactive gaseous intermediate in the form of syngas which can then be converted to a plethora of fuels and chemicals via traditional petrochemical and catalytic synthesis routes which have been previously commercialized. In the following section these thermochemical conversion pathways are considered in more detail.

### 1.1.3 The Thermochemical Conversion of Biomass

The thermochemical conversion of biomass has been employed by mankind as a technology for the generation of heat for cooking and warmth for at least 1.2 million years and can therefore be classified as one of humanities' oldest technologies [19]. The main conversion employed through history has been open-air (naturally aspirated) combustion of raw biomass - woody, herbaceous and dried animal dung - for heat, light and cooking. Low-temperature pyrolysis of biomass to charcoal has been employed by mankind as a fuel updgrading and preservation technology for 30,000 years, with the earliest evidence being it's application in charcoal cave drawings. Its large-scale ramp-up as a commercial enterprize was in parallel with the development of metallurgy in the early Bronze Age due to charcoal's higher combustion temperature resultant from its lower O:C ratio, manafested through its higher heating value [65]. Since the development of steam engines, biomass combustion has also been employed industrially for the production of mechanical work, propulsive power and most recently electricity.

Modern thermochemical conversion technologies consist of high-temperature thermal conversions with controlled sub-stoichiometric oxygen amounts - fast pyrolysis

in an oxygen free environment and gasification in a reduced oxygen environment - aimed at converting solid biomass to higher-value liquid fuels and chemicals rather than heat and/or work [112].

Gasification is a moderate-temperature ($700 - 1000°C$)thermochemical conversion process which converts carbonaceous materials into a homogeneous gaseous mixture of thermally and chemically usable chemicals. This gaseous product, known as producer or synthesis gas (syngas), is ideally composed primarily of $H_2$ and CO, but the complete combustion products $CO_2$ and $H_2O$ as well as $CH_4$ and a tar fraction ($C_{6+}H_nO_m$) make up the difference.

Because of its heating value, syngas can be used as a fuel for a gas turbine in order to generate electricity in an Integrated Gasification Combined Cycle (IGCC) power plant. The use of biomass-derived fuel in IGCC plants with carbon capture and sequestration forms the basis of potential carbon-negative electricity production scenarios [46]. Also, syngas can be used as the basic hydrogen and carbon building blocks for the chemical synthesis of chemicals and fuels. In particular, there exist a number of commercially available synthesis routes for syngas to drop-in-ready petroleum substitutes for spark and compression ignition engine technologies such as alcohols (methanol, ethanol and mixed higher alcohols), synthetic gasoline, Fischer Tröpsch (FT) diesel as well as dimethyl ether (DME). In Table 1.2 typical chemical distributions of commercially available FT diesel and synthetic gasoline processes are tabulated. It is clear that high quality fuels of comparable or better quality than their petroleum-derived equivalent can be marketed.

## 1.2 Fluidized Bed Biomass Gasification

Due to biomass' low mass and energy density as well as the high cost of grinding biomass to small particle sizes necessary for entrained gasification Fluidized Bed (FB) reactor technology has been identified as ideal for providing sufficient solids and gas residence times necessary to convert solid biomass particles of realistic sizes (¿1mm diameter) to syngas for downstream conversion. In a Fluidized Bed Biomass Gasifier

Table 1.2: Synthetic hydrocarbon product distributions from FT Synthesis and the ExxonMobil MTG process. [45, 134]

| | Fischer-Tröpsch | | MTG |
|---|---|---|---|
| | Co Catalyst | Fe Catalyst | ZSM-5 |
| Methane | 5 | 8 | 0.7 |
| Ethylene | 0 | 4 | - |
| Ethane | 1 | 3 | 0.4 |
| Propylene | 2 | 11 | 0.2 |
| Propane | 1 | 2 | 4.3 |
| Butylenes | 2 | 9 | 1.1 |
| Butane | 1 | 1 | 10.9 |
| C5 -160C | 19 | 36 | 82.3 |
| Distillates | 22 | 16 | - |
| Heavy Oil/Was | 46 | 5 | - |
| Water Sol. Oxygenates | 1 | 5 | 0.1 |

(FBBG), raw biomass (dry or containing some moisture) is fed into a vigorously fluidized bed of a material with high thermal inertia such as sand or olavine (which has been shown to offer tar-cracking catalytic properties) which is maintained at moderate temperatures ($700 - 1000°C$. The fluidizing gas is often a mixture of the oxidant ($O_2$ or air), steam ($H_2O$) and recycled syngas components such as $CO_2$ and $CH_4$. It is intended that solids conversion occurs uniformily through the bed, and that secondary gas-phase reaction of the produced gases occur through the emulsion phase as well as in the long freeboard section above the bed before the product gases leave the reactor. In the following section the physical and chemical processes which occur in a FBBG are described and these are illustrated in Figure 1-5.

### 1.2.1 The Physical and Chemical Processes of Biomass Gasification

The processes external to and within biomass during gasification in a fluidized bed reactor are complex and highly interdependent. It is necessary to be able to directly model both the chemical and physical properties intrinsic to these thermochemical conversions on the particle scale as well as the secondary reaction occuring in the gas-

phase in order to better inform modeling of conversion processes at the reactor scale. There are a number of challenges to modeling biomass which must be considered (and are in the sections to follow) such as complex pyrolysis chemistry, particle morphology and heat transfer as well as the secondary gas-phase reaction of the devolatilization products and the need to be able to model the process across many sizes from sawdust (1mm) to woodchips (¿1cm).

Thermochemical conversion of biomass (and solid fuels in general) is characterized by the complex interplay of heat transfer, gaseous species transport, the primarily pyrolysis chemistry of the raw solid, heterogeneous chemistry of the char and gas-phase secondary pyrolysis and oxidation chemistry of the gaseous pyrolysis products [37, 39]. As such models of each of these processes are needed to fully represent the process. Due to the highly interdependent nature of the process it is important to note that the fully integrated models utility will be limited by the sub-model with the lowest fidelity, as such it is important to utilize rigorous models and simplify only where necessary and where the sensitivity of the model to the simplification is small. In the following sections the process steps are described in further detail and modeling approaches are discussed.

### Stages of Conversion

The thermochemical conversion of biomass is a continuous process defined by the interplay of a number of complex processes and cannot, strictly speaking, be characterized as a series of discrete steps, however it is useful to consider the primary stages when qualitatively discussing conversion. With this framework the conversion can be thought of being composed of the following steps:

1. *Drying* - Characterized by processes occurring at temperatures around 100°C in which moisture is liberated by evaporation.

2. *Devolatilization* - The chemical conversion by which the raw biomass is converted to gases (>70%) and char. These conversions happen in the temperature range of 200°C<600°C, and the product distributions are a function of the

reaction temperature.

3. *Secondary pyrolysis and gas phase reactions* - The intermediate devolatilization products undergo further pyrolytic reactions, heterogeneous reactions with the char, tar cracking & oxidation and PAH growth reactions in the gas-phase of the reactor.

4. *Char consumption* - After the solid devolatilization process is complete, the remaining solids undergo relatively slower oxidation reactions as well as loss from the reactor through fines elutriation. Models of this conversion have been developed for biomass char elsewhere and this step is not addressed in this work [43, 95].

The major chemical conversion pathways of biomass in a FBBG are illustrated in Figure 1-6. During the first stage of conversion, devolatilization, more than 80% of the solids mass is converted to a variety of gaseous products. In the next section, previous work on modeling these major conversion processes are briefly reviewed.

## 1.3 Multi-Scale Chemistry Modeling

The thermochemical conversion of biomass has been an active area of intense research since the mid 1970s due to concerns of energy security and global warming; further a considerable amount of work has been done more generally on the conversion of coal and other solid carbonaceous fuels. All of the work in this area has lead to considerable insights and understanding which can be utilized in the development of predictive conversion models. Further, there has been some effort toward the development of predictive models of biomass pyrolysis, gasification and combustion. Major previous works are discussed below.

The previous attempts at the development of a comprehensive predictive model of FBBGs those including the interactions of heat transfer, mass transfer, fluid dynamics and chemical conversion have previously use a severely limited model of the chemical conversion trading knowledge of the compositions of the tars for

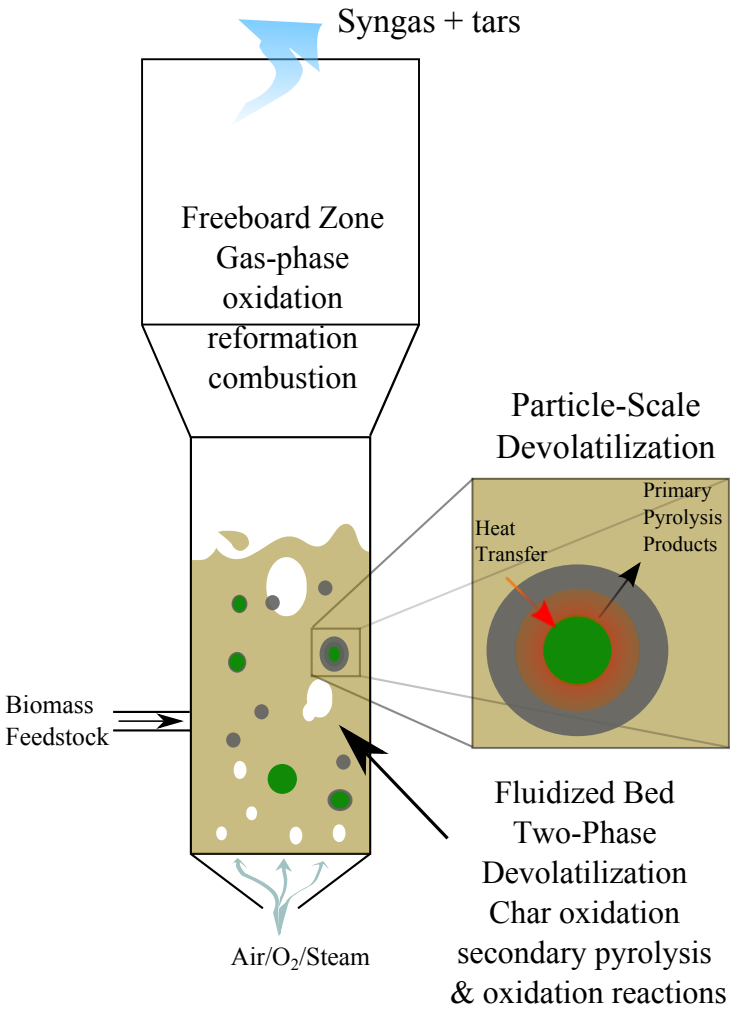


Figure 1-5: Schematic of a fluidized bed biomass gasifier.

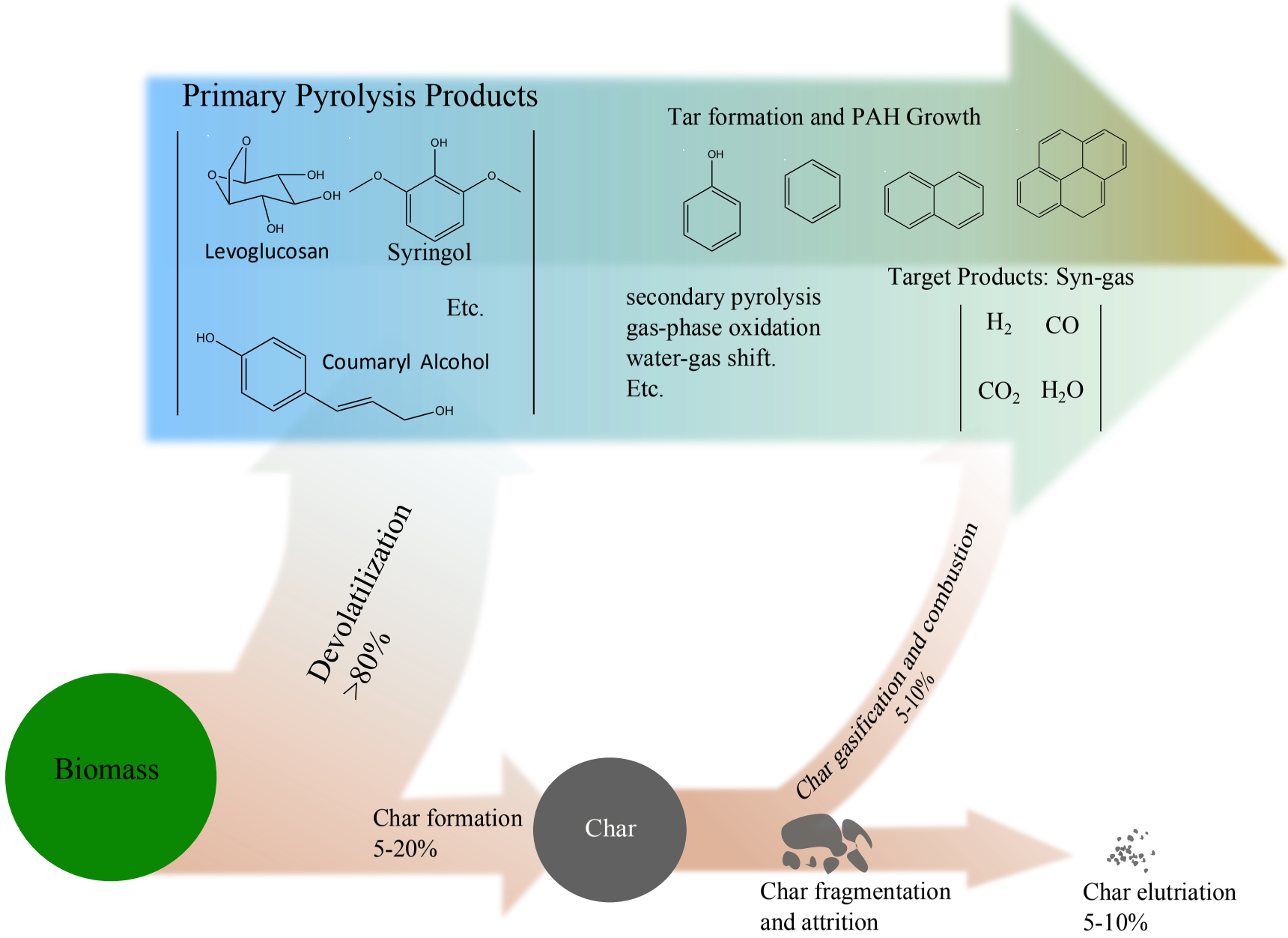


Figure 1-6: The carbon conversion pathways of biomass under fluidized bed gasification conditions.

computational simplicity. The most complex models utilize a reaction network of four pseudo-components and five reaction pathways for particle devolatilization while the existence of hundreds of species has been experimentally confirmed.

Much work in the field of the chemical conversion of biomass has been aimed at understanding the reaction pathways of the pure components of biomass (cellulose, hemicellulose and lignin) and much qualitative insight into the intermediate pyrolysis products can be gleaned from many previous studies on cellulose and hemicellulose [2–7, 32] and lignin [5, 10, 71, 73, 111]. Additionally, there has been more limited work towards the development of more comprehensive reaction pathway models of the conversion of these molecules including Ranzi et al and Neves et al [106, 119].

In Pyle and Zarors 1984 study simplified predictive models of the conversion of biomass were developed for certain limiting cases kinetic control, external heat transfer control, etc utilizing simplified geometries a one step chemical mechanism and isotropic heat and mass transfer [114]. In each of these simplified limiting cases explicit analytical solutions are outlined, however it is important to note that many of these simplifications are very strong and render the generality of the models applicability. Recently there has been work undertaken towards the development of more rigorous particle models of thermochemical biomass conversion, such as those of Lu et al and Yang et al, which capture anisotropic characteristics of biomass, utilize competing reaction pathways (albeit highly simplified) and are able to consider the effects of external flows [91,143]. These more advanced models however do not utilize a sufficiently extensive chemistry model to represent the variation of tar components in different reaction conditions.

More recent work has been focused on the improvement of critical sub-models necessary for improved fidelity of particle-scale conversion models. Also there has been substantial work towards improving the modeling capabilities of the secondary gas-phase reaction of devolatilization products which can accurately predict the conversion of biomass to syngas as well as capture the dynamics of tar growth and conversion [26, 42, 118–120].

Lastly, there exist a number of comprehensive reviews of biomass conversion mod-

eling both at the reactor and particle scale from which to draw empirical data and theoretical observations at the heart of the modeling enterprise. These include works focusing primarily on the chemical conversion aspects [2, 3, 24, 39, 101, 113], reactor scale concerns [23, 31, 99, 124] and those focused on the development of predictive models of conversion at the particle scale [37, 39].

## 1.4 Scope of the Present Study

This primary focus of this thesis is the consideration and development of predictive multi-scale chemistry models of biomass gasification in a fluidized bed reactor.

In Chapter 2 the conversion of solid biomass to reactive gaseous intermediates and char, or the devolatilization step, is analyzed. Further, a detailed lagrangian particle model incorporating external and internal heat transfer with thermochemical kinetic conversion is developed and used to to identify the major controlling parameters of biomass devolatilization in the FBBG operating regimes.

In Chapter 3 a shrinking-core model of biomass devolatilization for use in reactive Eulerian CFD simulations of FBBGs is developed and validated against the lagrangian particle model developed in Chapter 2

In Chapter 4 the gas-phase conversion of the devolatilization gasses from the biomass fuel to syngas, tars and other byproducts are considered. A 1-D reactor network model of a FBBG is developed which takes the particle-scale devolatilization model developed in Chapter 2 as an input.

In Chapter 5 the particle and reactor network models developed in Chapters 2 and 4 respectively are applied to a fluidized bed pyrolysis reactor developed at the National Renewable Energy Laboratory (NREL) in order to investigate the inpact of particle diamter and temperature on polycyclic aromatic hydrocarbon formation and growth.

In Chapter 6 the influence of the superficial gas velocity on the fluidization regime, solids-phase mixing and devolatilizing particle segregation is assessed in context of the influence on the chemical conversion. Reactive 3D CFD simulations are employed

to study the inter-dependencies of these parameters. The reactor network model developed in Chapter 4 is extended to capture these effects.

In Chapter 7 the influence of the ratio of the bed diameter to the fuel particle diameter on solids mixing and solid-reaction zone segregation (drying and devolatilization). Reactive 3D CFD simulations are employed.

In Chapter 8 overall results, trends and conclusions from this multi-scale work are drawn and recommendations for future work are given.

# Chapter 2

# Modeling of Biomass Devolatilization in a Fluidized Bed Gasifier

Particle-scale modeling of the thermochemical conversion of biomass offers insight into the fundamental physics of biomass conversion, and has been previously utilized as a tool to predict the physical evolution such as mass loss rates and resultant char density of a devolatilizing particle. Seminal work by Bamford et al. [14] investigated the conversion of biomass under combustion conditions utilizing a 1-D infinite slab model coupling heat transfer with a one-step reaction model of conversion. This analysis was extended by Pyle and Zaror [114] to cylindrical and spherical geometries with experimental validation of the center-line temperature. Advances in chemistry modeling were made by Chan et al. [27, 28] by incorporating the primary pyrolysis model of Shafizadeh [130] to predict gas, tar and char yields.

Detailed particle-scale modeling studies have improved the physical representation of the particle, but have continued to use simplified models of biomass pyrolysis: Babu and Chaurasia [11] considered the impact of a shrinking diameter particle, Lu et al. [91] coupled with gas-phase combustion reactions and Yang et al [143] developed a 2-D formulation of the particle within a reacting flow to study the interplay of combustion processes with particle conversion. Additionally, there has been informa-

tive experimental work performed on both herbaceous and woody biomasses under coal-fired combustion conditions [20], and under fluidized bed conditions [93,121,122].

The incorporation of detailed pyrolysis models into a particle model has been explored under high-temperature flash pyrolysis conditions [42], Blondeau and Jeanmart investigated devolatilization of an anisotropic particle under severe temperatures (greater than 1000K) [22], and Ranzi et al integrated comprehensive chemistry with a spherical particle model into a reactor-scale model of a fixed bed biomass gasifier and a traveling grate combustor [118].

Here, we consider two common reactor configurations for the study of biomass gasification: (1) particle devolatilization undergoing natural convective heating in an isothermally heated experimental thermogravinometric analysis (TGA) reactor at moderate temperatures [114], which is common in particle-scale experimental studies of devolatilization, and (2) devolatilization in an atmospheric pressure FBG at high temperatures [138]. Both of these set-ups are discussed in section 2.2.

In section 2.3, the mathematical model of the thermochemical conversion of biomass at the particle scale is described. Then, in section 2.4 the physical and chemical processes occurring in the two reactor regimes are analyzed and a sensitivity analysis of the particle model is employed to assess the impact of physical parameters on the predicted chemical species distribution of primary pyrolysis. Finally, in section 2.5 implications for gasifier operation are discussed.

First, however, in section 2.1 the physiochemical processes of devolatilization are discussed with particular focus on the pyrolysis chemistry of the major lignocellulosic fractions - cellulose, hemicellulose and lignin.

## 2.1 Physiochemical Process of Devolatilization

The devolatilization of dry biomass is characterized primarily by the interplay of the kinetics and thermochemistry of primary pyrolysis reactions and heat transfer to and through the biomass itself. In the following subsections these processes are discussed in detail and fundamental scientific and modeling work for the prediction of these

processes are reviewed.

### 2.1.1 Chemistry

Relative to coal, the volatile content of biomass is much larger (¿80%), and thus plays a larger roll in defining the whole conversion process. Devolatalization is the stage in which, after or concurrently with drying, raw biomass begins to chemically convert to gases and tars leaving behind a high-carbon solid residue known as char. The devolatilization process is characterized by being oxygen deprived and thus a pyrolysis process, where the pyrolysis products do not undergo oxidation until they leave the particle and mix into the reacting gases of the emulsion and freeboard. Below the pyrolysis chemistries of pure components are considered followed by global models for raw biomass.

#### Pure Component Pyrolysis Models

The bulk of work that has been done towards understanding the chemical mechanism of biomass pyrolysis has been in studying pure component reactions those of cellulose, hemicellulose and lignin. The goal of this work is to be able to then integrate these reaction mechanisms in order to approximate the chemistry of whole raw biomass. The most developed work in this regard has been for pure cellulose. Additionally, these reaction mechansisms are assumed to be analogous to that for hemicellulose, save for different kinetic constants and dehydrated sugar monomers. There has been much less work on the modeling of lignin pyrolysis mechanisms, although there do exist a small number of in-depth studies. In the following sections the studies of these pure components are considered.

#### Cellulose and Hemi-Cellulose Pyrolysis

Cellulose is the most studied component of biomass pyrolysis. The pure cellulose that is studied is purified via the Kraft paper making process so is often paper samples that are used (filter paper, for example) though there are a few incidences natural

pure cellulose such as cotton. It is important to note that the experimental results for these pure cellulose samples may not be applicable to the cellulose portion of raw biomass due to the harsh separation process [30], or the lack of other components such as lignin and ash, which have a non-linear effect on the conversion of cellulose. Pure cellulose studies are informative however because the intermediates, levoglucosan and the anhydrosugars, are found to be major components of the evolved tars.

Cellulose pyrolysis is characterized by competing reaction pathways at different temperature ranges. At low temperatures (below $300°C$) the primary reactions are depolymerizations to oligosaccharides along with minor weightloss with remaining levoglucosan and oligosaccharides above $250°C$.

From $300 - 500°C$ the reaction pathways are dictated by the crystalline and fine structures of the cellulose. In crystalline areas reaction is suppressed to higher temperatures with selective evolution of anhydrosugars versus levoglucosan.

In practice, solid phase cellulose is not exposed to temperatures above $500°C$ as the majority of cellulose is converted to intermediates, gas and char by the time the solid temperatures approach $500°C$. Thus, at these temperatures the gas-phase phase reactions of levoglucosan and other intermediates begin to dominate. The most advanced models for cellulose pyrolysis allow for competitive pathways to either dehydrated cellulose or to depolymerized cellulose (levoglucosan) along with pathways to a number of oxygenated derivatives.

In this thesis the devolatilization model developed by the CRECK modeling group at Politecnic Milano is employed in the development of a particle-scale devolatilization model. In the kinetically controlled regime, this kinetic model has been shown to accurately predict the mass-loss curves of cellulose hemicellulose and lignin for various reactor heating rates. In Figure 2-1 kinetic predictions of cellulose devolatilization are compared with experimental data published by Milosavljevic & Suuberg (1995) [102].

### Lignin Pyrolysis

Whereas cellulose and hemicellulose are characterized by long repeating chains of one (or a hand full of) sugars, lignin is a highly branched mesh of a number of different

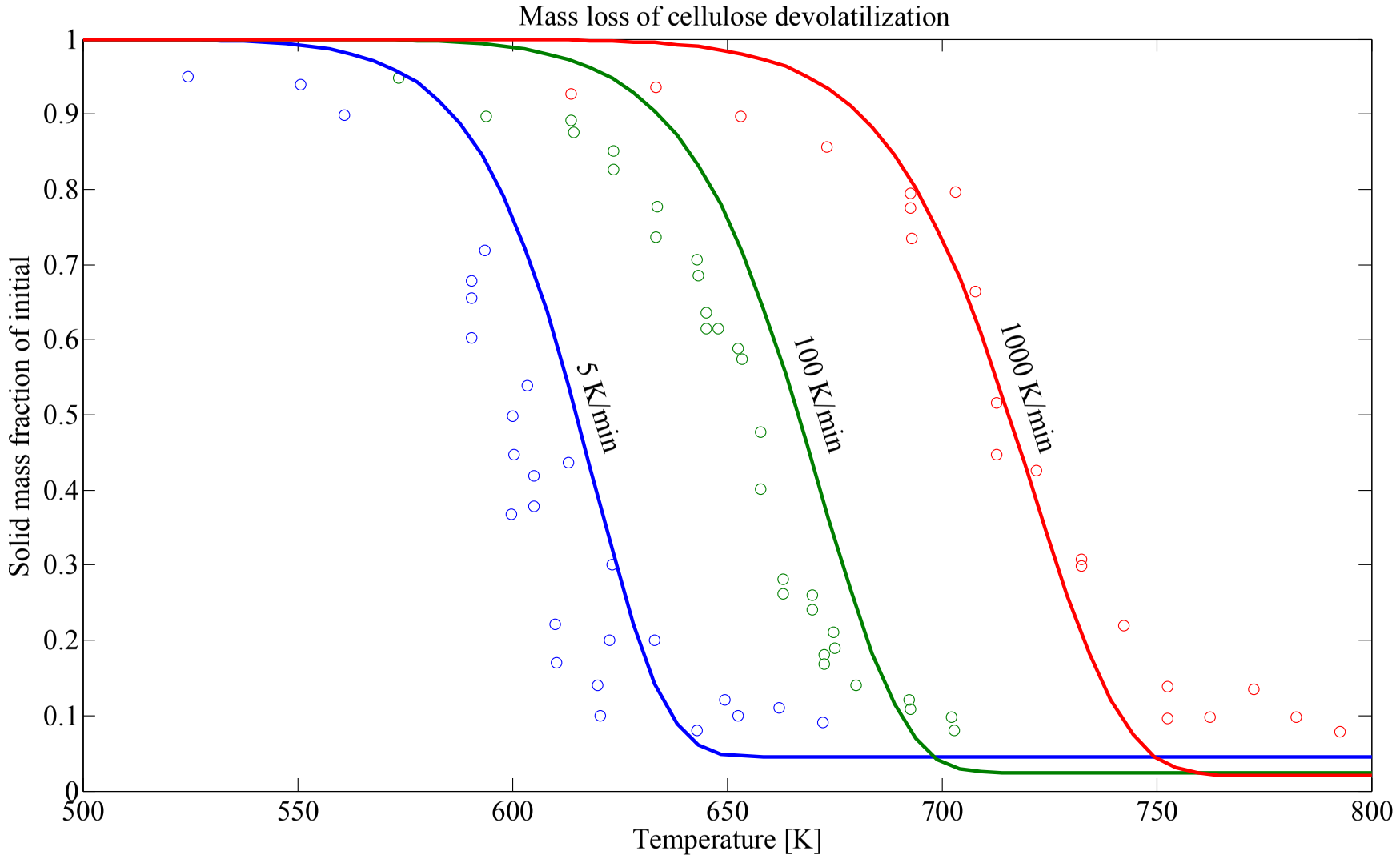


Figure 2-1: The mass-loss curves predicted by the CRECK kinetic model of devolatilization vs experimental data of Milosavljevic & Suuberg [102] at various heating rates.

aromatic monomers [73,79,111]. Also because of the nature of the Kraft process which is aimed at maintaining the integrity of the cellulose for use as paper Kraft lignin is greatly changed because the process is aimed at making the lignin soluble. Therefore, the active sites have been altered along with the cross-branching structures [5, 109].

In Figure 2-2 the kinetically controlled mass-loss curves of cellulose, hemicellulose and pinewood (cellulose, hemicellulose and lignin) are compared with experimental data collected by William & Bessler (1996), exhibiting excellent qualitative and good quantitative agreement at two heating rates [140].

The most advanced models of lignin pyrolysis do involve representative intermediates such as the dehydrated monomers, along with competing reaction pathways leading to char, tar and vapors. However it is important to note that a number of the products are empirical such as refractory condensables and permanent gases which are not representative of a specific compound but generally a mixture of a number of different compounds. These pathways are often arrived at by the use of model compound studies, where a number of simpler compounds with similar active groups and bonds are used to model the kinetic behavior of the different groups. These results are then integrated together to come to a representative mechanism for the larger compound with a number of similar active groups and sites. This has been a necessary way to study lignin reaction pathways due to the complexity of the macro-molecule [79].

## 2.2 Modeling Framework

Biomass gasification is a process defined by the interplay of a number of complex processes and cannot, strictly speaking, be characterized as a series of discrete steps. However it is useful to consider the primary stages of conversion when qualitatively discussing conversion. With this framework the conversion can be thought of being composed of the following steps:

1. *Drying* - characterized by processes occurring at temperatures $\leq$100°C in which so-called "free water" (i.e. moisture) is liberated by evaporation.

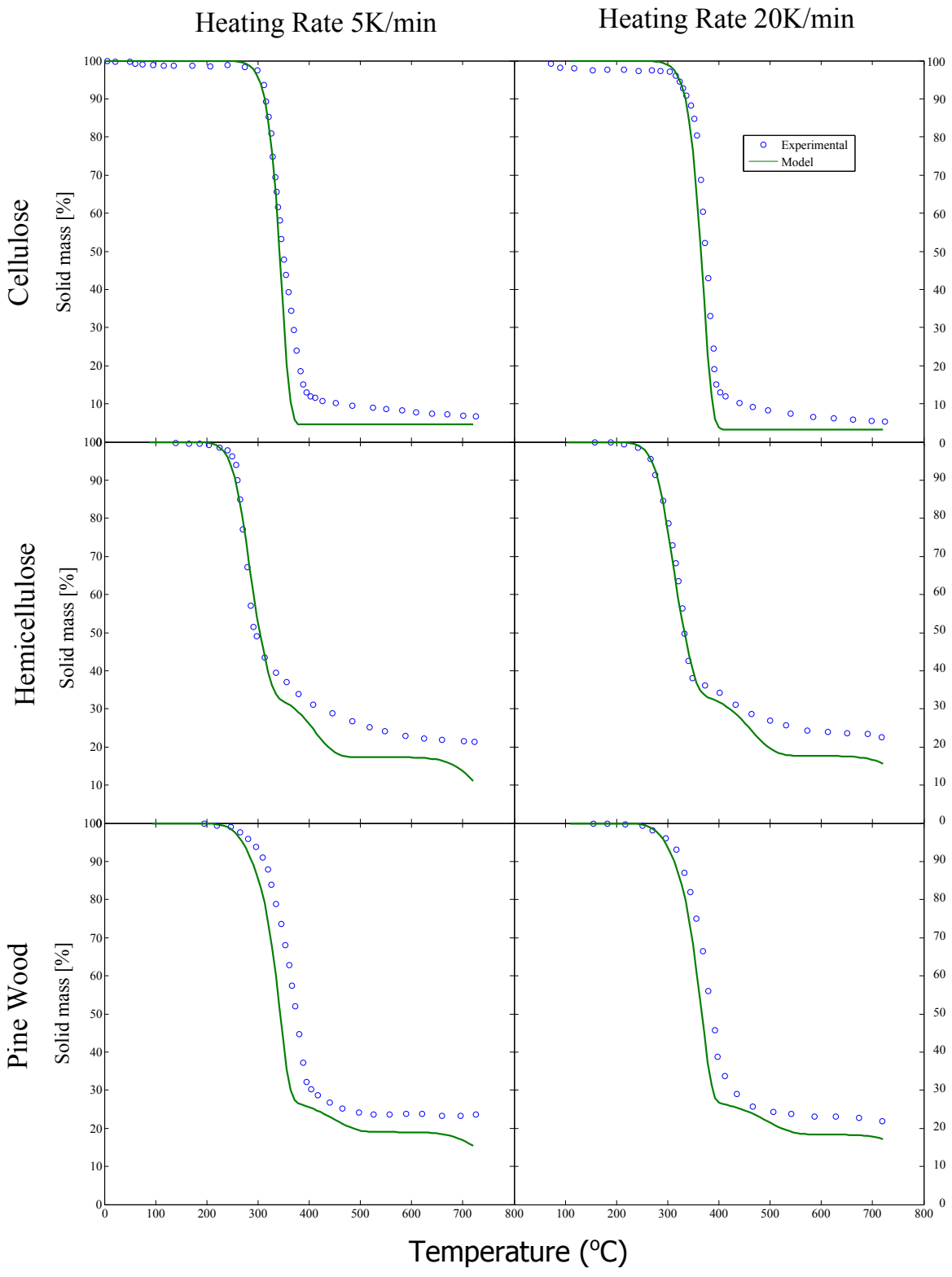


Figure 2-2: CRECK Kinetic model mass-loss curve versus experimental measurements of pure-component devolatilization at defined heating rates. Experimental data is from Williams & Bessler, 1996 [140].

2. *Devolatilization* - the chemical conversion by which the raw biomass is converted to gases (>70%) and char. These conversions happen in the temperature range of 200°C<600°C, and the product distributions are a function of the reaction temperature.

3. *Secondary pyrolysis and gas phase reactions* - many of the intermediate pyrolysis products can undergo further pyrolytic reactions, heterogeneous reactions with the char, as well as tar-cracking & -oxidation, and PAH growth in the gas-phase of the reactor.

4. *Char consumption* - after the pyrolysis processes are complete, the remaining solids undergo a relatively slower oxidation process, as well as loss through elutriation. Models of this conversion have been developed for biomass char elsewhere and are therefore not addressed here, see [43, 95].

In Figure 2-3 these devolatilization processes occurring within a particle are illustrated fora single particle of biomass in an FBG.

In this work, we are concerned with devolatilization (or primary pyrolysis) since we must accurately predict the distribution of gas-phase primary pyrolysis products and char to properly model the overall carbon conversion. Two representative experimental conditions have been selected for interrogation of the dynamics of biomass devolatilization: (1) Natural Convective pyrolysis and (2) Fluidized Bed Gasifier (FGB) conditions. The former condition, characterized by moderate temperatures and low external heat-transfer coefficients, is typical of reaction conditions used for the study of devolatilization in thermogravimetric analyses (TGA) while the later, characterized by higher temperatures and heat transfer coefficients, is representative of realistic reactor conditions relevant to industrial processes.

The devolatilization of a biomass particle in a both a natural convective TGA and in a FBG are the result of the complex interplay of heat and mass transfer with pyrolysis kinetics. It is crucial in analyzing such complex phenomena to first assess their relative time scales. These are summarized in Table 2.1. Specific heat ($c_p$), conductivity ($k$), and density ($\rho$) were estimated by Babu and Chaurasia [11], while

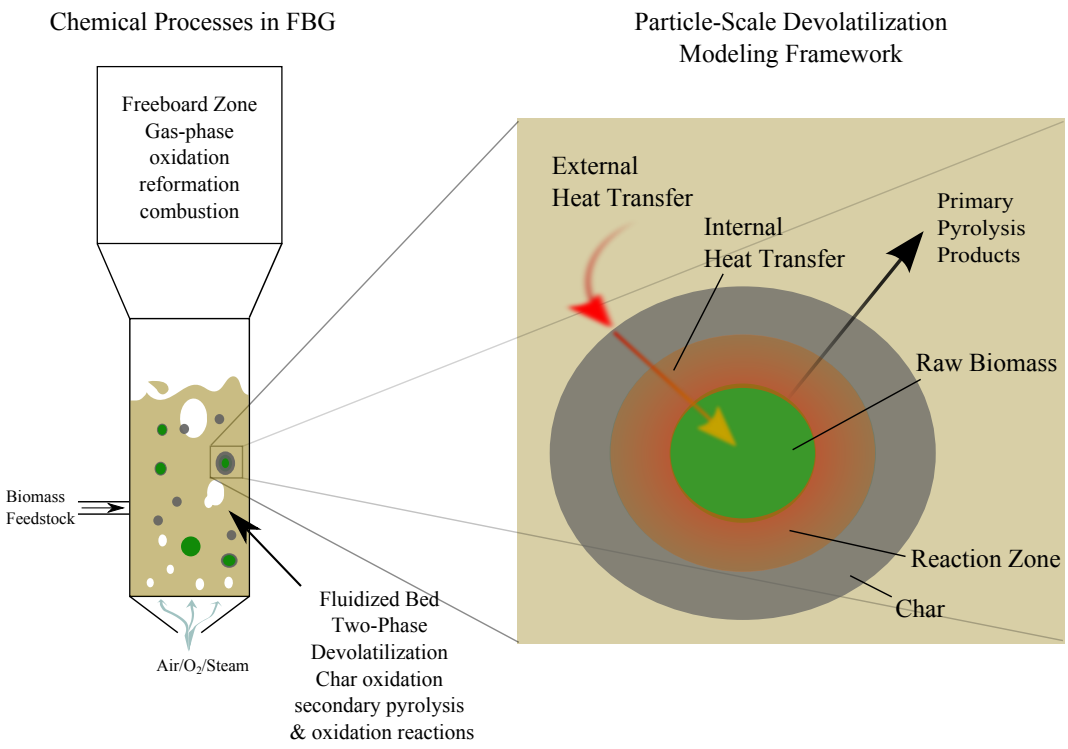


Figure 2-3: Schematic of particle-scale devolatilization processes in a FBG.

the values for diffusivity ($D$), gas viscosity ($\mu$), and permeability ($B_0$) are adapted from Lu et al. [90]. The solid mass loss reaction rate ($K$) was evaluated for pine wood using the primary pyrolysis mechanism of Ranzi et al. [26,119,120]. The length scales described in table 2.1 include the micro-scale - corresponding to the pore diameters - and macro scale - reflecting the overall biomass particle diameter.

From this time-scale analysis it is apparent that for a model of biomass pyrolysis to be generally applicable over these ranges of length scales and reactor temperatures it must accurately model the slow processes: internal & external convective heat transfer, internal conductive heat transfer and primary pyrolysis reaction kinetics. Each of these processes are, on both the micro and macro length scales, two to eight orders of magnitude slower than internal mass diffusion and intra-particle fluid flow.

For each of these two cases, the natural convective TGA devolatilization and the FBG devolatilization we can qualitatively characterize their anticipated controlling factors with three dimensionless numbers employed by Pyle and Zaror [114] to char-

Table 2.1: Order of magnitude analysis of chemical and physical phenomena during biomass devolatilization for intra-particle processes (Micro-scale) and inter-particle processes (Macro-scale) at the experimental conditions of Pyle and Zaror [114] - and the FB conditions of van Paasen and Kiel [138].

| | **Characteristic Time (s)** | | | |
|---|---|---|---|---|
| | Micro-Scale $L = 10\mu m$ | | Macro-Scale $L = 1cm$ | |
| Transport or Reaction Process | TGA [114] | FBG [138] | TGA [114] | FBG [138] |
| Diffusion, $L^2/D_{eff}$ | $10^{-5}$ | $10^{-5}$ | $10^{1}$ | $10^{1}$ |
| Intra-particle fluid flow, $\mu L^2/\Delta p B_0$ | $10^{-5}$ | $10^{-5}$ | $10^{1}$ | $10^{1}$ |
| Convective Heat Transfer, $(\rho c_p)_g L/h$ | $10^{1}$ | $10^{3}$ | $10^{4}$ | $10^{3}$ |
| Conductive Heat Transfer, $(\rho c_p)_s L^2/k$ | $10^{-3}$ | $10^{-3}$ | $10^{3}$ | $10^{3}$ |
| Primary Pyrolysis Kinetics, $1/\bar{K_l^{-1}}$ | $10^{3}$ | $10^{3}$ | $10^{3}$ | $10^{3}$ |

$D_{eff} \approx 10^{-5} m^2 s^{-1}$
$(\rho c_p)_s \approx (8)10^6 Jm^{-3}K^{-1}$
$(\rho c_p)_g \approx (2)10^3 Jm^{-3}K^{-1}$
$\mu \approx (3)10^{-5} Pas$
$\Delta p \approx (3)10^4 Pa$

$B_0 \approx 10^{-14} m2$
$h \approx 10 Wm^2 K^{-1}$
$k \approx (3)10^{-1} WmK^{-1}$
$\bar{K_l^{-1}} \approx (5)10^{-4} s^{-1}$

Table 2.2: The non-dimensional characterization of each devolatilization case using the pyrolysis numbers and Biot number. The values in Table 2.1 are used with the model particle radius of 7.5mm.

| | TGA [114] | FBG [138] |
|---|---|---|
| Internal Pyrolysis Number, $Py^{int}$ | 1.3 | 1.3 |
| External Pyrolysis Number, $Py^{ext}$ | 0.28 | 8.3 |
| Biot Number, $Bi$ | 0.21 | 6.25 |
| Controlling factor | External Heat Transfer | Internal Heat Transfer |

acterize the relative influences of internal and external heat transfer relative to the kinetic rate: the biot number ($Bi = hL/K$), the internal pyrolysis number ($Py^{int} = k/K\rho c_p L^2$) and the external pyrolysis number ($Py^{ext} = Bi \cdot Py^{int} = h/K\rho c_p L$). These are tabulated in Table 2.2. For both cases the internal pyrolysis number is expected to be roughly constant since the devolatilization reactions have been shown to occur within a relatively narrow band of temperatures. It is important to note however, that for both cases since $Py^{int}$ is close to one the devolatilization kinetics will play a relatively equal role to heat conduction. Rather it is the influence of the external heat transfer coefficient which dominates the regime of devolatilization in this case, so it is expected that the TGA devolatilization will occur under the control of external heat transfer, while the FBG devolatilization will be controlled by both heat conduction and reaction kinetics in equal measure.

## 2.3 Mathematical Model

### 2.3.1 Primary Pyrolysis Kinetic Model

The primary pyrolysis reactions of biomass describe the conversion of the solid macromolecules cellulose, hemicelluose and lignin to a complex mixture of primary pyrolysis gases and char via solid intermediates. The primary pyrolysis of biomass occurs in the temperature range of 200°-600°$C$ depending on the reactor conditions. Hemicellulose reacts the fastest followed by lignin, then cellulose.

The kinetic mechanism of biomass pyrolysis, gasification and combustion devel-

oped by the Chemical Reaction Engineering and Chemical Kinetics (CRECK) laboratory at Politecnico di Milano is used in this modeling effort. It is comprised of a nineteen reaction primary pyrolysis (devolatilization) mechanism for cellulose, hemicellulose, lignin and trapped pyrolysis gases coupled with nearly 11,000 gas-phase reaction secondary pyrolysis, and combustion mechanism [26, 119, 120]. This mechanism has been proposed and validated previously and has been applied as a sub-model in reactor-scale modeling work. This model was used in modeling biomass flash pyrolysis in a drop-tube entrained flow reactor [42], and in the modeling of a traveling grate biomass combustor [118,120] and for high-temperature pyrolysis conditions [22].

In this work, the primary pyrolysis and trapped gas reactions are applied, coupled with a particle heat transfer model, to describe the solid-phase devolatilization. These reactions are summarized in table 2.3 and with the species summarized in table 2.4. This devolatilization mechanism is visualized in figure 2-4. Here it is observed that the reaction mechanism of each of the primary solid species follow the pyrolysis pathway proposed and described by Shafizadeh [130], where first depolymerization occurs via competing processes of chain scission and dehydration. The depolymerized species then undergo further pyrolysis to light gases and char or to gas-phase monomers such as levoglucosan, xylan and synapol aldehyde.

The coupling of this particle devolatilization model with the secondary gas-phase reactions for reactor-scale gasifier modeling is considered in forthcoming work.

### 2.3.2 Conservation of Energy

The first law energy conservation equation for the solid phase written in the non-conservative form is:

$$\rho(r,t)c(r,t)\frac{\partial T(r,t)}{\partial t} = \nabla \cdot (k(r,t)\nabla T(r,t)) + \dot{q}(r,t), \tag{2.1}$$

where $\rho$ is the solid-phase density, $c$ is the solid-phase heat capacity, $T$ is the temperature, $k$ is the solid-phase thermal conductivity, and $\dot{q}$ is the volumetric heat generation from the pyrolysis reactions. For generality these parameters are allowed to evolve in

Table 2.3: CRECK primary pyrolysis mechanism [120]. Reactions 1-15 describe the evolution of the primary biomass components - cellulose (CELL), hemicellulose (HCE), lignin (LIG-X) and their derivatives. Reactions 16-19 describe the evolution of the primary pyrolysis products caught in the cellular matrix.

| Reactions | Rate Expression $\left[\frac{1}{s}\right]$ | Heat of Reaction $\left[\frac{kcal}{kg}\right]$ | Rxn. No. |
|---|---|---|---|
| $CELL \longrightarrow CELL_a$ | $8 \times 10^{13} exp(-46000/RT)$ | 107 | (1) |
| $CELL_a \longrightarrow 0.95HAA + 0.25Glyoxal + 0.20CH_3CHO + 0.20C_3H_6O + 0.25HMFU + 0.16CO_2 + 0.23CO + 0.1CH_4 + 0.9H_2O + 0.61Char$ | $1 \times 10^{9} exp(-30000/RT)$ | 215 | (2) |
| $CELL_a \longrightarrow Levoglucosan$ | $4T exp(-46000/RT)$ | 175 | (3) |
| $CELL \longrightarrow 5H_2O + 6Char$ | $8 \times 10^{7} exp(-32000/RT)$ | -260 | (4) |
| $HCE \longrightarrow 0.4HCE_1 + 0.6\,HCE_2$ | $1 \times 10^{10} exp(-31000/RT)$ | 131 | (5) |
| $HCE_1 \longrightarrow 0.75T[H_2] + 0.125H_2O + 1.4CO + 0.8CO_2 + 0.5CH_2O + 0.25CH_3OH + 0.125C_2H_5OH + 0.625CH_4 + 0.25C_2H_4 + 0.675Char$ | $3 \times 10^{9} exp(-27000/RT)$ | 107 | (6) |
| $HCE_1 \longrightarrow Xylose$ | $3T exp(-11000/RT)$ | 169 | (7) |
| $HCE_2 \longrightarrow 0.5CO_2 + 0.5CH_4 + 0.25C_2H_4 + 0.8T[CO_2] + 0.8T[COH_2] + 0.7CH_2O + 0.25CH_3OH + 0.125C_2H_5OH + 0.125H_2O + Char$ | $1 \times 10^{10} exp(-33000/RT)$ | 62 | (8) |
| $LIG_C \longrightarrow 0.35LIG_{CC} + 0.1pCoumaryl + 0.08Phenol + 0.41C_2H_4 + H_2O + 0.495CH_4 + 0.32CO + T[COH_2] + 5.735Char$ | $4 \times 10^{15} exp(-48500/RT)$ | 144 | (9) |
| $LIG_H \longrightarrow LIG_{OH} + C_3H_6O$ | $2 \times 10^{13} exp(-37500/RT)$ | 125 | (10) |
| $LIG_O \longrightarrow LIG_{OH} + CO_2$ | $1 \times 10^{9} exp(-25500/RT)$ | 122 | (11) |
| $LIG_{CC} \longrightarrow 0.3pCoumaryl + 0.2Phenol + 0.35C_3H_4O_2 + 1.2H_2 + 0.7H_2O + 0.65CH_4 + 0.6C_2H_4 + T[COH_2] + 0.8T[CO] + 6.5Char$ | $5 \times 10^{6} exp(-31500/RT)$ | 69 | (12) |
| $LIG_{OH} \longrightarrow LIG + 0.5\,H_2 + H_2O + CH_3OH + 0.45CH_4 + 0.2C_2H_4 + 1.4T[CO] + 0.6T[COH_2] + 0.1T[H_2] + 4.15Char$ | $3 \times 10^{8} exp(-30000/RT)$ | 24 | (13) |
| $LIG \longrightarrow C_{11}H_{12}O_4$ | $8T exp(-12000/RT)$ | 138 | (14) |
| $LIG \longrightarrow H_2O + 0.5CO + 0.2CH_2O + 0.4CH_3OH + 0.2CH_3CHO + 0.2C_3H_6O + 0.6CH_4 + 0.65C_2H_4 + T[CO] + 0.5T[COH_2] + 5.5Char$ | $1.2 \times 10^{9} exp(-30000/RT)$ | -50 | (15) |
| $T[H_2] \longrightarrow H_2$ | $1 \times 10^{5} exp(-24000/RT)$ | | (16) |
| $T[CO] \longrightarrow CO$ | $1 \times 10^{13} exp(-50000/RT)$ | | (17) |
| $T[COH_2] \longrightarrow CO + H_2$ | $5 \times 10^{11} exp(-65000/RT)$ | | (18) |
| $T[CO_2] \longrightarrow CO_2$ | $1 \times 10^{13} exp(-50000/RT)$ | | (19) |

Table 2.4: Primary pyrolysis modeling species employed in CRECK model [120].

| **Solid Phase** | | **Gas Phase** | | |
|---|---|---|---|---|
| Primary Components and Products | Reactive Intermediates | Trapped Gasses | Product Gases | Chemical Formula |
| Cellulose (CELL) | Activated Cellulose (CELLa) | Hydrogen (T[$H_2$]) | Hydrogen | $H_2$ |
| Hemicellulose (HCE) | Activated Hemicellulose (HCE1) | Carbon Monoxide (T[CO]) | Water | $H_2O$ |
| Carbon-Rich Lignin (LIGC) | Activated Hemicellulose (HCE2) | CO+H2 (T[$COH_2$]) | Carbon Monoxide | CO |
| Hydrogen-Rich Lignin (LIGH) | Activated Lignin (LIGCC) | Carbon Dioxide (T[$CO_2$]) | Carbon Dioxide | $CO_2$ |
| Oxygen-Rich Lignin (LIGO) | Activated Lignin (LIGOH) | | Formaldehyde | $CH_2O$ |
| Char C | Activated Lignin (LIG) | | Methane | $CH_4$ |
| | | | Methanol | $CH_3OH$ |
| | | | Glyoxal | $C_2H_2O_2$ |
| | | | Ethylene | $C_2H_4$ |
| | | | Acetaldehyde | $CH_3CHO$ |
| | | | Hydroxyacetaldehyde | $C_2H_4O_2$ |
| | | | Ethanol | $C_2H_5OH$ |
| | | | Malonaldehyde | $C_3H_4O_2$ |
| | | | Oxetane+Propyleneoxide | $C_3H_6O$ |
| | | | Xylofuranose | $C_5H_8O_4$ |
| | | | Phenol | $C_6H_5OH$ |
| | | | 5-(hydroxymethyl)-furfural | $C_6H_6O_3$ |
| | | | Levoglucosan | $C_6H_{10}O_5$ |
| | | | pCoumaryl | $C_9H_{10}O_2$ |
| | | | 3-(4-hydroxy-3,5-dimethoxyphenyl)acryaldehyde | $C_{11}H_{12}O_4$ |

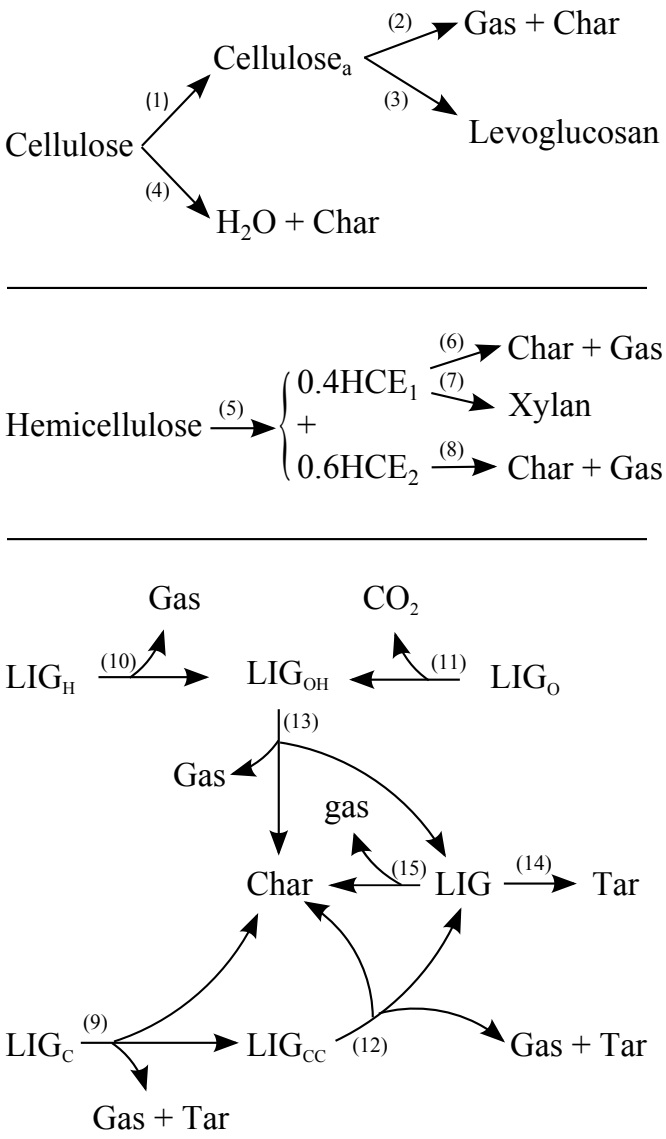


Figure 2-4: Illustration of the primary pyrolysis mechanisms of cellulose, hemicellulose and lignin. The reaction numbers are noted (see Table 2.3).

time.

Given that the conductivity, $k$, is dependent on the solid constituents and temperature which are both evolving in time it is non-constant and has spatial gradients within the reacting particle, we apply the distributive law of the dot product yielding:

$$\rho(r,t)c(r,t)\frac{\partial T(r,t)}{\partial t} = \nabla k(r,t)\nabla T(r,t) + k(r,t)\nabla^2 T(r,t) + \dot{q}(r,t), \tag{2.2}$$

where $\nabla^2$ is the Laplacian operator. In a 1-D axisymmetric frame the Laplacian can be written as:

$$\nabla^2 = \left(\frac{\partial^2}{\partial r^2} + \frac{N-1}{r}\frac{\partial}{\partial r}\right), \tag{2.3}$$

where $N$ is 3 for a spherical particle, 2 for an infinite cylindrical particle and 1 for an infinite slab. Application of this modified symmetric operator yields:

$$\rho(r,t)c(r,t)\frac{\partial T(r,t)}{\partial t} = \frac{\partial T(r,t)}{\partial r}\left(\frac{\partial k(r,t)}{\partial r} + k(r,t)\frac{N-1}{r}\right) + k(r,t)\frac{\partial^2 T(r,t)}{\partial r^2} + \dot{q}(r,t). \tag{2.4}$$

The volumetric heat source function, $\dot{q}(r,t)$, is the heat generated by the chemical reactions and is a function of the temperature:

$$\dot{q}(r,t) = \sum_{i \in S} R_i(T,r)h_i(T), \tag{2.5}$$

where $R_i(T,r)$ is the volumetric net rate of production of species $i$, and $h_i(T)$ is the enthalpy of species $i$. This is summed over the whole set of species, $S$, in the kinetic model.

Because $(\rho c_p)_g << (\rho c_p)_s$ we can assume that the product devolatilization gas is in thermal equilibrium with the solid. Additionally, due to fast volatile release

rate [27,28], we neglect gas-phase reactions secondary reactions. These are left to be modeled in the gas phase of the reactor.

### 2.3.3 Conservation of Species and Mass

Solid species evolution is calculated from the chemical kinetics model of primary pyrolysis developed by Ranzi et al. [118–120]. The mass fraction evolution of species $i$ is given by:

$$\rho(r,t)\frac{\partial \mathbf{y}_i(r,t)}{\partial t} = R_i(r), \tag{2.6}$$

where $\mathbf{y}_i(r)$ is the mass fractions of species $i$, $R_i$ is calculated by summing the total creation/destruction rates of species, $i$, for each reaction in the chemical mechanism used in the model. We can then write:

$$R_i(r) = \sum_{j\in R}(\xi_j(r)) = \sum_{j\in R}\left(A_j e^{-E_{a,j}/RT}\nu_{i,j}\prod_{k\in S} y_k^o\right), \tag{2.7}$$

where $\xi_j$ is the rate of reaction $j$, $A$ is the pre-exponential factor, $E_a$ is the activation energy and $v_{i,j}$ is the stoichiometric coefficient of the species $i$ in reaction $j$ (see Table 2.3). The concentrations of the reactants, $y_k^o$, are for all the species $k$ participating in the reaction $j$, and $o$ - the order of the reaction in the species $k$ - is one only when the species $k$ takes part in the reaction $j$, otherwise it is zero.

For the gas phase we assume that intraporous accumulation is negligible due to fast volatile release rate. We can then calculate the mass flux of volatiles at a specified radius:

$$\dot{m}_g(r) = \frac{1}{r^{N-1}}\int_0^r \varsigma^{N-1}\sum_{i\in G} R_i(\varsigma)d\varsigma, \tag{2.8}$$

where $\varsigma$ is used as a dummy variable for integrating over the radius. When $r \to R_p$ then $m_g$is the total flux of volatiles leaving the devolatilizing particle and the time integral of this quantity is the total produced devolatilization gases.

Table 2.5 summarizes the thermophysical values and correlations used in this

Table 2.5: Thermophysical properties and modeling parameters used in this study. The reactor temperature and external convective heat transfer coefficients are varied to represent the Natural convective pyrolysis conditions of Pyle & Zaror [114] and the fluidized bed gasifier conditions of van Paasen & Kiel [138].

| **Property** | **Correlation/Value** | **Source** |
|---|---|---|
| *Reactor Temperature* | $T_R = \mathbf{773, 1073}[K]$ | [114, 138] |
| *External convective heat transfer coefficient* | $h_c = \mathbf{8.4, 250}[W/m^2K]$ | [58, 114] |
| *Biomass particle radius* | $r_p = 7.5mm$ | [114] |
| *Initial biomass density* | $\rho_{b0} = 650[kg/m^3]$ | [11] |
| *Biomass heat capacity* | $c_{p,b}(T) = 1112 + 4.85T[J/kgK]$ | [80] |
| *Char heat capacity* | $c_{p,c}(T) = 1003.2 + 2.09T[J/kgK]$ | [80] |
| *Biomass thermal conductivity* | $k_b(T) = 0.13 + .0003T[W/mK]$ | [80] |
| *Char thermal conductivity* | $k_c(T) = 0.08 - 0.0001T[W/mK]$ | [80] |
| *Effective thermal conductivity* | $k_{eff} = (1 - y_c)k_b + y_c k_c + \epsilon k_{gas} + 13.5\sigma dT^3/\omega[W/mK]$ | [27] |
| *Gas thermal conductivity* | $k_gas = 25.77 \times 10^{-3}[W/mK]$ | [38] |
| *Emissivity coefficient* | $\omega = 0.95$ | [11] |
| *Initial void fraction (porosity)* | $\epsilon = 0.5$ | [11] |
| *Pore diameter* | $d = 2 \times 10^{-5}[m]$ | [11] |
| *Stefan-Boltzmann constant* | $\sigma = 5.67 \times 10^{-8}[W/m^2K^4]$ | |

modeling study for biomass, char and the reactive intermediates. Where possible, temperature-dependent correlations were identified due to the broad range of temperatures which the solids experience. Two external heat transfer coefficients are reported representing each of the reactor conditions considered.

### 2.3.4 Initial and Boundary Conditions

It is apparent that in order to solve this dynamical system a proper boundary condition description is needed. At the interior point, $r$=0 , a zero Neumann boundary condition is required. This is necessary since, if there were a non-zero flux at this point, axisymmetry would be broken. Additionally, this boundary condition also absolves us of the singularity in the Laplacian operator, $\nabla^2$, for $N > 0$, created by the $r^{-1}$ term.

At the particle surface the boundary condition is deduced from the physics of interfacial heat transfer. Here, a non-zero Neumann boundary condition is calculated by summing both the convective and radiative heat transfer between the reactor and the particle surface. These two boundary conditions can be summarized:

$$\frac{\partial T(r,t)}{\partial r}\left(\frac{\partial k(r,t)}{\partial r}+k(r,t)\frac{N-1}{r}\right)\Bigg|_{r=0}=0, \tag{2.9}$$

$$k(r_p,T(r_p))\frac{\partial T(r,t)}{\partial r}\Bigg|_{r=r_p}=h_c(T(r_p,t)-T_R)+\epsilon\sigma\left(T(r_p,t)^4-T_R^4\right), \tag{2.10}$$

where $T_R$ is the particle's local reactor temperature which can be specified as a time-dependent function to represent unsteady conditions and migration through reactor zones during mixing or as a specified constant for isothermal reactor conditions.

The initial conditions are uniform temperature and species concentration through the particle. The temperature can be prescribed, and the initial species concentrations can be calculated from assays of different types of biomass. These are given as:

$$T(r,t)|_{t=0} = T_0 y_i(r,t)|_{t=0} = y_{i,0}, \forall i \in S. \tag{2.11}$$

### 2.3.5 Numerical Method

This nonlinear system of partial differential equations is solved with the method of lines approach. Centered $2^{nd}$ order finite difference stencils are used to approximate the spatial derivatives. The thermochemical and kinetic calculations are done using the open-source code Cantera 2.0 [63]. The resulting system of ordinary differential equations is integrated in time using the MATLAB stiff solver ODE15s.

## 2.4 Results and Discussion

Pyle and Zaror [114] studied biomass pyrolysis experimentally using dry cylindrical pine wood particles of varying diameters of 0.6, 1.5 and 2.2cm. The particles were placed in an electric heater maintained isothermally at $500°C$ (773 K) under nitrogen gas. Up to five thermocouples were installed in the particle at different depths to record the interior temperatures, in particular that of the centerline. The dried biomass cylinders were initially at an ambient temperature of $25°C$ (303K). By validating the predicted center-line temperature of this externally heated pyrolyzing particle, the fidelity of both the heat transfer as well as thermochemical reaction models are demonstrated since the center-line temperature is influenced by both occurring through the entire particle radius.

This experiment is numerically repeated to strong agreement utilizing the particle devolatilization model developed in section 2.3. In figure 2-5 the predicted center-line temperature of a devolatlizing 1.5cm pine cylinder is plotted against the experimental data reported by Pyle and Zaror, in addition the temperature predictions of both Babu and Chaurasia [11] and Jalan and Srivastava [72] are shown, given each of their advanced heat transfer formulations they both find good agreement with the center-line temperature prediction while utilizing simplified devolatilization chemistry mechanisms.

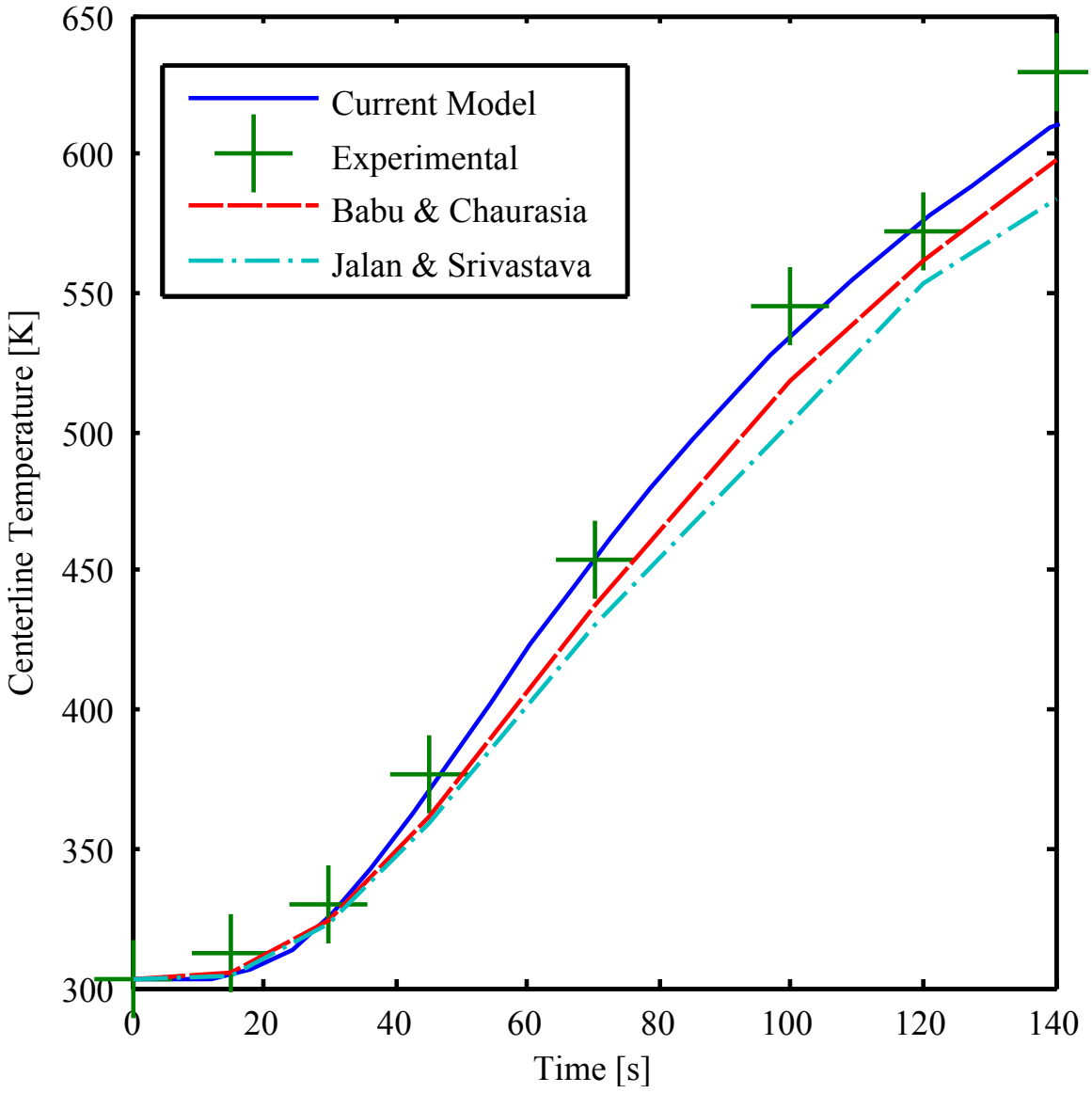


Figure 2-5: Validation of predicted center-line temperature of 1.5cm radius cylinder devolatilizing in a $500°C$ (773K) oven against experimental data from Pyle and Zaror [114], and comparison against the models of Babu & Chaurasia [11] and Jalan & Srivastava [72].

In figure 2-5 it is shown that the current model accurately captures the delay in the initial heat-up of the particle centerline due to the time it takes the thermal wave to traverse the radial thickness of the particle. Subsequently the centerline heats up nearly linearly so long as the temperature is much less than the reactor temperature, accurately reflecting measurement.

Although Babu and Chaurasia [11] and Jalan and Srivastava [72] are able to accurately predict the centerline temperature evolution, the current model employs a detailed devolatilization scheme allowing for further interegation of the dynamics of conversion based on devolatilization species evolution. In figure 2-6(a) the accumulations of a selection of major primary pyrolysis species are shown for a particle undergoing devolatilization at the same isothermal natural convective conditions described above [114]. The largest accumulation is for levoglucosan ($C_6H_{10}O_5$), the dehydrated product of cellulose. The oxygenated products from lignin, 3-(4-hydroxy-3,5-dimethoxyphenyl)acryladehyde ($C_{11}H_{12}O_4$), and hemicellulose, xylofuranose ($C_5H_8O_4$) are shown as well. We observe a delay in the reaction's onset due to the time it takes for the surface of the particle to reach a temperature at which conversion proceeds at an appreciable rate. It is notable that this delay is at least as long as the delay of the initial centerline heat-up observed in figure 2-5, this is the case because under the conversion conditions described the rate of internal heat transfer is faster than external heat transfer allowing for the heat transfered to the surface of the particle to diffuse inward keeping the surface temperature below the temperature required for the onset of devolatilization. This observation confirms the non-dimensional analysis made in table 2.2 for the natural convective case.

Additionally, we observe an acceleration in the rate of conversion as the conversion nears completion. These changes in rate are more apparent in figure 2-6(b) where the rate of accumulation is plotted. As the thermal and reaction front reaches the center of the particle, the overall heat transfer surface-area to reacting volume ratio increases rapidly, causing the reaction temperature to increase, therefore increasing the rate of conversion for the core of the particle. This effect is analyzed in more detail below.

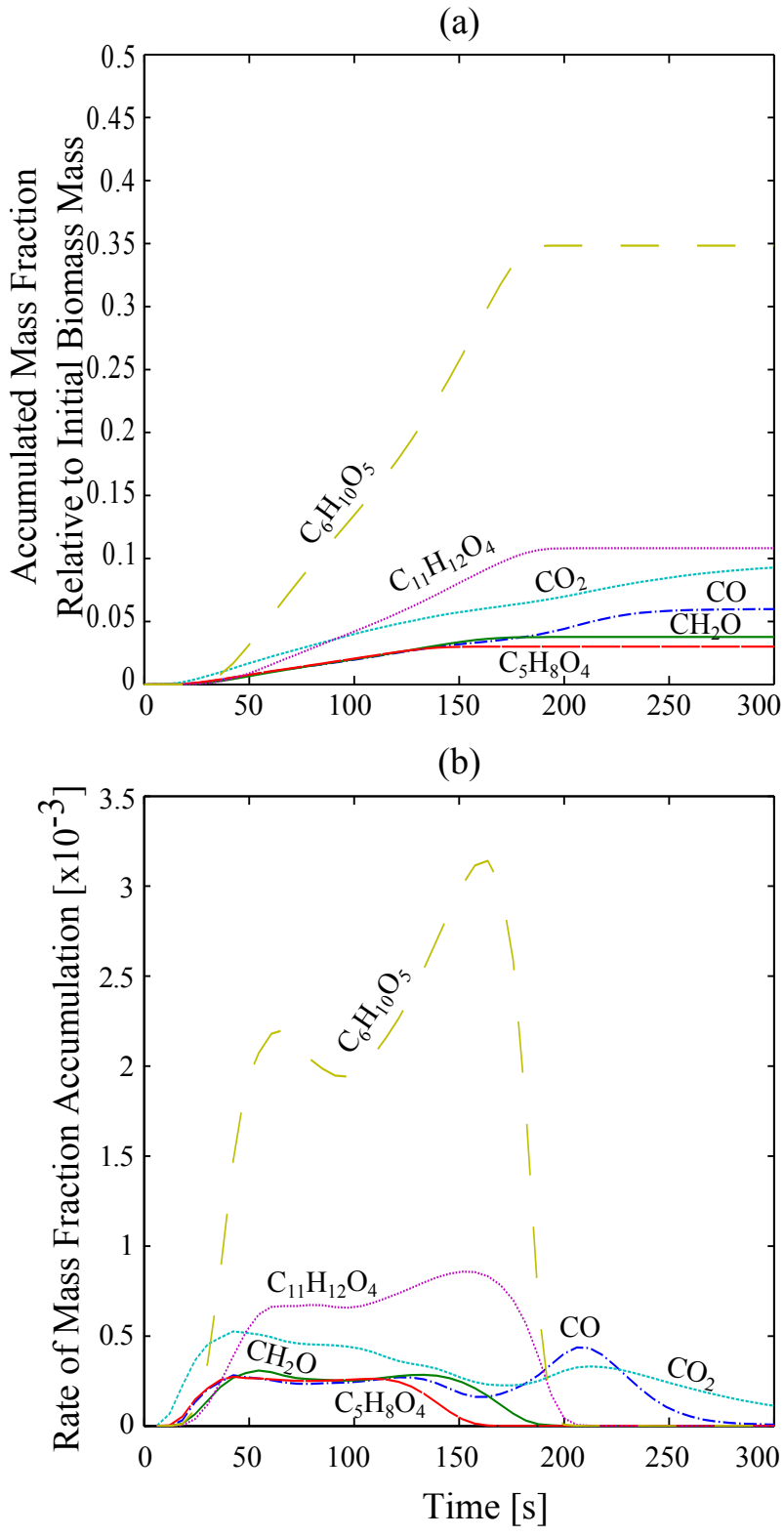


Figure 2-6: In (a) the accumulated mass fractions of major primary pyrolysis products is plotted with respect to time for a particle undergoing conversion at the conditions specified by [114]. In (b) the derivative of these mass fractions is plotted.

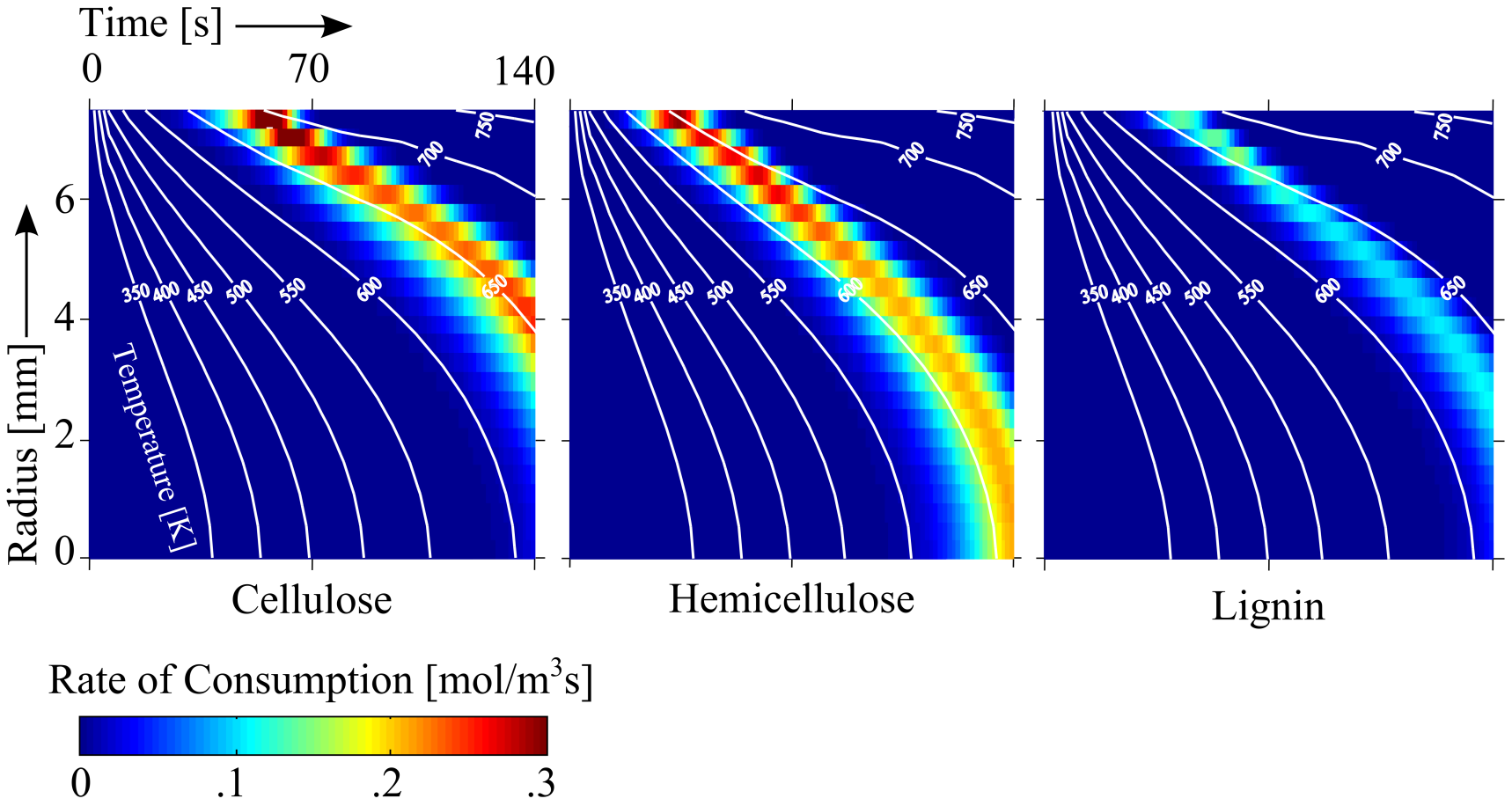


Figure 2-7: Reaction rates of primary pyrolysis reactions in a particle undergoing pyrolysis at the conditions prescribed by Pyle and Zaror [114]. In these plots the horizontal axis is time in seconds, and the vertical axis is the particle radius in millimeters. It is readily apparent that biomass undergoes a sequential thermochemical conversion.

In figure 2-7 the rates of consumption of each of the major constituents of biomass as well as the internal isotherms are plotted against time and particle radius in a devolatilizing particle at the natural-convective conditions discussed above. It is observed that the major components react sequentially, with hemicellulose reacting at the surface in a sharp pyrolysis wave first, followed by a broader wave of lignin pyrolysis reactions and finally cellulose devolatilizes in a sharp wave. This is accounted for by the fact that hemicellulose reacts fastest at low temperatures whereas cellulose is more recalcitrant requiring higher pyrolysis temperatures. Furthermore, it is observed that these conversions occur at evolving temperatures through the process; At these conditions the peak rates of consumption of hemicellulose evolves between approximately $650K$ and $610K$, cellulose between $700K$ and $650K$ and lignin between $660K$ and $630K$.

### 2.4.1 Comparison of TGA and FBG Devolatilization Regimes

The dynamics of devolatilization are strongly dictated by the controlling process(es) of specific reaction conditions, influencing the chemical conversion as well as the timescales of conversion. In Figure 2-8 the normalized mass-loss curves and rates are plotted for each TGA and FBG devolatilization. In order to compare these two cases on a similar basis, a characteristic thermal time, $t^0$, is defined such that $T(r = 0, t^0) = 0.99T_R$. It is noticeable that the two cases are characterized by different dynamics, where the TGA conditions are first subject to a heat-up period where devolatilization is not occurring, under FBG conditions devolatilization occurs nearly instantaneously with a strong peak initially. This is likely due to very fast external heat transfer to the surface of the particle where reactions are able to begin, this is then moderated by the much slower internal heat transfer into the subsequent layers and the dynamics then reflect that of the slower TGA case. Due to the higher temperature of the FBG conditions the devolatilization process completes long before the thermal heat-up completes indicating that the devolatilization occurs at temperatures well below reactor conditions.

As has been observed in both Figures 2-6 and 2-7, the primary pyrolysis reactions

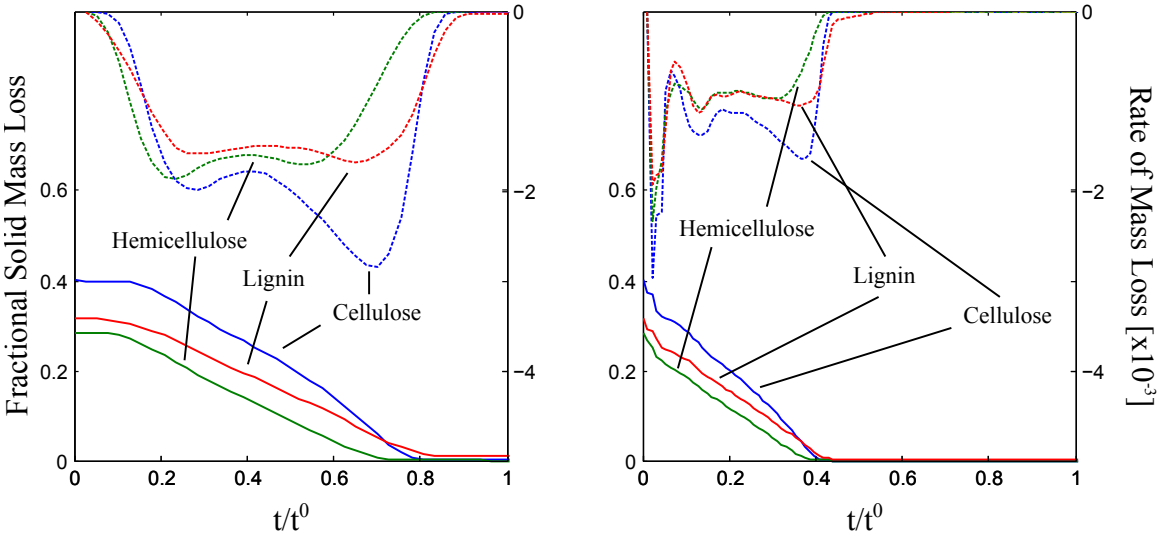


Figure 2-8: The mass loss curves of cellulose, hemicellulose and lignin (along with their reactive intermediates) are plotted for both cases considered: (a) natural convective TGA devolatilization and (b) FBG devolatilization. The solid curves are the mass fractions remaining in the solid, and the dotted lines are the differential mass loss curves. Here the same normalized time, $t/t^0$ is used.

occur at temperatures which evolve through the conversion process. In order to more rigorously determine the temperature at which each reaction occurs through the conversion, we define the effective temperature of reaction $j$ as:

$$T^j_{eff}(t) = \frac{1}{\int_0^r \xi_j(r,t)dr} \int_0^r \xi_j(r,t)T(r,t)dr. \tag{2.12}$$

where $\xi_j(r,t)$ is the rate of reaction $j$. The effective temperature is then the weighted mean of the temperature in the particle where the weights are the rates of the reaction of interest.

The effective temperatures of the pyrolysis reactions, grouped by primary biomass species, are plotted in Figure 2-9 for both the TGA conditions of Pyle and Zaror as well as under FBG conditions as described by van Paasen & Kiel [138], these conditions are summarized in Table 2.5. Under both TGA as well as the FBG conditions, it is observed that the reactions occur at varying temperatures. First a ramp-up of the effective reaction temperatures is observed, indicative of the heating up of the surface of the particle to reactive temperatures. While the onset of the ramp-up of the

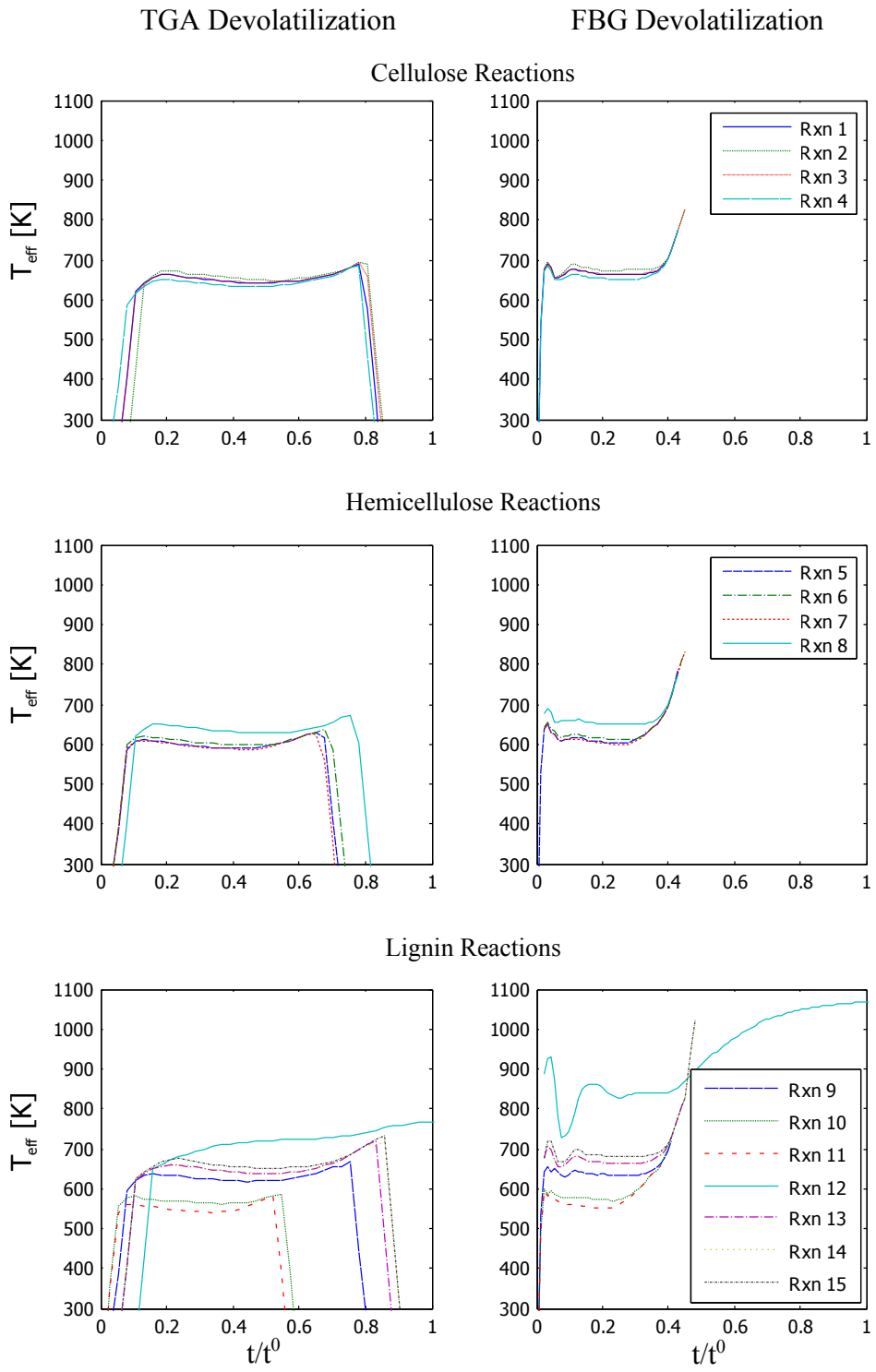


Figure 2-9: The temperatures at which the primary pyrolysis reactions occur are plotted for each of the reaction conditions. In order to compare these two cases on a similar basis, a characteristic thermal time $t^0$ was defined such that $T(r = 0, t^0) = 0.99T_R$.

effective reaction temperatures is immediate for the FBG conditions, sequential onset of specific reactions are observed for the slower TGA conditions. For the cellulose reactions reactions (4) and (1) initialize first followed by reactions (2) and finally (3) which are reactions of the intermediate reactive species $CELL_a$, similar dependence is observed for hemicellulose and lignin as well. Next the effective reaction temperatures level out at temperatures below the reactor temperature, which is indicative of the importance of heat transfer to the process. Here it is also observed that the reactions of the intermediate solid species occur at higher temperatures than the reactions of the raw biomass species since they occur on the back-end of the pyrolysis wave where the temperatures have continued to increase. Finally, as the reactions near completion the effective temperature of the reactions begins to increase indicating decreasing heat transfer limitations and therefore a shift to a kinetic regime as the conversion completes. This shift is caused because once the reaction wave has reached the center of the particle the temperature continues to increase as there is no longer cooler unreacted biomass ahead of the wave for heat to diffuse into and so the local temperature continues to increase thus increasing the effective reaction temperature of the center-line reacting zone. The pyrolysis reactions are then largely extinguished, save for the lignin reaction (12) of the intermediate $LIG_{CC}$ which is characterized by slow kinetics.

### 2.4.2 Sensitivity Analysis of Modeling and Control Parameters

The predictive capability of modeling the devolatilization of a biomass particle is dependent on a number of physical and chemical parameters in the model. It is, therefore, the aim of this work to quantify the relative impact of controllable parameters on primary pyrolysis products in order to identify optimal configurations to minimize primary tar production in order to maximize the desired product gas concentrations. In previous works and here the classification primary tars is used to describe the devolatilization species other than $H_2$, CO, $H_2O$ and $CO_2$. In the gas-phase, these

primary tars undergo additional pyrolytic, cracking and oxidation reactions toward the abovementioned target species as well as polymerization reactions leading to tar growth and Polycyclic Aromatic Hydrocarbon (PAH) formation [86].

As previously discussed, two reactor conditions are considered in this work: natural convective devolatilization (TGA conditions), as typified by the experiments of Pyle and Zaror [114], and devolatilization in a fluidized bed gasifier, utilizing the conditions described in the experimental work of van Paasen and Kiel [138]. The primary differences in these two cases are the reactor temperature and the convective heat transfer coefficient as summarized in Table 2.5. In order to quantify the primary pyrolysis products, numerical simulations were run for 600 seconds to assure the devolatilization had come to completion, which is approximately 3× the average pyrolysis time for natural convective pyrolysis and nearly 6× that for fluidized bed pyrolysis. The cumulative production of each species was then used to calculate the mass fractions, $Y_i$, of each species. Then, the relative species sensitivities are calculated as:

$$S_{i,p} = \frac{dln(Y_i)}{dln(p)} = \frac{dY_i}{dp}\frac{p}{Y_i}, \tag{2.13}$$

where $S_{i,P}$ is the relative sensitivity of the mass fraction of species $i$ to the parameter $p$. This metric is then used to assess the impact of controllable parameters on the devolatilization gas species distribution.

In Figure 2-10 the relative impact of a number of controllable parameters - reactor temperature and initial biomass particle temperature, particle radius and convective heat transfer coefficient - as well as modeling parameters - biomass density, radiative emissivity, particle porosity as well as pore diameter - are shown. The RMS of the mass fractions of the devolatilization gas is used here to show the relative impact of each of these parameters since each parameter effects the entire species distribution (by mass fraction) differently. At the TGA conditions, particle radius and biomass density dominate the determination of devolatilization gas mass-fraction distribution. At FBG conditions, the influence of external heat transfer and the initial particle tem-

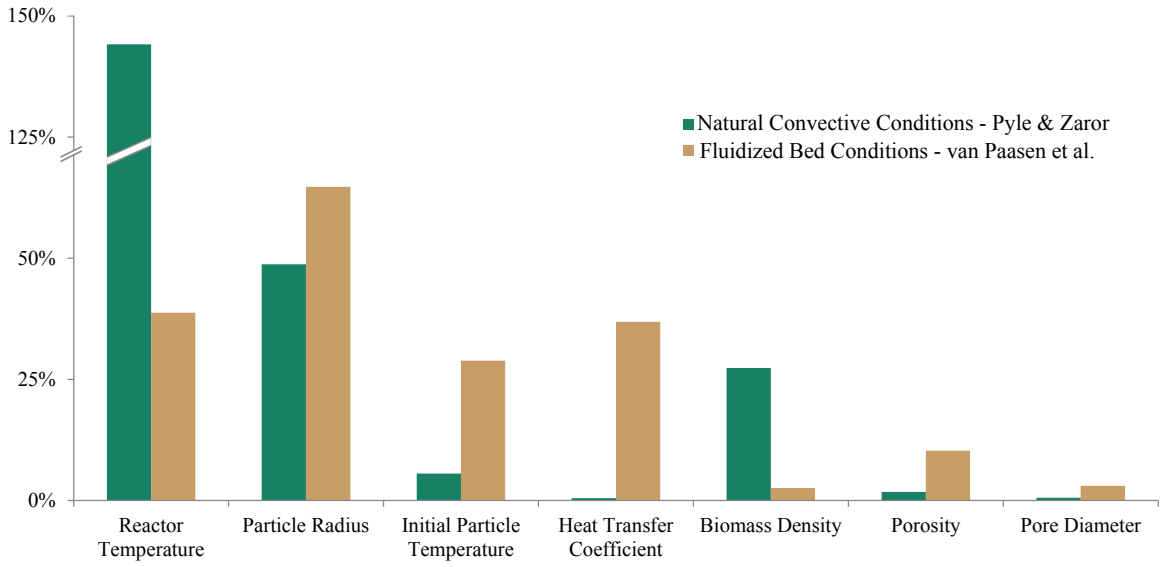


Figure 2-10: Root Mean Square of relative species sensitivities, $\sqrt{\frac{1}{n}\sum_{i=1}^{n} S_{i,p}^2}$, of the final species mass-fraction distribution to modeling parameters ($P$) for both reactive cases.

perature play a commensurate role, whereas the sensitivity to biomass density drops. This is perhaps counter-intuitive since by non-dimensional analysis it was shown that the TGA conditions are heat transfer limited while at the FBG conditions external heat transfer is very fast yielding little control on the conversion rate. The pyrolysis numbers, however, only dictated the rate of conversion and here it is observed that the influence on the chemistry is decoupled from this limitation with heat transfer rates playing an important role in the chemical products due to their strong influence on the outer particle effective reaction temperatures. Another important observation is that the sensitivity of the species distribution to reactor temperature decreases at higher temperatures, since as observed in Figure 2-9, the effective reactor temperatures are much lower than the reactor temperature. As reactor temperature increases, the effective reaction temperatures are increasingly limited by both internal heat transfer and reaction kinetics and is therefore not greatly effected by increases in external temperature. These controllable parameters - Reactor Temperature, Particle Radius, Initial Particle Temperature, External Heat Transfer Coefficient and Biomass Density- which have varying importance across reactor conditions are further explored

in the remainder of this section and operational recommendations are drawn for FBG reactors.

In Figure 2-11 the evolution of internal temperature distribution, the sensitivity of the center-line temperature and the overall mass-loss curves are shown. At early stages in the conversion process the internal particle temperature is most sensitive to the initial particle temperature and then to the density and radius of the particle as well as the reactor temperature - parameters which play a strong role in the thermal process. As the unsteady conversion process reaches completion the center-line temperature is dominated by the reactor temperature and particle radius. However, in the fluidized bed regime, it is observed that the initial particle temperature continues to play an important roll. It is observed that in both cases, but especially in the FBG case, that the primary pyrolysis reactions reach completion before the center-line temperature approaches the reactor temperature. Rather, the reactions proceed quickly at the effective reaction temperatures shown in Figure 2-9 before the particle reaches higher temperatures.

### 2.4.3 Effect of Reactor Parameters on Primary Pyrolysis Species Distribution

In the above section four controllable parameters - reactor temperature, particle radius, initial particle temperature and the external heat transfer rate - have been identified which directly affect the devolatilization dynamics, and therefore the composition of the devolatilization gas distribution from raw biomass fuel. A full sensitivity analysis is used to analyze the effect of these parameters on the distribution of the primary pyrolysis products of devolatilization, which are summarized in Table 2.6 along with the nominal mass fractions for each of the species for a pinewood particle as previously described under FBG conditions.

Of particular interest is the influence of these parameters on the large oxygenated products such as the dehydrated monomers of hemicellulose and cellulose - e.g. xylofuranose and levoglucosan - as well as the aromatic tar precursors evolved from lignin -

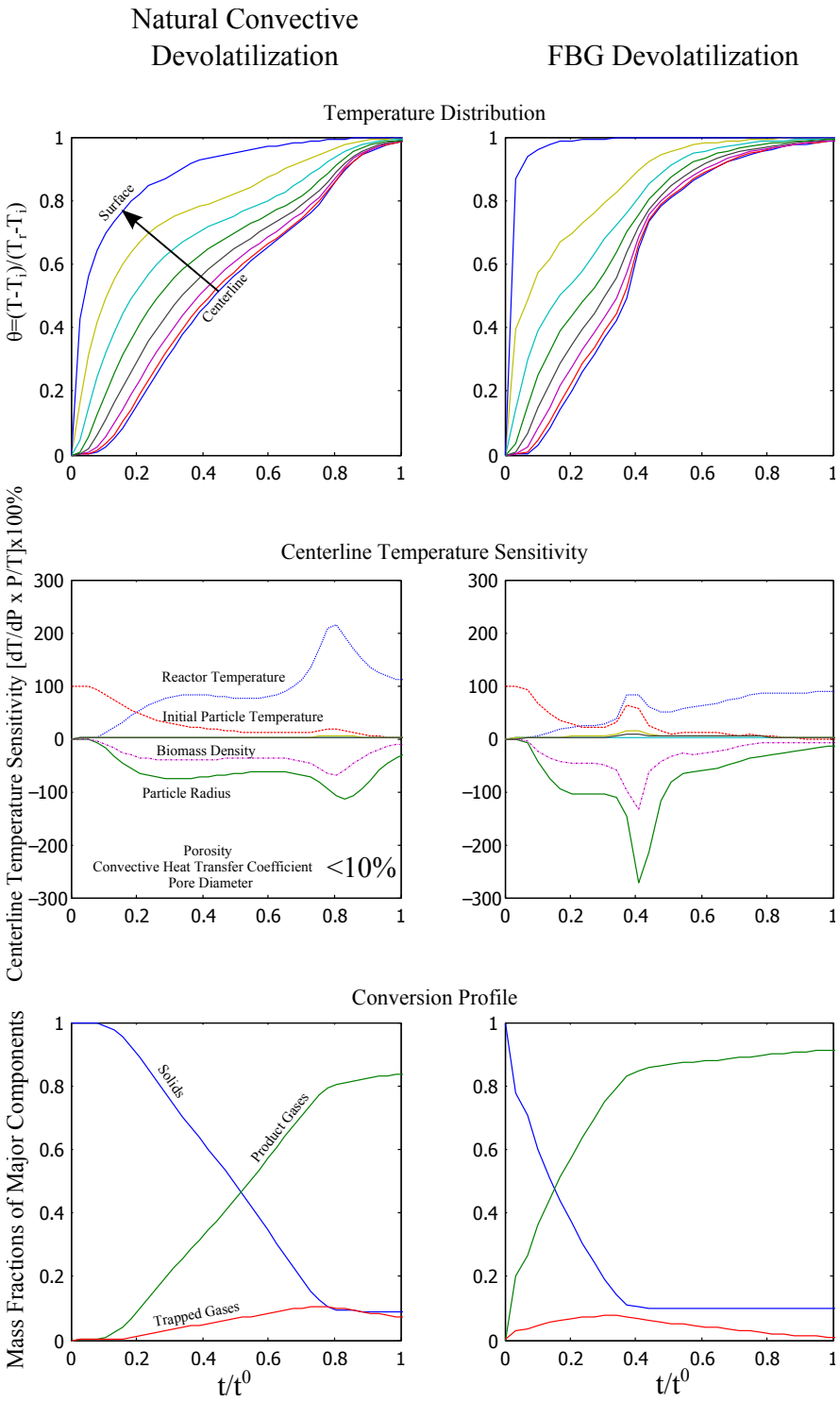


Figure 2-11: The internal temperature distribution of reacting particles are shown in the top row. The sensitivity of the center-line temperature during devolatilization is shown in the middle row. The overall solid conversion is shown in the bottom row for comparison.

Table 2.6: Relative sensitivities, $S_{i,p}$, of primary pyrolysis products mass-fractions to operational and modeling parameters at FBG conditions.

| **Species** | **Mass Fraction at Base Case** | **Reactor Temperature** | **Particle Radius** | **Initial Particle Temperature** | **Heat Transfer Coefficient** |
|---|---|---|---|---|---|
| *Hydrogen* | 0.20% | 1% | 1% | 9% | 15% |
| *Water* | 4.80% | 22% | -10% | 6% | 10% |
| *Carbon Monoxide* | 9.10% | 18% | -16% | -18% | -32% |
| *Carbon Dioxide* | 12.70% | -21% | -7% | -16% | 21% |
| *Formaldehyde* | 6.10% | -15% | -9% | -27% | 23% |
| *Methane* | 4.00% | 1% | -11% | -15% | 18% |
| *Methanol* | 3.80% | 17% | -11% | -18% | 28% |
| *Glyoxal* | 1.20% | 49% | -51% | 38% | 26% |
| *Acetylene* | 3.70% | 8% | -11% | -12% | 17% |
| *Acetaldehyde* | 0.90% | 67% | -51% | 25% | 39% |
| *Hydroxyacetaldehyde* | 4.60% | 49% | -51% | 38% | 26% |
| *Ethanol* | 1.80% | -17% | -9% | -27% | 21% |
| *Malonaldehyde* | 0.40% | -2% | 5% | 69% | -18% |
| *Oxetane+Propyleneoxide* | 2.60% | 112% | -29% | 12% | 59% |
| *Xylofuranose* | 1.80% | -67% | 80% | -24% | 83% |
| *Phenol* | 8.00% | 9% | 4% | 42% | 30% |
| *5-(hydroxymethyl)-furfural* | 2.60% | 49% | -51% | 38% | -26% |
| *Levoglucosan* | 34.50% | -15% | 18% | 14% | 11% |
| *pCoumaryl* | 1.70% | 8% | 4% | 44% | 29% |
| *3-(4-hydroxy-3,5-dimethoxyphenyl)acrylaldehyde* | 2.70% | 10% | 29% | 4% | -14% |
| **RMS Average Sensitivity** | **-** | **40%** | **31%** | **29%** | **32%** |

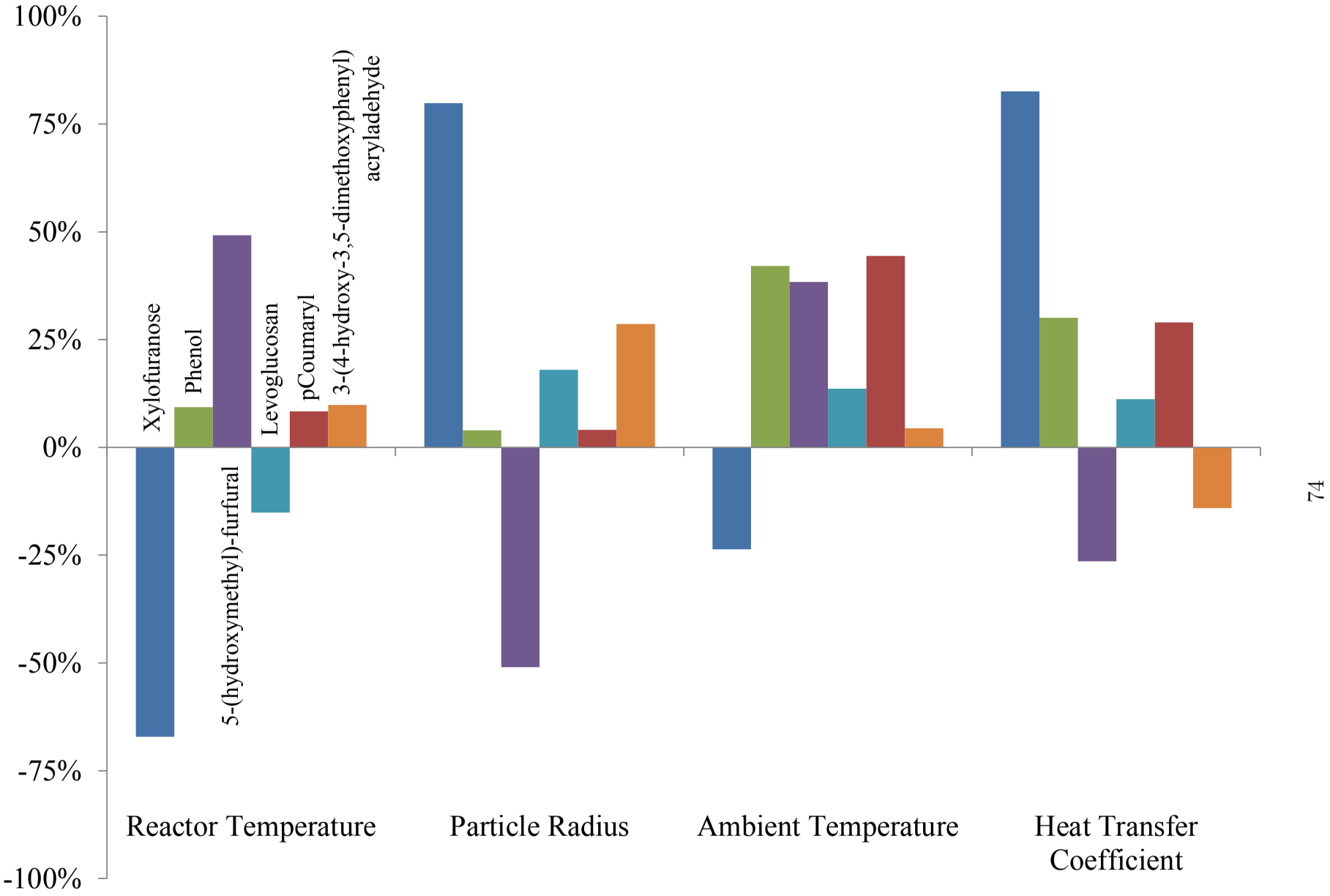


Figure 2-12: Sensitivity, $S_{i,p}$, of large oxygenated primary pyrolysis products with respect to operational and modeling parameters at FBG devolatilization conditions.

e.g. pcoumaryl, 3-(4-hydroxy-3,5-dimethoxyphenyl)acryladehyde (synapol aldehyde) and phenol. In Figure 2-12, the sensitivities for these species are plotted. Taking levoglucosan, for example, which is the product of cellulose via reaction (1) followed by reaction (3), we see that at a slightly higher reactor temperature the final mass fraction of levoglucosan is decreased due to the increase in light gas production from hemicellulose and lignin, not as would be calculated based on consideration of the sensitivity of the cellulose mechanism alone, as this would require an assumption of either a constant temperature or implied heating rate, which is not necessary with a particle model.

In Figure 2-13, the influence of particle radius on devolatilization in a fluidized bed (fast heat transfer) environment is illustrated by using pine particles of radius 7.5mm and .75mm, representative of woodchips and sawdust respectively. In Figure 2-13a the dynamics of the conversion in a reactor at $650K$ is shown, while in Figure 2-13b the conversion at $950K$ is shown. At both temperatures the small particle undergoes conversion with similar dynamics where internal heat transfer effects are negligible. For the large particle, however it is observed at low temperatures a delay is observed before the onset of reactions due to the conduction of heat from the hot surface to the center of the particle, then the conversion occurs characteristically of a mixed heat transfer and kinetic control. At the higher reaction temperature, the larger particle no longer exhibits a delay in the onset of reaction due to the faster external heat transfer relative to internal conduction. While the external heat transfer coefficient is held constant, the driving force of the temperature difference is increased allowing the surface to heat up faster. Then the conversion continues under internal heat transfer control.

The onset of internal heat transfer control is discernible in Figure 2-13c, where the conversion time with respect to reactor temperature transitions to a relatively flat regime. It is at this point where the external heat transfer driving force is sufficiently fast, and well above the effective reaction temperatures of the devolatilization reactions that internal heat transfer becomes limiting producing strong internal temperature and reaction gradients.

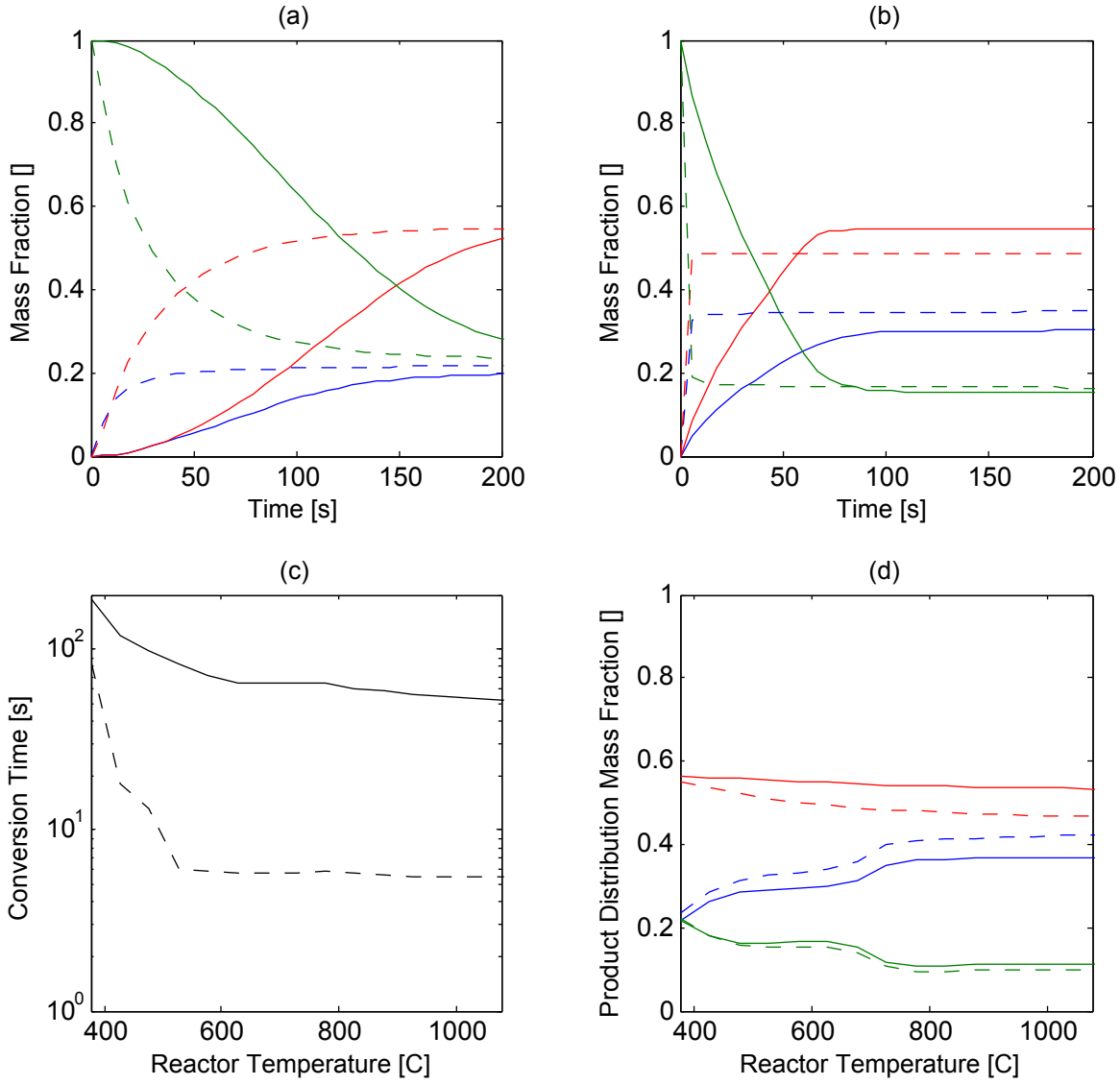


Figure 2-13: The radius of the particle influences dynamics of conversion, the time of conversion as well as the final product distribution. Here the conversion of a 7.5mm (solid lines) and .75mm (dashed lines) particles are compared at (a) 377C and (b) 677C. In (c) the conversion times for each of these cases are compared, and in (d) the final product distributions are shown for various reactor conditions. Green lines represent the solids, red lines the primary oxygenates/tars and blue lines the light gases (CO, $CO_2$, $H_2$ and $H_2O$).

The influence of particle radius on the final product distribution is shown in Figure 2-13d. In this case the distribution is lumped into three product classes: (1) Light Gases - the target gases CO, $CO_2$, $H_2$ and $H_2O$. (2) solids - comprised predominately of char as well as unreacted intermediate solids, (3) primary tars and reactive oxygenates - the remainder of the gaseous species. For smaller particles, while the change in char production is negligible over the range of reactor temperatures, the distribution of gas products is affected appreciably at temperatures above $400°C$ with smaller particles producing a larger ratio of target-gases to tars and their precursors. This trend has been experimentally validated under both pyrolysis and gasification conditions [93, 121, 122]. Therefore, the utilization of finer ground particles is of interest for minimizing gasifier tar production.

## 2.5 Implications for Gasifier Operation

Operational decisions at the macro-scale of gasifier operation have an impact on the particle-scale conversion of biomass through physical and kinetic influence, as has been shown. The first order effect is the individual operational parameter influence on the particle's average temperature history.

1. **Smaller particles decrease tar-precursor species yields.**
   Smaller particles, due to their higher surface-area-to-volume ratio, heat up more quickly and experience higher effective reaction temperatures during conversion. This favors the higher temperature conversion pathways which skew toward producing lighter gases the target gasification products while decreasing primary tars and other reactive oxygenates.

2. **Particle radius directly influences conversion times.**
   Biomass gasification in a fluidized bed requires careful balancing of solids mixing, devolatlization and gas-phase mixing and reactions in order to maximize carbon conversion and overall process efficiency. Beyond effecting the chemical composition of devolatilization the particle radius also influences the time of de-

volatilization, allowing for a way to adjust it in order to achieve well-distributed devolatilization throughout the bed.

3. **Increasing the fluidization gas flow can improve chemical conversion.** By increasing the fluidization gas velocity in the gasifier, higher heat transfer rates can be achieved, thus the yielding higher amounts of the lighter target gases by increasing the effective reaction temperatures. Additionally, by improving mixing, a more uniform bed temperature and conversion is achieved.

4. **A higher initial biomass temperature decrease char production and therefore overall carbon conversion effiency.**
   Biomass can be pre-heated by introducing it into the gasifier directly from the dryer - if one is employed. The affect of this is similar to increasing the average particle temperature, however a preheated particle has a uniformly raised temperature allowing for a higher effective reaction temperature as it reacts in the gasifier.

To first order, the general effect of adjusting these parameters: particle radius, heat transfer rate - via increased fluidization gas velocity - and the initial particle temperature is a change in the char/gas/tar ratios. However, an appreciable effect is observed on the distribution of gas species concentrations, because they are dependent on the complex interplay of the physical and chemical processes at work. As such, in the design and operation of biomass gasification systems a consideration of particle characteristics via a detailed particle-scale devolatilization model is crucial.

## 2.6 Conclusions

In this work, the influence of parameters describing the thermochemical conversion of biomass on the resulting distribution of devolatilization products has been explored. A full sensitivity analysis has been applied to asses the relative impact of these parameters. In particular, four controllable parameters - reactor temperature, particle radius, initial particle temperature and the effective heat transfer coefficient

- were found to play an important role in the primary pyrolysis product distributions. Particle radius has been found to be a particularly important parameter in controlling the conversion time as well as the gaseous product distribution, with smaller particles leading to lighter gaseous product due to increased effective reaction temperatures. Additionally, It is therefore concluded that in order to accurately model the devolatilization of biomass particles of realistic length scales in a fluidized bed gasifier a detailed particle model is necessary to capture the complex interaction of physical and chemical phenomena.

# Chapter 3

# Biomass Devolatilization Modeling in an Eulerian Framework

## 3.1 Introduction

The reacting environment inside of a FBBG is characterized by the interplay of chemical kinetics, heat transfer and mixing (of both the gaseous and solid phase). These later two processes are purely hydrodynamic though they strongly influence the overall chemical conversion. As such it is necessary to investigate the overall influence of the hydrodynamics on biomass conversion in a fluidized bed reactor environment. Due to the capital intensity of experimental reactor systems, computational fluid dynamic (CFD) modeling is an important analysis tool allowing researchers a way to investigate reactor design and the influence of operational parameters on gasifier performance. A fully reactive CFD model of biomass gasification must take into account the interplay of the complex phenomena of (1) chemical conversion  solid fuel devolatilization and char gasification along with the homogeneous gas-phase oxidation reactions, (2) heat and mass transfer between the reactive solid and gaseous phases and (3) the multi-phase hydrodynamics [61].

In this chapter a shrinking-core devolatilization model is developed for use in Eulerian reactive CFD simulation. An eulerian framework for modeling the gas-, sand- and biomass-phase in a gasifier is chosen due to its scaleability to industrially

relevant reactor sizes, whereas lagrangian models of reactors are often limited to extremely small scales primarily of academic interest.

In section 3.2 the controlling regimes of biomass devolatilization are considered and non-dimensional analysis is used to identify processes needing to be modeled in an eulerian model of devolatilization. In section 3.3 a shrinking-core model of devolatilization is developed. Next, the model's predictions are compared to the lagrangian modeling framework developed in Chapter 2 and sources of error are discussed.

## 3.2 Controlling Regimes of Biomass Devolatilization

Biomass devolatilization is a complex conversion consisting of the complex interplay of devolatilization kinetics, external convective heat transfer from the reactor to the biomass particle and internal conduction of heat through the particle to the reacting zone [39]. In order to fully capture the dynamics of particle devolatilization for thermally large particles (i.e. particles $>$ 1mm), resolution of the internal temperature gradients is necessary [20]. This type of detailed model is naturally Lagrangian in nature and cannot be easily implemented in an Eulerian CFD simulation since particle history lost as part of the Faustian bargain for the Eulerian framework's simpler hydrodynamic modeling framework.

Under certain reaction conditions, however, the controlling factor of the devolatilization process can be ascertained and a simpler model of conversion can be employed. In their work, Pyle and Zaror [114] proposed two dimensionless groups which, in addition to the Biot Number qualitatively predict the regime of a particle's devolatilization: the internal pyrolysis number and the external pyrolysis number. These numbers are defined as:

Table 3.1: The controlling regimes of biomass devolatilization can be described by the Biot number as well as the internal and external pyrolysis numbers [114]. Outside of these controlling regimes a devolatilization model must take into account each of these processes.

| Controlling Regime | $Bi$ | $Py^{int}$ | $Py^{ext}$ |
|---|---|---|---|
| Kinetically Limited | small | large | large |
| External Heat Transfer Limited | small | | small |
| Internal Heat Transfer Limited | large | | small |

$$Bi = \frac{\tau_{cond}}{\tau_{conv}} = \frac{h_p D_p}{k_p} \tag{3.1}$$

$$Py^{int} = \frac{\tau_{kin}}{\tau_{cond}} = \frac{k_p}{K \rho c_p D_p^2} \tag{3.2}$$

$$Py^{ext} = \frac{\tau_{kin}}{\tau_{conv}} = \frac{h_p}{K \rho c_p D_p}. \tag{3.3}$$

Where $\tau_X$ is the characteristic time of the process $X$, $h_p$ is the external heat transfer coefficient, $D_p$ is the characteristic length (diameter) of the particle, $k_p$ is the conductivity of the particle, $K$ is the rate of devolatilization, $\rho$ is the mass density of the particle and $c_p$ is the heat capacity of the particle. The characteristic time of heat conduction is defined as $\tau_{cond} = \rho c_p D_p^2 / k_p$. Similarly, $\tau_{conv} = \rho c_p D_p / h_p$ is the characteristic time of convective heat transfer. The characteristic time of chemical conversion are characterized by $\tau_{kin} = 1/K$ where $K$ is calculated from the arrhenius kinetics of devolatilization $K = AT^b exp(-E_a/RT)$. From the definition it is quickly noted that $Py^{ext} = Py^{int} \cdot Bi$. In Table 3.1 the three controlling regimes of biomass devolatilization, and their associated non-dimensional characterizations as described by Pyle & Zaror, are summarized. In their work Pyle & Zaror went on to develop simplified models for each of the limiting cases. For the majority of realistic Fluidized Biomass Gasifier (FBBG) cases these limiting conditions aren't satisfied, requiring a which a model which accounts for the interplay of each of these effects.

In Figure 3-1 contours of these dimensionless groups are plotted with respect to the logarithms of the particle diameter and the external heat transfer coefficient

where the contour values of $10^{-1}$ and $10^{1}$ are chosen to represent the cut-offs of "small" and "large" respectively indicating an order of magnitude difference between the timescales. The controlling regimes described in Table 3.1 are then mapped out. Additionally, colored bands indicate the range of estimated heat transfer coefficients using the correlation of Turton and Levenspiel and Ranz [117, 137] for biomass fuel particles in a fluidized bed with superficial gas velocities of 1, 10 and 100 cm/s respectively since these will likely span the entire expected operational space.

### 3.2.1 Heat Transfer Modeling

In realistic FBBGs the external heat transfer coefficient of a particle is a function of both the effective particle diameter and the flow conditions of the reactor, $h_p = f(Re_p, Pr)$. The particle Reynolds number is calculated as:

$$Re_p = \frac{D_{eff} u_0 \rho_g}{\mu_g}, \tag{3.4}$$

where $D_{eff}$ is the effective diameter of the particle, $u_0$ is the supeficial gas velocity in the bed, $\rho_g$ is the mass density of the gas phase and $\mu_g$ is the dynamic viscosity of the gas phase. In realistic systems it is rarely the case that perfectly spherical particles are employed, rather an effective particle diameter can be used to use correlations made for spherical particle. The effective particle diameter of a particle of any shape is defined as the diameter of a sphere with a volume equal to that of the particle of interest. The effective diameter can be calculated as:

$$D_{eff} = 2R_{eff} = \frac{6V_p}{\phi_s SA_p}, \tag{3.5}$$

where $R_{eff}$ is the effective particle radius, $V_p$ is the volume of the particle, $\phi_s$ is the sphericity of the particle and $SA_p$ is the surface area of the particle. The sphericity of the particle is defined as the ratio of the surface area of a sphere of equivalent volume to that of the particle:

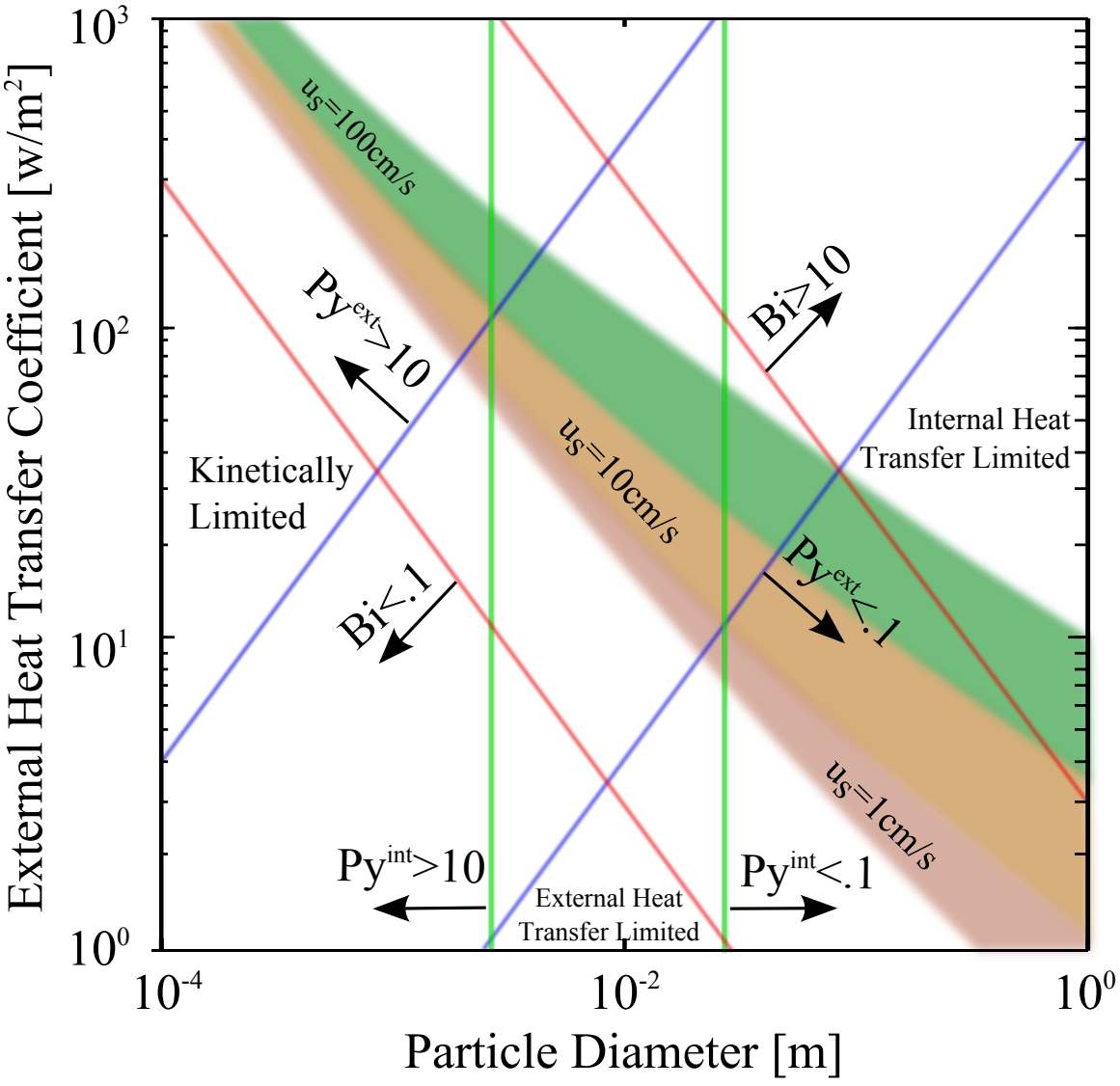


Figure 3-1: The devolatilization of biomass has three controlling regimes described by the biot number (Bi), the internal pyrolysis number ($Py^{int}$) and the external pyrolysis number ($Py^{ext}$). Here, these non-dimensional numbers are plotted for a wood particle with respect to particle diameter and the external heat transfer coefficient.

$$\phi_s = \left( \frac{SA_{sph}}{SA_p} \right)_{V_{sph} \equiv V_p}. \tag{3.6}$$

Since the surface of a sphere is known to be a surface area minimizing solid this value is necessarily positive and less than or equal to one for any solid particle [98]. This value can be calculated easily for any solid of regular geometry (platonic, cylindrical, etc.) or estimated by experimental means (see for example Kunii & Levenspiel [81]).

There exist a number of correlations to estimate the heat transfer coefficient of a particle in a fluidized bed reactor, the best known of which was reported by Kunii and Levenspiel in their second edition classic text [81] as:

$$Nu_p \cong 2 + (0.6 - 1.8) Re_p^{\frac{1}{2}} Pr^{\frac{1}{3}} \tag{3.7}$$

where $Nu_p$ is the Nusselt number of the particle and $Pr$ is the Prandlt number of the fluidizing gas phase. The range of values $(0.6 - 1.8)$ are taken from the two correlations calculated by Turton & Levenspiel and Ranz respectively [117, 137].

The Prandlt number of the gas phase fluidizing medium is defined by:

$$Pr = \frac{C_{p,g} \mu_g}{k_g}, \tag{3.8}$$

where $C_{p,g}$ is the specific heat capacity of the gas and $k_g$ is the thermal conductivity of the gas phase. From the Nusselt number definition,

$$Nu_p = \frac{h_p D_{eff}}{k_g}, \tag{3.9}$$

the particle heat transfer coefficient can be calculated.

The correlation for the solid-gas heat transfer coefficient employed in MFiX is based on the work of Gunn [64] for dense multi-phase flows:

$$Nu_p = (7 - 10\epsilon_g + 5\epsilon_g^2)(1 + 0.7 Re_p^{0.7} Pr^{\frac{1}{3}}) + (1.33 - 2.4\epsilon_g + 1.2\epsilon_g^2) Re_p^{0.7} Pr^{\frac{1}{3}} \tag{3.10}$$

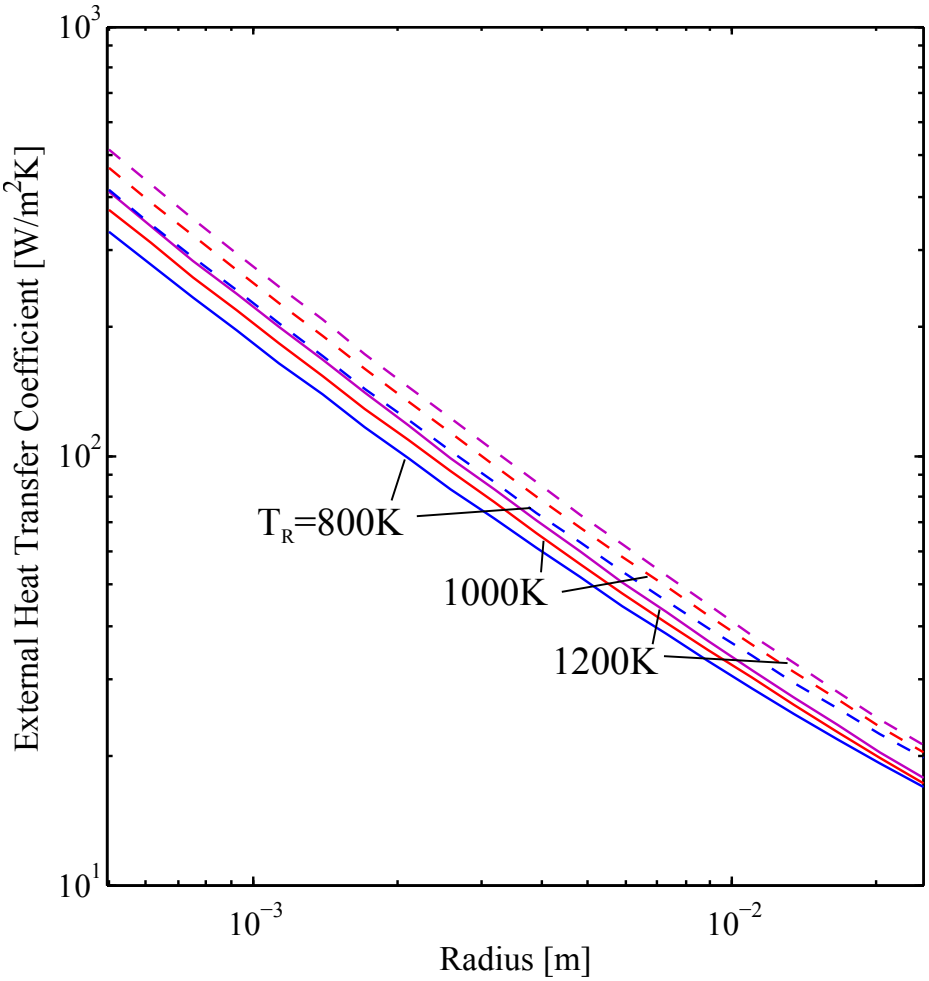


Figure 3-2: The external heat transfer coefficient calculated using the correlation of Gunn is plotted against particle radius for both spherical (solid lines) and cylindrical geometry (dashed lines) for three reactor temperatures and a superficial gas velocity of 10cm/s.

where $\epsilon_g$ is the local voidage. The heat transfer coefficients for spherical and cylindrical particles in a fluidized bed environment are plotted in Figure 3-2. It is observed that the effect of the non-spherical geometry, by increasing the effective surface area (therefore the particle has a smaller effective radius than is measured on the cylinder) the particle experiences faster heat transfer on the order of 20-25%. Additionally, the dependence against the superficial gas velocity in the reactor can be quantified and is shown in Figure 3-3. Here the heat transfer coefficient of a spherical particle of 4.8mm radius is shown for three reactor temperatures with respect to superficial gas velocities of 1, 10 and 100 cm/s respectively.

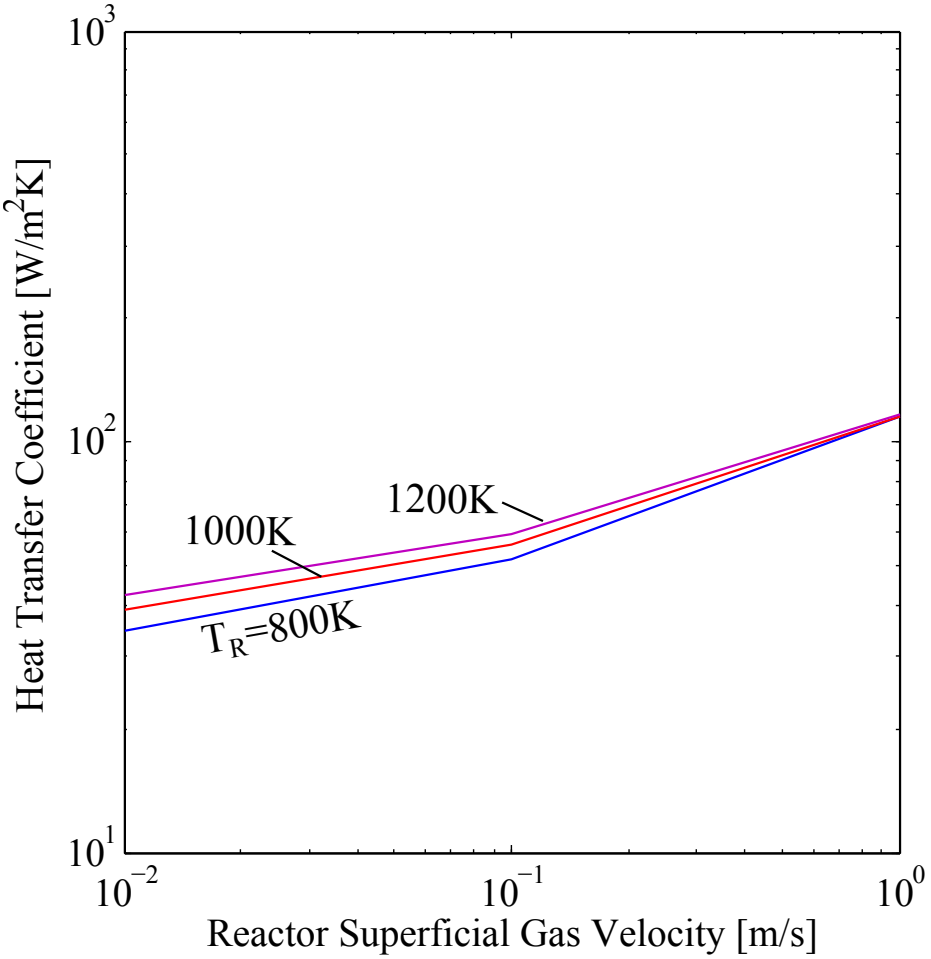


Figure 3-3: The dependence of the external heat transfer coefficient is plotted against reactor superficial gas velocity for a spherical particle having a radius of 4.8mm.

Table 3.2: The empirical three competing reaction devolatilization mechanism of biomass employed in CFD simulations [59].

| Reaction | Rate Expression [1/s] | Reaction Number |
|---|---|---|
| Biomass $\longrightarrow$ Gas | $1.43 \times 10^4 exp(-88600/RT)$ | (1) |
| Biomass $\longrightarrow$ Tar | $4.13 \times 10^6 exp(-112700/RT)$ | (2) |
| Biomass $\longrightarrow$ Char | $7.38 \times 10^5 exp(-106500/RT)$ | (3) |

In this shrinking-core model internal heat transfer, via conduction through the particle, is not directly modeled since it this requires internal time-dependent gradients to be calculated for each particle. Rather, it is modeled through the inclusion of a Fourier number effect on the effective kinetics of conversion via a serial resistance model. This is further developed and discussed in section 3.3.

### 3.2.2 Devolatilization Chemistry Modeling

In developing this shrinking core model a three-step competing reaction network is employed as is common in the literature of reactive CFD studies [59]. These reaction networks are fit empirically for different fuels, and care should be taken to use proper kinetics for a given fuel. In table 3.2 the parameters of this kinetic mechanism of devolatilization are tabulated.

## 3.3 Shrinking Core Model

In an eulerian modeling framework, less information on intra-particle conditions can be known as in a Lagrangian framework due to the lack of particle time history. As such, an assumption about the internal conditions must be made: Devolatilization occurs on an infinitesimally thin annular reaction zone between the unreacted core and char annular region.

A stronger assumption of kinetics occurring as an infinite rate is sufficient for thermally large particles; yielding a sufficient model based solely on the rate of heat transfer through the particle and has been shown to provide prediction of conversion rates at a good degree of accuracy for reactor design [66, 67]. For thermally small

particles this yields poor results since in this regime particle conversion is dictated by reaction kinetics. Detailed modeling efforts of thermally intermediate particles have shown evolving sensitivity to major physical and chemical parameters during conversion [114], however a simplified model is still desirable for reactor modeling implementations.

Shrinking core models with finite chemistry have been developed for the integration of oxygen diffusion limitations in char consumption models in coal combustion and gasification where an ash layer remains on the particle [75, 144]. In this case the effective rate is calculated as a series resistance of the kinetic rate of oxygen reacting with char and the diffusion of oxygen through the external ash layer:

$$k_{eff} = \frac{2}{\frac{1}{k_{kin}} + \frac{1}{k_{diff}}} \tag{3.11}$$

where $k_{eff}$ is the effective reaction rate, $k_{kin}$ is the kinetic reaction rate and the rate of diffusion is defined to be $k_{diff} = (R_p D_g)/(R_p - r_c)r_c$ the rate of diffusion of a gas with diffusivity $D_g$ through the ash layer from the surface ($R_p$) to the reacting core ($r_c$). This is a natural formulation since both are concentration driven processes and the total rate then can be calculated as:

$$Rate = k_{eff} c_g, \tag{3.12}$$

where $c_g$ is the concentration of the reactive gas in the surrounding bulk gas-phase at the surface of the particle.

Biomass devolatilization, on the other hand, is a mixture of a thermally and concentration driven process and a series resistance shrinking core model is developed to take into account these effects.

In an Eulerian model of a reacting fuel a limited number of vector quantities are tracked and solved for the solid phase- the local gas and solid temperatures, $T_g$ and $T_s$, the mass fractions of the solid components of biomass, $y_b$, and char, $y_c$, as well as the particle density, $\rho_p$, and particle radius, $R_p$. Given these values the extent of the reaction, and therefore the reacting core radius $r_c$ can be calculated:

$$r_c = \sqrt[3]{\frac{\rho_p}{\rho_b} y_b} R_p. \tag{3.13}$$

We now estimate the rate of thermal conduction through the char layer as:

$$k_{cond} \cong \frac{Fo_c}{t} = \frac{\alpha_c}{(R_p - r_c)^2} \tag{3.14}$$

where $Fo_c$ is the Fourier number of the char layer and $\alpha_c$ is the thermal diffusivity of char. Since we do not have access to the time history of the particle we divide out the time, $t$, and are left with this estimate of the rate of heat conduction.

We now define the effective rate of devolatilization as:

$$k_{eff} = \frac{1}{\frac{1}{k_{kin}} + \frac{x}{k_{cond}}}, \tag{3.15}$$

where $x$ is a fitting parameter needed to properly scale the relative timescales of the chemical and thermal rates. This formulation has a similar functional form as that developed for char oxidation with an important distinction. While this has the appearance of a harmonic mean it is purposefully not normalized to sum to one, as there is no constraint on the fitting parameter $x$ to conform to this.

Coupled with the lumped capacitance heat transfer model described in the previous section and employed in available multi-phase flow simulation packages such as MFiX this is sufficient to predict the devolatilization rates and chemical dependence on internal heat transfer effects as is demonstrated in the next section.

## 3.4 Results and Discussion

Two particle geometries are considered: (1) spherical and (2) cylindrical with an aspect ratio (L/D) of 3 representative of wood chips. These are each solved using the 1-D axisymetric model developed in chapter 2 where the simplified 3 reaction model shown in table 3.2 is employed in lieu of the detailed CRECK pyrolysis model. Each are solved assuming spherical symmetry (for cylindrical particles, an effective diameter is calculated).

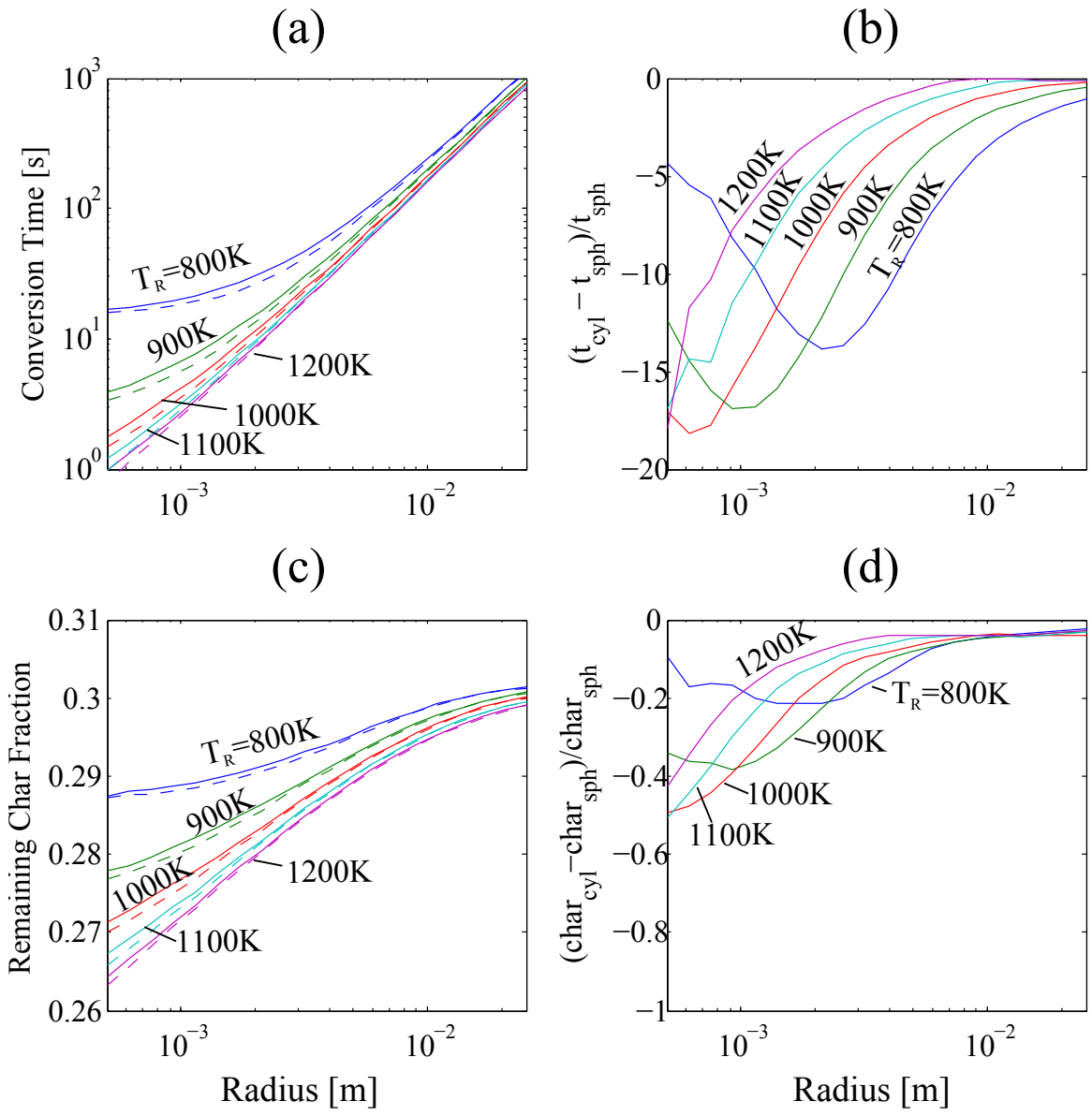


Figure 3-4: The effects of particle geometry and radius on conversion time and chemistry in the detailed particle model are illustrated. In (a) the conversion time of biomass particles are shown relative to particle radius, where the solid lines are the spherical particles and the dashed lines are cylindrical. In (b) the percentage difference between the conversion times of each geometry are shown relative to diameter. In (c) The predicted char fraction is shown relative to particle radius for various reactor temperatures. In (d) the percentage difference between the predicted char fractions of each geometry are shown.

In Figure 3-4 the influence of particle radius and geometry on devolatilization time and predicted char from the lagrangian model are illustrated. In Figure 3-4(a) the conversion times of both spherical and cylindrical particles are plotted for various reactor temperatures relative to particle radius. It can be observed that for high temperatures and increasing particle radius the conversion time scales as:

$$t_{devol} \propto R_p^2 \propto Fo^{-1}, \tag{3.16}$$

indicating a internal heat transfer controlled regime. While this holds for small particles in high temperature reactor conditions, where effective devolatilization reaction rates are very fast, at lower temperatures a transition is observed from an internal heat transfer controlled process to a kinetic one as the conversion time demonstrates independence from the particle radius effects. In between these two extremes we are faced with a complex conversion regime that is sensitive to kinetics as well as internal and external heat transfer. This sensitivity to external heat transfer is illustrated in Figure 3-4(b) where the percentage difference in conversion times for spherical and cylindrical particles are plotted against particle radius; since the primary difference in thermal effects between these two geometries is manifested through the heat transfer coefficient this comparison is ideal to show its effect. It is observed that for low reactor temperatures where the transition from kinetic to internal heat transfer control is easily observed there is a peak sensitivity which shifts downward with respect to particle radius. At radii larger than this peak sensitivity, as the Biot number increases internal heat transfer effects dominate external ones, while at radii smaller than this peak we observe again a decreasing influence in external heat transfer effects due to a shrinking external pyrolysis number. In Figure 3-4(c) these same influences can be observed on the chemical conversion illustrated by the predicted char fraction at the end of the process. Here, while the sensitivity is much weaker we more clearly observe the transition region for low temperatures where it is not until much larger radii that the predicted char fraction flattens out indicating that full kinetic control is achieved and therefore reaction temperatures are purely dictated by the internal heat transfer

rate. Similarly at smaller radii the flattening is observed for the lowest temperatures where it is observed that the reaction temperature is then influenced most strongly by kinetics. In Figure 3-4(d) where the influence of the predicted char fraction is plotted it is observed that the overall sensitivity to heat transfer is quite small indicating that the determination of the effective devolatilization reaction temperatures in the reacting zone and therefore the chemical process is mostly dominated by the kinetics and internal heat transfer within a fluidized bed. This is the case because of the very fast heat transfer experienced in this environment by design of the reactor.

### 3.4.1 Calculation of the fitting parameter, $x$

Ideally one would like for this shrinking core model to demonstrate quantitatively both of the effects of particle radius on both the conversion time and the chemical conversion as shown through predicted char content. However, since CFD simulations cannot employ large detailed chemical mechanisms capable of predicting reactive intermediates and tar growth/consumption without unacceptably long run times it is the focus hear to achieve fidelity in the prediction of conversion times and to accept error in char prediction. This is also an ideal approach when the sensitivity of each of these is considered, since the conversion time is proportional to the square of the particle radius, while the char varies within a margin of uncertainty we will expect that any model error incurred in the prediction of chemical species will be acceptable so long as it occurs on the proper conversion scale so as CFD can be used as a tool to analyze the relative effects of devolatilization times and mixing.

In order to solve for $x$, a minimization strategy was used, with an objective function:

$$Err(x) = (t_{sc}(x) - t_{lagrange})/t_{lagrange}, \tag{3.17}$$

where $Err$ is the error of prediction of the conversion time of the shrinking core model, $t_{sc}$, and the detailed lagrangian particle model, $t_{lagrange}$. Next a multi-variate curve fitting was employed to find a smooth function able to approximate alpha given

| parameter | $u_0 = 0.01m/s$ | $u_0 = 0.1m/s$ | $u_0 = 0.01m/s$ |
|---|---|---|---|
| a | -20.78 | -0.04978 | 11.65 |
| b | 0.03983 | 0.004536 | -0.01636 |
| c | -1.64E-05 | -2.03E-06 | 6.23E-06 |
| d | 0.3009 | -0.09204 | -0.5188 |
| e | -0.003442 | -0.00472 | -0.00673 |

Table 3.3: Fitting parameter values for equation 3.19 at three superficial gas velocities representative of the operational space.

the effective particle radius, reactor temperature and superficial gas velocity.

This procedure has produced the following fit:

$$x = a + bT_R + cT_R^2 + dln(R_{eff}) + eR_{eff}^{-1}, \tag{3.18}$$

In Figure 3-5 these fits are plotted for the three superficial gas velocities, .01, .1 and 1 m/s respectively. Here we can see we achieve a good fit across operational parameters. It should be noted however, that this procedure and fit produces physically unrealistic negative alphas for small particle sizes and low temperatures. This is because at these small particle sizes very little sensitivity is found with respect to this parameter reflecting conductive heat transfer since we are in a regime dominated by kinetics. As such we simply modify the fit:

$$x = max(0, a + bT_R + cT_R^2 + dln(R_{eff}) + eR_{eff}^{-1}). \tag{3.19}$$

Now, when $x = 0$ we are in a purely kinetically controlled regime and when $x > 0$ we are able to capture the internal heat conduction effects.

### 3.4.2 Devolatilization Model Validation

In figure 3-6 the predicted conversion times and char concentrations of a spherical particle from the shrinking core devolatilization model are are compared with the predictions from the detailed lagrangian devolatilization model. It is observed that good quantitative agreement is achieved across particle lengths and reactor temperatures

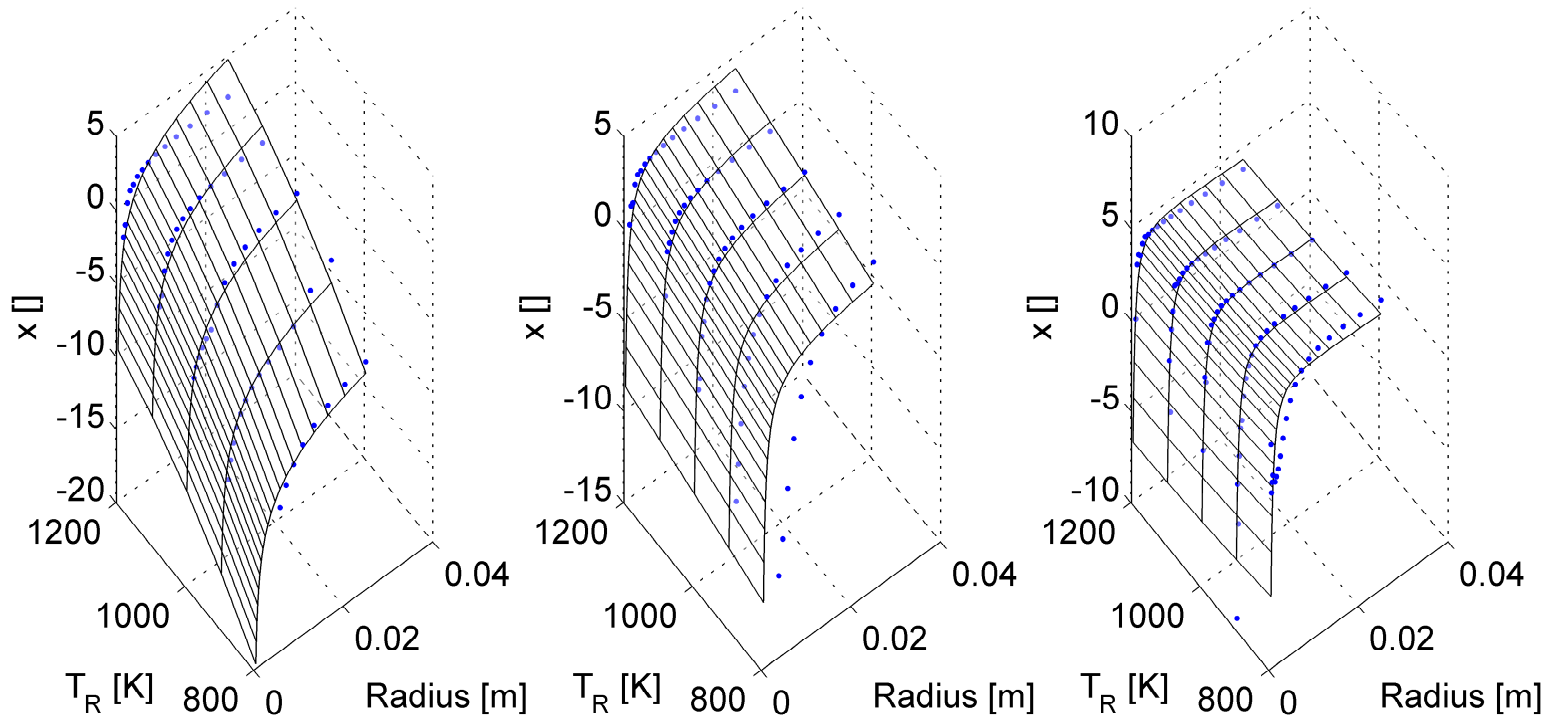


Figure 3-5: The calculated $x$ values (blue dots) along with the fitted function $x = f(T_R, R_{eff}, u_0)$ are plotted for three superficial gas velocities .01, .1 and 1 m/s respectively.

for the predicted conversion time. Importantly, as can be observed in figure 3-6(a) at low reactor temperatures (800K) the transition from kinetic control to internal heat transfer control is preserved indicating that the shrinking core model is able to capture these physics in a simple set of of ODEs as compared to the PDE required to describe the lagrangian particle.

In figure 3-6(b) it is also observed that while there is error incurred in the prediction of char at higher particle sizes the overall qualitative agreement is good and the dynamics are also preserved. This error is likely due to the assumption that reactions occur within an infinitesmally thin reaction zone, and as such at one temperature instead of in a wide reaction zone where a range of temperatures are experienced by the reacting biomass.

## 3.5 Conclusions

In this chapter a shrinking-core devolatiliziation model was developed and validated against the detailed lagrangian particle model framework developed in chapter 2utilizing a simplified devolatilization chemistry suitable for fully reactive CFD studies of biomass gasifiers of industrially relevant sizes. This shrinking core model is employed in the CFD studies employed in chapter 6 where the influence of solids-solids mixing and segregation on the overall chemical process is interrogated.

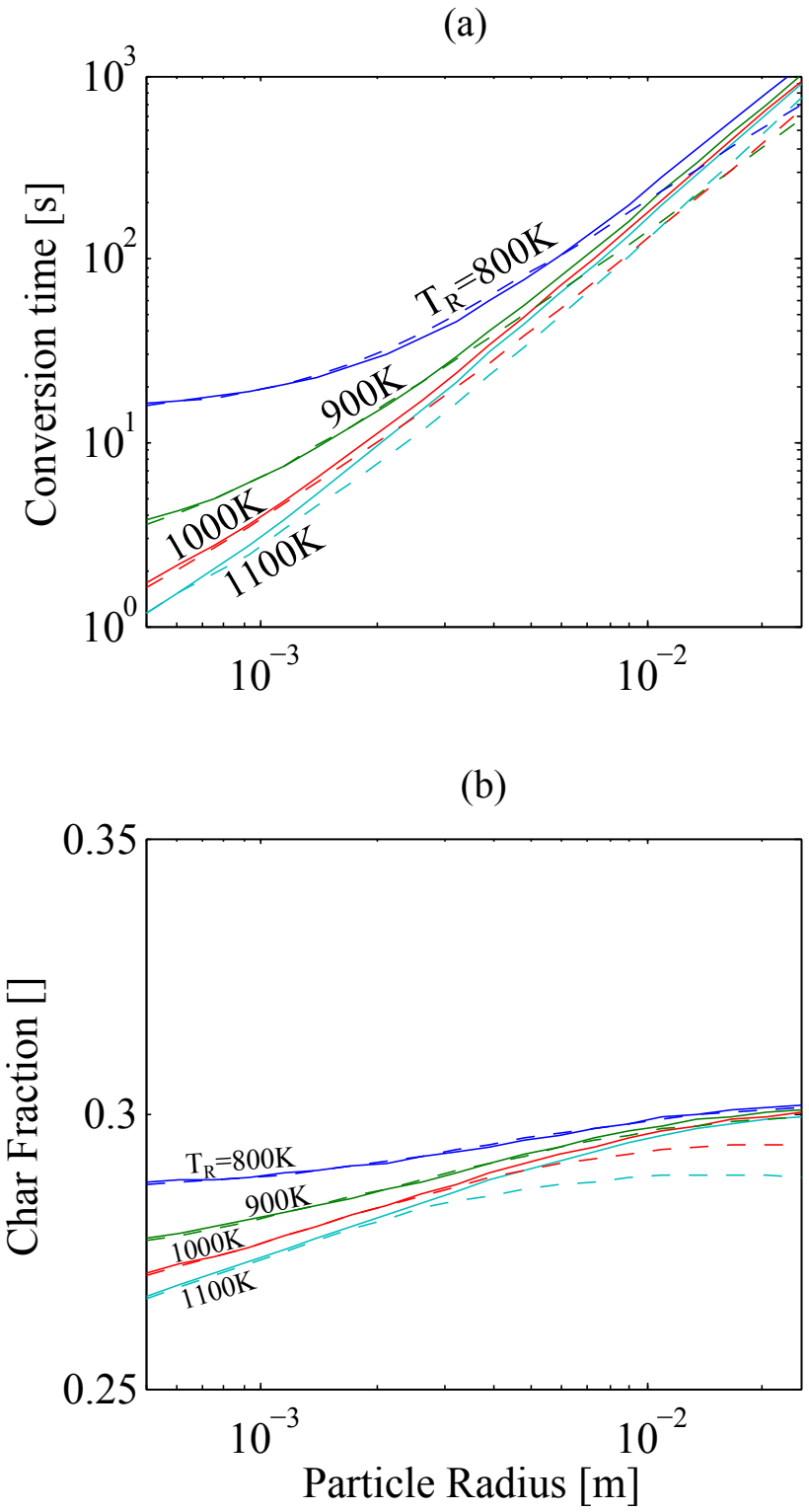


Figure 3-6: In (a) the predicted conversion times of the lagrangian devolatilization particle (solid lines) and the shrinking core devolatilization model are compared for various reactor temperatures against particle radius. In (b) the predicted char fractions are compared at the same conditions.

# Chapter 4

# Gas-Phase Species Modeling in a Fluidized Bed Biomass Gasifier

## 4.1 Introduction

Fluidized Bed Biomass Gasification (FBBG) has been identified as a promising technology for biomass gasification due to the specific physical properties of biomass. However, under typical operating conditions for FBBG ($700 - 1000°C$), tars exist in the product gas as a complex mixture of aromatic hydrocarbons in significant quantities ($2 - 50 g/Nm^3$) [101]. Within this range of operating temperatures, there is a strong temperature dependence for both the tar composition and the overall tar yield. This is reflected in an increasing dew-point of tars above $800°C$ where large PAH growth is favored, while the overall tar concentration of the product gas decreases due to improved kinetics of tar oxidation [88]. These dependencies are highly non-linear and therefore simple global mechanisms fail to account for tar composition evolution. In which case, a chemical kinetic model of sufficient fidelity is required for reactor modeling efforts.

The CRECK Modeling Group at Politecnico di Milano [26, 118–120] has proposed and developed a kinetic mechanism of biomass conversion encompassing the devolatilization and gas-phase thermochemical conversion of biomass with general applicability to various reactor regimes: pyrolysis ($300 - 650°C$), gasification ($700 -$

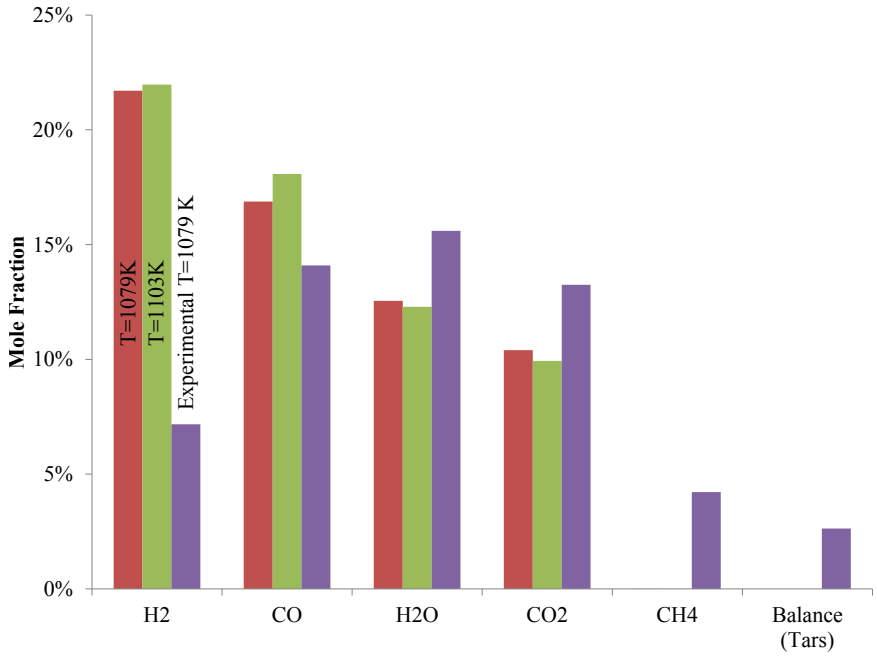


Figure 4-1: Comparison of equilibrium concentrations and experimental measurements of the major gas-phase products of beech wood gasification at two bed temperatures [138].

$1000°C$), and combustion ($> 1000°C$). This mechanism is sufficiently tractable in kinetic simulations utilizing idealized 0-D or 1-D reactors, however efforts to include detailed spatial representations make the computational cost of modeling grow exponentially, owing to the need to track many hundreds of species in each spatial node. It is, therefore, necessary to limit the spatial resolution of a reactor-scale simulation and instead model the reactor hydrodynamics with a reactor network that captures the relevant hydrodynamics dictating chemical residence times.

The validity of a model of biomass gasification is, to first order, dependent on its ability to predict the major constituents of syn-gas production: hydrogen, carbon monoxide, carbon dioxide and water. Additionally, the ability to predict methane and tars - both undesired side-products which decrease the carbon conversion efficiency and require capital intensive clean-up operations before downstream synthesis steps - is crucial because minimization of their production is an important goal of gasifier design and operation.

Equilibrium modeling has been used to predict simple operational metrics of

Table 4.1: General reaction pathways of the thermal decomposition of tars, adapted from Li & Suzuki (2009). [86]

| Reaction Class | Generic Reaction |
|---|---|
| Cracking | $pC_nH_x \rightarrow qC_mH_y + rH_2$ |
| Steam Reforming | $C_nH_x + nH_2O \rightarrow (n + (\frac{x}{2}))H_2 + nCO$ |
| Dry Reforming | $C_nH_x + nCO_2 \rightarrow \frac{x}{2}H_2 + 2\,nCO$ |
| Carbon Formation | $C_nH_x \rightarrow nC + \frac{x}{2}H_2$ |

biomass gasifiers, such as the cold gas efficiency [88, 127]. However, experimental results refute this approach for prediction of the outlet gas composition. Equilibrium calculations strongly over-predict hydrogen and under-predict methane and tar concentrations at temperatures relevant to FBBG. Figure 4-1 compares Gibbs Minimization equilibrium calculations performed at two representative temperatures (1079K and 1103K) with the experimental measurements from van Paasen and Kiel of major gas species exiting an air-blown FBBG [138]. While the equilibrium calculations predict virtually no methane or tars, in actuality the experiment shows appreciable quantities of both, demonstrating that the gas phase conversion is kinetically limited.

Previous study and modeling of tar evolution has focused on high-temperature tar clean-up technology for solid fuel conversion. Jess [76] experimentally studied the thermal reactions of aromatic hydrocarbons - naphthalene, toluene and benzene - as representative tar model compounds from solid fuel pyrolysis (coal and biomass) at slight pressure (160 kPa) and temperatures between $700-1400°C$. A clear order of tar oxidation reactivity was shown: toluene >>naphthalene >benzene. Further, a simple mechanism and associated kinetic parameters were estimated for kinetic modeling of tar destruction but not tar growth or PAH formation. In addition, oxygenated hetero-cyclic tars, such as phenol, were neglected, even though these compounds play an important role in biomass tar formation and destruction. Fourcault et al. [50] considered a high-temperature tar destruction mechanism in a plasma torch at $1100°C$. For their modeling framework, Fourcault et al. used the reaction classes proposed by Li and Suzuki [86] (see Table 4.1) and estimated kinetic parameters for model tar compounds.

In their review of tar conversion, Li and Suzuki [86] considered tar reforming for biomass gasification, extending the consideration beyond simple one-ring tars such as benzene and toluene and two-ring aromatics such as naphthalene to represent PAHs and soot production pathways. Li and Suzuki observed that even small concentrations of tars with high dew-points can severely impair downstream processing. They reported that the tar dew-point is dominated by large PAHs even at extremely small concentrations ($0.1 mg/Nm^3$), concluding that the fundamental understanding and modeling of the primary and secondary tar conversions of solid fuels is a crucial aim. Beyond considering tar destruction pathways, Font Palma (2013) [49] reviewed the tar growth mechanisms from biomass pyrolysis products, and has developed a simple kinetic model of biomass gasification including tar creation and evolution of aromatics and small PAH compounds [48]. Unfortunately, no model which accounts for all tar compounds of interest has yet been employed in literature to predict tar formation and destruction, as well as the major-phase species produced in during FBBG.

## 4.2 Modeling Framework

Biomass gasification is defined by the interaction of a number of complex processes and cannot be completely characterized as a series of sequential steps since many process occur concurrently. However, a natural description of biomass gasification takes the form of the following major processes:

1. *Drying* - Characterized by processes occurring at temperatures around 100°C in which moisture is liberated by evaporation.

2. *Devolatilization* - The chemical conversion by which the raw biomass is converted to gases (>70%) and char. These conversions happen in the temperature range of $200 - 600$°C, and the product distributions are a function of the reaction temperature.

3. *Secondary pyrolysis and gas phase reactions* - The intermediate devolatilization products undergo further pyrolytic reactions, heterogeneous reactions with the

char, tar cracking & oxidation and PAH growth reactions in the gas-phase of the reactor.

4. *Char consumption* - After the solid devolatilization process is complete, the remaining solids undergo relatively slower oxidation reactions as well as loss from the reactor through fines elutriation.

In Figure 4-2 the conversion pathways of biomass under fluidized bed gasification conditions are illustrated. The majority of the mass of the biomass is liberated during devolatilization to the gas-phase where the devolatilization products undergo a multitude of reactions. The remaining solid mass after devolatilization, known as char, is consumed by steam gasification and oxidation reactions but also by entrainment and elutriation out of the bed.

## 4.3 Reactor Network Gasifier Model

The conversion of biomass in a FBBG is governed by the complex interplay of bed hydrodynamics, heat transfer and chemistry. Modeling efforts must consider each of these phenomena with sufficient fidelity to accurately represent the conversion while being mindful of the computational cost associated with increased model complexity. In the following subsections the RNM developed for this work along with the physio-chemical sub-models employed are discussed.

### 4.3.1 Chemistry Modeling

The CRECK kinetic model has broad applicability across thermal and reactive conditions - from low temperature pyrolysis to high temperature combustion. The mechanism consists of a two-stage model: (1) solid devolatilization reactions and (2) the subsequent gas-phase reactions of the devolatilization gases.

The devolatilization model consists of 19 reactions of 12 solid species, 4 trapped gases which are slowly released from the solid matrix and 19 gas-phase devolatilization products which are detailed in Table 4.2. The devolatilization model is a linear

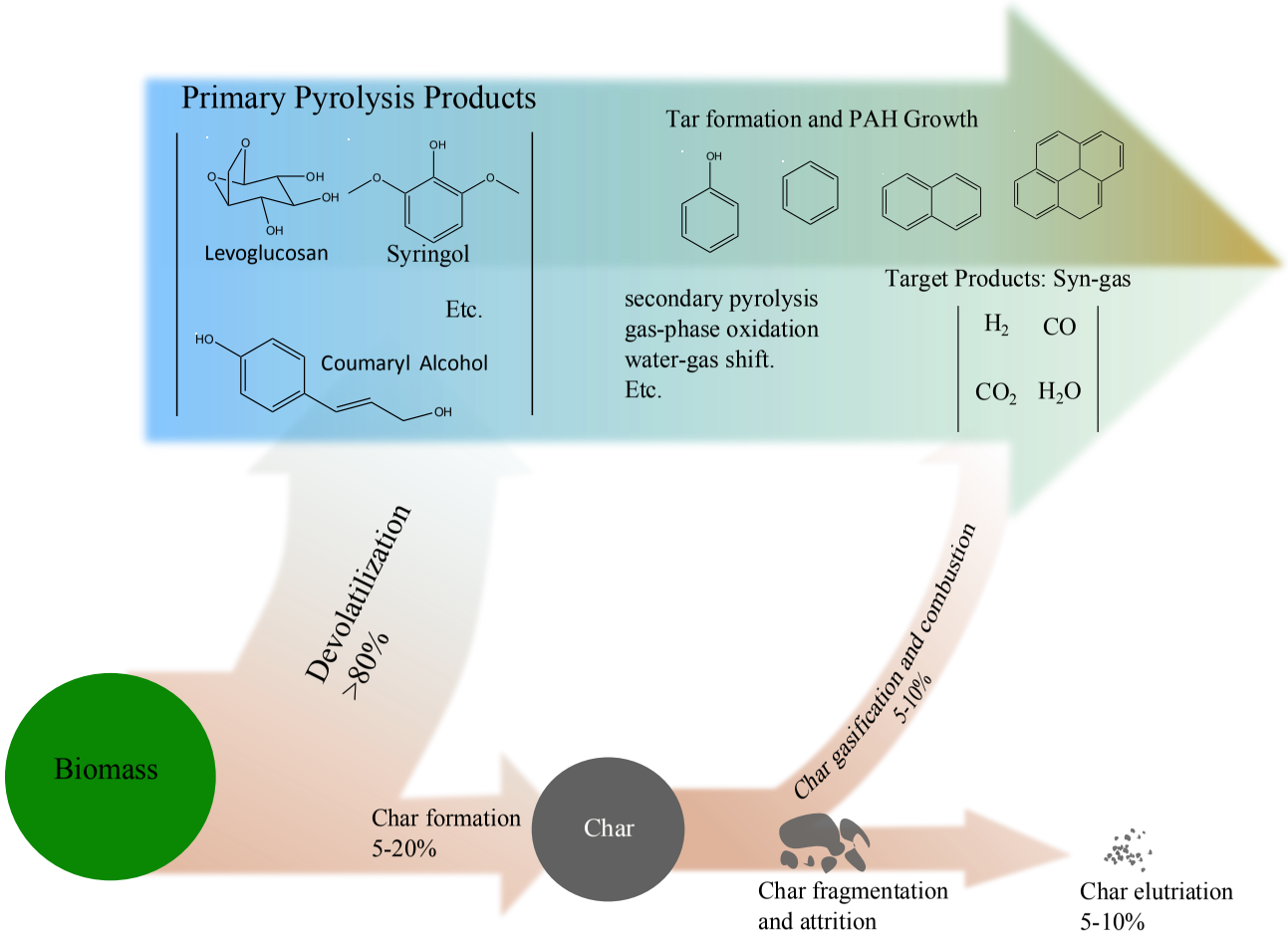


Figure 4-2: The thermochemical conversion pathways of biomass under fluidized bed gasification conditions.

superposition of the reactions of each of cellulose, hemicellulose and lignin, which allows for an accurate description of any biomass so long as its ratios of these biopolymers can be estimated. In this work, this kinetic devolatilization model is coupled with heat-transfer calculations for a particle scale representation of the conversion to more accurately model the conversion of particles of varying sizes. This particle model is discussed in the next section.

The devolatilization products from the first conversion stage are then used as an input for the gas-phase secondary pyrolysis and oxidation mechanism which includes further pyrolysis and oxidation reactions of tars, as well as the detailed combustion reactions of hydrocarbons.

The target product of gasification is syn-gas. As such, it is crucial for a reactor model to be able to predict the conversion of the devolatilization products to these species as well as methane and tars - the major byproducts of conversion. Table 4.3 shows the gas-phase species of interest in this study for validating against experimental measurements. The tar species which are directly modeled in the CRECK model are grouped into their respective tar classes as described and applied by van Paasen & Kiel in their experimental study [138].

### 4.3.2 Particle Devolatilization Model

FBBG allows for the utilization of biomass particles of varying size. During biomass devolatilization, the internal temperature profile of large particles is critical to predicting the resulting yields of char, primary tars, and light gases [40]. For this work devolatilization is modeled utilizing the CRECK primary pyrolysis mechanism described above, implemented in a single particle model which couples the kinetics with both internal and external heat transfer (see Chapter 2). The results of these calculations at two bed temperatures (1079 & 1103K) are shown in Table 4.4. Here, the particle diameter was assumed to be 1mm, characteristic of the reported experimental diameters: $0.75mm < d_p < 2mm$. For beech wood the initial lignin fraction was reported to be $24\%_{wt,daf}$. Given the ultimate analysis, the resultant hemicellulose and cellulose fractions were calculated to be $36\%_{wt,daf}$ and $40\%_{wt,daf}$ respectively us-

Table 4.2: Primary pyrolysis modeling species employed in the devolatilization mechanism [120].

| **Solid Phase** | | **Gas Phase** | | |
|---|---|---|---|---|
| Primary Components and Products | Reactive Intermediates | Trapped Gasses | Product Gases | Chemical Formula |
| Cellulose (CELL) | Activated Cellulose (CELLa) | Hydrogen (T[$H_2$]) | Hydrogen | $H_2$ |
| Hemicellulose (HCE) | Activated Hemicellulose (HCE1) | Carbon Monoxide (T[CO]) | Water | $H_2O$ |
| Carbon-Rich Lignin (LIGC) | Activated Hemicellulose (HCE2) | CO+H2 (T[$COH_2$]) | Carbon Monoxide | CO |
| Hydrogen-Rich Lignin (LIGH) | Activated Lignin (LIGCC) | Carbon Dioxide (T[$CO_2$]) | Carbon Dioxide | $CO_2$ |
| Oxygen-Rich Lignin (LIGO) | Activated Lignin (LIGOH) | | Formaldehyde | $CH_2O$ |
| Char C | Activated Lignin (LIG) | | Methane | $CH_4$ |
| | | | Methanol | $CH_3OH$ |
| | | | Glyoxal | $C_2H_2O_2$ |
| | | | Ethylene | $C_2H_4$ |
| | | | Acetaldehyde | $CH_3CHO$ |
| | | | Hydroxyacetaldehyde | $C_2H_4O_2$ |
| | | | Ethanol | $C_2H_5OH$ |
| | | | Malonaldehyde | $C_3H_4O_2$ |
| | | | Oxetane+Propyleneoxide | $C_3H_6O$ |
| | | | Xylofuranose | $C_5H_8O_4$ |
| | | | Phenol | $C_6H_5OH$ |
| | | | 5-(hydroxymethyl)-furfural | $C_6H_6O_3$ |
| | | | Levoglucosan | $C_6H_{10}O_5$ |
| | | | pCoumaryl | $C_9H_{10}O_2$ |
| | | | 3-(4-hydroxy-3,5-dimethoxyphenyl)acryaldehyde | $C_{11}H_{12}O_4$ |

Table 4.3: Tars and Major gas-phase species considered. Tars are listed in their respective classification as described and applied by van Paasen & Kiel [138].

| Class # | Species Name | Chemical Formula |
|---|---|---|
| Class 1 (GC undetectable) | N/A | N/A |
| Class 2 (hetero-cyclic aromatics) | Phenol | $C_6H_5OH$ |
| | Cresol | $C_7H_7OH$ |
| | Napthol | $C_{10}H_7OH$ |
| | Syringol | $C_8H_{10}O_3$ |
| | pCoumaryl | $C_9H_{10}O_2$ |
| | Sinapoyl Aldehyde & isomers | $C_{11}H_{12}O_4$ |
| Class 3 (1-ring aromatics) | Xylene | $C_8H_{10}$ |
| | Styrene | $C_6H_5C_2H_3$ |
| | toluene | $C_7H_8$ |
| | Benzene | $C_6H_6$ |
| Class 4 (light PAH [2-3 ring]) | Naphthalene | $C_{10}H_8$ |
| | acenaphthalene+isomers | $C_{12}H_8$ |
| | Biphenyl | $C_{12}H_{10}$ |
| | Fluorene | $C_{13}H_{10}$ |
| | phenanthrene+anthracene | $C_{14}H_{10}$ |
| | benzylphenylmethane | $C_6H_5C_2H_4C_6H_5$ |
| | Diphenylmethane | $C_6H_5CH_2C_6H_5$ |
| Class 5 (heavy PAH [4-7 ring]) | pyrene+isomers | $C_{16}H_{10}$ |
| | 7,12-Dimethylbenz(a)anthracene & iso. | $C_{20}H_{16}$ |
| | Corannulene and isomers | $C_{20}H_{10}$ |
| Major components | nitrogen | $N_2$ |
| | oxygen | $O_2$ |
| | hydrogen | $H_2$ |
| | water | $H_2O$ |
| | carbon-monoxide | CO |
| | carbon-dioxide | $CO_2$ |
| | methane | $CH_4$ |

Table 4.4: Calculated devolatilization product mass fractions for 1mm ash-free beech particles undergoing devolatilization at fluidized bed conditions at two bed temperatures given in a dry and as-delivered (wet) basis.

| | Temperature = 1079K | | Temperature = 1103K | |
|---|---|---|---|---|
| Species [kg/kg biomass] | Dry | Delivered | Dry | Delivered |
| Levoglucosan | 37.29% | 28.61% | 36.42% | 28.31% |
| Carbon Dioxide | 13.78% | 10.58% | 13.78% | 10.71% |
| Carbon Monoxide | 9.79% | 7.52% | 10.22% | 7.94% |
| Formaldehyde | 6.60% | 5.06% | 6.51% | 5.06% |
| Water | 5.14% | 14.25% | 5.12% | 14.28% |
| Acetic Acid | 5.01% | 3.84% | 5.10% | 3.97% |
| Methane | 4.32% | 3.32% | 4.28% | 3.32% |
| Methanol | 4.05% | 3.11% | 4.01% | 3.11% |
| Ethylene | 4.04% | 3.10% | 4.00% | 3.11% |
| Synapoyl aldehyde | 2.97% | 2.28% | 2.86% | 2.23% |
| 5-(hydroxymethyl)-furfural | 2.77% | 2.12% | 2.82% | 2.19% |
| Oxetane+Propyleneoxide | 2.76% | 2.12% | 2.75% | 2.14% |
| Ethanol | 1.99% | 1.53% | 1.96% | 1.53% |
| Xylofuranose | 1.94% | 1.49% | 1.85% | 1.44% |
| 4-(3-hydroxy-1-propenyl)phenol(pCoumaryl) | 1.86% | 1.43% | 1.86% | 1.45% |
| Glyoxal | 1.27% | 0.98% | 1.30% | 1.01% |
| Acetaldehyde | 0.94% | 0.72% | 0.95% | 0.74% |
| Phenol | 0.86% | 0.66% | 0.86% | 0.67% |
| Malonaldehyde | 0.47% | 0.36% | 0.48% | 0.38% |
| Hydrogen | 0.25% | 0.19% | 0.29% | 0.22% |
| Char | 7.51% | 6.74% | 6.91% | 6.20% |

ing the methodology described by Ranzi et al. to match the atomic balance of the biomass with the modeling compounds CELL, HCE and LIG-X [119].

It can be noted that at these temperatures the predicted char yield is relatively low; approximately $6.9 - 7.5\%$ by weight of the initial dry biomass. The major mass yields from devolatilization are levoglucosan, carbon dioxide, and carbon monoxide. Together they account for 56%wt of the volatiles. Levoglucosan comprises the greatest fraction because it comes from the depolymerization of cellulose, which is the largest lignocellulosic fraction in the biomass. When considering the molar flow rates, carbon monoxide, carbon dioxide and water comprise 40% of the pyrolysis volatiles by volume. Other minor fractions such as pCoumaryl and synapoyl aldehyde - gases derived from lignin - play important roles in tar formation and therefore their accurate prediction is crucial. Additionally, it is notable that the temperature dependence of

the devolatilization gas distribution is quite weak at these high temperatures since the particles are not small enough to be kinetically controlled, internal heat transfer plays an important role in defining the temperature of devolatilization.

### 4.3.3 Reactor Geometry and Flow Characteristics

For air-blown gasification, the feeding rate of the air is defined by the air-fuel equivalence ratio (ER). The ER is defined as:

$$ER = \frac{\dot{m}_{\mathrm{O}_2,actual}}{\dot{m}_{\mathrm{O}_2,stoichiometric}}, \tag{4.1}$$

where $\dot{m}_{\mathrm{O}_2,actual}$ is the actual mass flow rate of oxygen into the gasifier and $\dot{m}_{\mathrm{O}_2,stoichiometric}$ is the mass flow rate of oxygen required for stoichiometric combustion. The ER is one of the most important adjustable parameters characterizing biomass gasification, as it affects the chemistry both (1) directly through the availability of oxygen and (2) indirectly through the gasifier temperature. The stoichiometric oxygen requirement is dependent on the chemical composition of the biomass and is readily calculated from the ultimate analysis of the biomass:

$$\left.\frac{\dot{m}_{\mathrm{O}_2}}{\dot{m}_{biomass}}\right|_{stoich} = \left(Y_{\mathrm{C}}\frac{MW_{\mathrm{O}_2}}{MW_{\mathrm{C}}} + \frac{Y_{\mathrm{H}}}{4}\frac{MW_{\mathrm{O}_2}}{MW_{\mathrm{H}}} - \frac{Y_{\mathrm{O}}}{2}\frac{MW_{\mathrm{O}_2}}{MW_{\mathrm{O}}}\right)\left[\frac{kg_{\mathrm{O}_2}}{\mathrm{biomass}}\right], \tag{4.2}$$

where $\dot{m}_x$ is the mass flow-rate of the species $x$. $Y_{\mathrm{C}}$, $Y_{\mathrm{H}}$ and $Y_{\mathrm{O}}$ are the mass fractions of carbon, hydrogen and oxygen respectively of the fuel on a dry and ash-sulfur- & chlorine-free basis. $MW_x$ is the molecular weight of the species $x$ in kilograms per kmol. If air is assumed to be $76.47\%_{wt}$ $\mathrm{N}_2$ and $23.53\%_{wt}$ $\mathrm{O}_2$, then, for a given ER and biomass, the air feed rate to fuel feed rate is calculated to be:

$$\frac{\dot{m}_{air}}{\dot{m}_{biomass}} = \frac{ER}{0.2353}\left.\frac{\dot{m}_{\mathrm{O}_2}}{\dot{m}_{biomass}}\right|_{stoich}. \tag{4.3}$$

Given the mass flow-rate of air and devolatilized biomass as well as the operating pressure and temperature, the incoming superficial gas velocity can be estimated.

The superficial gas velocity is defined as the volumetric flow rate of gas divided by cross sectional area of the bed. This quantity defines the hydrodynamic state of the fluidized bed and determines the residence times of the volatiles in the multi-phase region and the freeboard [58]. In their experimental work, van Paasen & Keil held the ER to 0.25 with a mass flow rate of biomass of $1kg/hr$, resulting in an air flow-rate of 1.266 kg/hr and a devolatilization gas flow rate of approximately .93 kg/hr yielding an estimated superficial gas velocity of 0.38m/s at 1979K. The incoming superficial gas velocity is approximately $14 - 15\times$ the minimum fluidization velocity of 270$\mu$m silica sand at the operating temperatures resulting in the bed operating in the turbulent/slugging fluidization regime [58].

Given the superficial gas velocity, the effective bed volume is necessary to characterize the residence time of the gases in the multiphase region while, for the freeboard, both volume and length are required. The volume of the multiphase region is calculated as:

$$V_{bed} = \epsilon_{mf} \pi h_{bed,expanded} \left( \frac{D_{bed}}{2} \right)^2, \tag{4.4}$$

where $\epsilon_{mf}$ is the voidage of the bed at minimum fluidization, $h_{bed,expanded}$ is the height of the expanded bed, and $D_{bed}$ is the (fixed) diameter of the bed. Due to incoming flow velocity, the voidage in the bed increases from its static value, and the bed expands from its reported static height of $0.149m$ to a calculated $0.268m$. The gas-phase volume of the multiphase region is, therefore, estimated to be $1153cm^3$. The fluidized bed reactor is designed with additional height before the expansion zone for the freeboard. Therefore, the remainder of the bed height acts as part of the freeboard. As such - taking into account the expansion zone - the effective freeboard volume is calculated to be $6493cm^3$, with an effective length of 70.9cm.

At these flow conditions with a bed temperature of 1079K, the calculated gas residence time in the multi-phase region is approximately $0.65 - 0.7$ seconds, while in the freeboard it is estimated to be $3.7 - 3.9$ seconds. This agrees with the reported gas residence time in the freeboard of $3.6 - 4$ seconds [138].

By defining two inlet stream flows and maintaining the reactor volumes and lengths as constant, the air-fuel equivalence ratio is independently varied for parametric study. As the air-fuel equivalence ratio increases, more air is fed into the gasifier. This slightly reduces the residence time of the volatiles in both the bed and freeboard region. However, by holding the geometry constant, the residence time calculations are adjusted accordingly.

### 4.3.4 Reactor Network Model

Fluidized bed gasifiers exhibit complex hydrodynamic behavior. A variety of simplifying assumptions are adopted to represent the reactor as a combination of idealized reactors:

- *Biomass Drying and Devolatilization occurs uniformly through the bed.* - This assumption is valid and applicable when pyrolysis is much slower than the characteristic mixing time for the solid [116]. van Paasen & Kiel used biomass particles with diameters ranging from 0.75-2mm whose devolatilization time is calculated to be approximately $1-2$ seconds, which is lower than the estimated mixing time of this reactor. The circulation time of this vigorously fluidized bed is calculated to be 0.7 seconds using the correlation of Rowe [125]. As a result, for a continuous feed, the wood particles are assumed to undergo drying and devolatilization uniformly mixed throughout the fluidized bed.

- *Heterogeneous char oxidation and gasification reactions are neglected.* - This assumption is valid when the average residence time of char particles is much shorter than the characteristic time required for the heterogeneous gasification reactions to proceed. The residence time of the char particles is limited by their tendency to be elutriated out of the fluidized bed. The characteristic time of wood-chip char elutriation is estimated as $d_{char}/(k_{att}(U_0/U_{mf}-1)) \approx 110s$ for this reactor condition where $d_{char}$ is the calculated fragmented char particle diameter [62], and $k_{att}$ is an emperically derived attrition rate constant [30, 128]. The characteristic time for gasification depends strongly on temperature and

pressure, but at $800°C$ it has been shown to be relatively slow (with characteristic times between 1100-4000 seconds) [43]. Based on the reported carbon conversion (93%), we compare the calculated char yield of $7\%_{wt}$ from particle-scale beech devolatilization model to confirm this assumption. Therefore, we believe it is justified to assume that the carbon conversion via char oxidation is negligible and elutriation dominates.

- *The fluidized bed region of the reactor is modeled as an isothermal continuously stirred reactor (CSTR).* - This assumption is valid when the bubbles are relatively small and mixing is vigorous. As bubble size shrinks, the mass transfer resistance between the bubble and emulsion phase vanishes. As noted by Gomez-Barea & Leckner, [62] experimental evidence shows that while sharp gradients may exist locally at the distributor, most of the bed exists with spatially constant gas concentrations and at a uniform temperature, consistent with a CSTR assumption.

- *The freeboard is modeled as an isothermal plug flow reactor (PFR).*- Modeling the freeboard as a PFR is commonly assumed since solids concentrations are low and, therefore, little axial mixing can occur [116]. Additionally, the experimental reactor was externally heated to maintain a uniform temperature justifying the isothermal assumption.

Given the above assumptions and geometric calculations, we can describe the fluidized bed gasifier as a series of two ideal gas-phase reactors: a CSTR and PFR, where the CSTR has two inlet streams: (1)the devolatilization products predicted from the particle devolatilization model and (2)the inlet air stream. The resulting RNM is illustrated in Figure 4-3. The RNM calculations are implemented in the commercially available chemical kinetic solver, CHEMKIN-PRO [123].

### 4.3.5 Experimental Validation Data

A variety of experimental investigations have been dedicated to studying fluidized bed gasification of biomass, and it is important to discerningly choose data sets relevant

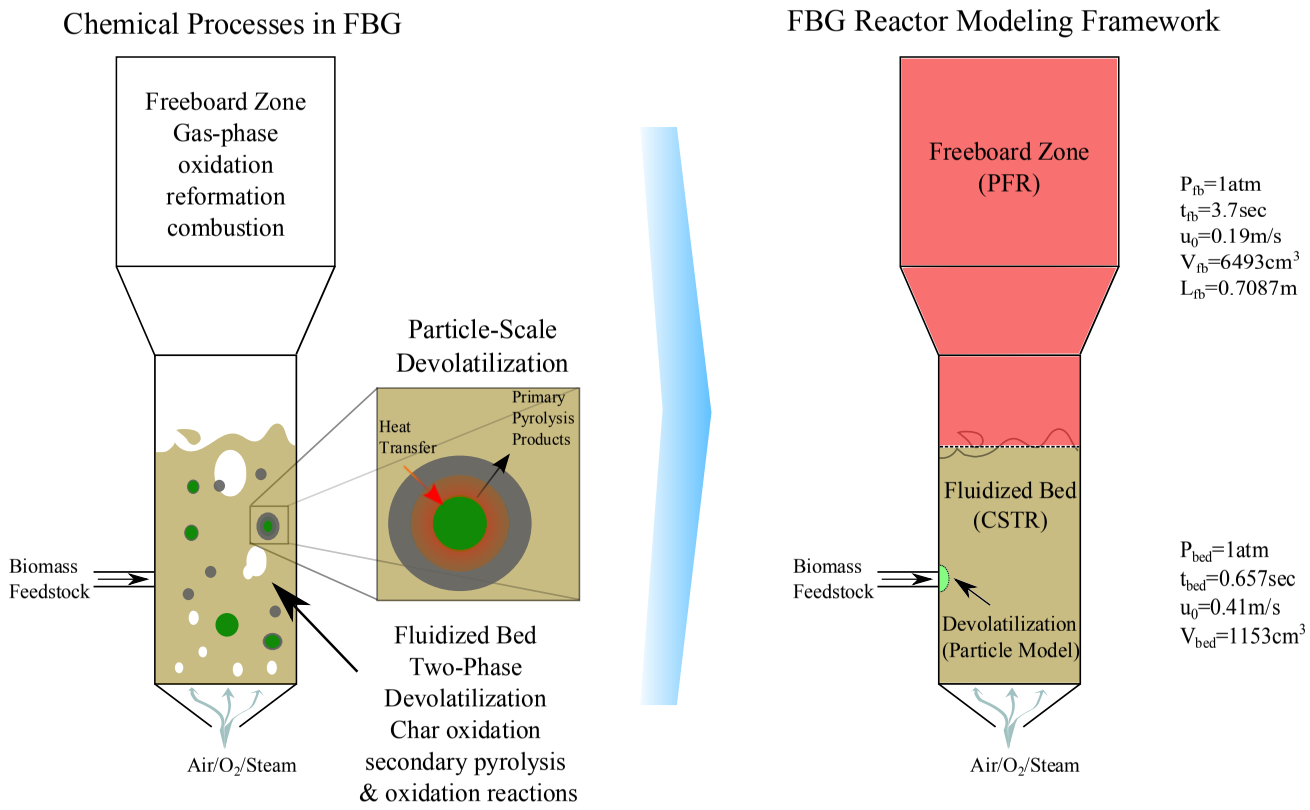


Figure 4-3: The modeling framework employed to simulate air-blown FBBG. Because the devolatilization is assumed to occur uniformly through the well-mixed bed we can equivalently assume that the CSTR model of the gas phase has two inputs, the air stream and a biomass devolatilization product stream. The geometric characteristics of the RNM calculated from the reported geometry of the van Paasen & Kiel [138] reactor are shown on the right.

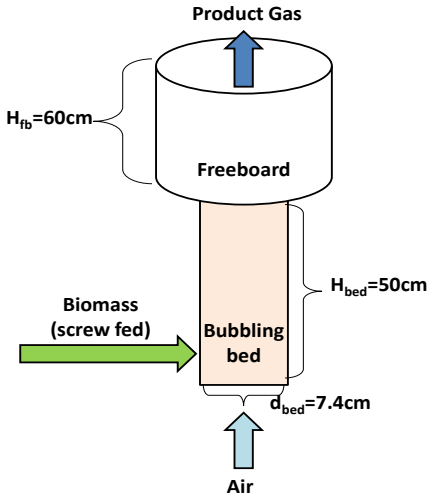


| | van Paasen and Kiel, 2004 |
|---|---|
| **Bed diameter (m)** | 0.074 |
| **Biomass feed rate (kg/hr)** | 1 |
| **Bed temperature (K)** | 1000-1172 |
| **Pressure (atm)** | 1 |
| **Air equivalence ratio (ER)** | 0.25-0.26 |
| **Feedstock** | Beech, Willow (0.75 -2mm) |
| **Fluidizing medium** | Silica sand (270 µm) |

Figure 4-4: Schematic of the experimental air blown FBBG used by van Paasen and Kiel [138].

for validation of this RNM. The experimental work chosen for validation in this study are summarized in Table 4.5. Most experimental investigations, such as that of Narvez et al. [105], report only the concentrations of major species, the total gas yield and the total tar concentration in the product gases. While these studies offer some insight and are important validation points, they say nothing about the actual composition of the tars produced.

In their experimental work, van Paasen and Keil defined five tar classes based on their chemical characteristics, following the tar maturation scheme reported by Milne (see Table 4.3) [101]. They subsequently reported concentrations for each of these classes of tar in the output gas. In addition to reporting the tar class concentrations, they also report major gas species. The schematic of the bubbling fluidized air-blown gasifier operated at atmospheric pressure at a bed temperature range of 1000-1173K $(727 - 900°C)$ by van Paasen & Keil [138] is shown in Figure 4-4.

Table 4.5: Summary of the experimental studies of air-blown FBBGs used for validation.

| | | Narvaez et al [105] | van Paasen & Kiel [138] |
|---|---|---|---|
| Gasifier Specifications | Operating Regime | Bubbling bed | Bubbling - Slugging |
| | Bed Diameter [cm] | 6 | 7.4 |
| | Bed Height [cm] | 30 | 50 |
| | Free Board Diameter [cm] | 12 | 10.8 |
| | Freeboard Height [cm] | 20 | 60 |
| | Bed Material | Silica sand | Silica sand |
| | Fluidizing Agent | Air | Air |
| Operating Conditions | Superficial Gas Velocity [m/s] | $2\times u_{mf}$ specified | 0.38 |
| | Temperature Range [$C^{\circ}$] | 700 - 850 | 750 - 950 |
| | Air-Fuel ER | 0.20 - 0.45 | 0.25 - 0.26 |
| Feedstock | Species | Pine wood | Beech wood, Willow wood and Cellulose |
| | Moisture (%wt delivered) | 19 - 23.5 | 10.2 |
| | Ultimate Analysis (%wt, daf) | C:50, H:5.7, O:44.1, N:0.1-0.3, S:0.03 | Beech: C:48.8, H:6.0, O:44.5, N:0.14, S:0.017, Cl:0.005<br>Willow: C:49.4, H:6.0, O:39.0, N:0.87, S:0.05, Cl:0.015 |
| Data Employed Here | | Total Tar Yield<br>Total Gas Yield<br>Gas Species Yields | Total Tar Yield<br>Tar Class Yields<br>Gas Species Yields |

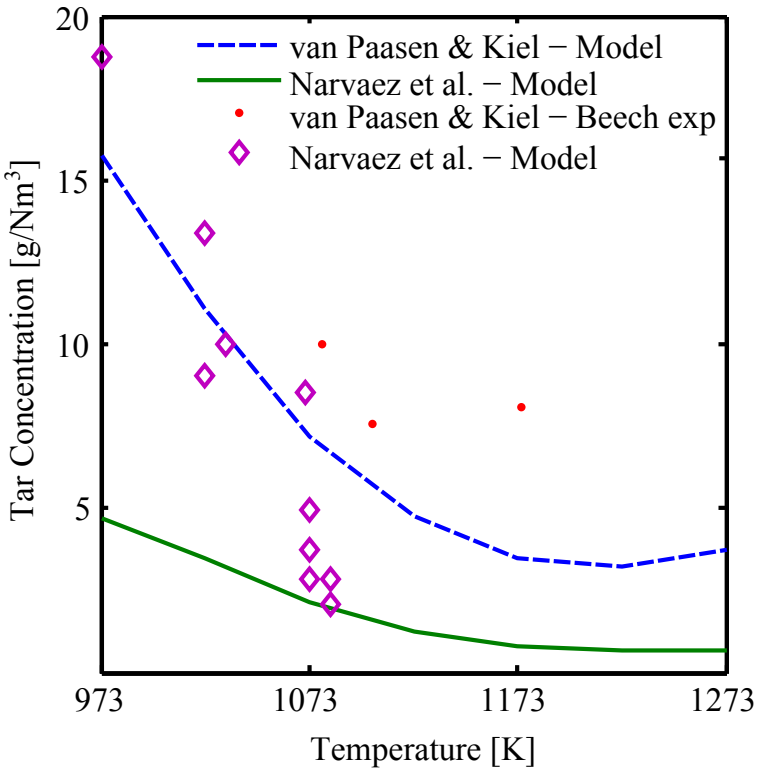


Figure 4-5: Comparison of the RNM predicted tar concentration with experimental data [105, 138] for a fixed air-fuel equivalence ratios of $ER = 0.25$for van Paasen & Kiel and 0.30 for Narvaez et al. The total predicted tar concentration is taken to be the sum of all stable hydrocarbon species $C_{6+}$ [94] at the freeboard (PFR) exit.

## 4.4 Results and Discussion

### 4.4.1 Experimental Validation

To the best knowledge of the authors, this is the first time the thermochemical biomass mechanism developed by the CRECK group has been implemented to describe a FBBG. As such, important validation comparisons are made against the available experimental data discussed above.

In Figure 4-5, the present model's predictions for the variation of total tar content with respect to the operational bed temperature are compared with the experimental data of from Narvaez et al. [105] and van Paasen & Keil [138] at a fixed ERs of .3 and .25 respectively, where the total tar is defined to be the sum of all stable hydrocarbons $C_{6+}$ as proposed by Maniatis and Beenackers [94]. The present model is able to

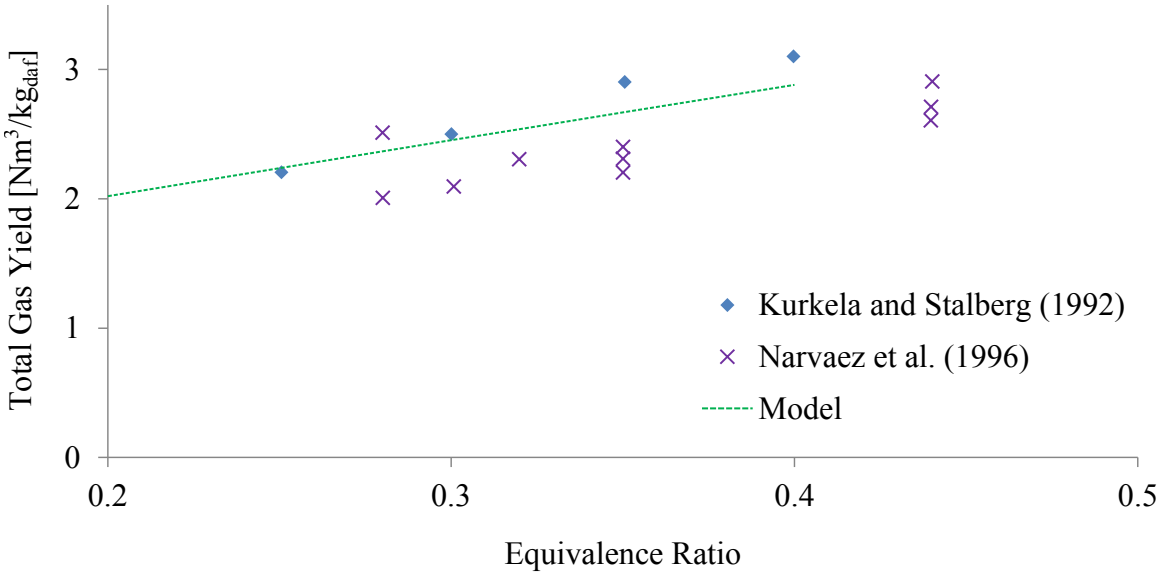


Figure 4-6: Comparison of predicted total gas yield ($Nm^3/kg_{fuel,daf}$) with experimental data [105] prediction of gas yield. $T_{bed} = 800°C$.

quantitatively predict the amount of tars and accurately represent the reduction of the total tars with higher temperatures, where the kinetics of tar oxidation are vastly improved. A minimum tar content of $2.5mg/Nm^3$ is predicted at $1223K$ by the RNM for the van Paasen & Kiel condition, above this temperature an up-tick in tar concentration is predicted reflecting formation and growth of PAH at higher temperatures predicted theoretically [101]. This is not predicted for the Narvaez conditions where a higher ER is employed, this suggesting that a higher oxygen concentration impedes PAH growth at elevated temperatures. While interesting, the temperature range at which this is observed is likely higher than FBBGs will reasonably be operated commercially due to concerns of ash agglomeration leading to defluidization [54].

In Figure 4-6, the variation of the total gas yield per unit of input fuel ($Nm^3/kg_{fuel,daf}$) predicted by the RNM is compared with experimental data of Narvaez et al. [105]. Here, the bed temperature is held constant at $800°C$, and the equivalence ratio is varied from 0.2 to 0.4. In an air-blown gasifier, the increase in total gas yield with increased ER is largely attributable to the larger nitrogen injection. However, at higher ER there is more oxygen available to convert tars and other hydrocarbon species, therefore increasing the total number of moles of gas produced as well.

In Figure 4-7, the RNM prediction of major gas species at the PFR outlet are compared with experimental measurements [105, 138]. Here, the hydrogen concentration is predicted with good quantitative agreement by the RNM, reflecting the kinetic limitation of hydrogen production relative to the equilibrium prediction. An increase in hydrogen production is predicted at increasing temperatures, trending toward equilibrium, which is explained by faster kinetics of steam tar reforming reactions at elevated temperatures [105] (see Table 4.1). At low temperatures CO concentration is over-predicted by the RNM using the kinetic model of CRECK, while $CO_2$ concentration is under-predicted in the same regime. At increasing temperatures, however, it is observed that the RNM predictions achieve better agreement. This could indicate that the CO oxidation kinetics employed in the CRECK mechanism are not well tailored to this low temperature regime. The $H_2O$ concentration prediction of the RNM show large discrepancy with the experimental results at all temperatures. However, qualitatively a downward trend is predicted which is reflected both in the equilibrium calculations and the experimental results. The cause of this discrepancy is uncertain, however it could be due to experimental error in calculating the final water concentration if the biomass was allowed to dry after it's moisture was calculated. The RNM $CH_4$ predictions are in excellent agreement across all temperatures indicating the accuracy of the kinetic model in reflecting the recalcitrance of methane at gasification temperatures.

In Figure 4-8, the RNM predictions of each of the measurable classes of tars are compared with experimental data [138]. These trends are qualitatively in line with the temperature ranges of tar evolution proposed by Milne [101] with oxygenated heterocyclic (Class 2) tars dominating at low temperature, one-ring aromatic (Class 3) tars evolving at moderate temperatures, and polycyclic aromatic (Class 4 and 5) tars evolving at higher temperatures. In the case of Class 2 tars, the model predictions appear to give a good agreement with experimental measurement, and the trend with respect to temperature is matched well. Class 3 tars are properly predicted within an order of magnitude of the measurements for beech wood and also show qualitative temperature trend agreement. The Class 3 tar measurements from willow

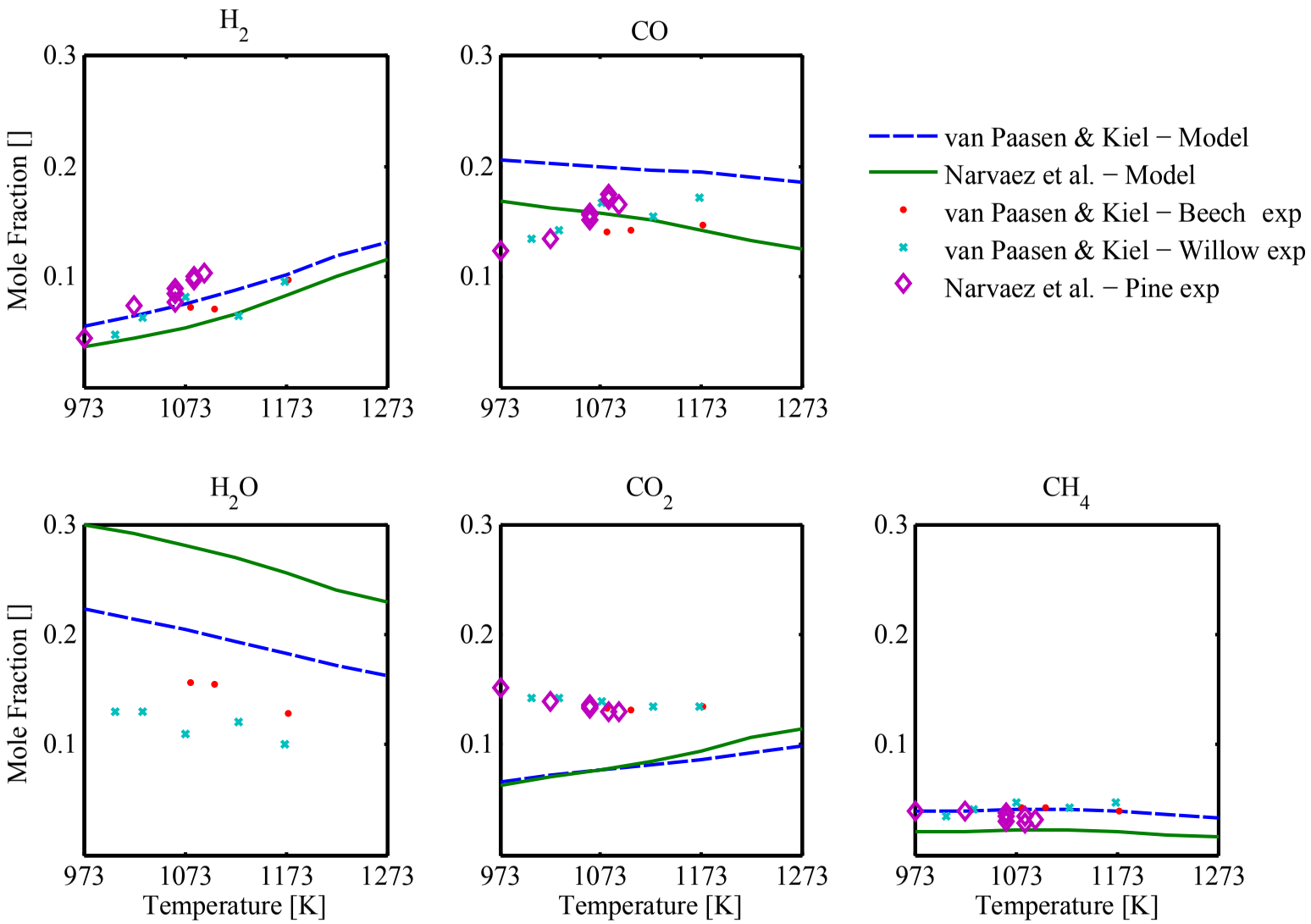


Figure 4-7: Comparison of RNM outlet gas composition (% vol wet) predictions and experimental measurements, equilibrium predictions and model predictions with modified CO oxidation kinetics versus temperature. Experimental data from Narvaez et al and van Paasen & Kiel [105, 138].

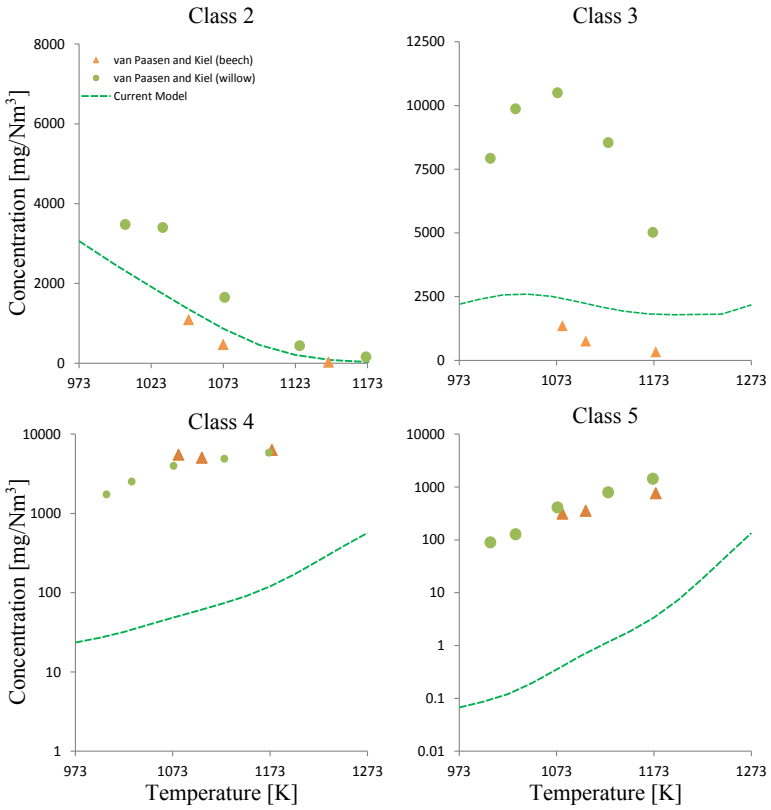


Figure 4-8: Comparison of RNM outlet tar composition versus temperature. Experimental data is from van Paasen and Kiel [138].

wood are, in our opinion, suspect due to their large disagreement with that of beech wood, since for each other class they are in much closer agreement. Finally, Class 4 and 5 tars (representing small and large PAHs respectively) are under-predicted by an order of magnitude by the RNM. However, qualitatively the trend is accurately predicted, showing an exponential increase in their concentration with respect to temperature. It can also be observed that, at higher temperatures, it appears that the model predictions and experimental measurements are converging, suggesting that the kinetic model employed is well suited to predict PAH growth in higher temperature entrained flow gasifiers and combustors. However, the development of better PAH growth mechanisms at moderate temperatures is of critical importance.

In Figure 4-9 the predicted evolution of major gases and tar classes are plotted with respect to gas residence time for three operating temperatures in the van Paasen & Kiel reactor. It is observed that temperature plays an important role in defining

the evolution of the gas-phase species concentrations, in particular those of the major species, $H_2$, $H_2O$, CO and $CO_2$. At 973K it is observed that the concentrations of these species become static after the oxygen in the system is exhausted, implying that their concentrations are determined primary via the oxidation of light hydrocarbons and tars in the bed and early in the freeboard where the remaining oxygen is consumed. Here tar conversion is also dominated early by oxidation of class two tars, followed by slow steam reforming of class two tars and conversion of Class 2 tars to Class 3 tars via dehydration. At moderate temperatures (1123K) it is observed that more of the oxygen is consumed initially in the bed zone and again quickly exhausted in the freeboard. From here, however, noticible evolution of the main syngas species is observed due to increased rate of the water gas shift reaction. Tar evolution is again defined early on by oxidation of class two tars, followed by tar class conversion from Class 2 to 3 tars and a slow growth of class 4 (small PAH compounds). Again, the total concentration of Class 5 tars in relatively negligible. At the highest temperatures (1273K) it is observed that nearly all of the oxygen is consumed in the bed zone and the overall influence of oxygen in the PFR is evident only in the earliest moments, observable as the short time where the total tar concentration is decreasing. Then the evolution of the major species is dominated by increased water gas shift kinetics. Tar evolution is dominated by tar growth after the oxygen is exhausted. It is observed that the total Class 2 tars continues to decrease while Class 3 tar concentration remains relatively constant and Class 4 and Class 5 tar concentrations grow accordingly.

### 4.4.2 Mechanism Analysis

As discussed in the previous subsection, the predictions of major species and total tar concentration are generally good. However, there exist interrelated discrepancies in the predictions of CO, $H_2O$ and $CO_2$ as well as short comings in the prediction of classes 3-5, in particular the rate of PAH growth may be under-predicted. In this section the relevant reactions which directly affect these predicted species concentrations are further analyzed and discussed, and finally suggestions for further research and refinement of kinetic parameters are given.

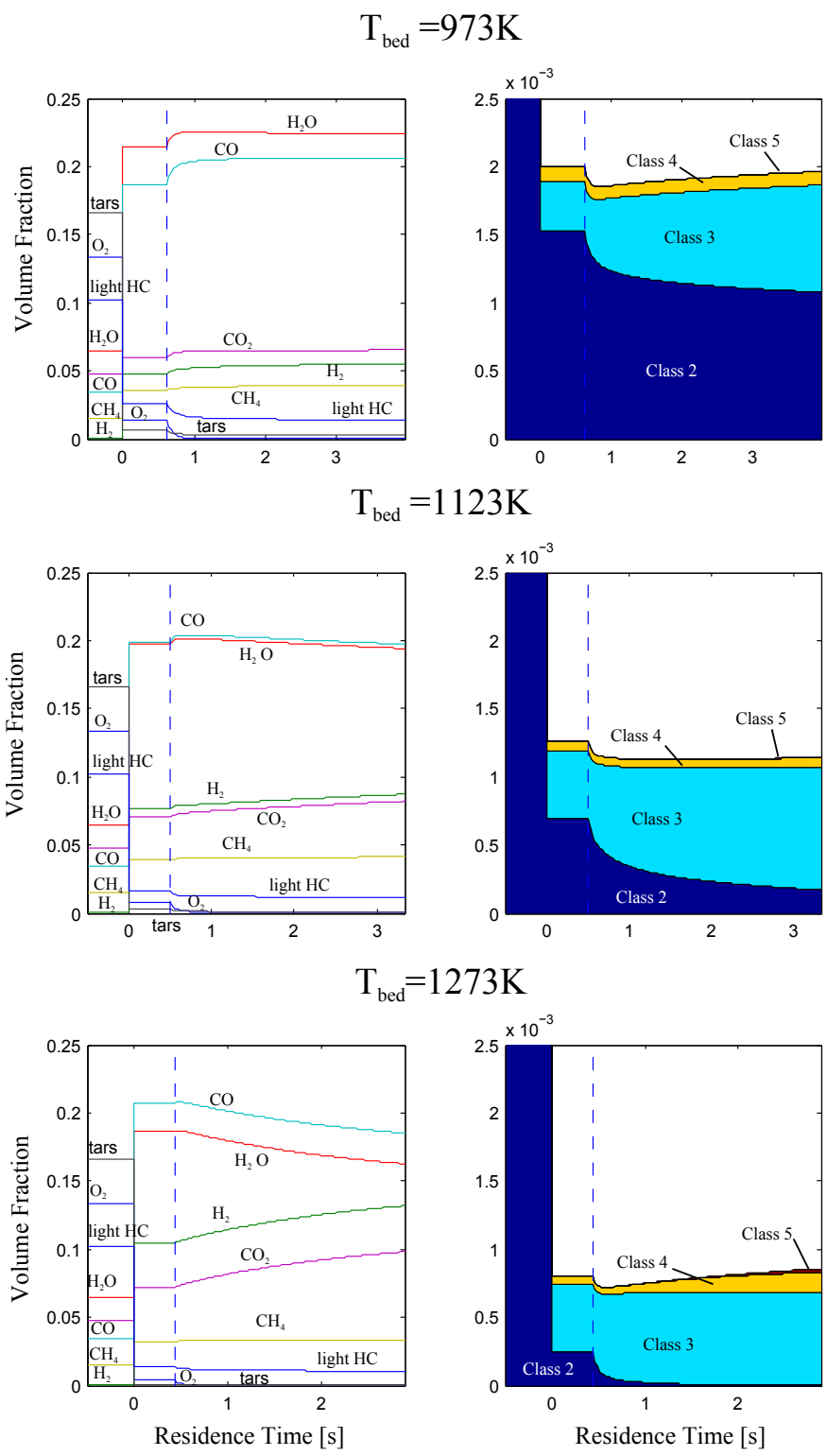


Figure 4-9: Predicted major gas species (left) and tar class (right) evolution is plotted against residence time for three operating conditions for the van Paasen & Kiel reactor.

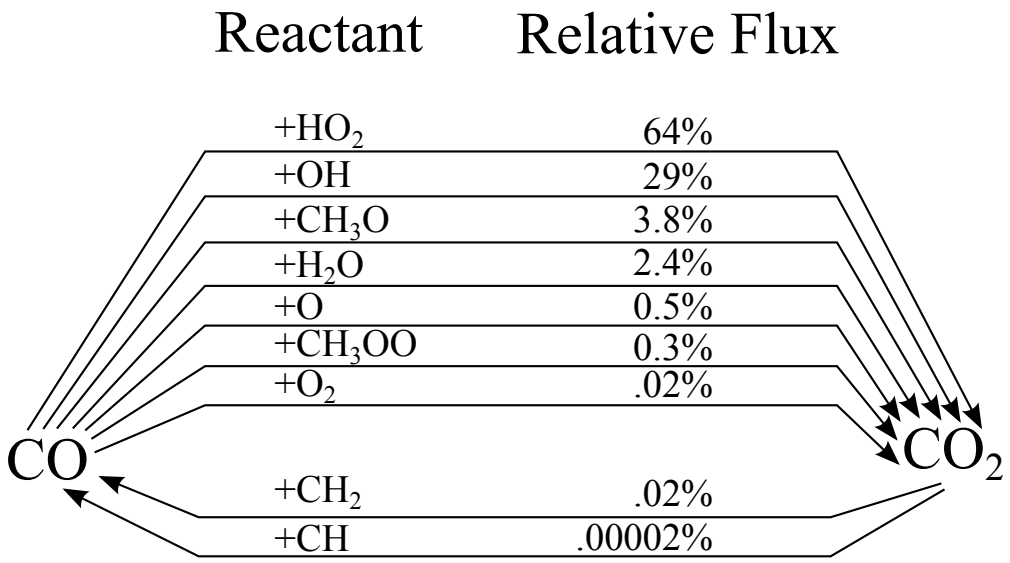


Figure 4-10: The major reaction pathways from CO to $CO_2$. The dominate pathways involve radicals of $H_2O$, $\cdot HO_2$ & $\cdot OH$.

**CO oxidation Kinetics**

It is observed in Figure 4-7 that the current model's predictions of CO and $CO_2$ are related in that given the over-prediction of CO, $CO_2$'s under-prediction is resultant since it is the direct oxidized product of CO and they both show inverse temperature dependent trends further validating their interconnected chemical nature. The oxidation of CO to $CO_2$ has been shown in the literature to occur not via a naïvely intuitive pathway involving oxygen, $CO + O_2 \rightleftharpoons CO_2$ or $CO + \cdot O \rightleftharpoons CO_2$, but rather it is dependent on water, in particular the radicals of $H_2O$: hydroxyl, $\cdot OH$, and hydroperoxyl, $\cdot HO_2$ [9, 53, 78, 87, 100, 103]. Therefore, the fact that there is also evidence of over-prediction of $H_2O$ exiting the gasifier lends credence to the possibility that the kinetic mechanism currently employed under-predicts the rates of the reactions of CO with the hydroxyl and hydroperoxyl radicals.

In order to assess the inaccurate predictions of CO, $H_2O$ and $CO_2$, a full flux and sensitivity analysis of these species was performed within the current model. In Figure 4-10 the oxidation and reduction reactions between CO and $CO_2$ are ordered by their relative flux within the model at 1073K. Here, the dominance of the hydroxyl and hydroperoxyl radicals is verified, as they constitute $\sim 93\%$ of the conversion ($> 95\%$

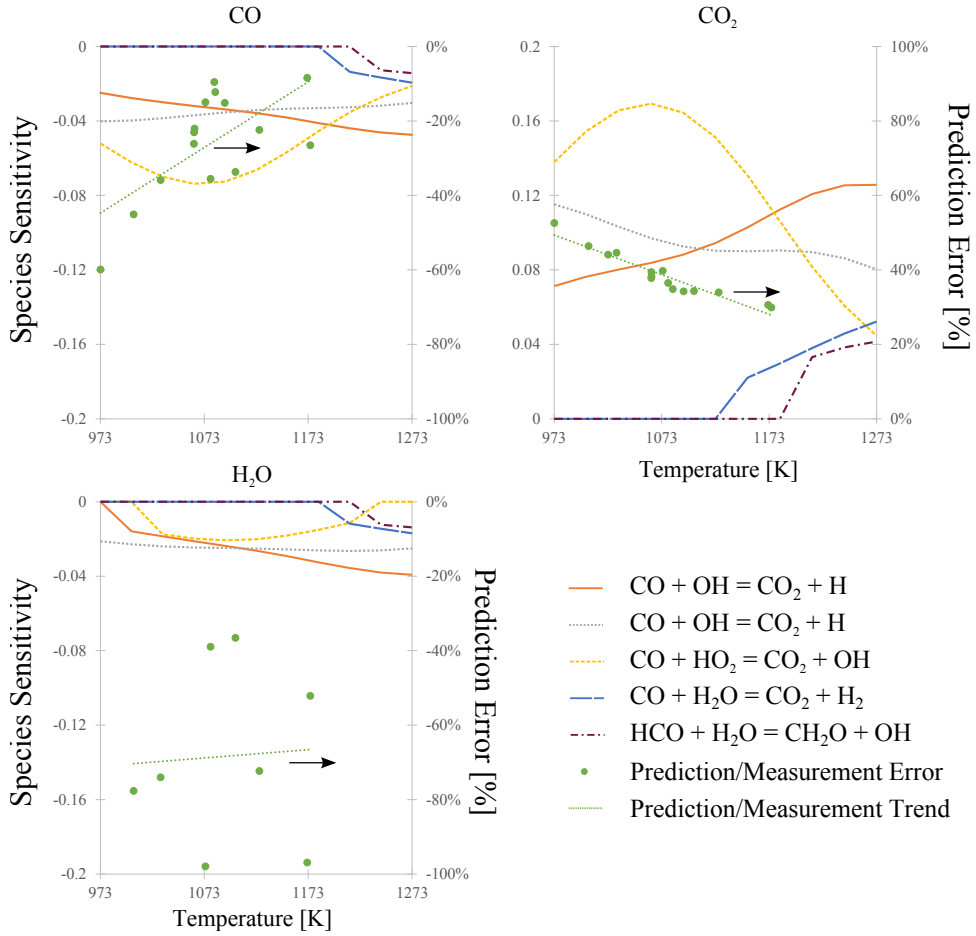


Figure 4-11: The sensitivities of CO, $CO_2$ and $H_2O$ to important CO oxidation reactions are plotted with respect to temperature (left axis). Additionally, the negative of the error of the model prediction relative to the reported measurements ($Error = -(Prediction - Measurement)/Measurement$) for each of the species relative to the experimental data plotted in Figure 4-7. The negative of error is used for ease of plotting with the sensitivities.

when direct reaction with water is included via the water gas shift reaction). On the other hand, the reactions of CO with $O_2$ and the oxy- radical $\cdot O$ are shown to constitute less than 1% of the conversion. Under gasifying conditions, where the total oxygen concentration is purposefully limited to sub-stoichiometric levels in order to limit the oxidation of CO and $H_2$, oxygen and its radicals will naturally be scarce.

In Figure 4-11 the sensitivities of each of the species CO, $H_2O$ and $CO_2$ are plotted with respect to temperature for selected reactions identified through the sensitivity analysis of these species. Also, the relative error of the predictions and the experi-

mental measurements are plotted. For both CO and $CO_2$ the relative errors show a clear trend with respect to temperature as decreasing in magnitude, suggesting that the target reaction(s) for correction should similarly exhibit sensitivity of a decreasing magnitude with respect to temperature. While the errors of the predictions of CO and $CO_2$ show a temperature dependent trend, the errors for $H_2O$ are highly scattered and with no statistical certainty are able to predict a clear trend. This is likely due to high experimental error in measuring both the feedstock moisture and the concentration of water at the exit. Further, this value often goes unreported due to the challenge of controlling environmental humidity and, therefore, the flow into the gasifier for air blown systems. However, it is clear from these reported data that water content is under predicted to some degree with errors ranging from 40-95%.

From Figure 4-11 it can be established that the water gas shift, $CO + HO_2 \rightleftharpoons CO_2 + OH$, and the reaction of water with the formyl radical do not play important roles in establishing the final concentrations of these species of interest in the lower temperature ranges due to their negligible sensitivities in the CRECK model. However, below 1100K the equilibrium constant of the water gas shift is greater than unity (up to 1.62 at 973K) implying favorable conditions for the forward reaction to occur [108, 132]. It has been reported in literature that the char, ash and reactor walls have a strong catalytic effect on the water gas shift (WGS) reaction [21,61], and as such modified WGS kinetics should be employed in the CRECK model following those reported by Gomez-Barea & Leckner [61].

Additionally, the reaction $CO + \cdot OH \rightleftharpoons CO_2 + \cdot H$ plays a crucial role in the oxidation of CO within this temperature regime, contributing approximately 30% of the total flux as shown in Figure 4-10. In the CRECK mechanism, as well as in other models available in the literature, this reaction is modeled using two reactions with different kinetic parameters in order to capture the different temperature regimes [78, 100]. From the sensitivities plotted in Figure 4-11 it is noted that the second of these has a decreasing species sensitivity magnitude with temperature, and the cross-over point of the species sensitivities is at the temperature where the reaction rate of the first reaction overtakes the second to represent the higher temperature

Table 4.6: Modified reaction parameters for CO oxidation reactions and water gas shift reaction for $k = AT^b exp(-Ea/RT)$. Modified WGS kinetics are taken from Biba et al. [21], CO oxidation kinetics are proposed.

| Reaction | CRECK values | | | Modified expression | | |
|---|---|---|---|---|---|---|
| | A [1/s] | b [] | $E_a$ [cal/mol] | A [1/s] | b [] | $E_a$ [cal/mol] |
| $CO + H_2O = CO_2 + H_2$ (WGS) | $2.78 \times 10^6$ | 1 | 3000 | $2 \times 10^{11}$ | 1 | 38000 |
| $CO + \cdot HO_2 = CO_2 + \cdot OH$ | $3 \times 10^{13}$ | 1 | 23000 | $3 \times 10^{14}$ | 1 | 23000 |
| $CO + \cdot OH = CO_2 + \cdot H$ | $9.6 \times 10^{11}$ | .14 | 7352 | $9.6 \times 10^{12}$ | .14 | 7352 |
| | $7.32 \times 10^{10}$ | .03 | -16 | $7.32 \times 10^{11}$ | .03 | -16 |

conversions.

The last reaction of interest, $CO + \cdot HO_2 \rightleftharpoons CO_2 + \cdot OH$, which accounts for approximately 64% of the flux between CO and $CO_2$. Additionally, this reaction plays an important role at lower temperatures with decreasing importance at higher temperatures.

In Figure 4-12 the major gas species are predicted using the RNM with with modified reaction kinetics for the oxidation of CO. Two modifications are employed: (1) where the WGS reaction kinetics are modified to reflect the literature values proposed by Biba et al. [21, 61, 62], and (2) where the order of magnitude of the pre-exponential, A, factors of the reactions $CO + \cdot HO_2 \rightleftharpoons CO_2 + \cdot OH$ and $CO + \cdot OH \rightleftharpoons CO_2 + \cdot H$ are increased by one (see Table 4.6). It can be seen that this increase in either of these CO oxidation reaction rates not only improve the quantitative agreement of the predictions of each CO and $CO_2$ as well as (to a lesser extent) $H_2O$, but they also correct the temperature dependent trends to properly reflect higher CO concentrations with increasing temperatures. Additionally, it is observed that these corrections only impact the predictions of $H_2$ and $CH_4$ in a minor way, further bolstering the evidence that it is the under-prediction of these reaction rates in the CRECK model at this temperature that explain the discrepancies.

### Major Species Devolatilization Conversion Pathways

In order to get insight into the conversion pathways of biomass gasification under fluidized bed conditions, the major reaction pathways of important biomass devolatilization species are further discussed. The following reaction pathways were generated

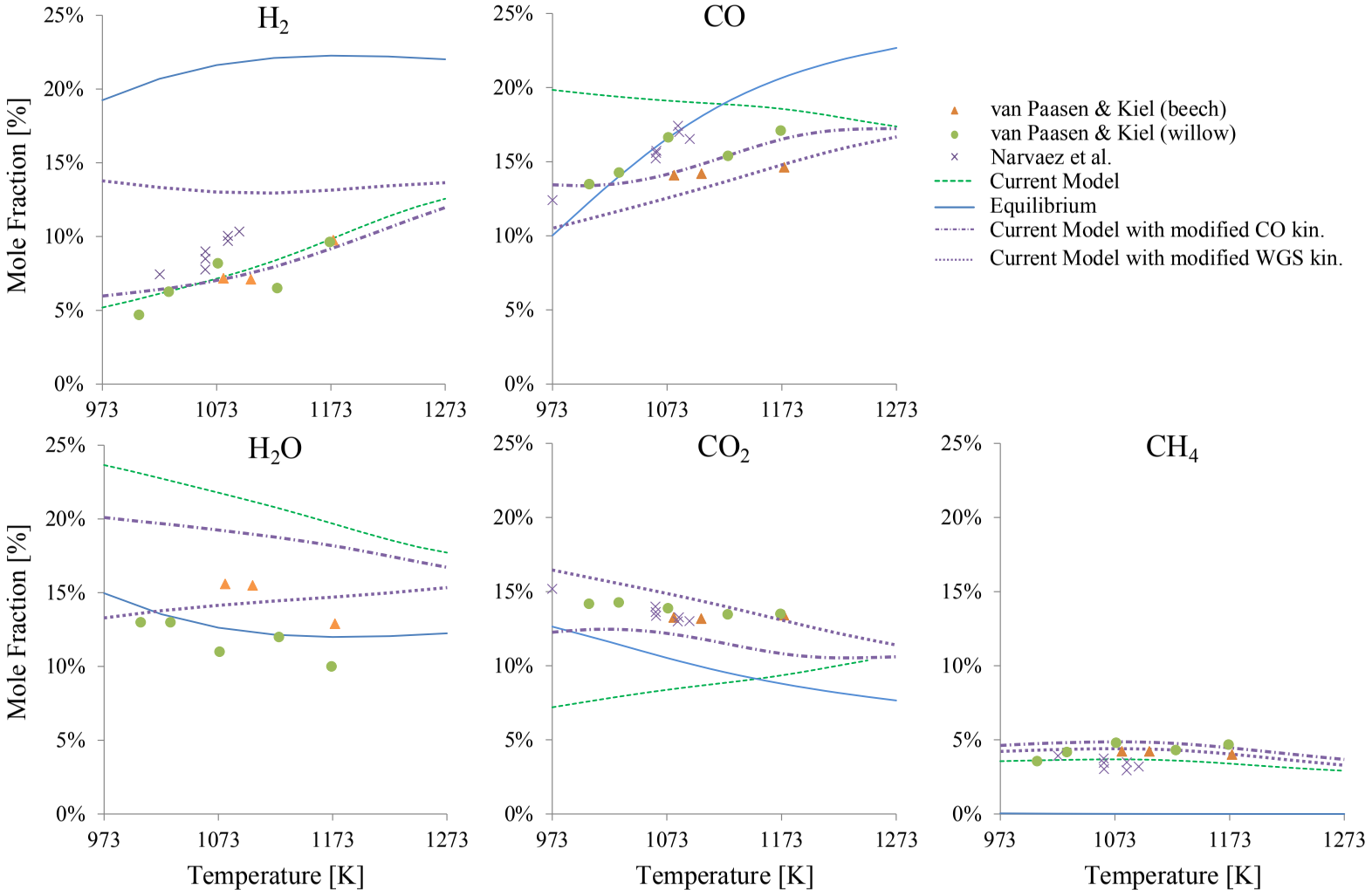


Figure 4-12: Comparison of RNM outlet gas composition (% vol wet) predictions and experimental measurements, equilibrium predictions and model predictions with modified CO oxidation kinetics versus temperature. Experimental data from Narvaez et al and van Paasen & Kiel [105, 138].

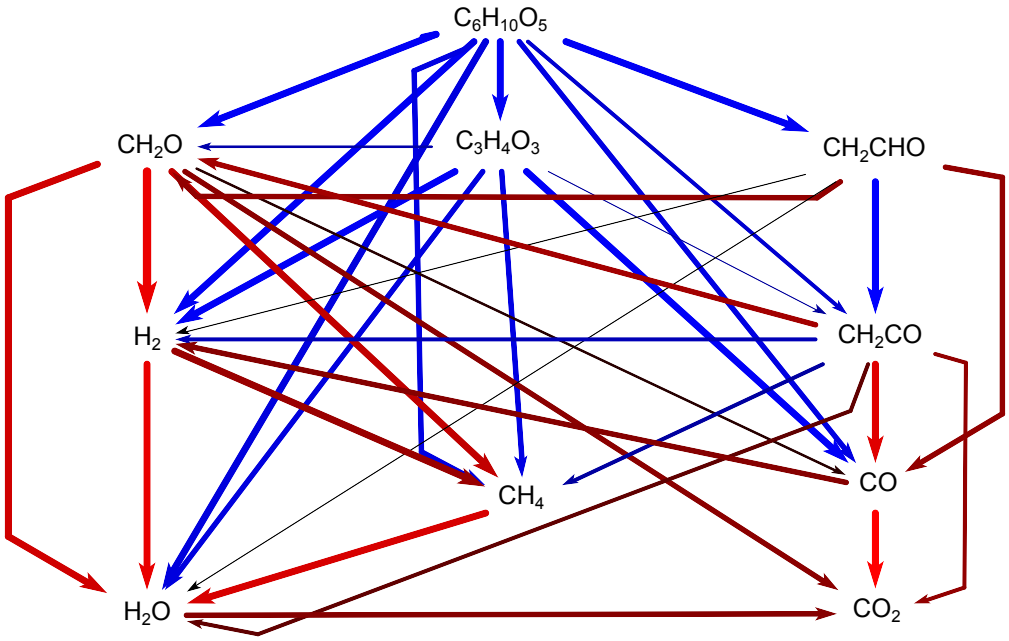


Figure 4-13: The major conversion pathways of levoglucosan at FBBG conditions. The thickness of the arrows represent the relative flux between two species, and the coloration represents the thermicity of the reaction - red being exothermic and blue for endothermic.

by post-processing the CSTR zone (bed) of the RNM of the van Paasen reactor using the CHEMKIN-PRO Reaction Path Analyzer [123]. The bed temperature is 1073K, and the ER employed is 0.25.

In Figure 4-13, the major conversion pathways of levoglucosan ($C_6H_{10}O_5$) are shown. As previously discussed, levoglucosan constitutes a major fraction of the devolatilization species and, therefore, is of particular interest. Due to its high level of oxidation, levoglucosan undergoes endothermic reactions, producing syn-gas as well as reactive intermediates such as formaldehyde ($CH_2O$), and the hydrogen-abstracted radical of acetylaldehyde ($\cdot CH_2CHO$). These intermediates undergo exothermic reactions to complete conversion to syn-gas, water, carbon-dioxide and methane.

Hemicellulose, as the most reactive biomass constituent, readily converts to light gases during devolatilization. However, xylofuranose ($C_5H_8O_4$) is also an important product of hemicellulose devolatilization. The conversion pathway of xylofuranose is shown in Figure 4-14. As for levoglucosan, xylofuranose is also heavily oxidized and must undergo endothermic conversions to reduce the species. Since both are

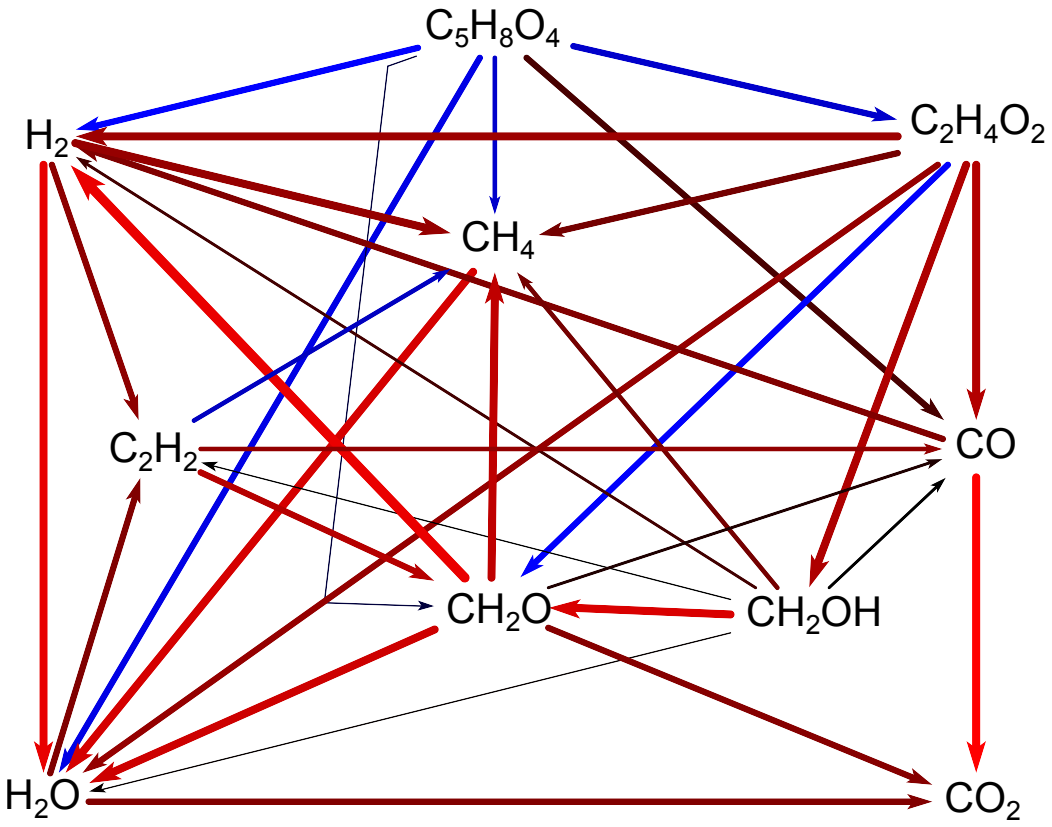


Figure 4-14: The major conversion pathways of xylofuranose at FBBG conditions. The thickness of the arrows represent the relative flux between two species, and the coloration represents the thermicity of the reaction - red being exothermic and blue for endothermic.

dehydrated sugar monomers, similar conversion pathways are observed for both xylofuranose and levoglucosan.

Capturing the conversion pathways of lignin-derived devolatilization products, such as synapoyl aldehyde ($C_{11}H_{12}O_4$), syringol ($C_8H_{10}O_3$) and pCoumaryl ($C_9H_{10}O_2$) is of critical importance for modeling biomass gasification, as it is from these species which the majority of tars and PAH compounds are created [96, 97]. These devolatilization products of lignin share a phenolic backbone (see Figure 4-15) and, therefore, undergo simple transformation to phenol, which plays a central role in tar evolution.

In Figure 4-16 the major conversion pathways of synapoyl aldehyde are illustrated. Synapoyl aldehyde can undergo a cracking reaction to produce carbon monoxide, and subsequently other light product gases such as carbon-dioxide. However, it is the con-

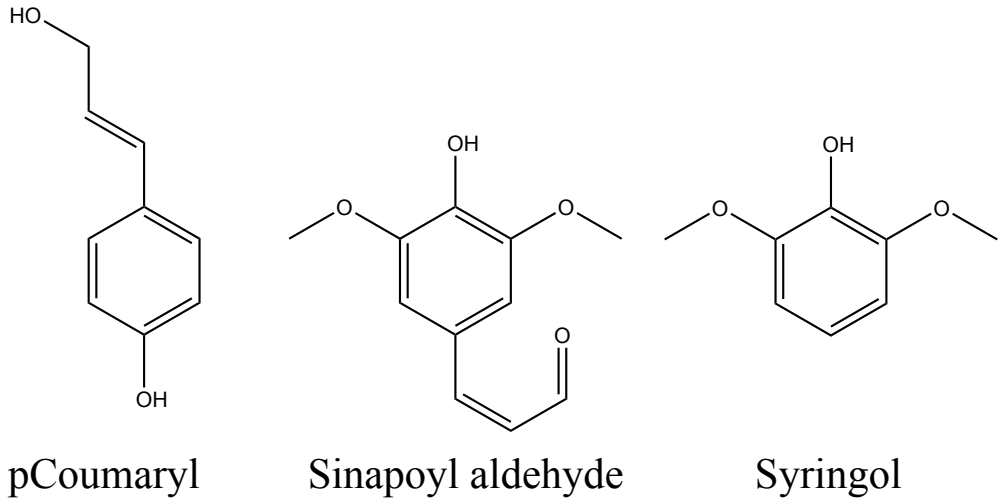


Figure 4-15: Synapoyl aldehyde, syringol and pCoumaryl are important devolatilization products of lignin due to their function precursors to tar formation.

version that proceeds via syringol which is of primary interest for tar modeling since a major product of syringol conversion is phenol. Phenol can be further consumed through cracking, steam reforming and oxidation to generate target species such as carbon monoxide. Due to the endothermic nature of this pathway, it is important at higher temperatures as evidenced by phenol's diminished concentration at higher operating temperatures.

Competing with these consumption reactions of phenol are tar formation and PAH growth pathways in which phenol and its hydrogen-abstracted radical ($\cdot C_6H_5O$) play central roles. Figure 4-17 illustrates major carbon-conversion pathways leading to PAH growth as well as the generation of each tar class. Benzene (Class 3) is generated from Phenol (Class 2) through a set of radical reactions:

$$C_6H_5OH + \cdot H \rightleftharpoons \cdot C_6H_5O + \cdot H_2 \tag{4.5}$$

$$\cdot C_6H_5O + O \rightleftharpoons \cdot C_6H_5 + O_2 \tag{4.6}$$

$$C_6H_5OH + \cdot H \rightleftharpoons C_6H_6 + \cdot OH \tag{4.7}$$

$$C_6H_6 + M \rightleftharpoons \cdot C_6H_5 + M + \cdot H. \tag{4.8}$$

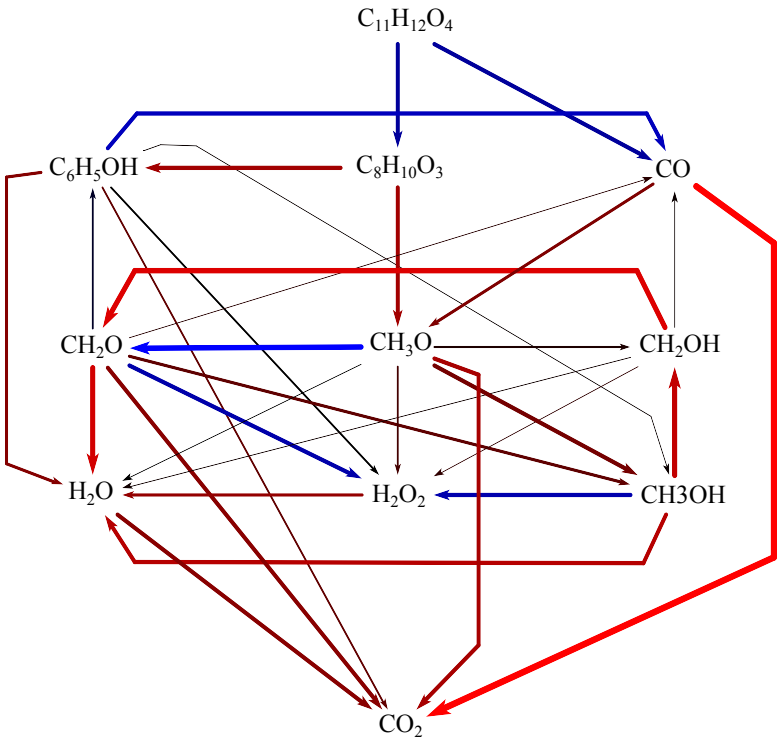


Figure 4-16: The major conversion pathways from synapoyl aldehyde at FBBG conditions. The thickness of the arrows represent the relative flux between two species, and the coloration represents the thermicity of the reaction - red being exothermic and blue for endothermic.

Importantly, benzene can then be converted back to phenol via $\cdot C_6H_5O$ or to its hydrogen-abstracted radical ($\cdot C_6H_5$). From $\cdot C_6H_5$ PAH products can be formed through radical reactions with unsaturated hydrocarbons such as acetylene through the Frenklach mechanism [17, 18, 52]. The CRECK mechanism employed here models PAH growth with a lumped approach, to capture the dynamics of PAH growth through the radical addition of hydrogen-abstracted radicals of aromatic building blocks. For example, one of the major formation pathways of pyrene (Class 5) is radical reaction of benzene and naphthalene (Class 4) with the hydrogen-abstracted radical of the other:

$$\cdot C_6H_5 + C_{10}H_8 \rightleftharpoons C_{16}H_{10} + \cdot H + H_2 \tag{4.9}$$

$$C_6H_6 + \cdot C_{10}H_7 \rightleftharpoons C_{16}H_{10} + \cdot H + H_2. \tag{4.10}$$

It is apparent that PAH growth takes on the type of polymerization chain reaction kinetic scheme in which each radical reaction forms a larger PAH compound in addition to another hydrogen radical. These radicals can then react with an aromatic compound to generate its radical, etc. It is in this way that PAH compounds achieve fast growth rates at high temperatures where the kinetics of radical formation is favorable. It is the case then, that while these radical reactions are modeled in the kinetic framework of the CRECK group, this lumped approach to modeling the Frenklach mechanism may explain why PAH compounds are currently being under-predicted.

Lastly, phenol plays an important role in tar consumption as well. In Figure 4-18, the major carbon-conversion pathways of phenol are illustrated. Again, the core radical reactions of phenol and benzene are important, as in PAH growth. However, it is seen that these reactive intermediates can undergo cracking reactions to carbon monoxide, or through cracking to cyclo-pentadiene ($cyc-C_5H_6$) and its hydrogen-abstracted radical ($cyc-C_5H_5\cdot$). These tar-like intermediates ultimately undergo conversion to smaller hydrocarbon species and carbon monoxide predominately through reaction with the hydroperoxyl radical:

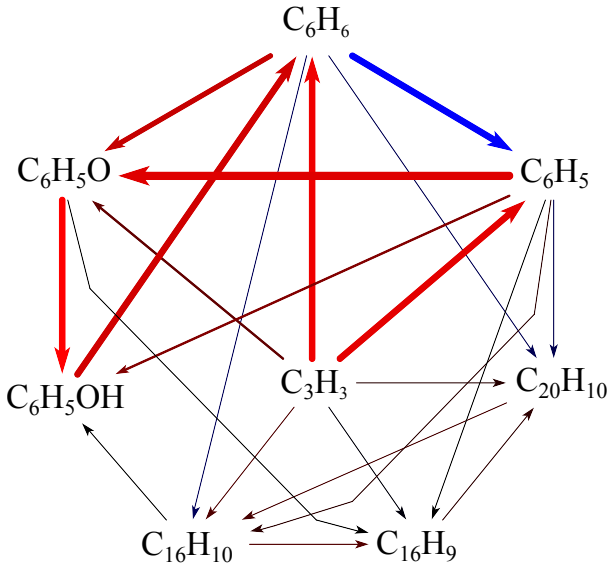


Figure 4-17: The major carbon-conversion pathways leading to PAH growth. The thickness of the arrows represent the relative flux between two species, and the coloration represents the thermicity of the reaction - red being exothermic and blue for endothermic.

$$C_6H_5O\cdot \longrightarrow cyc{-}C_5H_5\cdot + CO \tag{4.11}$$

$$\cdot H + cyc{-}C_5H_6 \longrightarrow H_2 + cyc{-}C_5H_5\cdot \tag{4.12}$$

$$cyc{-}C_5H_6 \rightleftharpoons cyc{-}C_5H_5\cdot + \cdot H \tag{4.13}$$

$$\cdot HO_2 + cyc{-}C_5H_5\cdot \longrightarrow C_4H_5 + CO + \cdot OH \tag{4.14}$$

$$\cdot HO_2 + cyc{-}C_5H_5\cdot \longrightarrow C_2H_4 + \cdot C_2H + CO + \cdot OH. \tag{4.15}$$

## 4.5 Conclusions

In this study, a RNM was developed to model the air-blown gasification of woody biomass in a fluidized bed gasifier. This RNM employs the detailed chemical kinetic model developed by the CRECK modeling group at Politecnico di Milano in order to capture the complex chemistry of tar production and evolution. This model exhibits good predictive capabilities of the major syn-gas species as well as hetero-cyclic aro-

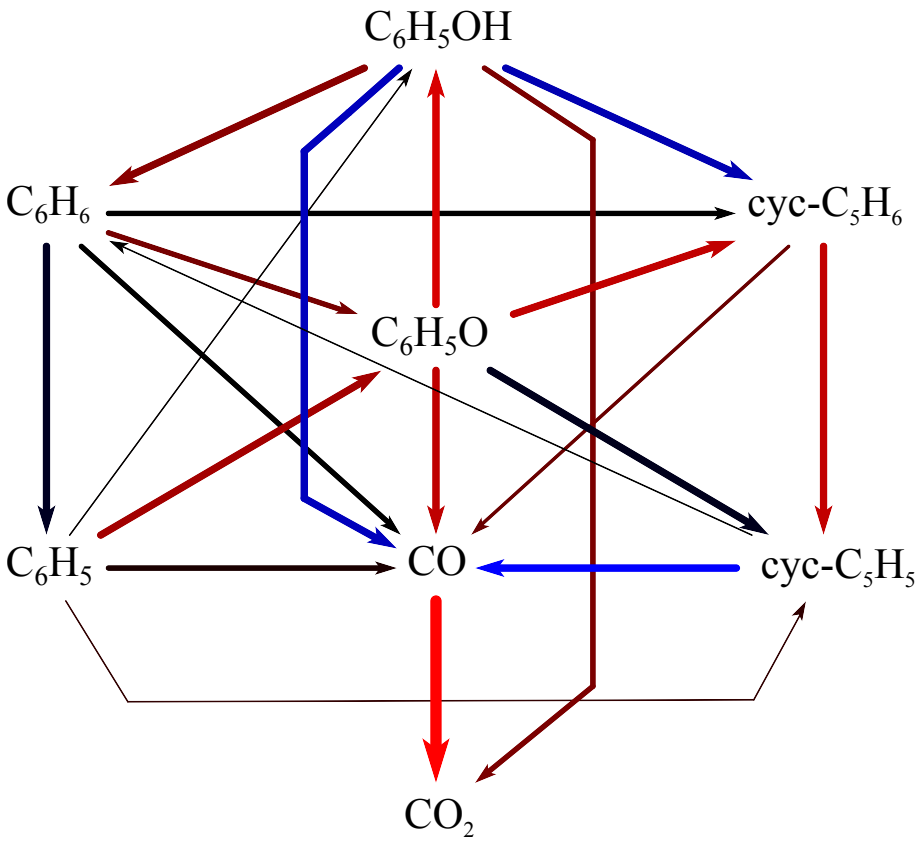


Figure 4-18: The major carbon-conversion pathways of phenol in a FBBG. The thickness of the arrows represent the relative flux between two species, and the coloration represents the thermicity of the reaction - red being exothermic and blue for endothermic.

matic (Class 2) tars and one-ring aromatic (Class 3) tar compounds across the range of potential FBBG operating temperatures ($700 - 1000°C$). It has been found, however, that the current kinetic model under-predicts the oxidation rate of CO by an appreciable amount. With the inclusion of a catalytic reaction for the WGS reaction or increased CO oxidation rates improved predictions of major gas species are significantly improved, however it is unclear if this is the sole explanation for this due to the strong sensitivity to other CO conversion pathways. Further experimental work is required to elucidate the influence of bed material, biomass ash and char on the reactivity of major oxidation pathways. Additionally, the mechanism of formation, evolution and PAH growth present in the kinetic model was analyzed for fluidized bed conditions. It was found that small and large PAH (Classes 4 and 5) tar concentrations are both under-predicted by an order of magnitude in the relevant operating regime, indicating that the radical PAH growth mechanism employed by the CRECK model may not be sufficient to describe tar growth in a FBBG, or that reactor-scale gas transport plays an important role which is not captured in modeling the bed as a CSTR. This later effect is considered in forthcoming work.

# Chapter 5

# Extension to Fluidized Bed Pyrolysis Reactor Conditions

## 5.1 Introduction

In Chapters 2 and 4 two major tools, a particle-scale devolatilization model and a subsequent reactor network model (RNM), were developed for the analysis of thermochemical biomass conversion in a fluidized bed reactor environment with a particular focus on prediction and validation under gasification conditions. In this chapter these models are employed to model a fluidized bed reactor operating under pyrolysis conditions. Without modification of the underlying sub-models and assumptions these reactor models are able to achieve a high degree of accuracy in predicting the chemical conversion in this oxygen deprived environment.

## 5.2 Fluidized Bed Pyrolysis Experimental Data

The influence of particle diameter and temperature on the thermochemical conversion of woody biomass have been studied in a laboratory-scale fluidized bed reactor under pyrolysis conditions by Gaston et al. at the National Renewable Energy Laboratory (NREL) in Golden, CO [56]. In Table 5.1 the NREL experimental fluidized bed reactor employed in the study by Gaston et al. are tabulated [56].

Table 5.1: Summary of experimental conditions of the NREL laboratory-scale fluidized bed reactor employed by Gaston et al. [56]. Further reactor details are available in the report.

| | | Gaston et al. [56] |
|---|---|---|
| Gasifier Specifications | Operating Regime | Bubbling bed |
| | Bed Diameter [cm] | 10.2 |
| | Bed Height [cm] | 61 |
| | Free Board Diameter [cm] | 15.4 |
| | Freeboard Height [cm] | 30 |
| | Bed Material | olivine (magnesium iron silicate) |
| | Bed Material size [$\mu$m] | 270 (mass averaged) |
| | Fluidizing Agent | $N_2$ |
| Operating Conditions | Superficial Gas Velocity [m/s] | 0.19 |
| | Temperature Range [$C^\circ$] | 500-900 |
| | Pressure [atm] | 1.06 |
| Feedstock | Species | White Oak |
| | Fuel Feed [g] | Batch ($8.3 \pm 0.4$g) |
| | Particle Diameters [mm] | 6, 13, 18, & 25 |
| | Moisture [%wt delivered] | 5.28 |
| | Ultimate Analysis [%wt, daf] | C:50.1, H:5.5, O:43.3, N:0.3, S:0.2 |

In their work, Gaston et al. injected batches (approximately 8g) of spherical particles of white oak at four particle diameters (6, 13, 18 & 25mm) into an externally heated reactor operated at five different temperatures (500, 600, 700, 800 & 900$^\circ C$) yielding a total of twenty cases. A molecular beam mass spectrometer (MBMS) was employed to make measurements of the organic (tar) compounds in the exit gas stream. A thermal conductivity detector (TCD) and a four channel non-dispersive infrared detector (NDIR) were employed to analyze the cooled gas for $H_2$, CO, $CO_2$ and $CH_4$. Solids devolatilization time was measured as the total duration of the recorded pulse in the gas analysis units. The total char yield was calculated from the total moles of carbon (CO + $CH_4$) evolved during a burn-off step after the completion of pyrolysis.

## 5.3 Modeling Framework

Biomass pyrolysis, as is also the case with gasification, is defined by the interaction of a number of complex processes as previously discussed in thesis for gasification. Here the processes relevant to pyrolysis are enumerated:

1. *Drying* - Characterized by processes occurring at temperatures around 100°C in which moisture is liberated by evaporation.

2. *Devolatilization* - The chemical conversion by which the raw biomass is converted to gases (>70%) and char. These conversions happen in the temperature range of $200 - 600$°C, and the product distributions are a function of the reaction temperature.

3. *Secondary pyrolysis and gas phase reactions* - The intermediate devolatilization products undergo further pyrolytic reactions, heterogeneous reactions on the char, sand & wall, tar cracking and PAH growth reactions in the gas-phase of the reactor.

Notably the only differences from gasification are the lack of oxidation reactions of both the char and the gas-phase species.

### 5.3.1 Devolatilization Modeling

As discussed in Chapter 2, the devolatilization step of the thermochemical conversion of biomass is inherently a dynamic pyrolytic process, devoid of oxidation reactions and dependent on external and internal heat transfer. In a gasification or combustion reactor the fast rate of gasses being expelled from the particle guarantee that oxygen is unable to reach the reacting particle until it completely devolatilization. As such, the devolatilization model developed in Chapter 2 should be able to be successfully applied to model the devolatilization of particles in a fluidized bed pyrolyzer.

Here, each experimental case is modeled at the particle diameters and temperatures employed in the experimental study as discussed in Section 5.2. For each particle

diameter and temperature combination an external heat transfer coefficient is calculated using the Nusselt number correlation given by Gunn for a fluidized bed [64]. The bed is assumed to be isothermal at the set temperature. Additionally, the mechanical action of the sand on the particle is assumed to be negligible and that fragmentation and attrition do not occur as reported by Gaston et al.

In order to model the overall batch process using the steady RNM, we use the calculated devolatilization gas release rates in the unsteady particle model to estimate a steady rate of devolatilization gas release in order to approximate the process. Given that approximately 8g of biomass was loaded at each experimental set point, the devolatilization gas release rate is calculated as:

$$\dot{m}_{devol} = \frac{m_s(t_{devol}) - .008}{t_{devol}} \left[\frac{kg}{s}\right], \tag{5.1}$$

where $m_s(t)$ is the mass of solid at time $t$, and $t_{devol}$ is the predicted devolatilization time.

### 5.3.2 Reactor Network Model

As with FBBGs, fluidized bed pyrolyziers exhibit the same complex hydrodynamic behavior. A enumerated in Chapter 4, a variety of simplifying assumptions are adopted to represent the reactor as a combination of idealized reactors:

- *Biomass Drying and Devolatilization occurs uniformly through the bed.* - This assumption is valid and applicable when pyrolysis is much slower than the characteristic mixing time for the solid [116]. Gaston et al. used very large biomass particles with diameters ranging from 6 to 25mm for which the calculated devolatilization times range from ten to 250 seconds, under varying temperature conditions, yielding a uniformly dispersed devolatilization zone.

- *Heterogeneous char oxidation and gasification reactions are neglected.* - This assumption is valid since the reactor was operated under pyrolysis conditions.

- *The fluidized bed region of the reactor is modeled as an isothermal continu-*

*ously stirred reactor (CSTR).* - This assumption is valid when the bubbles are relatively small and mixing is vigorous. As bubble size shrinks, the mass transfer resistance between the bubble and emulsion phase vanishes. As noted by Gomez-Barea & Leckner, [62] experimental evidence shows that while sharp gradients may exist locally at the distributor, most of the bed exists with spatially constant gas concentrations and at a uniform temperature, consistent with a CSTR assumption.

- *The freeboard is modeled as an isothermal plug flow reactor (PFR).*- Modeling the freeboard as a PFR is commonly assumed since solids concentrations are low and, therefore, little axial mixing can occur [116]. Additionally, the experimental reactor was externally heated to maintain a uniform temperature justifying the isothermal assumption.

Given the above assumptions and geometric calculations, we can describe the fluidized bed pyrolyzier as a series of two ideal gas-phase reactors: a CSTR and PFR, where the CSTR has two inlet streams: (1)the devolatilization products predicted from the particle devolatilization model and (2)the inlet air stream. The resulting RNM is illustrated in Figure 4-3. The RNM calculations are implemented in MATLAB utilizing the Open-Source code Cantera 2.0 for the thermochemical and kinetic calculations [63].

## 5.4 Results and Discussion

For each reaction condition employed experimentally, an equivalent RNM simulation has been undertaken. Here, the model predictions are compared with reported data from Gaston et al. [56] for both the predictions of the devolatilization process and the gas yields.

In Figure 5-1 the calculated devolatilization times at each case are compared with the reported experimental fit. It is observed that the model predictions agree well with the experimental fits, each yielding a power-law trend in accordance with theory

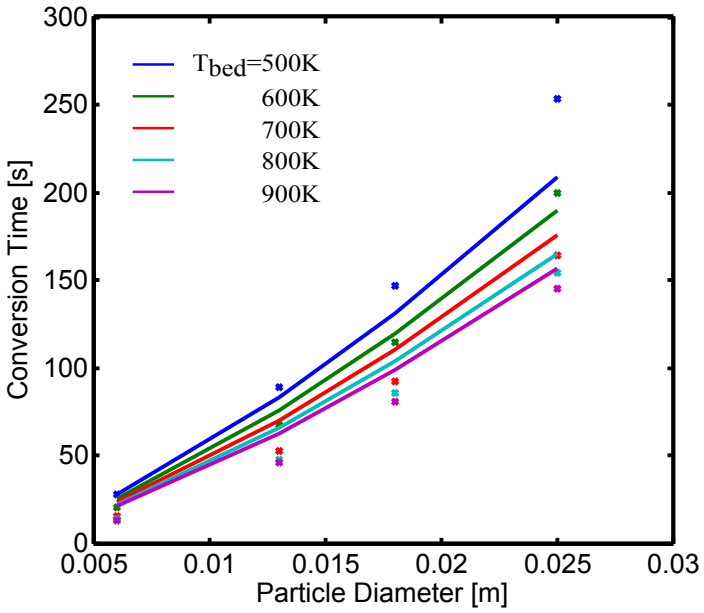


Figure 5-1: Particle size dependence of devolatilization time is plotted for both the reported experimental fit (solid lines, $t = exp(1013.2/T^{1.076})d_p^{1.414}$) from Gaston et al. [56] and the predicted model conversion times (x).

for thermally large particles where internal heat transfer dominates the conversion rate (see Chapters 2 and 3 for a more detailed discussion of the controlling regimes of devolatilization). A stronger temperature dependence is predicted by the particle devolatilization model than by the reported fit of experimental data. This is likely due to uncertainty in defining the end of devolatilization in the computational model, the time at which 99% of total mass loss is achieved, and experimental measurement, length of time of the measured gas signal, equivalently. Additionally, another potential source of disagreement is the utilized model for internal heat transfer (see Table tab:thermophysical-properties) which is not specifically tuned for white oak.

Text about Figure 5-2.

Additionally, the influence of temperature and particle diameter on the chemical conversion has been quantified experimentally. The influence of these parameters on the devolatilization process is evinced both through the resultant gas yields and more directly through the total char mass yield. In Figure 5-3 the predicted char yields are compared with the reported mean experimental values. It is clear that a good agreement is achieved for the inverse temperature dependence of char yield on

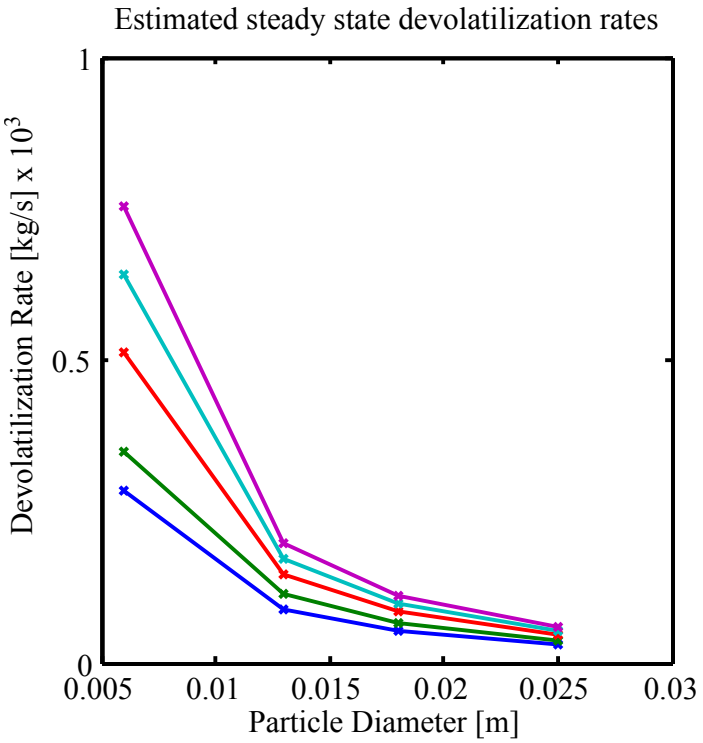


Figure 5-2: Estimated steady state devolatilization rate for each experimental condition.

temperature which is in agreement with theory. However, for the largest particles (25mm) the experimental results show little dependence. Model predictions show practically no influence of particle diameter on the char yield, while experimental results show a slight trend, most noticeable in the difference between the largest and smallest particle at each temperature.

In their interpretation of these experimental results, Gaston et al. found with a pairwise $t$ test that indeed the temperature dependence observed holds, most statistically significant is that of the 13mm particle, however it is only found that statistical significance could be shown between 6mm and 25mm particles at 500, 600 and 700$°C$.

In Figure 5-4 the influence of temperature on the gas yields measured at the exit of the pyrolysis reactor are compared for the experiment and the model predictions. It is immediately observed that excellent qualitative agreement is achieved for each major gas species and the remaining species fraction ('Water & Tars'). Unfortunately, the total yield of water was not measured experimentally, however in considering

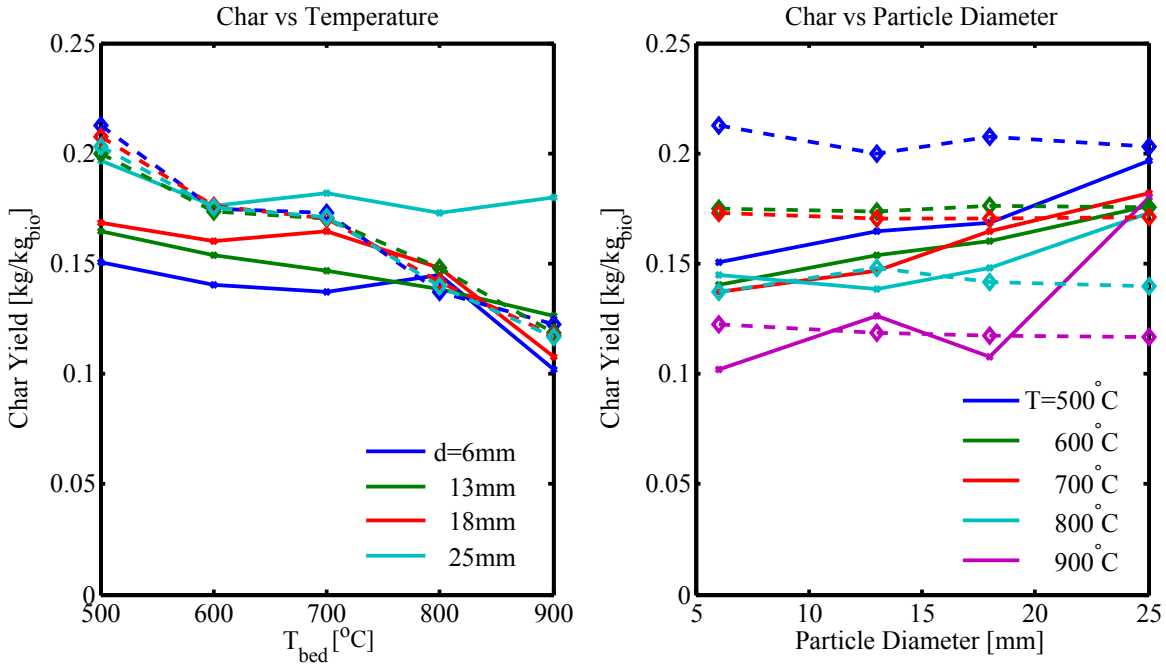


Figure 5-3: Temperature and particle size dependence of devolatilization char yield are plotted. The solid lines are from the reported experimental values from Gaston et al. [56] and the dashed lines are model predicted values.

the negligible temperature dependence predicted by the model it can be concluded that with increasing temperatures, the decrease in the predicted yield of the balance ('Water & Tars') can be attributed to tar cracking to smaller gas species - hydrogen, carbon monoxide, carbon dioxide and methane.

In Figure 5-5 the influence of particle diameter on the gas yields measured at the exit of the experimental pyrolysis reactor are compared with for both the experiment and the model predictions. It is noticeable that the particle diameter plays little, if any, role in the concentrations of major gas species at the exit in the experiments and this is also predicted by the model as well. This is not sufficient evidence to say that the particle diameter does not influence the chemical conversion, since locally at the particle surface it is expected that the devolatilizing gasses are strongly impacted by the particle diameter as discussed in Chapter 2, especially as the particle diameter decreases to the point that the control regime changes from heat transfer to kinetics. Rather, it is likely that these major gas species' concentrations are dictated primarly by the approach to pseudo-equilibrium of the fast reactions in the gas phase (WGS

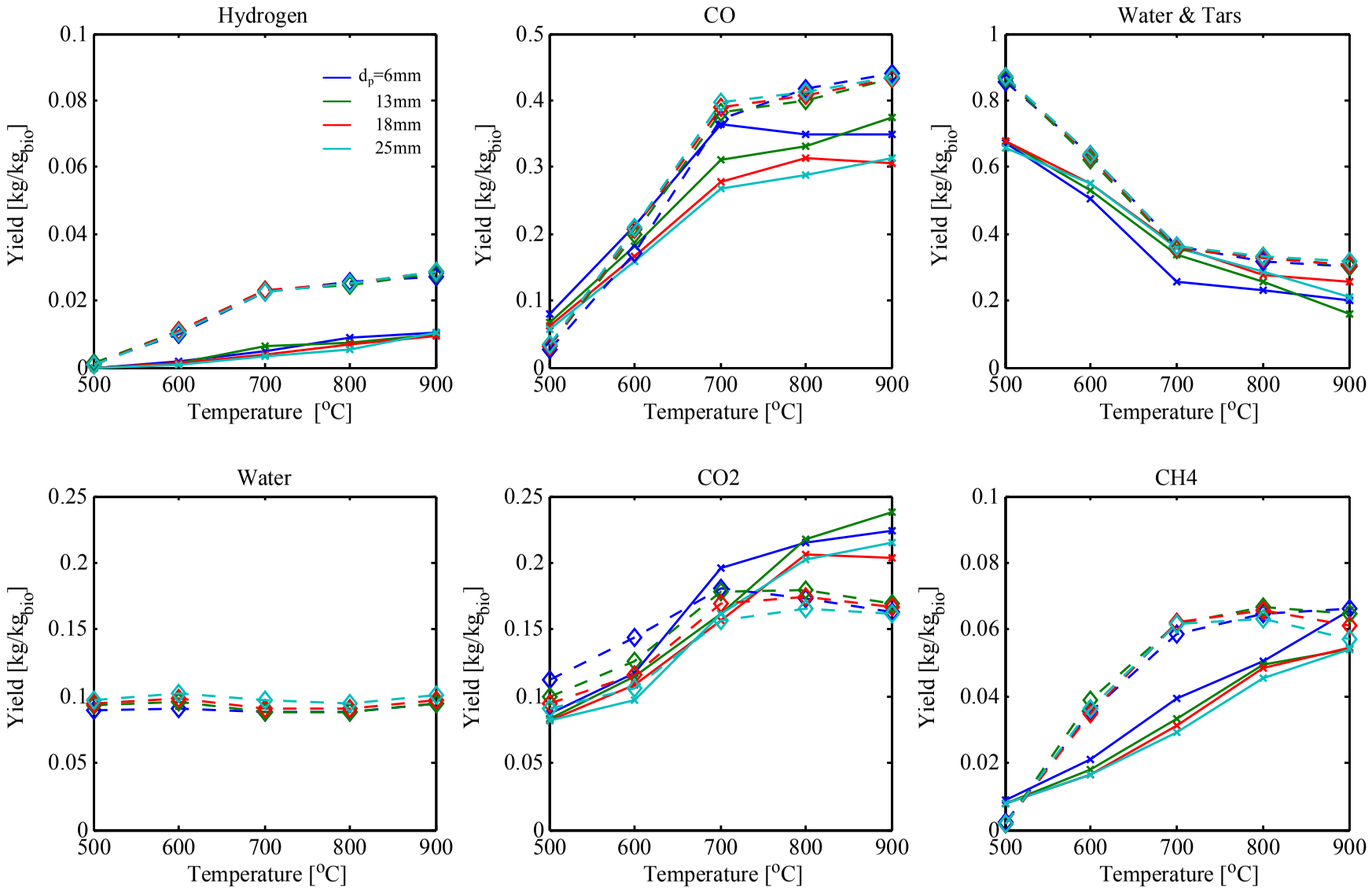


Figure 5-4: Temperature dependence of measured gaseous species at the oultet. Solid lines demarked with 'x' denote the experimental values from Gaston et al. [56], dashed lines demarked with diamonds denote the model predictions.

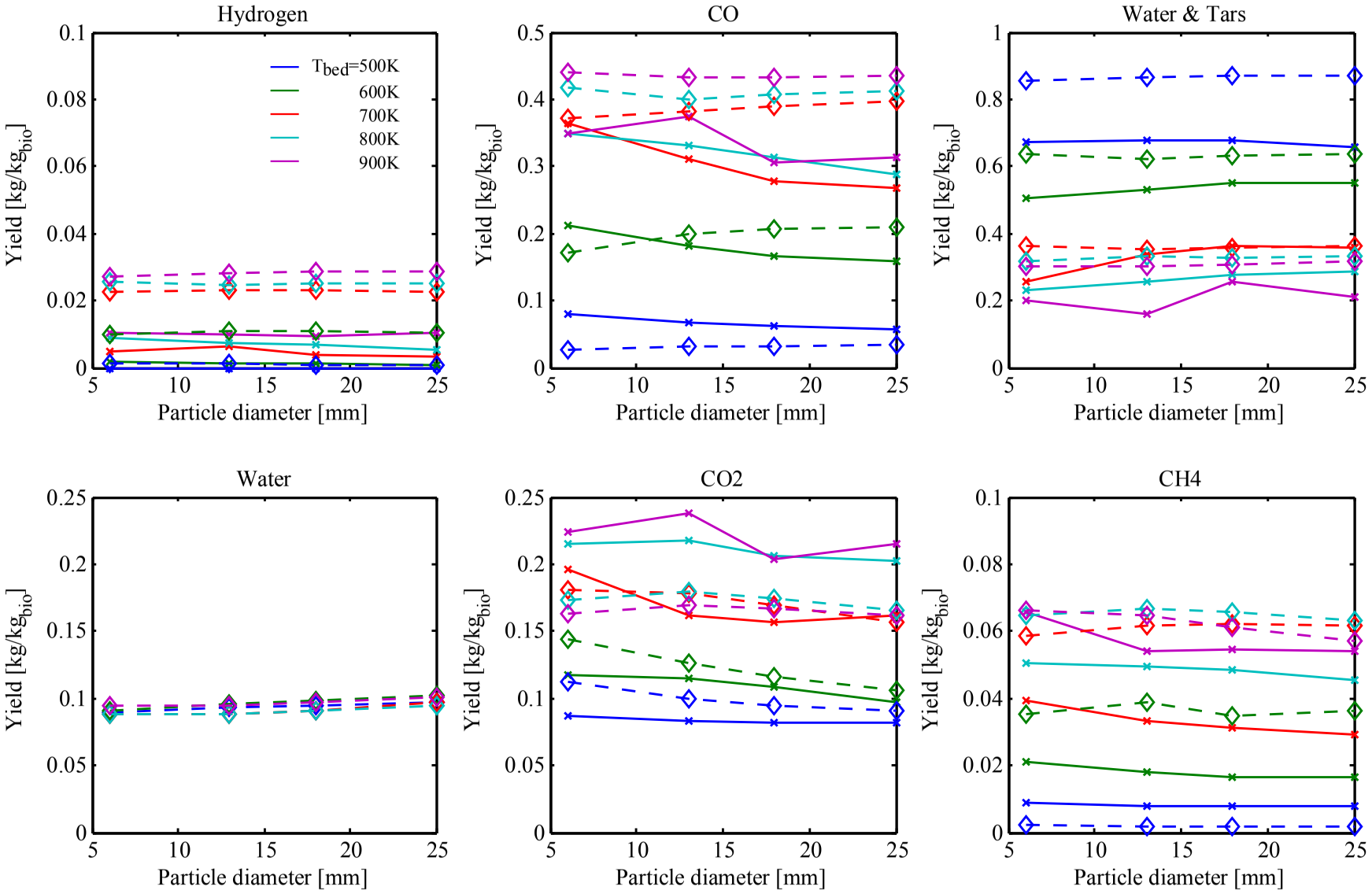


Figure 5-5: Particle size dependence of measured gaseous species at the outlet. Solid lines demarked with 'x' denote the experimental measurements from Gaston et al. [56], dashed lines demarked with diamonds denote the model predictions.

etc), and the influence of the particle diameter on devolatilization chemistry would primarily be detectible only in PAH concentrations which is strongly dependent on the initial concentrations of primary pyrolysis products.

In Figure 5-6 the predicted yields of each tar class are plotted against reactor temperature for each particle diameter investigated. The tar classes are the same as applied in chapter 4 and tabulated in Table tab:species. Class 2 tars, then, represent the primary pyrolysis species such as Coumaryl and other oxygenated aromatics such as phenol and cresol. Class 3 tars are 1-ring aromatics such as benzene and toluene. Class 4 and 5 tars are small (2-3 ring) and large (4+) ring PAH compounds respectively. As expected by theory, these temperature trends for the speciation of the tars are resultant from the increased rate of primary tar cracking and dehydration of Class 2 tars to class 3 species and at higher temperatures the improved rate of conversion to PAH compounds via the radical growth mechanism discussed in Chapter 4. Unlike under gasification conditions where at high temperatures most tar species are consumed via cracking and oxidation, here it is observed that the total tar yield remains relatively constant across the temperature range perhaps showing a slight uptick. This observation indicates that the major primary tar consumption pathway is through growth under pyrolysis conditions at high temperatures.

Due to limitations of quantitative measurement of tar species, the experimental yields of the tar classes were not reported in the paper of Gaston et al. However, trends are reported as the integrated MBMS signal and similar temperature trends are reported for the relative concentrations of primary (class 2), secondary (class 2/3) and PAH tar (class 4+5) compounds (see Figure 13 in [56]). This agreement gives us good confidence that the tar growth dynamics are being captured accurately.

In Figure 5-7 the influence of particle diameter on total tar yield and speciation is plotted. It is clear that the particle diameter plays a strong role in the dynamics of tar growth. At $900°C$, the temperature at which PAH growth is most active, it is observed that for both Class 2 and 3 tars the particle diameter plays a negligible role, indicating that the final concentration of these species is dependent primary on the global reactor temperature. However, it is observed that there is a weak influence of

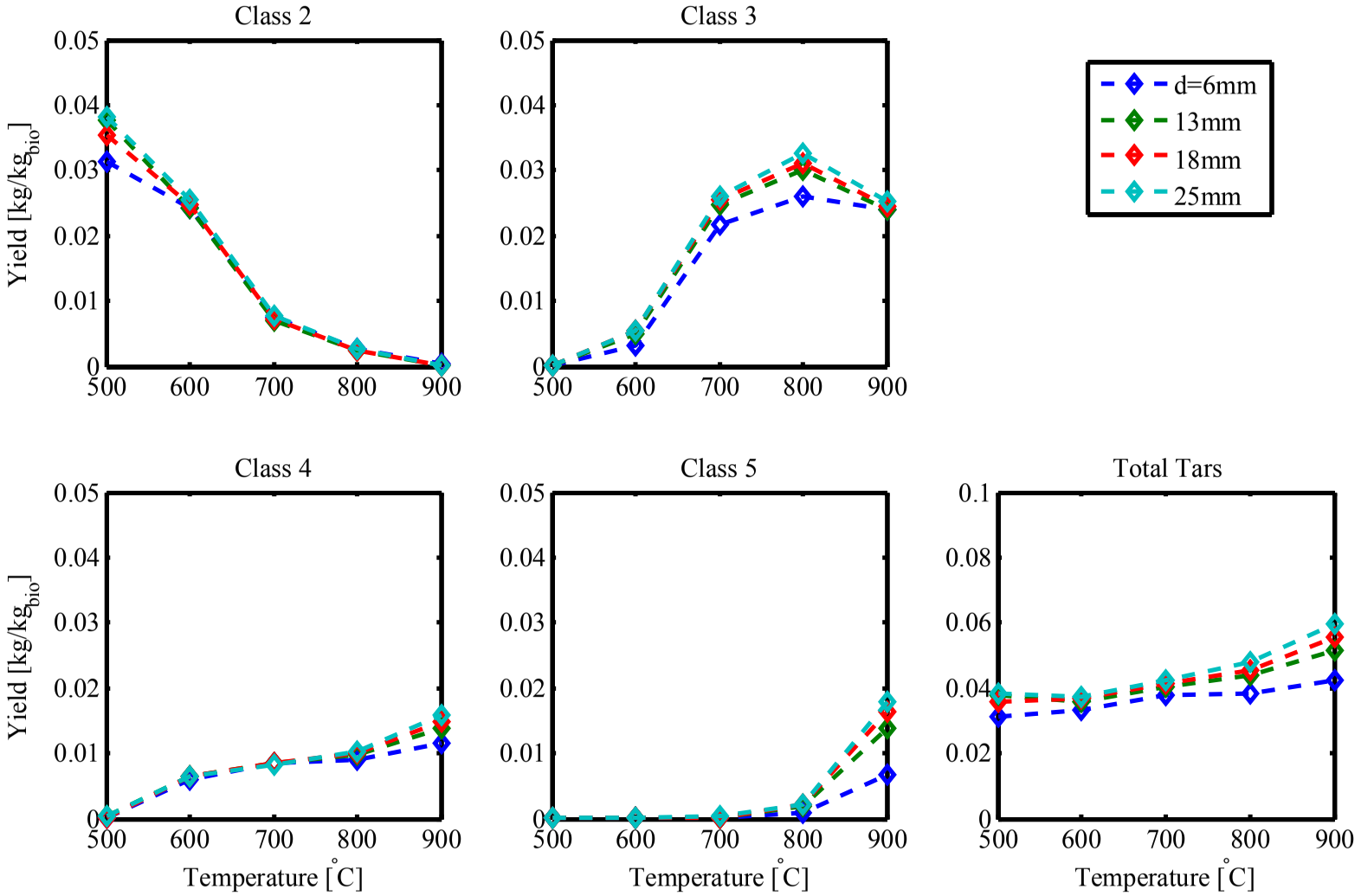


Figure 5-6: The influence of reactor temperature on the predicted tar yields at the exit of the reactor are plotted for each particle diameter.

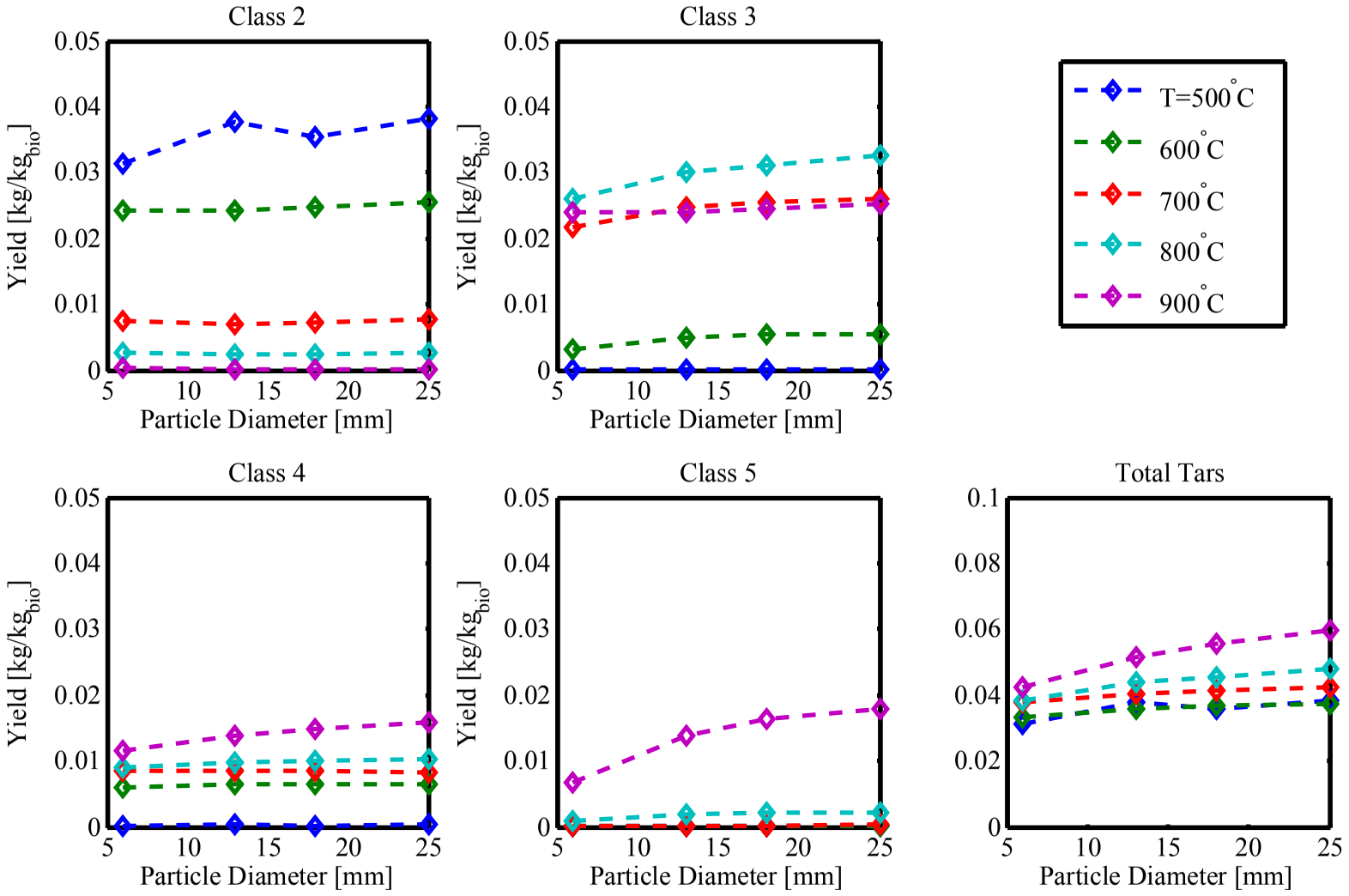


Figure 5-7: The influence of particle diameter on the predicted tar yields at the exit of the reactor are plotted for each reactor temperature.

particle diameter on class 4 tars and a much stronger influence on the final yield of large PAH compounds indicating that the change in primary devolatilization species distribution is playing an important role in defining the secondary tar conversion chemistry.

The influence of the particle diameter plays a secondary role to the reactor temperature in defining the thermochemical conversion and ultimate species yields at the reactor exit. The predictions of the light gaseous species important to gasification and pyrolysis modeling (hydrogen, carbon monoxide, carbon dioxide and water) are dictated primarly by the reactor temperature through their equilibrium concentrations at the temperature and the slower kinetic conversion of methane and tars at these temperatures shifting this equilibrium value. This secondary influence of the particle diameter manifests itself in the prediction of large PAH compounds due to the nonlinear nature of their creation via their radical growth mechanism, rendering their final concentration extremely sensitive to the initial condition.

In order to gain more insight into the mechanism of tar formation and growth, tar species concentrations are plotted versus residence time in Figure 5-8 for 25 mm particles at three temperatures. Tar evolution is plotted with respect to residence time, where $t < 0$ is the tar precursors released during devolatilization. The concentrations in the CSTR bed zone are plotted from $t = [0, t_{res,bed}]$ where $t_{res,bed}$ is the calculated residence time in the bed zone, and is indicated with a vertical dotted line. The concentration evolution in the PFR is plotted from $t = [t_{res,bed}, t_{res,tot}]$ where $t_{res,tot}$ is the total calculated residence time of gases in the bed plus the freeboard.

With increasing temperature the total initial concentration of primary tars are shown to increase. This is due to the increased rate of devolatilization with increased temperature as shown in Figure 5-2 since in fact total yields of primary tars are shown to be inversely dependent on reactor temperature above $600°C$ as will be shown in Figure 5-9. Since the devolatilization is slower for larger particles the overall volatile concentration in the reactor is lower for larger particles as the inflow rate of nitrogen was held constant in the experiment. In the top row of Figure 5-8 the concentrations of each tar class are plotted against the residence time. At low temperature ($600°C$)

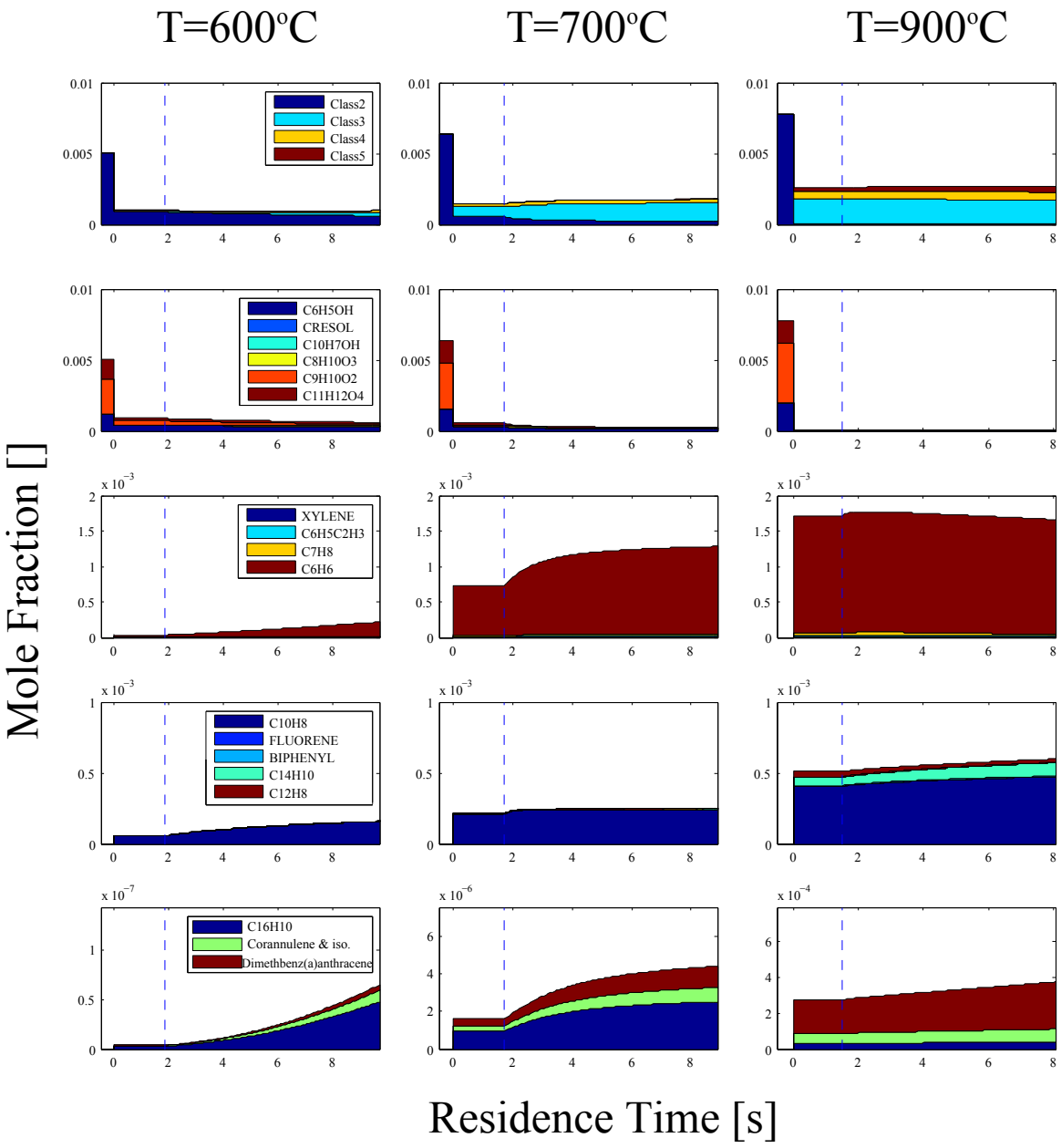


Figure 5-8: PAH growth versus residence time is plotted for three operating temperatures of the NREL reactor for 25mm particles.

Class 2 tars are continually the dominant species, with slow formation of Class 3 and Class 4 tars indicating slow formation of PAH compounds. With increasing temperature it is observed that the total tar concentration is increased and is dominated by Class 3 tars as well as increasing fractions of Class 4 and 5 tars. In each of the subsequent rows the evolution of the species making up each tar class are shown, where the Class 2 tar specitation is shown in the second row it is observed that the primary tar precursors released during devolatilization are all Class 2 tars: Phenol ($C_6H_5OH$), pCoumaryl ($C_9H_{19}O_2$) and Sinapoyl Aldehyde ($C_{11}H_{12}O_4$). Within the bed zone it is observed that most of the pCoumaryl and Sinapoyl Aldehyde are converted, and continue to convert through the PFR. Also, it is the case that almost all Class 2 tars are converted at elevated temperatures. Class 3 tars are dominated by benzene at all temperatures, with increased amounts of toluene ($C_7H_8$) present at elevated temperatures through the bed and peaking early in the PFR. The existence of this functionalized phenolic is indicative of radical PAH growth, since toluene can be formed via:

$$C_6H_6 + \cdot CH_3 = C_7H_8 + \cdot H \tag{5.2}$$

$$\cdot C_6H_5 + CH_4 = C_7H_8 + \cdot H \tag{5.3}$$

Indicating the existence of the phenyl radical ($\cdot C_6H_5$, necessary for PAH growth. Additionally, consumption of toluene via the second reaction produces phenyl radical which can then undergo conversion to PAH compounds via the Frenklach mechanism.

With increasing temperature it is observed that the concentration of Class 3 tars form a peak early in the freeboard, indicating their conversion to higher PAH compounds in this pyrolytic environment. This is confirmed at $900°C$ where the continued increase of Class 4 and 5 tars through the freeboard are in contrast to the decreasing Class 3 tar concentration. Additionally, no growth in Class 2 tars is observed indicating that only PAH growth is occuring.

Finally, it can be observed in Figure 5-8 that with increasing temperature the

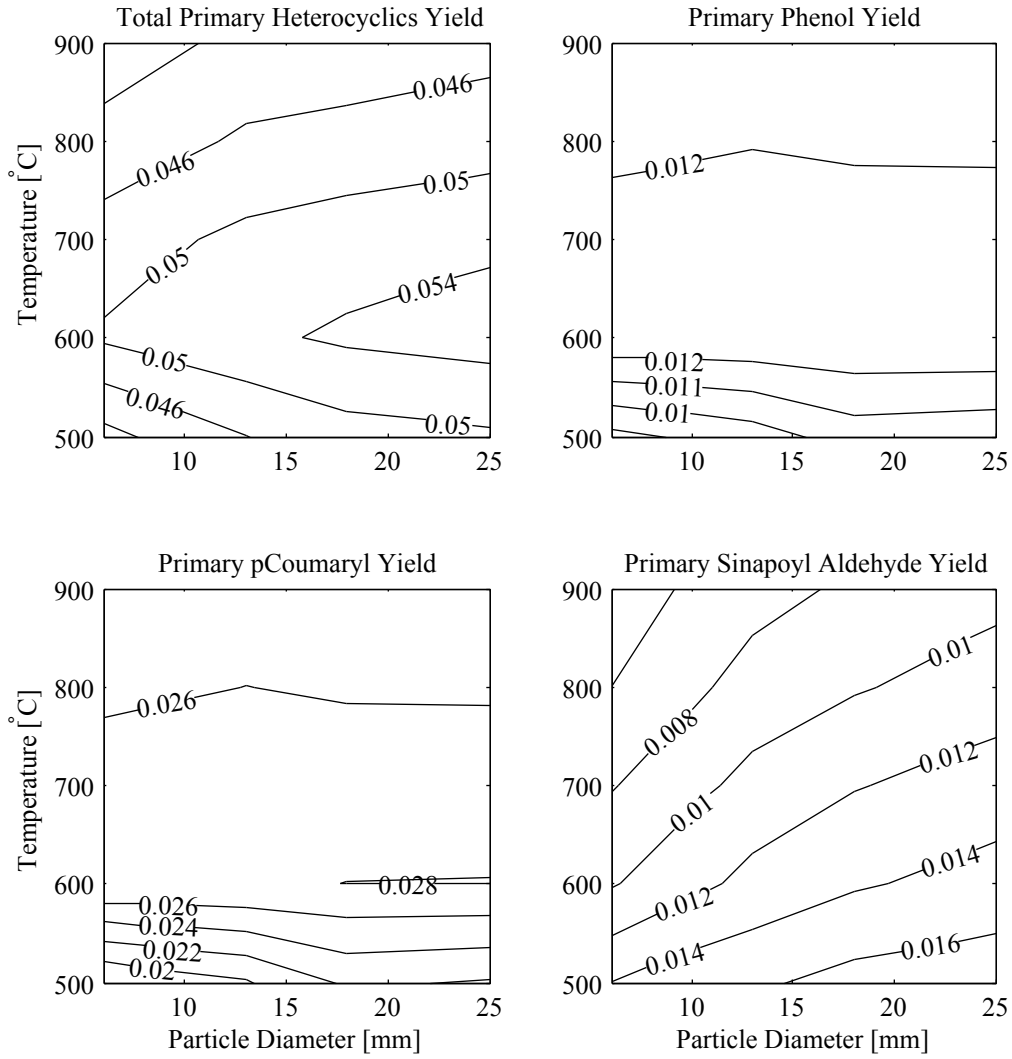


Figure 5-9: Dependence of primary tar yields on particle diameter and temperature.

limiting parameter to PAH growth shifts from being dominated by the kinetics of growth to being limited by the available Class 2 and 3 tars for ring addition. At $600°C$ Class 5 tar growth is exponential indicating free growth, while for $700°C$ the growth rate appears to transition from an early fast growth to a slow linear growth indicating a strong dependence on the available Class 3 tars. At $900°C$ where the kinetic rate of PAH growth is sufficiently fast linear growth is observed which is limited by the decreasing concentration of class 3 tars.

In order to better illustrate the influence of temperature and particle diameter on PAH formation and growth, the yields of primary tars from devolatilization and tar yields by class are plotted against particle diameter and temperature in Figures 5-9

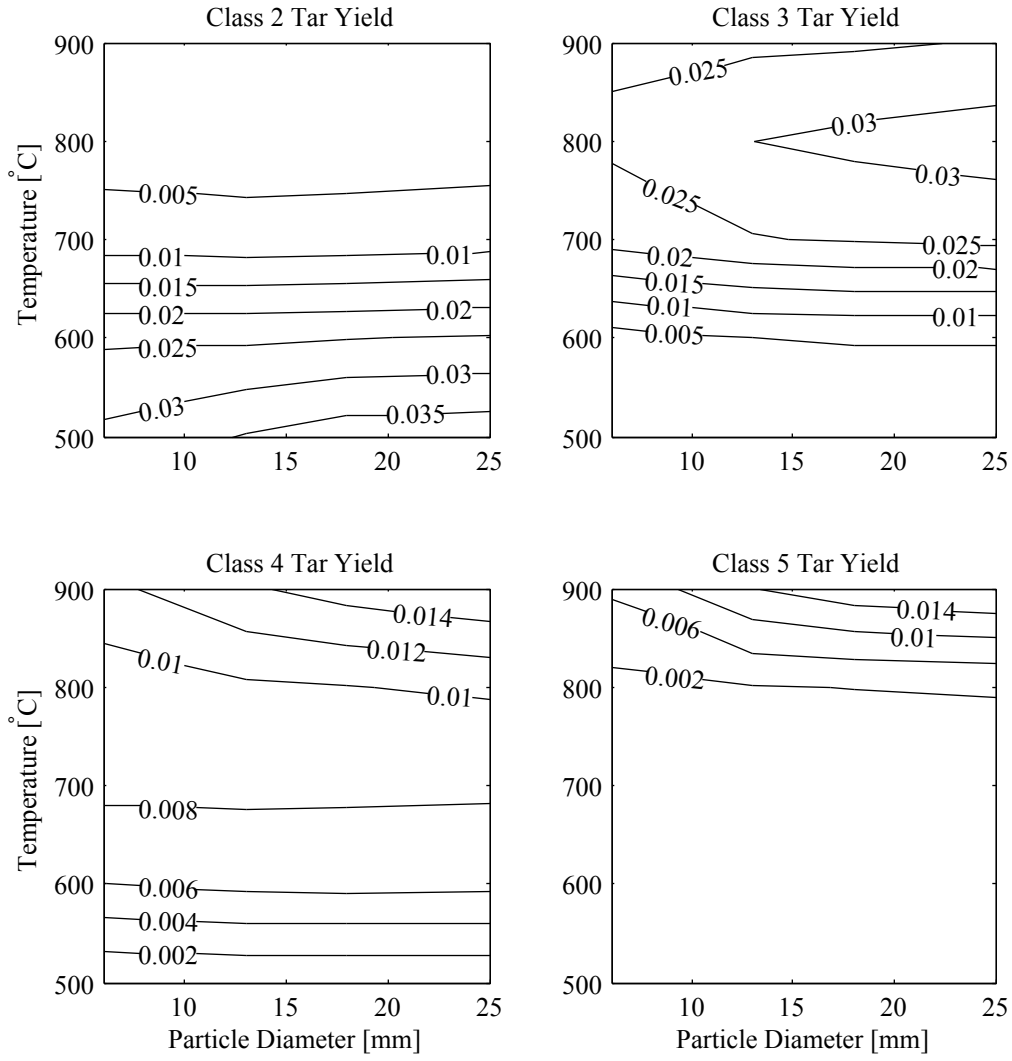


Figure 5-10: Dependence of tar class yields on particle diameter and temperature.

and 5-10 respectively.

In Figure 5-9 it is observed that with increasing temperature the total amount of primary tar peaks around $600°C$ for all particle diameters. This is driven primarily by the peak in pCoumaryl at this temperature as well as the peak in Phenol yield observed at between 600 and $700°C$. On the other hand, with increasing temperature, the yield of primary Sinapoyl Aldehyde is decreasing due to the elevated effective devolatilization temperature. With respect to particle diameter, there is increased total primary tars due to a strong dependence of Sinapoyl Aldehyde which increases with temperature.

In Figure 5-10 the yields of each class of tar are plotted versus reactor temperature

and particle diameter. As previously shown by figure 5-7 particle diameter dependence of tar is predicted for class 3, 4 and 5 tars. Class 3 tars demonstrate this dependence most starkly at $800°C$ while Class 4 and 5 do with increasing temperature to $900°C$. Given the strong particle diameter dependence PAH and synapoyl aldehyde, it is likely the case that increased PAH yield at higher particle diameters is due to the increased primary yield of Sinapoyl Aldehyde. This dependency is further demonstrated in Figure 5-11.

In Figure 5-11 the yields of each tar class exiting the reactor are plotted versus the primary Sinapoyl Aldehyde yields for each reactor temperature and particle diameter, where reactor temperatures are connected by lines and each particle diameter is indicated by markers. In order to better quantify the link between particle diameter, primary tar yields and tar class yields at the reactor exit a statistical analysis has been performed by calculating the Pearson correlation coefficient and the p-value of the potential correlation between the particle diameter and the primary tar yields (see Table 5.2), as well as between the yields of each class of tar and the primary tar yields and the particle diameter (see Table 5.3). The Pearson correlation coefficient is defined as:

$$\rho_{X,Y} = \frac{cov(X,Y)}{\sigma_X \sigma_Y} = \frac{E[(X-\mu_X)(Y-\mu_Y)]}{\sigma_X \sigma_Y} \tag{5.4}$$

where $cov(X,Y)$ is the covariance between two data sets $X$ and $Y$, $\sigma$ is the standard deviation of the data set and $E[]$ is the expected value of the data set. The p-value is the probability that this calculated correlation is not statistically significant.

In Table 5.2 the Pearson correlation coefficient and the associated p-values for each temperature are shown between the primary tars and the particle diameter. It is observed that for each temperature, a statistically significant correlation exists between the particle diameter and the total primary tar yield since the p-values are below 0.1 for all temperatures signifying at least a 90% confidence. Similarly at all temperatures Sinapoyl Aldehyde has a strong positive correlation, driving the total

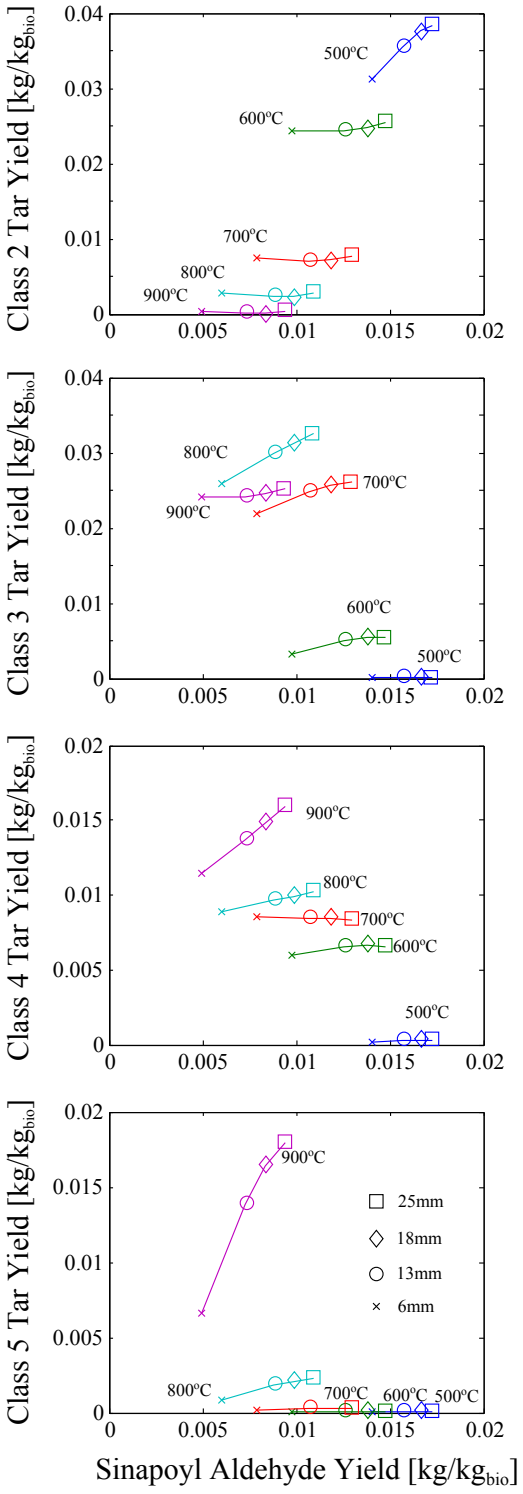


Figure 5-11: The dependence of predicted tar class yields on sinapoylaldehyde yields at each reaction condition specified in Gaston et al [56].

Table 5.2: Correlation values between particle diameter and primary tar yields at each operating temperature. The Pearson correlation coefficient ($\rho_{x,y}$) and p-values for the potential correlation are tabulated.

| Temperature [$°C$] | Phenol | | pCoumaryl | | Sinapoyl Aldehyde | | Total primary tars | |
|---|---|---|---|---|---|---|---|---|
| | $\rho_{x,y}$ | p-value | $\rho_{x,y}$ | p-value | $\rho_{x,y}$ | p-value | $\rho_{x,y}$ | p-value |
| 500 | 0.900 | 0.100 | 0.898 | 0.102 | 0.976 | 0.024 | 0.933 | 0.067 |
| 600 | 0.874 | 0.126 | 0.879 | 0.121 | 0.970 | 0.030 | 0.973 | 0.027 |
| 700 | 0.286 | 0.714 | 0.282 | 0.718 | 0.977 | 0.023 | 0.982 | 0.018 |
| 800 | 0.298 | 0.702 | 0.296 | 0.704 | 0.973 | 0.027 | 0.926 | 0.074 |
| 900 | -0.942 | 0.058 | -0.941 | 0.059 | 0.983 | 0.017 | 0.984 | 0.016 |

correlation between particle diameter and total primary tar yield. It is clear that Phenol and pCoumaryl do not exhibit strong positive correlation with respect to particle diameter except for at $500°C$. At $900°C$ Phenol and pCoumaryl demonstrate a negative correlation, while Sinapoyl Aldehyde has a very strong correlation, indicating that at these high conversion temperatures Sinapoyl Aldehyde is produced in lieu of Phenol and pCoumaryl with increasing particle diameter.

In Table 5.3 the correlations between the yields of each class of tar at the exit versus the primary tar species yields as well as particle diameter at each reactor temperature. It is notable that the statistical significance of the correlation between the yields of tars and the particle diameter shifts with respect to temperature. The total yield of class 2 tars shows the strongest dependence on diameter at 500 and $600°C$ while the PAH compounds, classes 4 and 5 show the most statistically significant diameter dependence at $700°C+$. In the cases where there is a statistically significant connection between the yield of tars at the exit and the particle diameter we can inspect the correlation statistics between the final tar yield and the primary tar yield. At $500°C$ where Class 2 tar yields have a statistically significant positive dependence on particle diameter statistical significance is also shown between each of the primary tar precursor yields. This is due to the fact that at low temperatures these primary tars do not fully react in the gas phase, exiting the reactor in tact and are then measured as Class 2 tars. At higher temperatures where class 4 and 5 tar yields demonstrate statistically significant dependence on particle diameter it is demonstrated that only Sinapoyl Aldehyde plays an important role in their increased

Table 5.3: Correlation values between the yield of each tar class and primary tar component yields along with particle diameter at each operating temperature. The Pearson correlation coefficient and p-values for the potential correlation are tabulated.

| Temperature [$°C$] | Phenol | | pCoumaryl | | Sinapoyl Aldehyde | | Particle Diameter | |
|---|---|---|---|---|---|---|---|---|
| | $\rho_{x,y}$ | p-value | $\rho_{x,y}$ | p-value | $\rho_{x,y}$ | p-value | $\rho_{x,y}$ | p-value |
| Class 2 | | | | | | | | |
| 500 | 0.972 | ***0.028*** | 0.972 | ***0.028*** | 0.994 | ***0.006*** | 0.946 | ***0.054*** |
| 600 | 0.870 | 0.130 | 0.876 | 0.124 | 0.813 | 0.187 | 0.929 | ***0.071*** |
| 700 | 0.949 | 0.051 | 0.948 | 0.052 | 0.276 | 0.724 | 0.474 | 0.526 |
| 800 | -0.852 | 0.148 | -0.852 | 0.148 | -0.148 | 0.852 | 0.083 | 0.917 |
| 900 | 0.503 | 0.497 | 0.506 | 0.494 | -0.362 | 0.638 | -0.184 | 0.816 |
| Class 3 | | | | | | | | |
| 500 | 0.919 | ***0.081*** | 0.918 | ***0.082*** | 0.973 | ***0.027*** | 0.916 | ***0.084*** |
| 600 | 0.717 | 0.283 | 0.718 | 0.282 | 0.963 | 0.037 | 0.869 | 0.131 |
| 700 | -0.054 | 0.946 | -0.059 | 0.941 | 0.989 | 0.011 | 0.935 | ***0.065*** |
| 800 | 0.536 | 0.464 | 0.534 | 0.466 | 0.999 | 0.001 | 0.961 | ***0.039*** |
| 900 | -0.705 | 0.295 | -0.703 | 0.297 | 0.807 | 0.193 | 0.902 | ***0.098*** |
| Class 4 | | | | | | | | |
| 500 | 0.975 | 0.025 | 0.975 | 0.025 | 0.959 | 0.041 | 0.875 | 0.125 |
| 600 | 0.622 | 0.378 | 0.622 | 0.378 | 0.914 | 0.086 | 0.787 | 0.213 |
| 700 | -0.410 | 0.590 | -0.405 | 0.595 | -0.944 | ***0.056*** | -0.991 | ***0.009*** |
| 800 | 0.531 | 0.469 | 0.529 | 0.471 | 0.999 | ***0.001*** | 0.965 | ***0.035*** |
| 900 | -0.986 | 0.014 | -0.985 | 0.015 | 1.000 | ***0.001*** | 0.985 | ***0.015*** |
| Class 5 | | | | | | | | |
| 500 | 0.281 | 0.719 | 0.284 | 0.716 | 0.009 | 0.991 | -0.057 | 0.943 |
| 600 | 0.687 | 0.313 | 0.687 | 0.313 | 0.945 | 0.055 | 0.836 | 0.164 |
| 700 | -0.125 | 0.875 | -0.130 | 0.870 | 0.975 | ***0.025*** | 0.904 | ***0.096*** |
| 800 | 0.605 | 0.395 | 0.603 | 0.397 | 0.989 | ***0.011*** | 0.928 | ***0.072*** |
| 900 | -1.000 | 1E-4 | -1.000 | 1E-4 | 0.990 | ***0.010*** | 0.946 | ***0.054*** |

yield with strong statistical significance.

Given these results the mechanism of the influence of particle diameter on PAH formation and growth is shown to be inextribly linked via the production of Sinapoyl Aldehyde and its lignin derived isomers.

## 5.5 Conclusions

In this chapter the modeling tools developed for FBBGs, the particle devolatilization model in Chapter 2 and the RNM in Chapter 4, have been employed in the analysis of a fluidized bed reactor operated under pyrolysis conditions. It is found that these models are able to predict to a good degree of accuracy the influence both the particle diameter and bed temperature on the thermochemical conversion of biomass under these pyrolytic conditions.

Further, these tools have allowed for a more detailed investigation of the physiochemical mechanisms underpinning this conversion and the influence of the temperature and particle diameter on the chemistry of tar formation and growth.

It is concluded that the particle diameter plays no major role in determining the exit concentration of the light gas species: $H_2$, CO, $H_2O$, $CO_2$ and $CH_4$. These major species are predominately controlled by the reactor temperature. However, it has been shown that the particle diameter plays a crucial role in the prediction of large PAH compounds, via the initial distribution of primary pyrolysis gases.

# Chapter 6

# Influence of Superficial Gas Velocity on Fluidization and Conversion Chemistry

## 6.1 Introduction

Good qualitative and quantitative agreement of predicted gas-phase species are achieved in chapter 4 for major gas species and total tars with a series RNM. However, in chapter 4 it was also shown that the prediction of CO, $CO_2$ and $H_2O$ concentrations is strongly dependent on catalytic effects of the bed materials on the water gas shift reaction as well as the oxidation of CO, and that the tendency of tar species to either crack or grow into PAH compounds is highly sensitive to the local availability of oxygen. If flow conditions are such that gases are able to by-pass the emulsion phase due to large bubbles and slugging then the overall catalytic effect may be reduced and predictions rendered inaccurate. Additionally, if the bed is not well-mixed for both the gas and solids reactions, then devolatilization gas and oxidant may not be uniformly mixed, resulting in locally rich zones thus increasing the likelihood of the formation of tar compounds. As such, the strong assumptions that both the fluidized bed behaves as a well-stirred reactor and that devolatilization happens uniformly

throughout the bed may not lead to accurate predictions since in this ideal limit, oxygen is uniformly available and localized concentration gradients are impossible.

In Figure 6-1 an instantaneous snapshot of a reactive CFD simulation of the van Paasen and Kiel gasifier shows the phenomena of gas bypass through the bubble phase. There is a strong correlation between the location of Nitrogen (a) and high voidage (d) and a strong negative correlation between the location of these values and the concentration of primary tars (b) and the location of devolatilization (c) itself. It is notable that the devolatilization occurs almost exclusively in the emulsion, and that the devolatilization gasses are most strongly concentrated in the emulsion throughout the bed. In this instance it is clear that the bed zone is far from homogenous and transport can play an important role in defining the chemical conversion.

This assumption of a well-stirred gas-phase in the bed zone and the uniform availability of oxygen likely has the strongest influence on the predicted tar composition at the outlet, since the conversion of tars from class 2 (phenolics) to class 3 on to larger PAH compounds (classes 4 and 5) is strongly impeded by the availability of oxygen. This is the case since there are shared hydrogen-abstracted radical intermediates between both the oxidation pathways of aromatic compounds as well as the growth mechanisms.

The mechanism of PAH formation and growth has been a topic of active research in combustion due to its central role in the formation of soot in rich premixed and non-premixed flames [82, 139]. Fundamental kinetic studies have elucidated the growth mechanism of PAH compounds [17, 18, 51, 52] and have explored the shared initiation step of benzene oxidation and PAH ring growth through the shared radical intermediates $C_6H_5\cdot$ and $C_6H_5O\cdot$ [55, 82, 89]. Additionally, there have been focused experimental studies on the formation of PAH compounds from biomass sources showing that the majority of PAH formation and growth is due to lignin [96, 97]. However, there has yet to be a focused kinetic modeling study of the influence of mixing and the availability of oxygen in determining the total amount of PAH compounds formed in the gasification of biomass in a fluidized bed gasifier.

In Figure 6-2 the conversion pathways of phenol and benzene through their hydro-

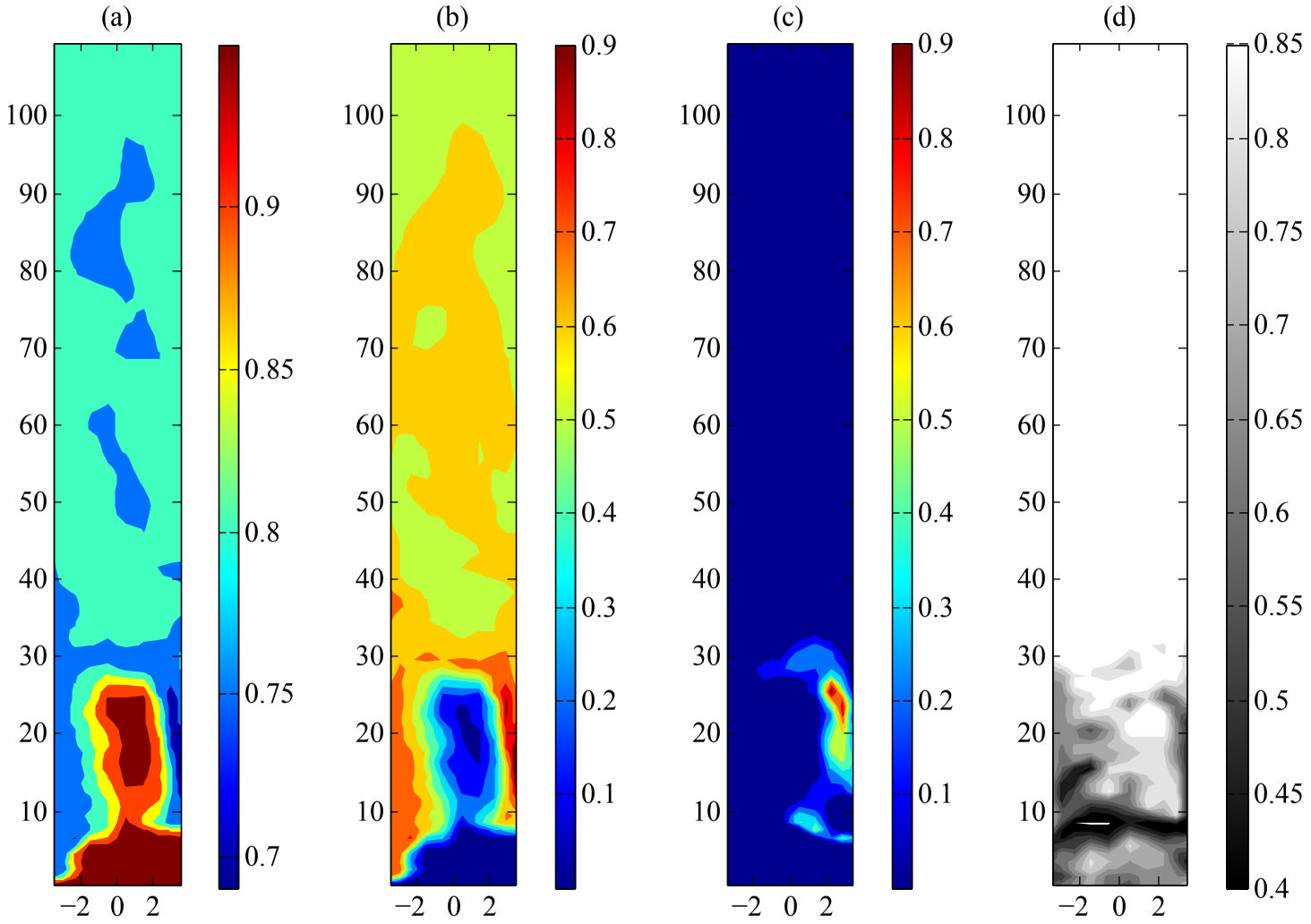


Figure 6-1: Radial slice of fully reactive CFD of van Paasen and Kiel gasifier. In (a) the normalized concentrations of nitrogen (indicative of the air) are plotted. In (b) the normalized concentration of primary tars are plotted. In (c) the normalized rate of devolatilization is plotted and in (d) the gas voidage is plotted.

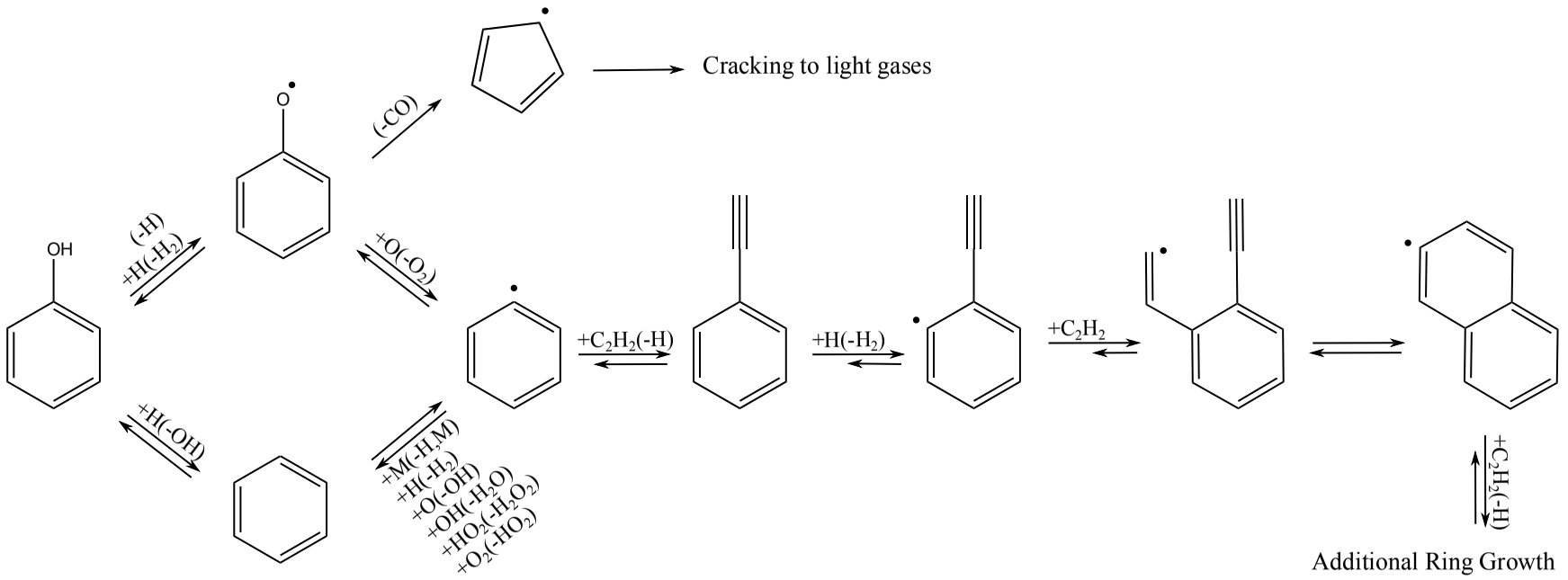


Figure 6-2: The mechanism of PAH formation from Phenol and benzene. The steps from the phenyl radical to the naphthyl radical constitute the Frenklach PAH formation mechanism [17, 18, 52]., and the reactions to cyclopentadiene constitute the mechanism of of benzene oxidation proposed by Fuji and Asaba and Lindstedt and Rizos [55,89]. The relative lengths of arrows connote relative forward and backward rates.

gen abstracted radicals $C_6H_5O_5\cdot$ and $C_6H_5\cdot$ respectively are illustrated. It is observed that of particular importance in predicting whether PAH formation will occur is the relative availability of $O_2$ and $C_2H_2$, since the phenyl radical ($C_6H_5\cdot$) can react with either of these to different results. With increasing ratios of $C_2H_2$ to $O_2$ PAH growth is expected to increase in a non-linear fashion, since as ethynyl groups ($H-C\equiv C-$) are added it becomes more difficult for the species to be oxidized due to the slow reverse (decomposition) reactions relative to the growth pathway. Further, once the naphthyl radical has been formed, additional rings can be added in an analogous fashion to the first ring addition creating more stable and larger PAH compounds. The relative difficulty of oxidizing 2+ ring PAH compounds also can have important consequences in reactors where oxygen is not well distributed producing zones of relatively rich conditions where the first ring can be formed, since the resultant PAHs may not be oxidized in a subsequent relatively lean zone due to slower oxidation kinetics.

In this chapter CFD simulations are employed in order to interrogate the assumptions of a well-stirred gas phase in the bed as well as the uniform devolatilization of biomass throughout the bed as not satisfying these assumptions will necessarily imply localities in the bed where the reactive conditions will be richer than the globally set oxidant-to-fuel ratio in the reactor where PAH growth may be favored. First, the impact of fuel particle diameter on devolatilization zone segregation is investigated. Two of the experimental reactors used for validation in Chapter 4, are simulated and an improved RNM is developed in order to capture the gas bypassing occurring in the slugging regime.

## 6.2 Fluidization Regimes and Gas-Phase By-Passing

FBBGs require a bed material with high thermal capacitance and favorable hydrodynamic properties ideally available at a low price. One such ubiquitous material is silica sand, $SiO_2$, for which the fluidization properties are well researched. With its high mass density ($\approx 2500 kg/m^3$) and nominal particle diameters ($40 < \bar{d}_p < 500 \mu m$) silica sand is classified as a Geldart B particle or a "Sand-like" particle in the well known

classification system of Geldart [58,81]. Quoting from Kunii and Levenspiel [81] these particles are characterized by a number of properties which have been shown to be captured by CFD simulation by the Reacting Gas Dynamics Lab [1]:

1. Small bubbles form at the distributor and grow and coalesce as they rise through the bed.

2. Bubble size increases roughly linearly with distance above the distributor and excess gas velocity, $u_0 - u_{mf}$.

3. Bubble size is roughly independent of mean particle size.

4. Vigorous bubbling encourages the gross circulation of solids.

In particular it is because of characteristics 1 and 4, in addition to its high thermal capacitance, that sand is chosen for FBBGs since solids circulation encourages a more well-mixed solids and gas-phase environment in the bubbling regime, thus maximizing contact between phases in an attempt to achieve overall homogeneity of the reactive environment.

However, due to the tendency of bubbles to grow and coalesce as a function of height (characteristics 1, 2 and 3), by increasing the gas flow, sand beds shift to slugging and turbulent regimes in which more gas goes to the bubble phase thus decreasing the overall gas/solids contact within the bed zone.

In Figure 6-3 the transitions of fluidization regimes are illustrated for increasing superficial gas velocity. For gas flows less than or equal to the minimum fluidization velocity, the gas-solids momentum exchange is insufficient to cause solids motion and a packed bed is maintained where gas flows through the voidage between the solids phase. With increased gas velocity above minimum fluidization, the bed transitions into a bubbling regime where small bubble formation, growth and coalescence dominates the solid mixing dynamics. With increasing gas velocity the bubble sizes continue to increase until the largest bubble diameters are of similar size to the overall bed diameter resulting in slugging flow, where bubbles as large as the bed lift up the whole bed entirely. As the gas velocities begin to approach the terminal velocity of

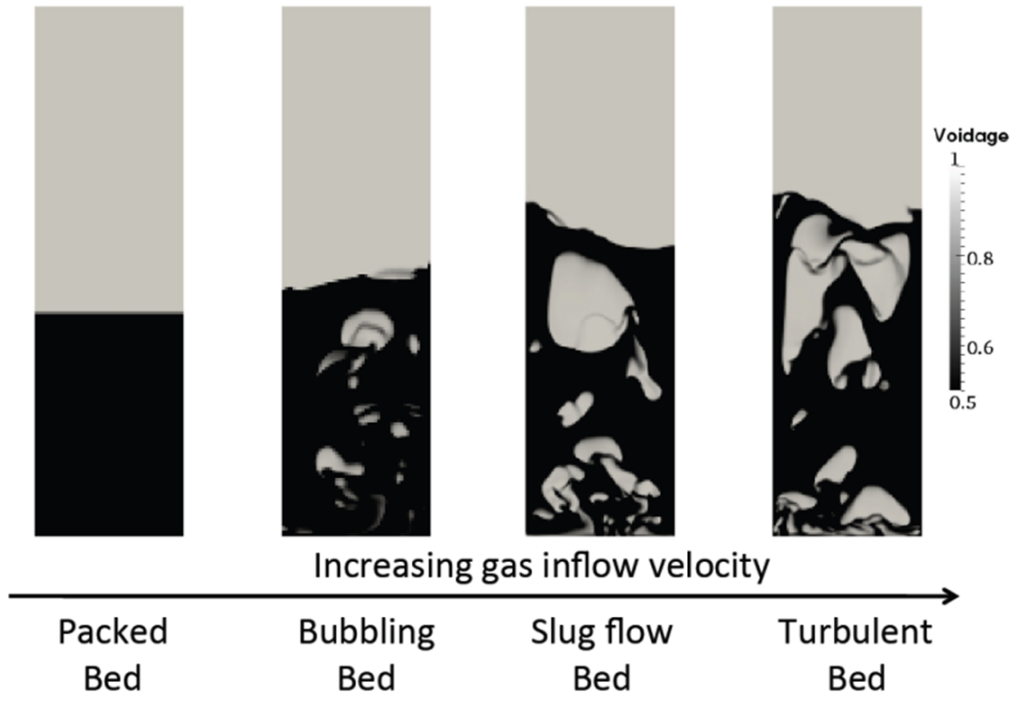


Figure 6-3: Fluidization regimes are strongly sensitive to the gas velocity transitioning through multiple regimes. In the packed bed ($U_0/U_{mf} < 1$) no solids motion occurs and gas flows through the inter-particle voidage. In the bubbling regime ($1 < U_0/U_{mf} < 7-8$) solids motion is resultant from gas and bubble motion. In the slugging regime (($7-8 < U_0/U_{mf} < 12-13$) flow is characterized by the formation of bubbles on the scale of the bed diameter and a large amount of gas bypassing. Finally, for very fast flow rates ($U_0/U_{mf} > 12-13$) dynamics are dictated by the turbulent motion of solid clusters and voids of various sizes through the bed.

the solid material entrainment becomes appreciable for fines and bubble structures break down yielding a turbulent motion of solid clusters and voids of various sizes throughout the bed [81].

The motion of solids is directly related to the bubble dynamics of a fluidized bed, with faster bubbles increasing the rate of solids motion, and Rowe showed that the timescales of vertical mixing of solids are directly proportional to the superficial gas velocity [125].

$$\frac{\tau_c U_0}{h_{mf}} = \frac{1}{0.6(1 - U_{mf}/U_0)\left[1 - \frac{U_0 - U_{mf}}{U_B}\right]}[s], \tag{6.1}$$

where $h_{mf}$ is the bed height at minimum fluidization, $U_0$ is the gas flow velocity, $U_{mf}$ is the minimum fluidization velocity, and $U_B$ is the mean bubble velocity which can be calculated from a number of available correlations for specific particle and bed sizes (see Chapters 5 and 6 in Kunii [81]).

The effective solid-gas contact time, relevant for heterogeneous char consumption reactions and bed-material catalyzed reactions, is also dependent on the gas velocity but in an inverse way. As is observed in Figure 6-3, at higher gas velocities the overall bubble sizes increase and, therefore, more gases bypass the emulsion phase entirely without having intimate interaction with the solids. In a bubbling bed, where the bubbles are small, much higher mass transfer occurs between the bubble and emulsion phase since this transfer is a surface-area dependent phenomenon and smaller bubbles have higher surface area to volume ratios [62]. !!! In the following sections these two mixing phenomena, (1) solids-solids mixing and (2) solids-gas mixing, and their interaction with chemical conversion phenomena are analyzed in more detail. In Section 7.2 the influence of solid-solid mixing on solid devolatilization zone segregation is considered. Then, in Section 6.3 an improved RNM is proposed in order to capture the influence of gas bypassing the emulsion in the bubble phase. Finally, in Section 6.4 CFD modeling of experimental reactors is employed to gain further insight into these phenomena and to calculate the necessary geometric parameters to describe the RNM.

## 6.3 Improved RNM to Capture Gas By-Pass in the Bubble Phase

In Chapter 4 an RNM consisting of a particle devolatilization model followed by a CSTR representation of the bed and a PFR representation of the freeboard was developed and validated against available reactor data. It was shown that this simple model is able to capture both qualitative and quantitative trends in the prediction of the gas phase major species as well as tar fractions.

Modeling the bed zone as a CSTR depends on strong assumptions that are likely violated at very fast fluidization rates where slugs are formed, which is often the case in thin and tall research reactors. At fast fluidization ($U_0/U_{mf} > 8$) bubbles can no longer be assumed to be small and vigorous as required for a well stirred zone, rather bubbles continue to coalesce and slugs form allowing a significant fraction of fluidization gas to bypass the emulsion phase entirely, thus decreasing the solids-gas contact time and the overall mixing of the oxidant and devolatilization gasses, which are released within the emulsion, in the lower part of the bed where temperatures are generally hotter and kinetics faster due to the presence of char oxidation reactions. This could potentially have an important effect on the overall rates of a number of reactions, in particular that of the WGS reaction, for which the catalytic effect of the bed material was shown to play an important role in Chapter 4. Additionally, bypassing of oxidant gas through the bubble may increase PAH formation and growth within the emulsion where primary devolatilization products are created, since with oxidant bypass in the bubble phase it is expected that the emulsion phase would be relatively rich compared to the set global oxidant to fuel ratio for the reactor.

In Figure 6-4 a modified RNM is illustrated capable of capturing the effects of gas bypassing based on the two fluid model (TFM) proposed by Davidson [33, 34]. Instead of modeling the whole bed as a CSTR, an additional PFR is added in parallel in order to model the bypassing gas in the bubble phase. In the original formulation of the TFM, it was proposed that all of the excess gas above minimum fluidization would bypass the emulsion through bubbles. Here, it is accepted that with increasing

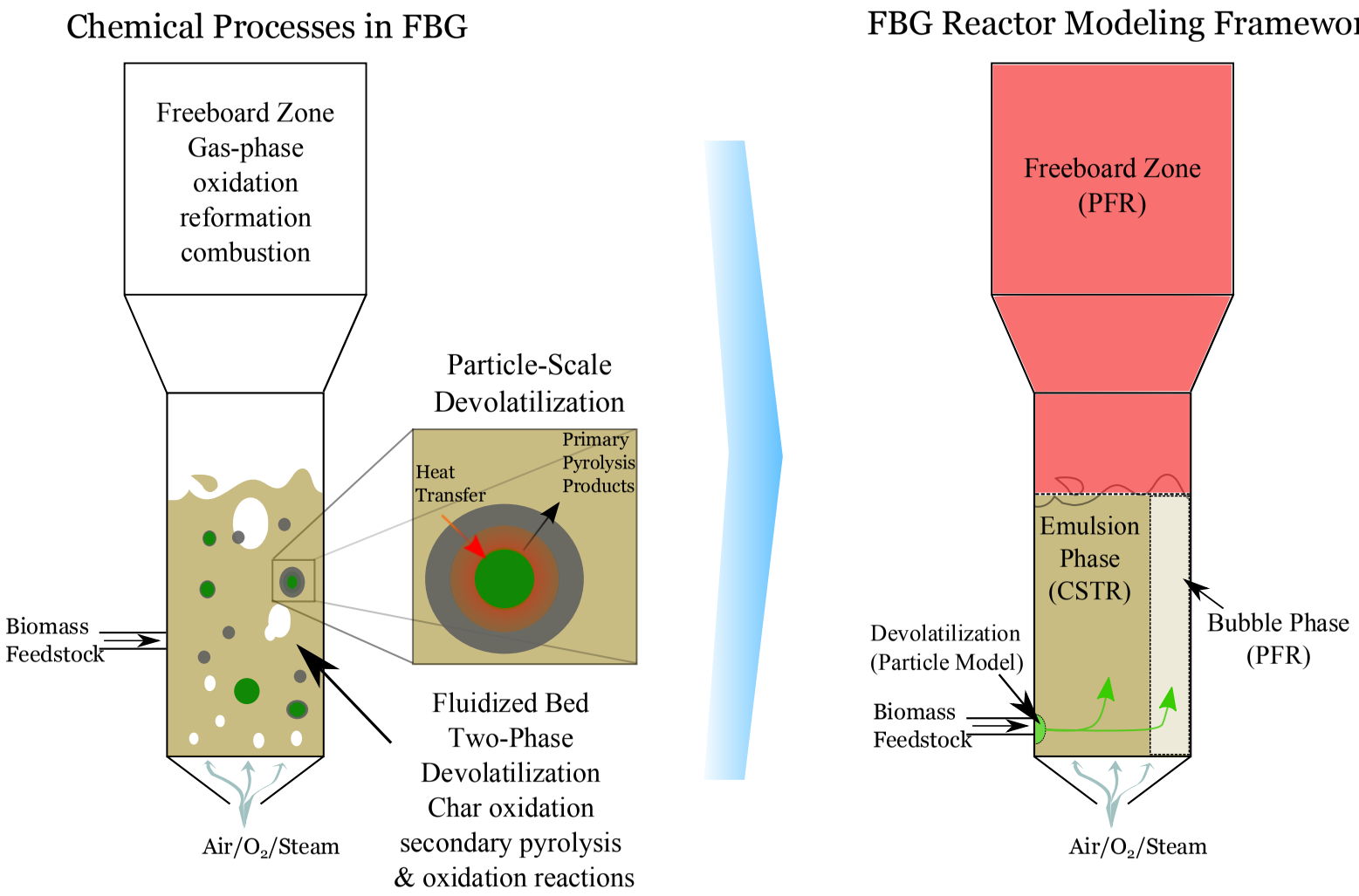


Figure 6-4: An improved RNM, based on the two fluid model (TFM) theory, where bypassing gas in the bubble phase is modeled as a PFR.

Table 6.1: Correlations of bed expansion from literature.

| | Formula | Reference |
|---|---|---|
| | $\frac{1}{1-\frac{U_0/U_{mf}-1}{U_{br}/U_{mf}+U_0/U_{mf}}}$ | TFM [33, 34] |
| $H/H_{mf} =$ | $\frac{1}{1-\frac{1}{1+\frac{1.3}{0.26+0.7exp(-0.0033d_p)(0.15+(U_0-U_{mf}))^{-.33}(U_0-U_{mf})^{-.8}}}}$ | Johnsson TFM [77] |
| | $\frac{1+14.31(U_0-U_{mf})^{.738}d_p^{1.006}\rho_p^{.376}}{\rho_g^{.126}U_{mf}^{.937}}$ | Babu Correlation [12] |

flow-rate conditions additional expansion in the emulsion is expected along with some of the increased amount of gas flowing through the emulsion, and CFD modeling is employed to characterize this complex dynamic.

This modeling approach has been applied with considerable success in modeling the gas-phase processes in fluidized bed natural gas combustion [68], VOC photodegredation in a fluidized bed reactor [8] and coal volatile combustion in a fluidized bed reactor [44]. In each of these modeling approaches simple hydrodynamic sub-models of bubble growth, and mass transfer between the bubble-phase and emulsion phase are employed to fully describe the bed geometry and flow characteristics. Here we use CFD simulation to calculate the necessary parameters.

In Figure 6-5 a simplified representation of this reactor model is shown. In order to fully describe this reactor network we need to first describe the geometry of each of the reactor zones. For the bed-zone the height of each of the Emulsion and Bubble reactors are given by the time-averaged bed height of the fluidized bed. Correlations are available for the bed expansion ratio, $H/H_{mf} = f(U_0/U_{mf}, U_{br}/U_{mf}, d_p/D, \rho_s/\rho_g)$, where H is the observed bed height and $H_{mf}$ is the expanded bed height at minimum fluidization velocity, $U_0$ is the inlet gas velocity and $U_{mf}$ is the inlet gas velocity at minimum fluidization and $U_{br}$ is the average bubble rise velocity for which correlations are available (see Kunii and Levenspiel [81]). Three common correlations are shown in Table 6.1.

In addition to the bed height, we need to calculate volumes of each of these reactor zones. Given the bed geometry and the calculated bed height, $H$, we know that the

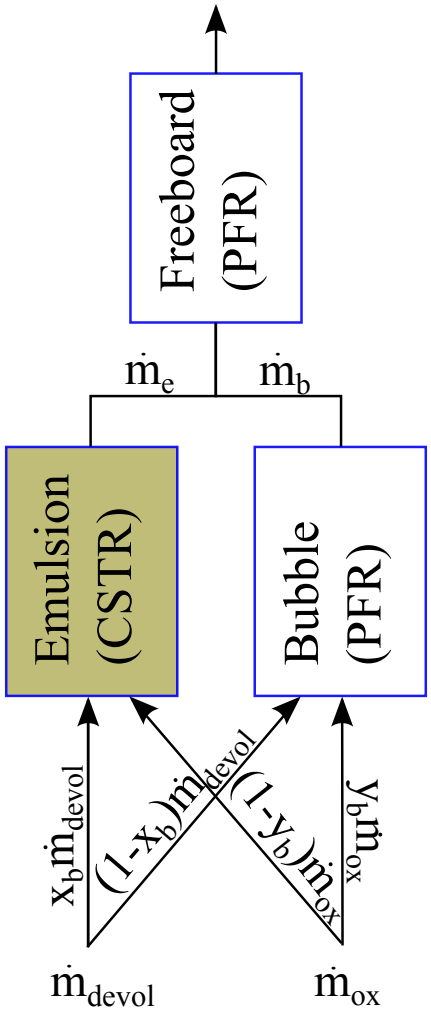


Figure 6-5: A simplified representation of the TFM RNM. By capturing the flow of devolatilization and oxidant gas through each reactor zone the overall influence of mixing on the chemical conversion pathways are more accurately captured. The variables employed to describe the flows are introduced and discussed in the text.

total gas bed volume is:

$$V_{bed}^{gas} = V_e^{gas} + V_b^{gas} = \epsilon_e V_e + \epsilon_b V_b = \epsilon_{bed} V_{bed} = \epsilon_{bed} H A_{bed}, \tag{6.2}$$

where $V_{bed}^{gas}$, $V_e^{gas}$ & $V_b^{gas}$ are the effective gas volumes of the bed, emulsion and bubble phases respectively. $V_{bed}$, $V_e$ & $V_b$ are the total bed, emulsion and bubble volumes respectively, and $A_{bed}$ is the cross-sectional area of the bed. The mean voidage over the bed is given by $\bar{\epsilon}_{bed}$. The emulsion phase has been reported to have a voidage approximately equal to that at minimum fluidization velocity [81] for non-reactive flows, however in this study will be calculated directly from CFD in order to capture any expansion occurring due to solids devolatilization. The bubble phase is assumed to be devoid of solids so we estimate $\epsilon_b \approx 1$, implying the bubble wake and cloud zone is considered as part of the emulsion phase. We then get the following linear system:

$$\frac{1}{V_{bed}} \begin{pmatrix} 1 & 1 \\ \epsilon_e & 1 \end{pmatrix} \begin{pmatrix} V_e \\ V_b \end{pmatrix} = \begin{pmatrix} 1 \\ \epsilon_{bed} \end{pmatrix}, \tag{6.3}$$

which can be solved for the reactor volumes given the emulsion voidage and average bed voidage and at the operating condition of interest.

For systems in which there is no devolatilization within the emulsion (Fischer-Tröpsch catalyst beds for example) this calculation can be somewhat simplified by assuming that the emulsion phase voidage is equal to the voidage at minimum fluidization. Tabulated data exists for the voidage at minimum fluidization conditions for a number of materials (see Table 6.2) or it can be experimentally determined or numerically with CFD. For round sand of $200 < d_p < 300$ this can be estimated to be $\epsilon_{mf} \approx 0.43$.

Finally, we need to solve for the mass fluxes of each of the devolatilization and the oxidant into the emulsion and bubble phases. Given the air-fuel ratio (A/F) and operating regime, we can calculate both the mass flow rates of the oxidant gas (air, steam, oxygen, etc) and the devolatilization gases from a particle model as was shown

Table 6.2: Voidage at minimum fluidization ($\epsilon_{mf}$) of various materials, reproduced from Kunii, 1991 [81].

| | Size, $d_p$(mm) | | | | | | |
|---|---|---|---|---|---|---|---|
| Particles | 0.02 | 0.05 | 0.07 | 0.10 | 0.20 | 0.30 | 0.40 |
| Sharp sand, $\phi_s = 0.67$ | - | 0.60 | 0.59 | 0.58 | 0.54 | 0.50 | 0.49 |
| Round sand, $\phi_s = 0.86$ | - | 0.56 | 0.52 | 0.48 | 0.44 | 0.42 | - |
| Mixed round sand | - | - | 0.42 | 0.42 | 0.41 | - | - |
| Coal and glass powder | 0.72 | 0.67 | 0.64 | 0.62 | 0.57 | 0.56 | - |
| Anthracite coal $\phi_s = 0.63$ | - | 0.62 | 0.61 | 0.60 | 0.56 | 0.53 | 0.51 |
| Absorption carbon | 0.74 | 0.72 | 0.71 | 0.69 | - | - | - |
| Fischer-Tröpsch catalyst, $\phi_s = 0.58$ | - | - | - | 0.58 | 0.56 | 0.55 | - |
| Carborundum | - | 0.61 | 0.59 | 0.56 | 0.48 | - | - |

in Chapter 4. Then we know from the conservation of mass that

$$\dot{m}_{devol} + \dot{m}_{ox} = \dot{m}_e + \dot{m}_b = \dot{m}_{tot}, \tag{6.4}$$

where $\dot{m}_i$ is the mass flow rate of the gases where the subscripts devol, ox, e and b are for the devolatilization gases, oxidant gases, the emulsion phase and the bubble phase respectively. Additionally, if we define $x_b$ and $y_b$ to be the fractions of the devolatilization gas and the oxidant gases to go to the bubble phase respectively, then we can write the following equations:

$$\dot{m}_e = (1 - x_b)\dot{m}_{devol} + (1 - y_b)\dot{m}_{ox}, \tag{6.5}$$

$$\dot{m}_b = x_b\dot{m}_{devol} + y_b\dot{m}_{ox}. \tag{6.6}$$

Since we know $\dot{m}_{devol}$ and $\dot{m}_{ox}$, we must find $x_b$ or $y_b$ and the rest will fall out naturally. Calculating these values turns out not be trivial, as information on the distribution of the devolatilizing particles, emulsion phase and bubble dynamics are required. In order to do this CFD studies will be used as outlined in section 6.4.

Given the reactor geometry and calculated bed height, H, the length and volume of the freeboard is calculated directly. Additionally, the gas properties needed to fully

calculate the residence time, the mass flow rate, $\dot{m}_f$, and the gas density, $\rho_g$, at the inlet of the freeboard are directly calculated from the exit of the bed-zone reactors.

## 6.4 CFD Modeling Framework

The hydrodynamic processes occurring within a fully reactive FBBG, including solid-solid gas-gas and gas-solid mixing, are intimately coupled with the thermal and chemical processes occurring in tandem. In order to model these interactions, fully reactive Computational Fluid Dynamic (CFD) modeling is employed. In this section the major sub-models employed - the Multi-Fluid Model and the chemical kinetic framework - are described.

### 6.4.1 Multi-Fluid Model

In these CFD simulations a multi-phase Eulerian framework is employed where the gas and solid phases are represented as interpenetrating continua. As such, the solid phases are governed by the Navier-Stokes equations with necessary closures describing the gas-solid and solid-solid interactions.

#### Continuity Equations

For a reacting system with $N_g$ gas-phase species, $M$ solid phases consisting of $N_{sm}$ chemical species in solid phase $m$, then the conservation equations for mass and momentum are solved for the gas and for each of the solid phases:
*Gas phase species conservation*

$$\frac{\partial}{\partial t}\left(\varepsilon_g \rho_g y_{gn}\right) + \nabla \cdot \left(\varepsilon_g \rho_g y_{gn} \mathbf{u}_g\right) = R_{gn}, \tag{6.7}$$

*Solid phase continuity*

$$\frac{\partial}{\partial t}\left(\varepsilon_m \rho_m y_{smn}\right) + \nabla \cdot \left(\varepsilon_m \rho_m y_{smn} \mathbf{u}_m\right) = R_{smn}, \tag{6.8}$$

*Gas phase momentum*

$$\frac{\partial}{\partial t}\left(\varepsilon_g \rho_g \mathbf{u}_g\right) + \nabla \cdot \left(\varepsilon_g \rho_g \mathbf{u}_g \mathbf{u}_g\right) = \nabla \cdot \bar{\bar{\tau}}_g - \varepsilon_g \nabla P_g + \varepsilon_g \rho_g \mathbf{g} - \mathbf{I}_{gm}, \tag{6.9}$$

*Solid phase momentum*

$$\frac{\partial}{\partial t}\left(\varepsilon_m \rho_m \mathbf{u}_m\right) + \nabla \cdot \left(\varepsilon_m \rho_m \mathbf{u}_m \mathbf{u}_m\right) = \nabla \cdot \bar{\bar{S}}_m - \varepsilon_m \nabla P_g + \varepsilon_m \rho_m \mathbf{g} + \mathbf{I}_{mm_2}, \tag{6.10}$$

where $\varepsilon$, $\rho$ $y$ and $u$ are the volume fraction, the density the mass fraction and the velocity of each phase and the subscripts g and m indicate the gas and the $m^{th}$ solid phase respectively (in the MFIX naming convetion $m = 0$ is employed in the intra-phase transfer terms to denote the gas phase). The subscript $n$ is the $n^{th}$ chemical species in the associated phase. $P_g$ is the gas pressure, $\mathbf{g}$ is the acceleration due to gravity, $\varepsilon_m \nabla P_g$ is the solid-phase buoyancy effect and $\mathbf{I}_{ml}$ is the inter-phase momentum exchange term between the phases m and $m_2$ ($m_2 = 0$ for gas); $\bar{\bar{\tau}}_g$ and $\bar{\bar{S}}_m$ are the gas and the solids stress tensors (for solid phase m) respectively. Finally, the source terms $R_{gn}$ and $R_{smn}$ are the rates of production of the $n^{th}$ species in the gas phase and the $m^{th}$ solid phase respectively.

Further details on these equations, including the closures and stress tensors can be found in previous work [13] and the publicly available MFIX theory documentation [135].

### Energy Equations

In multi-fluid reactive simulations both the gas and solid(s) temperatures must be solved simultaneously to accurately predict the local reaction rates. As such, both gas phase and solid phase energy conservation equations are employed which are coupled through inter-phase heat transfer terms:

*Gas Phase Energy Conservation*

$$\varepsilon_g \rho_g c_{pg} \left(\frac{\partial T_g}{\partial t} + \mathbf{u}_g \cdot \nabla T_g\right) = \nabla \cdot \left(\varepsilon_g k_g \nabla T_g\right) - H_{gm} - \Delta H_{rg}, \tag{6.11}$$

*Solid Phase Energy Conservation*

$$\varepsilon_{sm}\rho_{sm}c_{psm}\left(\frac{\partial T_{sm}}{\partial t}+\mathbf{u}_{sm}\cdot\nabla T_{sm}\right)=\nabla\cdot(\varepsilon_{sm}k_{sm}\nabla T_{sm})+H_{gm}-\Delta H_{rsm}, \quad (6.12)$$

where $c_{pg}$ and $c_{psm}$ are the specific heats of the gas phase and the $m^{th}$ solid phase respectively, $T_g$ is the temperature of the gas phase and $T_{sm}$ is the temperature of the $m^{th}$ solid phase. Heat transfer models are employed via conduction where $k_g$ and $k_{sm}$ are the material conductivities of the gas phase and the $m^{th}$ solid phase, $H_{gm}$ is the heat transfer from the gas to the $m^{th}$ solid phase, $\Delta H_{rg}$ is the total rate of heat release from reactions involving the gas phase, $\Delta H_{rsm}$ is the total rate of heat release from reactions involving the $m^{th}$ solid phase and $H_{wall}$ is a user-defined heat transfer coefficient for heat transfer from the wall to the gas.

For computational simplicity, MFIX assumes all solid phases except for the first one ($m \geq 2$) to be in thermal equilibrium, equation 6.12 then is solved independently for the first solid phase $m = 1$ and then solved using the average values of each additional solid phases $N_{sm} \geq m \geq 2$.

Of particular importance in accurately predicting the dynamics of chemical conversion of the solid fuel in the FBBG is the modeling of inter-phase heat transfer from the gas to the solid. Heat transfer between the gas phase and $m^{th}$ solid phase is:

$$H_{gm} = -\gamma_{gm}(T_{sm} - T_g), \quad (6.13)$$

where $\gamma_{gm}$ is the heat transfer coefficient between the fluid phase and the $m^{th}$ solid phase. Since the $2^{nd}$ to $N_{sm}^{th}$ solid phase are assumed to be in thermal equilibrium then the average of these heat transfer coefficients are used to solve for the transfer between the gas and the $2 - N_{sm}^{th}$ solid phase. This heat transfer coefficient is determined from $\gamma_{gm}^0$, the heat transfer coefficient in the absence of mass transfer defined as:

$$\gamma_{gm}^0 = \frac{6k_g\epsilon_{sm}Nu_m}{d_{pm}^2}, \quad (6.14)$$

where $Nu_m$ is the Nusselt Number for the $m^{th}$ solid phase, and $d_{pm}$ is the particle

diameter of the the $m^{th}$ solid phase. Given this, the total heat transfer coefficient $\gamma_{gm}$ is calculated to be:

$$\gamma_{gm} = \frac{C_{pg} R_{gm}}{e^{\left(\frac{C_{pg} R_{gm}}{\gamma^0_{gm}}\right)} - 1}, \tag{6.15}$$

where $R_{gm}$ is the rate of mass transfer from the gas phase to the $m^{th}$ solid phase. As developed in chapter 3, the Nusselt number correlation employed is from Gunn01978 [64]:

$$Nu_m = (7 - 10\epsilon_g + 5\epsilon_g^2)(1 + 0.7 Re_{mp}^{0.7} Pr^{\frac{1}{3}}) + (1.33 - 2.4\epsilon_g + 1.2\epsilon_g^2) Re_{mp}^{0.7} Pr^{\frac{1}{3}}, \tag{6.16}$$

where $Re_{mp}$ is the particle Reynolds number of the $m^{th}$ solid phase, and $Pr$ is the Prandlt number for the gas phase.

### 6.4.2 Chemistry Modeling

Due to the complexity of CFD simulations a premium is put on the application of a simple kinetic model with the ability to capture the major dynamics of conversion including drying and devolatilization of fuel particles of varying diameter, gas-phase reactions including secondary tar cracking and combustion reactions, and char gasification and combustion. In Table 6.3 the various reaction kinetics utilized in this work are highlighted, although most of the runs in this chapter utilize only the drying and devolatilization reactions (1)-(4) since they play the most imporant roles on the flow dynamics in the bed zone.

Simplified devolatilization models such as employed here are developed empirically using the data for specific biomasses under limited conditions. The devolatilization mechanism of di Blasi & Branca [40] was developed empirically for beech wood under fast (1000 K/min) heating rates ideal for fluidized bed conditions and exhibits the characteristically low char fraction predicted using the CRECK devolatilization model in the Lagrangian particle model developed in chapter 2 at gasification tem-

peratures (800-1000°$C$). Here, this kinetic model is utilized in the shrinking core modeling framework outlined in chapter 3. Due to the high sensitivity of the conversion dynamics to the fit parameter $x$ in the effective rate, $k_{eff} = 1/(\frac{1}{k_{kin}} + \frac{x}{k_{cond}})$ a functional fit, $x = f(T_r, U_0, ...)$, is not used but for each reactor condition considered the method outlined for solving for $x$ is used as a pre-processing step to solve for an exact value of $x$.

For fully-reactive CFD studies, the gas-phase conversion of the devolatilization gases must be captured as well as the oxidation and gasification reactions of the char. As previously noted for the devolatilization model, a premium is put on simplicity of these kinetic models for computational reasons. There are existing global gas-phase reaction mechanisms available which include global tar cracking as well as gas combustion reactions and have been employed in a number of previous modeling studies [35,59,142]. These reactions are tabulated ((5)-(9)) in Table 6.3. Additionally, three heterogeneous char combustion and gasification reactions, (10)-(12) in Table 6.3, have been identified. For fully reactive cases, the combustion reaction (12) adapted from Wurzenberger et al. and di Blasi & Branca [41, 141] purposefully neglects their reported conversion history term $(1 - X_C)^{1.2}$ where $X_C$ is the overall char remaining intended to capture diffusive effects, since in our Eulerian CFD framework this history is not accessible. It is likely inducing negligible error, however, since at the moderate operating temperatures employed in FBBGs the Thiele Modulus, or the ratio of the characteristic times of diffusion to reaction rate, can be estimated for char combustion at 1000K to be:

$$\phi^2 = \frac{kR_p^2 C_{\mathrm{O}_2,s}}{D_{O2}} \approx \frac{(3) \times (10^{-3})^2 \times 10^{-1}}{1.6 \times 10^{-4}} \approx 10^{-4} << 1. \tag{6.17}$$

Thus, it is expected that a kinetic model of char oxidation is sufficient.

It is not expected that perfect agreement with experiment will be possible with this reaction set due to its severely limited detail, however these reactions allow for qualitative understanding of the temporal and spatial distribution of the major conversion pathways of solid and gas-phase species, informing the development of RNM

Table 6.3: Devolatilization, Gas-Phase and Char Conversion mechanism employed for CFD studies.

| Reaction | Rate Expression | Source | Rxn. No. |
|---|---|---|---|
| *Devolatilization & Drying* | [1/s] | | |
| $\text{Biomass} \longrightarrow \cdot 3054\,H_2 + \cdot 1854\,CO + \cdot 1687\,CO_2 + \cdot 0671\,CH_4 + \cdot 2734\,H_2O$ | $4.379 \times 10^9 exp(-152700/RT)$ | [40] | (1) |
| $\text{Biomass} \longrightarrow 0.246\,\text{Tar}_1$ | $1.077 \times 10^{10} exp(-148000/RT)$ | [40] | (2) |
| $\text{Biomass} \longrightarrow 1.602\,\text{Char}$ | $3.269 \times 10^6 exp(-111700/RT)$ | [40] | (3) |
| $H_2O_{(l)} \longrightarrow H_2O_{(g)}$ | $5.13 \times 10^6 exp(-87900/RT)$ | [27, 142] | (4) |
| *Tar Cracking* | [1/s] | | |
| $\text{Tar}_1 \longrightarrow \cdot 22\,\text{Tar}_2 + 1.5709\,CO + \cdot 1970\,CO_2 + \cdot 4304\,CH_4 + \cdot 6704\,H_2$ | $2.30 \times 10^4 exp(-80000/RT)$ | [59] | (5) |
| *Gas-Phase Combustion Reactions* | $[mol/cm^3 s]$ | | |
| $CO + H_2O \longleftrightarrow H_2 + CO_2$ | $2.780 \times 10^6 exp(-1510/T)\,[[CO][H_2O] - [CO_2][H_2]/K_p(T)]$ | [59] | (6) |
| $2\,CO + O_2 \longrightarrow 2\,CO_2$ | $3.980 \times 10^(14) exp(-20119/T)[CO][O_2]^{.25}[H_2O]^{.5}$ | [59] | (7) |
| $2\,H_2 + O_2 \longrightarrow 2\,H_2O$ | $2.196 \times 10^{12} exp(-13127/T)[H_2][O_2]$ | [59] | (8) |
| $CH_4 + 2\,O_2 \longrightarrow CO_2 + 2\,H_2O$ | $5.16 \times 10^{13} T^{-1} exp(-15699/T)[CH_4][O_2]$ | [35] | (9) |
| *Heterogenous Char Reactions* | | | |
| $C + O_2 \longrightarrow CO_2$ | $1.5 \times 10^6 exp(-13078/T) p_{O_2}[C]$ | [41, 141] | (10) |
| $C + CO_2 \longrightarrow 2\,CO$ | $3.1 \times 10^6 exp(-215000/RT) p^{.38}_{CO_2}[C]$ | [16, 62] | (11) |
| $C + H_2O \longrightarrow CO + H_2$ | $2.6 \times 10^8 exp(-237000/RT) p^{.57}_{H_2O}[C]$ | [15, 62] | (12) |

models where accurate chemistry can be employed. In this chapter the influence of superficial gas velocity and particle diameter on the mixing conditions and, therefore, the construction of the improved RNM are studied using only the devolatilization chemistry and drying (rxns (1)-(4)) however in forthcoming work, fully reactive simulations are employed.

## 6.5 Numerical Method

In order to solve the above system of equations for FBBGs the open source code Multiphase Flow with Interphase eXchanges (MFIX) developed by the US Department of Energy at the National Energy Technology Laboratory (DOE-NETL) is used [135].

## 6.6 Results and Discussion

Two of the experimental reactors used as validation data in Chapter 4 are modeled using the reactive multi-fluid CFD framework detailed above utilizing only drying and devolatilization chemistry (reactions (1)-(4)) in order to probe the CSTR assumption for the bed zone and to propose an improved RNM representation. These particular reactors have been chosen due to the availability of many (though not all) details on the geometry and experimental set-up and run details (see Table 6.4). Each of these research reactors were operated with air as the oxidant, though Kurkela & Ståhlberg [70, 83] also use steam and a secondary air injection in the freeboard. Additionally, the Kurkela & Ståhlberg configuration offers other modifications of interest on the simple design of van Paasen & Kiel, namely it is operated at elevated pressure (4 bar) and has a bed diameter twice that of van Paasen & Kiel, allowing for observation of the impact of larger bed diameter on the overall solids-mixing.

The focus of these reactive FBBG experiments generally was on the impact of temperature and air-fuel ratio on the overall conversion of solid fuel and the resultant gaseous product distribution. Here, in addition to varying these parameters the impact of superficial gas velocity and fuel particle diameter on the conversion chemistry

Table 6.4: Summary of the experimental studies of air-blown FBBGs simulated with CFD.

| | | Kurkela & Ståhlberg [83] | van Paasen & Kiel [138] |
|---|---|---|---|
| Gasifier Specifications | Operating Regime | Bubbling bed | Bubbling - Slugging bed |
| | Bed Diameter [cm] | 15 | 7.4 |
| | Bed Height [cm] | 120 | 50 |
| | Free Board Diameter [cm] | 25 | 10.8 |
| | Freeboard Height [cm] | 230 | 60 |
| | Bed Material | Silica sand | Silica sand |
| | Bed Material size ($\mu$m) | 600 (mass averaged) | 250 |
| | Oxidant/Fluidizing Agent | Air & Steam | Air |
| Operating Conditions | Superficial Gas Velocity [m/s] | 0.6-1.2 | 0.38 |
| | Calculated Minimum Fluidization Velocity [m/s] | .1228 | .0253 |
| | Temperature Range [$C^{\circ}$] | 745 - 995 | 750 - 950 |
| | Air-Fuel ER | 0.25 - 0.4 | 0.25 - 0.26 |
| | Steam-Fuel ER | .08 - .34 | N/A |
| | Pressure (Bar) | 4 - 10 | 1 |
| | Secondary Air Feed at Freeboard | yes | no |
| Feedstock | Species | Pine wood, Peat & Coal | Beech wood, Willow wood and Cellulose |
| | Fuel Feedrate (kg/hr) | 40 | 1 |
| | Moisture (%wt delivered) | 6 - 11 | 10.2 |
| | Ultimate Analysis (%wt, daf) | C:50.2, H:6.1, O:43.4, N:0.1, S:0.00 | Beech: C:48.8, H:6.0, O:44.5, N:0.14, S:0.017, Cl:0.005<br>Willow: C:49.4, H:6.0, O:39.0, N:0.87, S:0.05, Cl:0.015 |

via the hydrodynamics and mixing is also studied.

In order to quantify the impact of gas bypassing and devolatilization gas mixing with the oxidant within the bed-zone, and to quantify the parameters necessary for the gas bypass RNM, a parametric CFD study has been undertaken for the van Paasen & Kiel reactor geometry with various feedstock and air flow rates, as summarized in Table 6.6. These flow conditions were selected to be able to explore both the bubbling regime closer to minimum fluidization velocity (Runs 1-4) and the slugging/turbulent regime representative of the experimental conditions reported (runs 5-7). As previously noted, the base case (Run 6, bolded) is operating well into a slugging regime. Both temperature (T=1073K) and the specified Air to Fuel Ratio (A/F=0.25) are held constant in order to investigate the effect of flow conditions on the conversion chemistry. Only biomass drying and devolatilization reactions are employed (Rxns (1)-(4)) in order to isolate these effects. The rest of the CFD modeling parameters are summarized in Table 6.5.

For each of these runs the resultant superficial gas velocity is calculated by considering both the contribution of the gas feed rate and the devolatilization gas from devolatilization, which happens throughout the bed. As such, the superficial gas velocities are estimates of the mean superficial gas velocity in the reactor, since it is increasing with height in the bed due to the devolatilization gas release.

### 6.6.1 Fuel particle segregation and the Devolatilization Zone

The timescale of mixing of the sand and fuel particles relative to the rate of drying and devolatilization dictates the overall distribution of fuel devolatilization within the reactor and is dependent on both the superficial gas velocity and the particle size (as will be discussed in detail in section 7.2). Here, the influence of total superficial gas velocity (inlet gas plus devolatilziation gas) on the location of devolatilization reactions is explored.

In Figure 6-6 the time-averaged concentration distribution of raw biomass in the van Paasen & Kiel bed [138] is plotted for each of the different superficial gas velocity operating points where $U_{mf}$ refers to the superficial gas velocity at minimum fluidiza-

Table 6.5: Summary of CFD simulation parameters for van Paasen & Kiel gas velocity parameteric study.

| | Parameter | Value(s) |
|---|---|---|
| Gasifier Specifications | Geometry | cylindrical |
| | Diameter [cm] | 7.4 |
| | Height [cm] | 178 |
| | Bed Material | Silica sand |
| | Bed Material Diameter [$\mu m$] | 250 |
| | Bed Material Density [$kg/m^3$] | 2500 |
| | Total Bed Material [kg] | 1 |
| | Biomass Feed Height [cm] | 10 |
| Operating Conditions | Temperature [$K$] | 1073 |
| | Air-Fuel ER [] | 0.25 |
| | Pressure [atm] | 1 |
| | Feedstock Species | Beech wood |
| | Fuel Feedrate [kg/hr] | variable (see Table 6.6) |
| | Feedstock Moisture [%wt] | 10.2 |
| | Air Feed Rate [kg/hr] | variable (see Table 6.6) |
| Simulation | Time [s] | 50 |
| | Time averaged span [s] | 20-50 |
| Initial Conditions | Bed Configuration | packed bed material at bottom |
| | Temperature | uniform |
| | Walls | Isothermal |
| Thermal Boundary Conditions | Distributor Plate (bottom) | Specified gas temperature (1073K) |
| | Biomass inlet | Speciefied biomass temperature (303K) |
| Chemistry Modeling | Heats of Reaction | 0 (isothermal assumption) |

Table 6.6: Superficial Gas velocity CFD parametric study for van Paasen & Kiel reactor [138]. The base-case (1 kilogram biomass per hour) is bolded. The total gas velocity is calculated by taking into account both the flow from the inlet as well as gas released from devolatilization.

| | Run 1 | Run 2 | Run 3 | Run 4 | Run 5 | **Run 6** | Run 7 |
|---|---|---|---|---|---|---|---|
| gas feed rate [kg/hr] | 0.1313 | 0.175 | 0.3500 | 0.6344 | 0.9516 | **1.2688** | 1.9031 |
| solids feed rate [kg/hr] | 0.1034 | 0.1379 | 0.2759 | 0.5 | 0.75 | **1** | 1.5 |
| Calculated total gas velocity [m/s] | 0.038 | 0.052 | 0.1 | 0.19 | 0.285 | **0.38** | 0.57 |
| Resultant $U_0/U_{mf}$ [] | 1.5 | 2 | 4 | 7.25 | 10.875 | **14.5** | 21.75 |
| Temperature [K] | 1073 | 1073 | 1073 | 1073 | 1073 | **1073** | 1073 |

tion. It is observed that due to the fast rate of drying and devolatilization relative to the mixing rates the overall concentration of raw biomass is concentrated heavily around the inlet. At increased gas velocity besides the high concentration at the inlet an increasingly dispersed amount of biomass is observed due to faster mixing. This is consistent with the predictions made in section 7.2 for the 1mm particles in this reactor.

In Figure 6-7 the time-averaged distribution of the gas release rate of biomass devolatilization is plotted. Here a trend can be observed with respect to superficial gas velocity rates. For the slowest flow conditions, $1.5U_{mf}$ it is observed that devolatilization occurs predominately above the inlet and at the surface of the bed zone, this is also true for $2U_{mf}$ although a small amount of devolatilization is observed below the feed. At these slow conditions the predominate dynamic is solid segregation due to the difference in particle density between the biomass and the sand. Since biomass' density is only one quarter that of the sand it quickly rises in these bubbling fluidized beds. Above $4U_{mf}$, however, this dynamic changes with the devolatilization zone observed below the inlet and with more radial penetration into the center of the bed with increasing superficial gas velocity. This indicates that at these increased flows there is likely significant solids velocity in the bed material down the walls that then entrain the biomass at the inlet down toward the distributor. When the flow is fast enough ($> 10U_{mf}$) it appears that the characteristic time of the biomass solids circulation is relatively faster than that of the devolatilization chemistry, which is constant due to the isothermal temperature inlet and walls (1073K), allowing for the

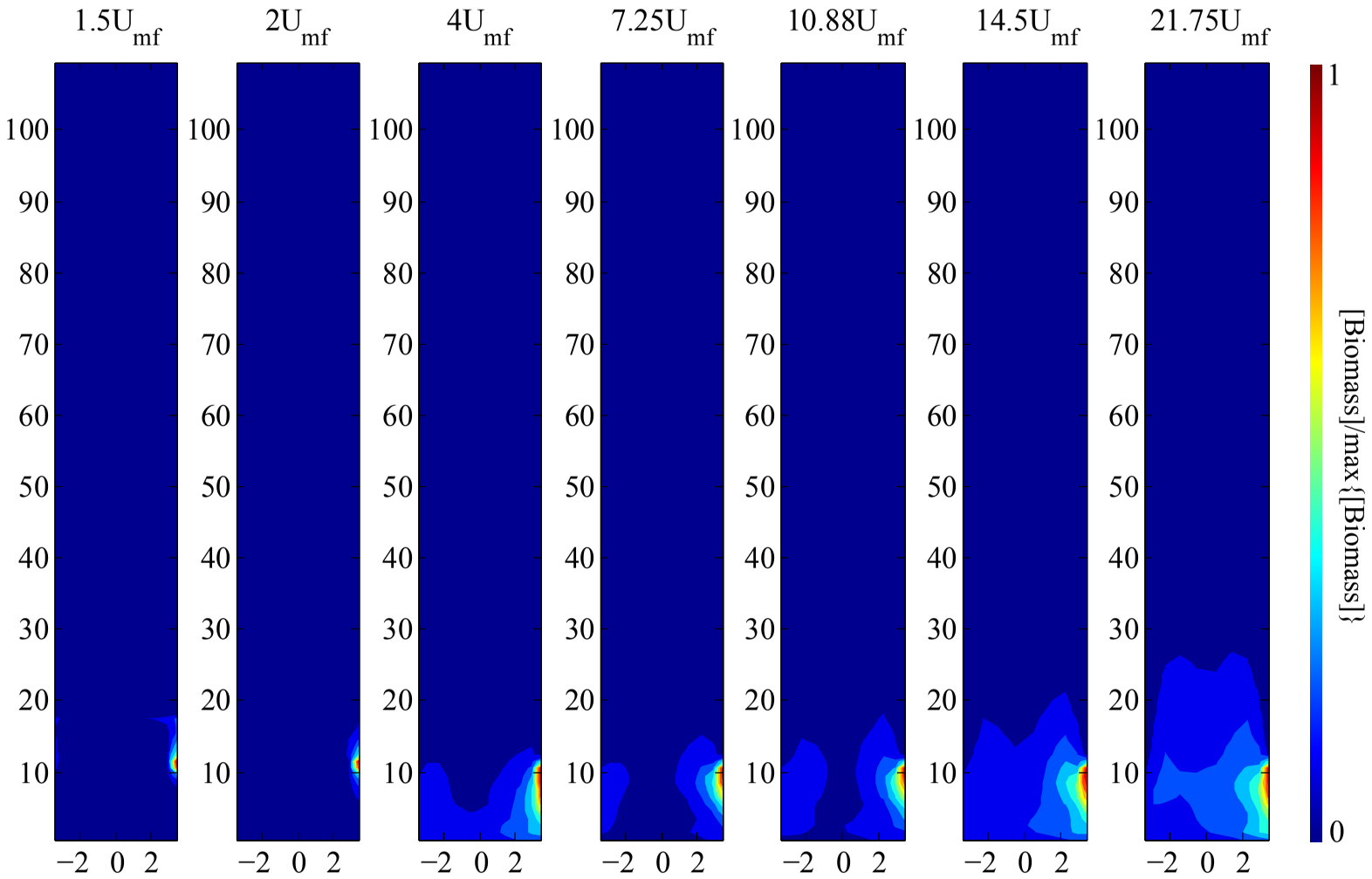


Figure 6-6: The time-averaged normalized ([bio]/max[bio]) raw biomass concentration distribution is plotted for multiple flow conditions as enumerated in Table 6.6. It is observed that under each of these flow conditions there is a strong localization around the inlet (10cm high on the right) with secondary distribution throughout the bed.

particles to then be entrained in the center of the bed and distributed throughout the reactor. Even at the fastest fluidization rate, however, it is observed that there is still a preferential devolatilization along the walls and near the inlet.

It is notable that there is strong correlation between the devolatilization reactions and the location of the emulsion. This manifests itself in the distribution of species in the gas phase. In Figure 6-8 the time-averaged spatial distributions of the normalized tar concentrations are plotted with respect to total superficial gas velocity. Here it is notable that there is a high degree of heterogeneity in the gas concentrations in the bed zone, with the preferential bubble pathway having a lean gas mixture and the emulsion exhibiting a rich mixture. At the lowest flow-rates the existence of strong devolatilization-zone segregation is apparent, while at increasing flow-rates the tendency of the formation of a torroidal emulsion and devolatilization zone on the walls becomes the dominant characteristic. This heterogeneity lends itself to the necessity to improve the gas-phase reactor model in order to capture the bypassing of gases through the central bubble channel in parallel to the toroidal emulsion zone.

### 6.6.2 Gas Flow and Bypassing in the Bed

#### Calculation and prediction of Bed Height

As developed in section 6.3 the bed height, $H$ is a crucial parameter for describing sub-reactors in the RNM framework. Due to the importance of this parameter a number of theoretical and empirical correlations exist. From reactive CFD data we calculate the bed height to be the axial point above which the time-average voidage of the cross section is always greater than .99. The time-averaged voidage of the reactor cross-sections can be calculated as a function of height above the distributor plate:

$$\bar{\epsilon}_g(z) = \int_0^{2\pi} \int_0^{D_b/2} \bar{\epsilon}_g(\mathbf{r}) r d\theta dr, \tag{6.18}$$

where $\bar{\epsilon}_g(z)$ is the cross-sectional and time-averaged voidage at the height $z$ above the bed, and $\bar{\epsilon}_g(\mathbf{r})$ is the time averaged voidage at the point $r = (r, \theta, z)$. Then we can define the bed height as the logical:

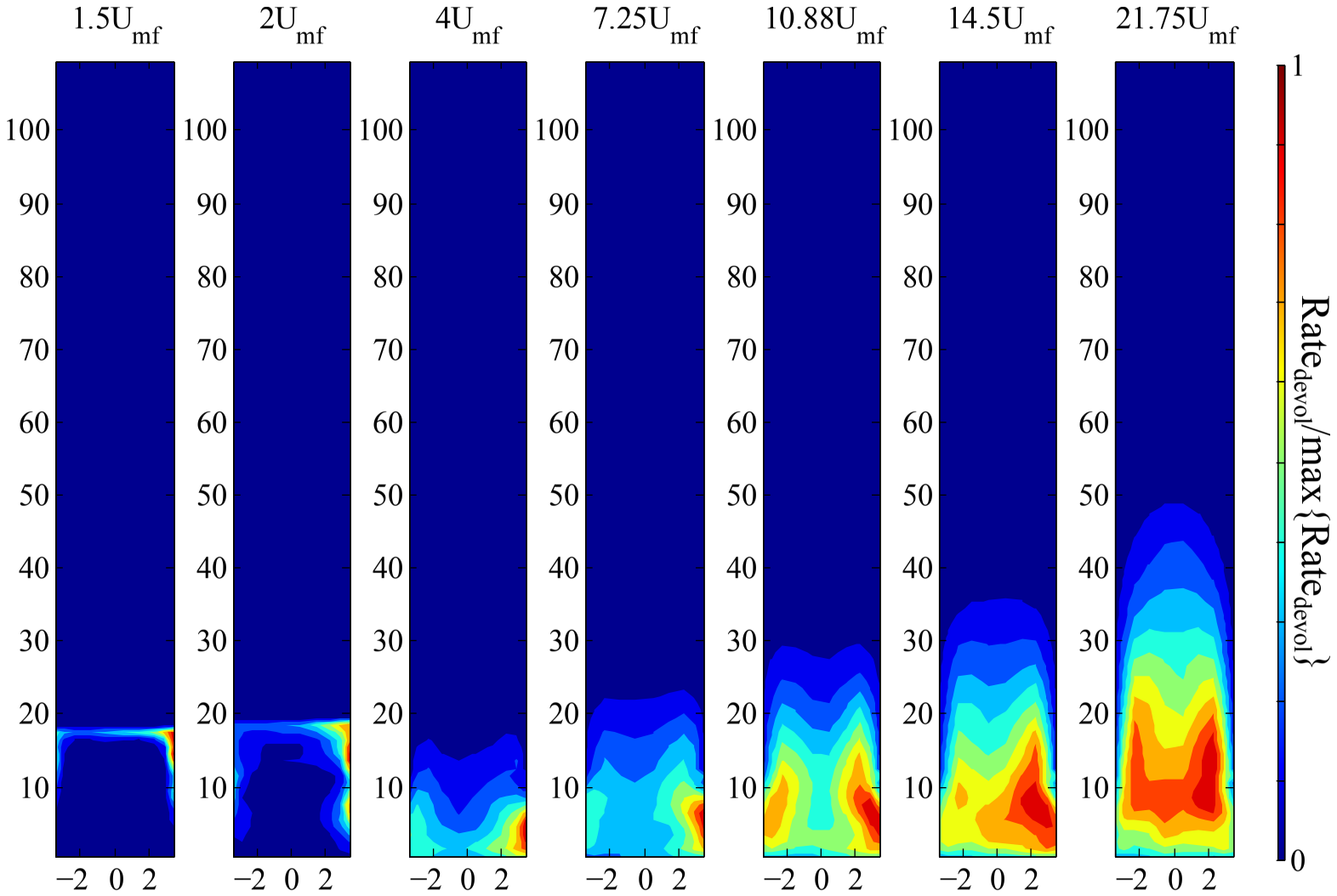


Figure 6-7: Contour plots of time-averaged sold-phase reactions are plotted for the base-case of van Paasen & Kiel (Run 6 in Table 6.6) [138]. The inlet is 10cm above the distributor on the right.

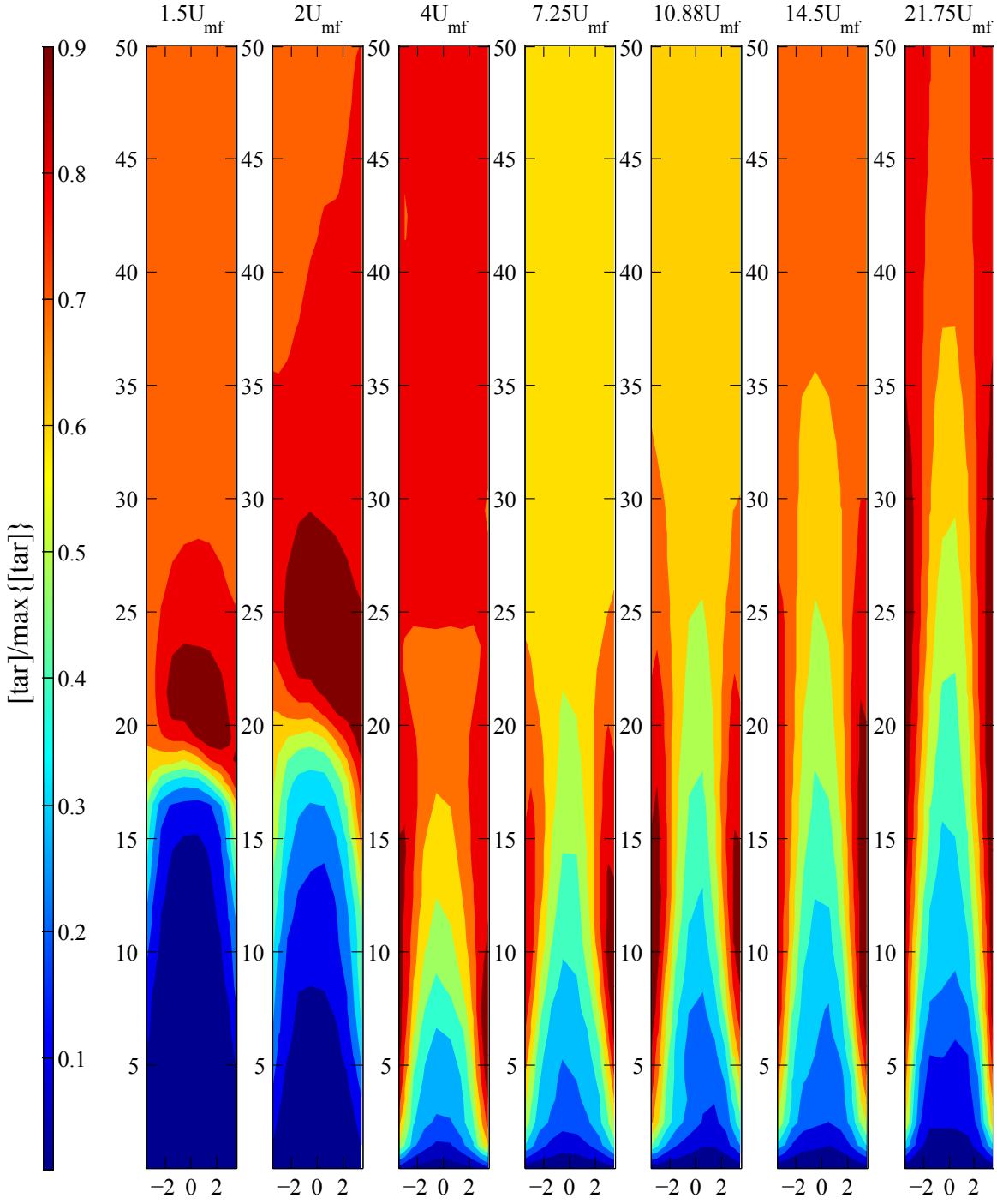


Figure 6-8: Influence of superficial gas velocity on the time-averaged spatial distribution of devolatilization tars in the lower half of the reactor.

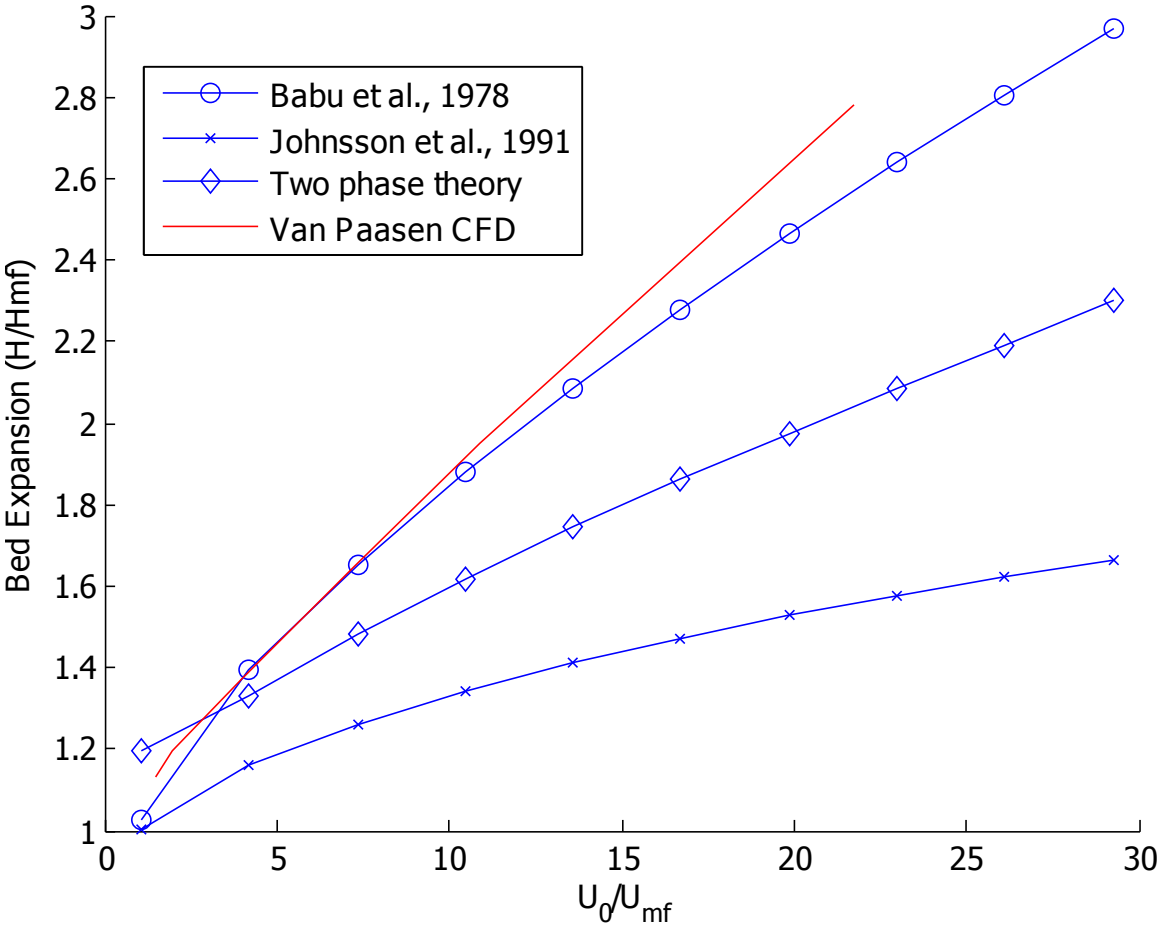


Figure 6-9: Theoretical (Two Phase Theory [33,34], Johnsson et al. [77]) and empirical (Babu [12]) correlations for the expansion of the van Paasen & Kiel [138] reactor geometry relative to superficial gas velocity are compared to reactive CFD results.

$$0.99 \leq \bar{\epsilon}_g(z)\big|_{z \geq H}\,, \tag{6.19}$$

is true.

In Figure 6-9 the time-averaged bed expansion calculated in the reactive CFD simulations of the van Paasen & Kiel bed are compared with three common expressions. The Two Phase Theory (TPT) [33,34] and Johnsson [77] predictions are theoretical in nature and were developed for non-reactive bubbling beds, as such we find that their predictions are highly divergent from CFD observation with increasing superficial gas velocity, where slugging begins to dominate. The correlation of Babu [12], based off experimental observation of a number of fluidized bed coal reactors, however, appears

to give good agreement with observed bed expansion.

### Emulsion and Bubble-Phase Volumes and Average Bed Voidages

In order to calculated the time averaged gas voidage of the entire bed, the function $\bar{\epsilon}_g(z)$ is again integrated from the distributor plate to the time-averaged bed height:

$$\epsilon_{bed} = \int_0^H \bar{\epsilon}_g(z)dz. \tag{6.20}$$

In order to calculate the total volumes of the emulsion- and bubble-phases in the bed, $V_e$ and $V_b$ respectively, using equation 6.3 we also need the voidage of the emulsion phase. In order to calculate this value, an instantaneous snapshot of the reactive CFD simulation (at t=20s) is employed in order to distinguish between the bubble and emulsion phases. A thresholding value for emulsion is employed where for voidage less than 0.8 it is considered to be the emulsion phase, and above 0.8 is considered to be a bubble. Then, the average voidage is calculated for the entire volume which is characterized as the emulsion phase.

The calculated emulsion voidage is plotted against a voidage threshold criterion in 6-10(a). Here it is observed that for increasing superficial gas velocity an increasing sensitivity of the calculated average voidage to the criteria is observed. This is physically reasonable, since this indicates that with increasing superficial gas velocity the transition between bubbles and the emulsion becomes smoother, signifying the increasing prevalence of a bubble cloud zone around bubbles of decreasing gas voidage to the emulsion. In Figure 6-10(b) the number of cells satisfying this criteria is plotted. Accordingly, it is noticeable that with increasing superficial gas velocity a discrete transition from the emulsion to the bubble is less prevalent, yielding to a more continuous transition from dense emulsion to a high gas-voidage emulsion cloud zone around the bubble to a bubble with significant amounts of entrained solids. Therefore, it is expected that with increasing superficial gas velocity there will be an increasing degree of sensitivity of the predicted voidage emulsion to the superficial gas velocity.

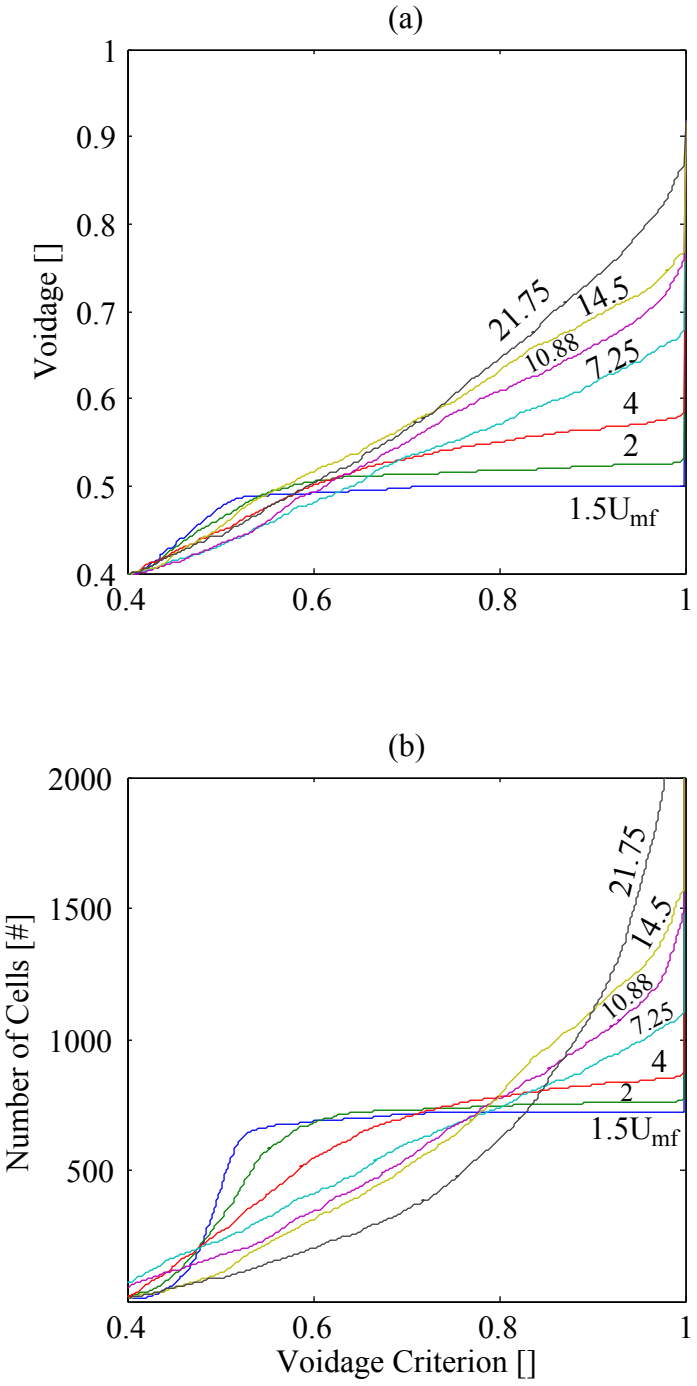


Figure 6-10: In (a) the average voidage of the emulsion phase calculated at an instantaneous snapshot of the reactive CFD (t=20s) of van Paasen & Kiel with respect to the Voidage threshold criterion. In (b) the number of cells satisfying this criterion are plotted.

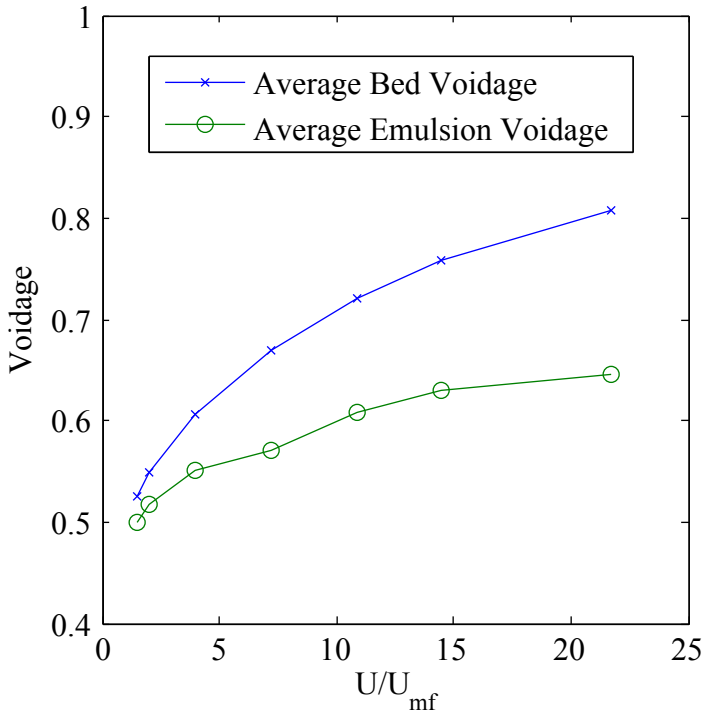


Figure 6-11: The average voidages over the entire bed and the emulsion are plotted with respect to superficial gas velocity operating conditions for the van Paasen reactor. The emulsion voidage is calculated as the average voidage of all cells with voidage less than or equal to 0.8.

In Figure 6-11 the average voidage over the bed, as calculated in Equation 6.20, and the average emulsion voidage, as described above, are plotted versus the superficial gas velocity. The increasing average bed voidage, and therefore gas content, is as expected due to the bed expansion with increasing superficial gas velocity. The increase in the emulsion gas content can be attributed to two main drivers. First, with increasing superficial gas velocity we also have increasing biomass feed-rates, as such there is more devolatilization occurring in the emulsion providing a uniform gas release. Additionally, as has been reported by Hilligardt and Werther [69] the flow-rate of gas through the emulsion is not constant with increasing superficial gas velocity as assumed in the origional TFT, but increasing, necessarily causing further expansion of the emulsion.

The difference between the average bed gas content and the emulsion gas content in Figure 6-11 is attributed to the increased volume of bubbles in the bed. Given this, we have sufficient information to calculate the total volumes of the emulsion and bubble-phase volumes $V_e$ and $V_b$ using equation 6.3.

### Flow through Emulsion and Bubble-Phase

The last parameters required for the RNM developed above is the division of flow of each of the devolatilization and oxidant gases through the emulsion- and bubble-phases. These are crucial to establish both of the residence times of the RNM reactors as well as the overall ratio of oxidant and devolatilization gases in each of the RNM reactor zones.

In Figure 6-12 azimuthal-averaged plots (see Figure 6-13) of the time-averaged voidage and gas velocity are shown for different inlet gas velocities. It is observed that there exists a toroidal emulsion zone around the walls of the bed, and that gas bypassing occurs through the center of the bed, where bubble coalescence occurs. As the inlet velocity increases bed expansion continues and a wider splashing zone is developed. Additionally, the emulsion phase is stretched higher along the walls as the inner bubble zone increases in radius. Due to the lower gas content, the drag and solids mixing in the emulsion (including flow down the wall) it is observed that the overall

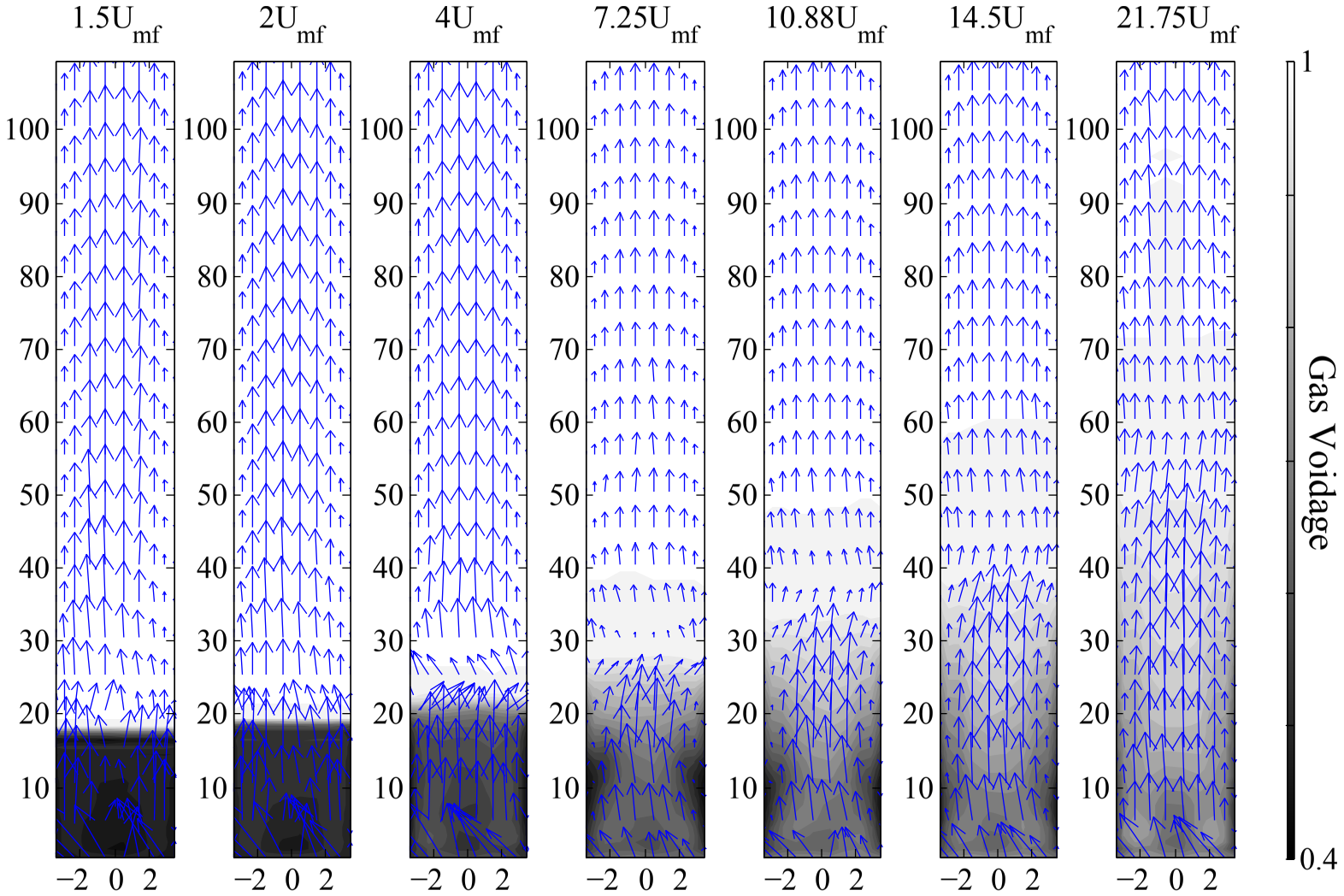


Figure 6-12: Time-averaged Velocity quiver plots are overlayed onto time-averaged voidage distributions for various superficial gas velocities in the van Paasen & Kiel [138] bed geometry.

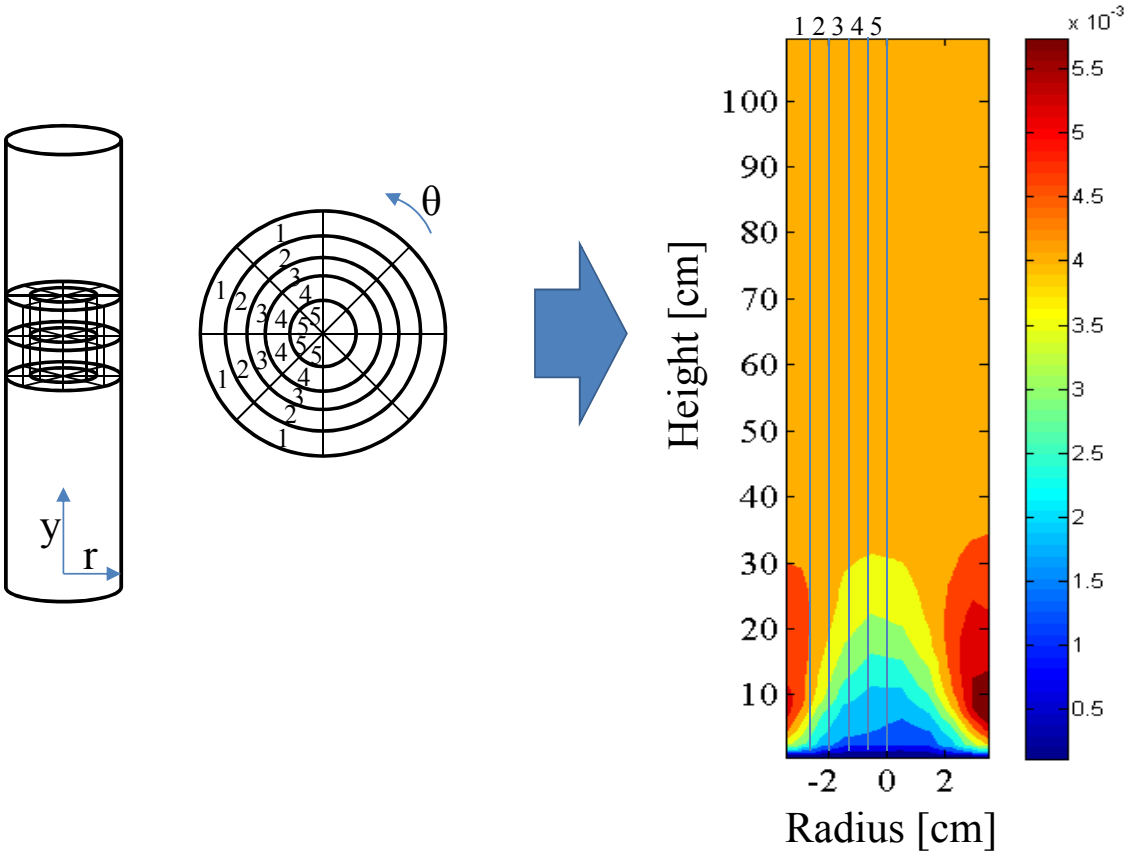


Figure 6-13: Visualization strategy for two dimensional azimuthal-averaged cylindrical bed plots. Each hemisphere is averaged at each cell radius.

upward gas mass-flux is lower through the emulsion zone relative to the preferential bubble path. In all cases, after the gas leaves the bed Hagen-Poiseuille flow is quickly established, characteristic of a plug flow reactor. Additionally, a transition to Hagen-Poiseuille flow is observed through the bed as the overall flow velocity increases to very high rates lending credence to the shift from a well-stirred bed to a plug flow dominated regime. At low superficial gas velocities (1.5 and $2U_{mf}$) it is observed that the gas preferentially travels through a preferential toroid, and the densest emulsion zones are found along the wall as well as in the center. Additionally, at very high velocity ($21.75U_{mf}$ again it is noted that the overall toroidal shape is breaking down and the gas recirculation downward along the wall is breaking down suggesting a decrease in overall bed mixing.

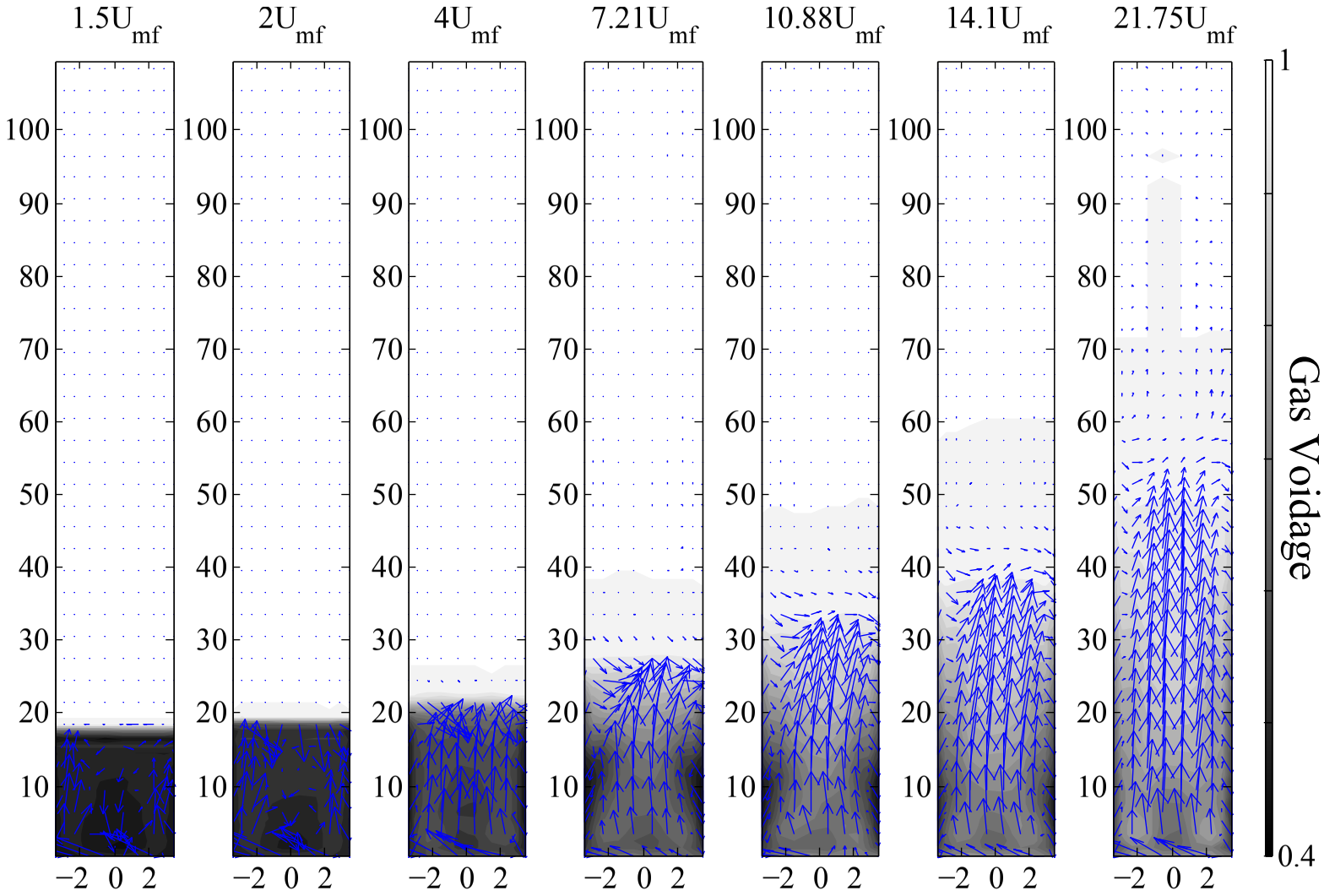


Figure 6-14: Time-averaged solids velocity quiver plots are overlayed onto time-averaged voidage distributions for various flow conditions in the van Paasen & Kiel bed geometry.

The calculated time-averaged solids velocities are plotted in Figure 6-14. Here we observe at the lowest two superficial gas velocities a similar velocity distribution mirroring the gas velocity distribution, where the solids are traveling upward through the preferential bubble path outside of the center, and then the solids recirculate downward through the middle of the bed. With increasing gas velocity it is observed that this trend inverts and the solids travel upward through the center of the bed, where the preferential bubble path is established and an outer recirculation zone is formed where the solids travel down the wall forcing strong gas-solid mixing within this emulsion zone. At the highest flow-rates it is observed that a large amount of entrainment is achieved and solids velocities are recorded at many places in the freeboard well above the calculated bed height. In cases from $4U_{mf}$ to $14.5U_{mf}$ a strong splashing zone is observed with fast time-averaged downward solids velocities and a recirculation in the direction of the solids inlet (to the right) it is clear that some degree of radial recirculation is being developed due to the inlet momentum below.

In order to calculate the division of the total gas flow through the emulsion- and bubble-phases we use the CFD simulation results in order to calculate the gas mass-flux weighted bed voidage with respect to bed height. This gass mass-flux weighted voidage then gives us information about the breakdown of flow through the emulsion- and bubble-phases. In Figure 6-15 both the average and mass-flux weighted bed voidages are plotted with respect to bed height. Here it is observed that as expected, with increasing superficial gas velocity the whole bed expands and the total splashing zone is extended at higher gas velocities, a clear transition from a well defined bed-freeboard interface for bubbling beds (1.5-$4U_{mf}$) is notable as the gas flowrate increases in observed. In (b) the average axial mass-flux weighted voidages are plotted versus reactor height. Here it is notable that the effective voidages are shifted up at all heights, particularly for faster flowrates ($4U_{mf}$ and above) where a significant amount of flow is through the bubble bath. The mass-flux weighted bed voidage can be used to quantify the breakdown of flow through the emulsion and bubble phase through the bed since it is essentially a metric of the effective voidage

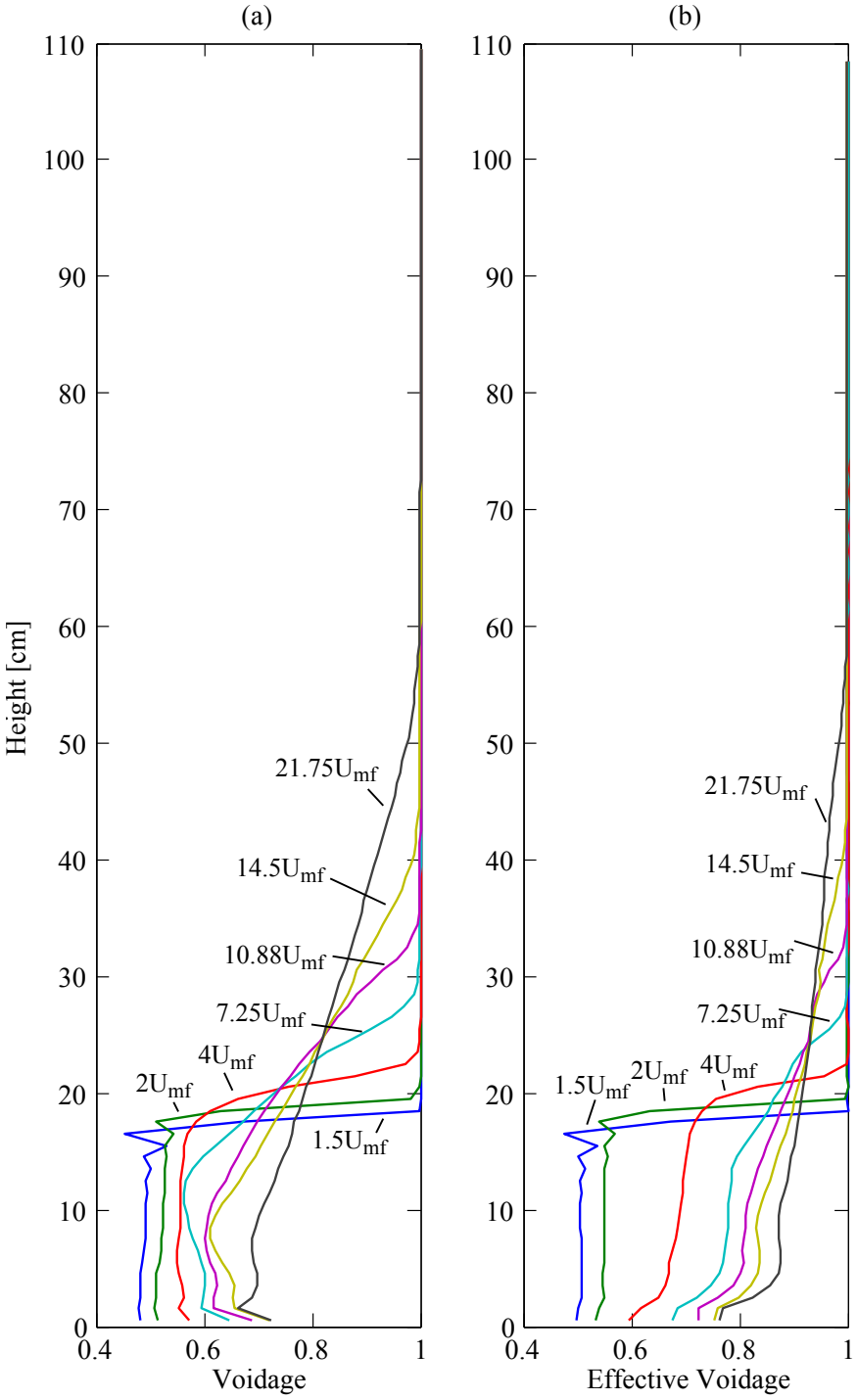


Figure 6-15: In (a) the average bed voidage versus bed height plotted for the van Paasen & Kiel reactive CFD under different flow regimes. The Average Axial Mass-Flux weighted voidage is plotted in (b) on the right.

experienced by the total mass flux through the bed. In the axial direction this is defined as:

$$\bar{\epsilon}_{g,\mathbf{m}}(z) = \frac{\int_0^{2\pi}\int_0^{D_b/2} \rho_g(\mathbf{r})\mathbf{V}_g((r))\bar{\epsilon}_g(\mathbf{r}) r d\theta dr}{\int_0^{2\pi}\int_0^{D_b/2} \rho_g(\mathbf{r})\mathbf{V}_g((r)) r d\theta dr}, \tag{6.21}$$

where $\bar{\epsilon}_{g,\dot{\mathbf{m}}}(z)$ is the mass weighted average bed voidage at height $z$ above the distributor plate, $\rho_g(\mathbf{r})$ is the local gas density, and $\mathbf{V}(\mathbf{r})$ is the local gas velocity in the axial direction. This can again be integrated over the bed height,

$$\epsilon_{bed,\dot{\mathbf{m}}} = \int_0^H \bar{\epsilon}_{g,\mathbf{m}}(z) dz, \tag{6.22}$$

yielding the mass-flux averaged bed voidage. This then, can be used to solve for the mass flows through the emulsion and bubble phase with the following linear system:

$$\frac{1}{\dot{m}_{tot}} \begin{pmatrix} 1 & 1 \\ \epsilon_e & 1 \end{pmatrix} \begin{pmatrix} \dot{m}_e \\ \dot{m}_b \end{pmatrix} = \begin{pmatrix} 1 \\ \epsilon_{bed,\dot{\mathbf{m}}} \end{pmatrix}. \tag{6.23}$$

In order to solve for the distribution of devolatilization gas between the emulsion and bubble-phase a similar metric can be employed to the mass flux of one of the chemical compounds present in the devolatilization gas flow. Here the concentration of primary tars, $\mathrm{tar}_1$, is used, however ideally, a non-reactive species is employed, such as argon, which is allowed to be released during devolatilization in minute quantities (i.e. argon yields on the order of $10^{-6}$kg/kg suffices) which can track with the reacting gases. Here, since no secondary gas-phase chemistry is employed in this study we use directly the devolatilization gases.

$$\bar{\epsilon}_{g,\mathbf{m},\mathrm{tar}_1}(z) = \frac{\int_0^{2\pi}\int_0^{D_b/2} y_{\mathrm{tar}_1}\rho_g(\mathbf{r})\mathbf{V}((r))\bar{\epsilon}_g(\mathbf{r}) r d\theta dr}{\int_0^{2\pi}\int_0^{D_b/2} y_{\mathrm{tar}_1}\rho_g(\mathbf{r})\mathbf{V}((r)) r d\theta dr}, \tag{6.24}$$

where $y_{\mathrm{tar}_1}$ is the mass fraction of $\mathrm{tar}_1$ (or any tracer species). As before this weighted voidage can be integrated as a function of bed height, yielding the effective voidage experienced by the devolatilization gas:

$$\epsilon_{bed,\dot{\mathbf{m}},\mathrm{tar}_1} = \int_0^H \bar{\epsilon}_{g,\mathbf{m},\mathrm{tari}}(z)dz. \tag{6.25}$$

Finally, this tar-mass-flux weighted bed voidage can be used to solve for $x_e$ and $x_b$ the fraction of devolatilization gas traveling through the emulsion and bubble phases respectively by solving the following system:

$$\frac{1}{\dot{m}_{devol}} \begin{pmatrix} 1 & 1 \\ \epsilon_e & 1 \end{pmatrix} \begin{pmatrix} x_e \\ x_b \end{pmatrix} = \begin{pmatrix} 1 \\ \epsilon_{bed,\dot{\mathbf{m}},\mathrm{tar}_1} \end{pmatrix}. \tag{6.26}$$

Now we can solve for the total RNM system given spatially resolved voidage, density, velocity and concentration data from CFD. The calculated values for each of the averaged bed voidages are plotted in Figure 6-16. At each superficial gas velocity the trend of $\epsilon_{bed,\dot{\mathbf{m}}} > \epsilon_{bed,\dot{\mathbf{m}},\mathrm{tar}_1} > \epsilon_{bed}$ makes intuitive sense since it is expected that the total mass flux of gases preferentially travels through a high voidage zone of the bed, which has a higher voidage than the bed on average, and the tars formed predominately in the emulsion, so $\epsilon_{bed,\dot{\mathbf{m}},\mathrm{tar}_1}$ is necessarily lower than $\epsilon_{bed,\dot{\mathbf{m}}}$. Also, as expected, in all cases the total voidage is going up due to bed expansion.

## 6.7 Predictions of Improved RNM

By using the methodology outlined in the previous section we can post-process CFD simulations to build a RNM able to capture more complex bed mixing dynamics. In order to explore the influence of the total superficial gas velocity on the RNM parameters we explore the influence of the variable flow conditions outlined in Table 6.6. Additionally, given the calculated RNM geometries under hot reactive conditions we also explore the influence of variable temperature at each flow condition by varying the bed temperature from 973K to 1273K in 50K increments.

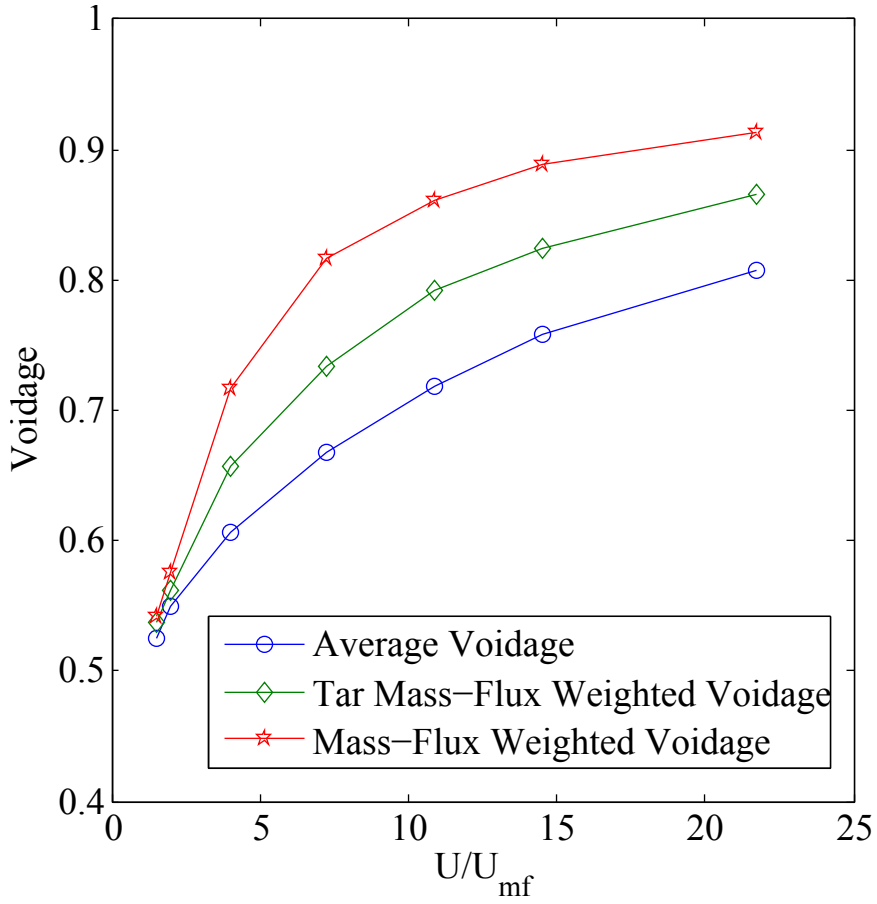


Figure 6-16: Calculated average ($\epsilon_{bed}$), tar-flux weighted ($\epsilon_{bed,\dot{\mathbf{m}},\mathrm{tar}_1}$) and total gas-flux weighted bed voidages ($\epsilon_{bed,\dot{\mathbf{m}}}$) versus superficial gas velocity.

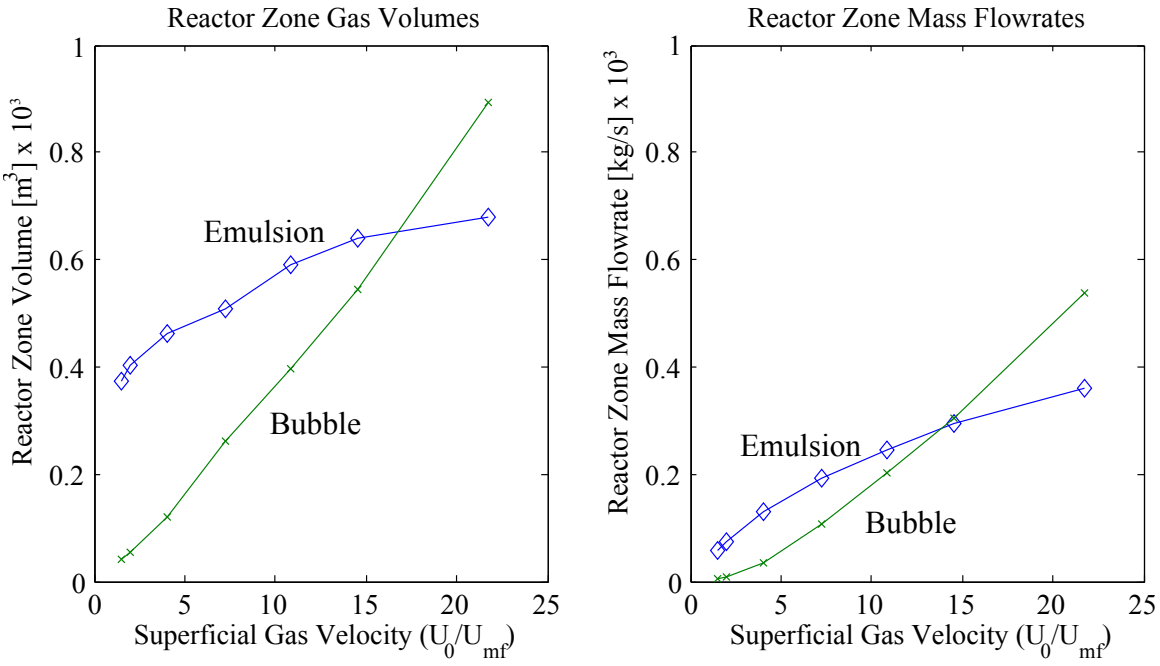


Figure 6-17: The predicted emulsion and bubble-phase gas volumes (left) and mass flow-rates of gases through these zones (right) are plotted with respect to superficial gas velocity.

### 6.7.1 RNM Geometry and Flow Characteristics

In Figure 6-17 the calculated bed geometry and flow characteristics are plotted with respect to the varied superficial gas velocity. The emulsion phase zone volume is observed to be increasing more slowly than the bubble zone indicating that, while there is increasing flow through the emulsion phase with increasing velocity, the majority of this gas instead travels through the bubble phase. This is corroborated in the right plot where it is observed that with increasing superficial gas velocity the amount of flow through the bubble phase is found to be increasing faster than that through the emulsion phase. This has been shown to be the case experimentally with an estimated $\frac{1}{3}$ of the excess gas flow found to travel through the emulsion [69, 81]. Above $14U_{mf}$ it is observed that more than 50% of the total flow is through the bubble phase, and above $17U_{mf}$ the volume of the bubble phase is found to be more than 50% of the total bed volume.

Increasing superficial gas velocity directly impacts the distribution of devolatilization and oxidant gases in the bed zone. In Figure 6-18 the calculated mass fractions

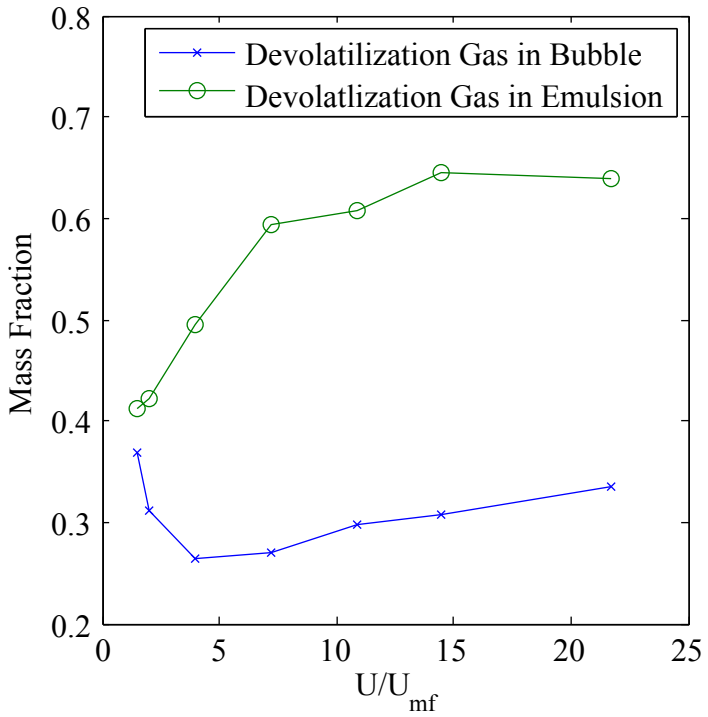


Figure 6-18: The mass fraction of the devolatilization gas is plotted for each bed zone versus the superficial gas velocity.

devolatilization gas in each reactor zone is plotted versus the operating superficial gas velocity. With higher superficial gas velocity it is observed that an increasing degree of gas segregation occurs, resulting in richer conditions in the emulsion phase than in the bubble phase. The effect is very pronounced at lower superficial gas velocities with the leanest bubble conditions occurring at $4U_{mf}$. This is likely due to the transition from exterior bubble paths close to the devolatilization zone at lower superficial gas velocities to a central preferential bubble path at $4U_{mf}$. As the superficial gas velocity increases the solids mixing rate continues to increases and devolatilization happens more uniformly improving the distribution of devolatilization gases.

Given the geometric and mass flow configurations shown in Figure 6-17 the influence of varying temperatures at each of these flow conditions on the residence times in the bed and freeboard zone is considered. In Figure 6-19 these residence times are plotted as contours for varying bed temperatures and inlet flow conditions. At low flow rates it is observed that the temperature has a very small effect on both the bed and freeboard residence times, which are much more sensitive to the flowrate

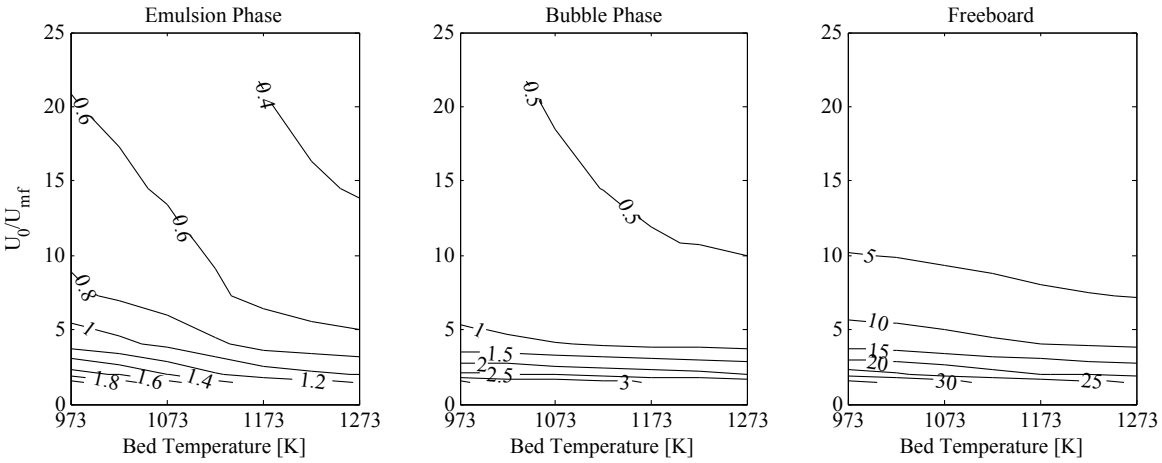


Figure 6-19: Calculated gas residence times in the bed and freeboard sections of the reactor are plotted as contours of both the bed temperature and flow conditions.

at this low regime (since the residence time scales as $1/U_0$), however at larger flow rates where the influence of the flow-rate decreases it is observed that with increasing temperatures the influence on the residence times is lessened. This is due to two effects. First is that of the lower gas density at higher temperatures, second, especially in the bed zone, is the increased gas expansion due to primary tar and hydrocarbon cracking to lighter gases, thus increasing the total molar flow rate.

### 6.7.2 Comparison of RNM predictions for van Paasen results

In order to assess the impact of capturing devolatilization/oxidant mixing in the bed-zone on the overall reactor conversion the reactor predictions from Chapter 4 are compared to the modified reactor predictions here for the base case (case 6). In Figure 6-20 the tar-class predictions for the simple RNM and the improved RNM are compared with the experimental data from van Paasen and Kiel. It is notable that the predictions of Class 2 and 3 tars are differ only slightly between the RNM and improved RNM. This is as expected since their oxidation and steam reforming reaction kinetics are relatively fast at these operating temperatures, while in the class 3 tar prediction it is notable that benzene is still rather recalcitrant, though slightly higher class 3 tars predicted implying a more favorable environment in the emulsion for their formation. Importantly, it is observed that the predictions of PAH

compounds, Class 4 and Class 5 tars are increased at each temperature, and at the lowest temperatures by an order of magnitude where their formation kinetics are very slow. This is indicative that capturing the heterogeneous gas distribution within the bed zone is crucial in order to predict PAH formation and growth. It is notable that the predictions are still 1-2 orders of magnitude short of the recorded experimental measurements. This could still be because the emulsion phase is assumed to be well-distributed and that devolatilization occurs throughout the emulsion in this model. As demonstrated in Section 6.6.1 devolatilization rarely occurs this uniformly and there likely exists very rich zones where devolatilization gas concentrations are near pyrolysis conditions allowing for free formation of PAH compounds. In order to capture this the bed zone likely needs to be further subdivided in order to capture the richest areas. This possibility is further considered in Chapter 7.

The predictions of major gas species are also affected. In Figure 6-21 the predicted concentrations of major gas species are plotted for the base case reactor conditions. It is observed that the predictions of Hydrogen and Carbon Monoxide are slightly affected at lower temperatures. The divergence is larger for water and carbon dioxide. With increasing temperature each of the predictions converge. This convergence is likely due to the faster kinetics at higher temperatures, so the resultant gases from the bed-zone, when well-mixed in the freeboard, are able to more quickly approach the global equilibrium values. Interestingly the methane concentrations are slightly lower at each temperature. This is due to the increased amount of oxygen available in the freeboard zone due to bypassing in the bubble phase. Early on the methane is then oxidized (along with other hydrocarbons and light tar compounds) this is likely directly contributing to the increased predicted concentrations of water and CO.

While improved predictions of PAH formation are observed by including this improved bed model capturing oxidant bypassing in the bubble-phase, further investigation of these effects is undertaken in the next section (Section 6.7.3) in order to quantify the effects of mixing on the chemical conversion.

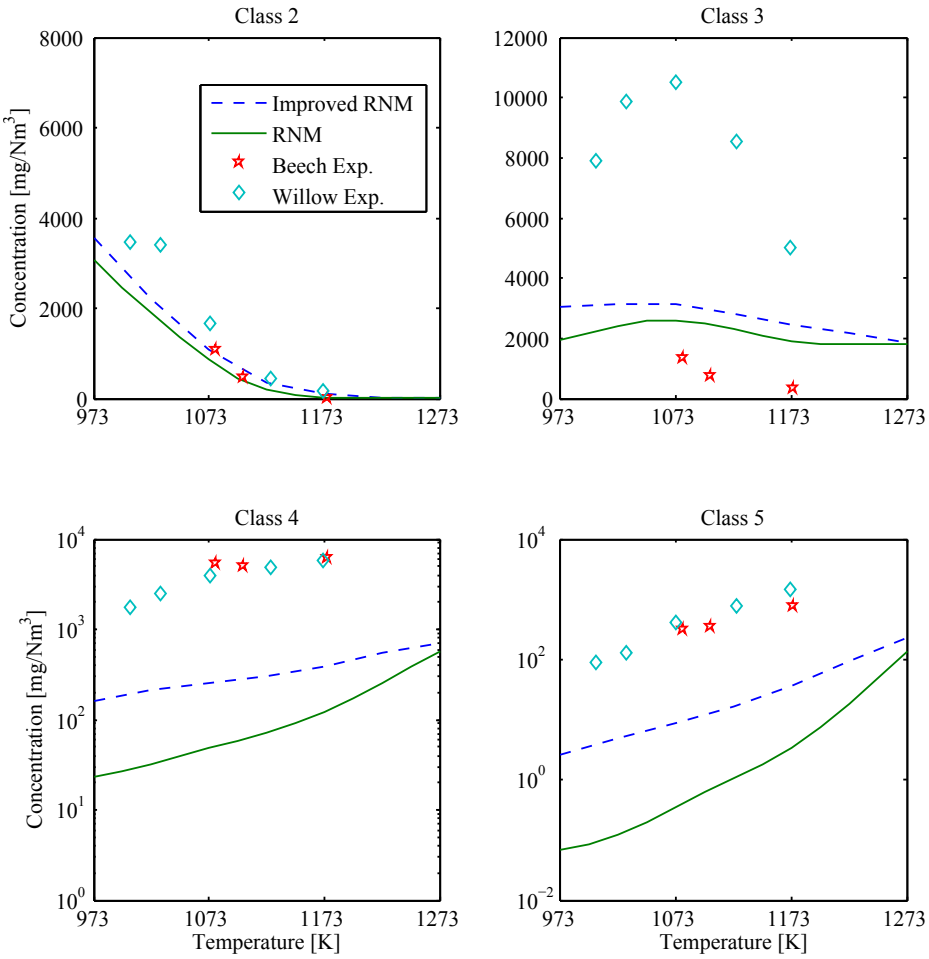


Figure 6-20: Influence of mixing on tar species prediction for the van Paasen & Kiel reactor under reactor conditions ER=0.25, $U_0 = 14.5U_{mf}$.

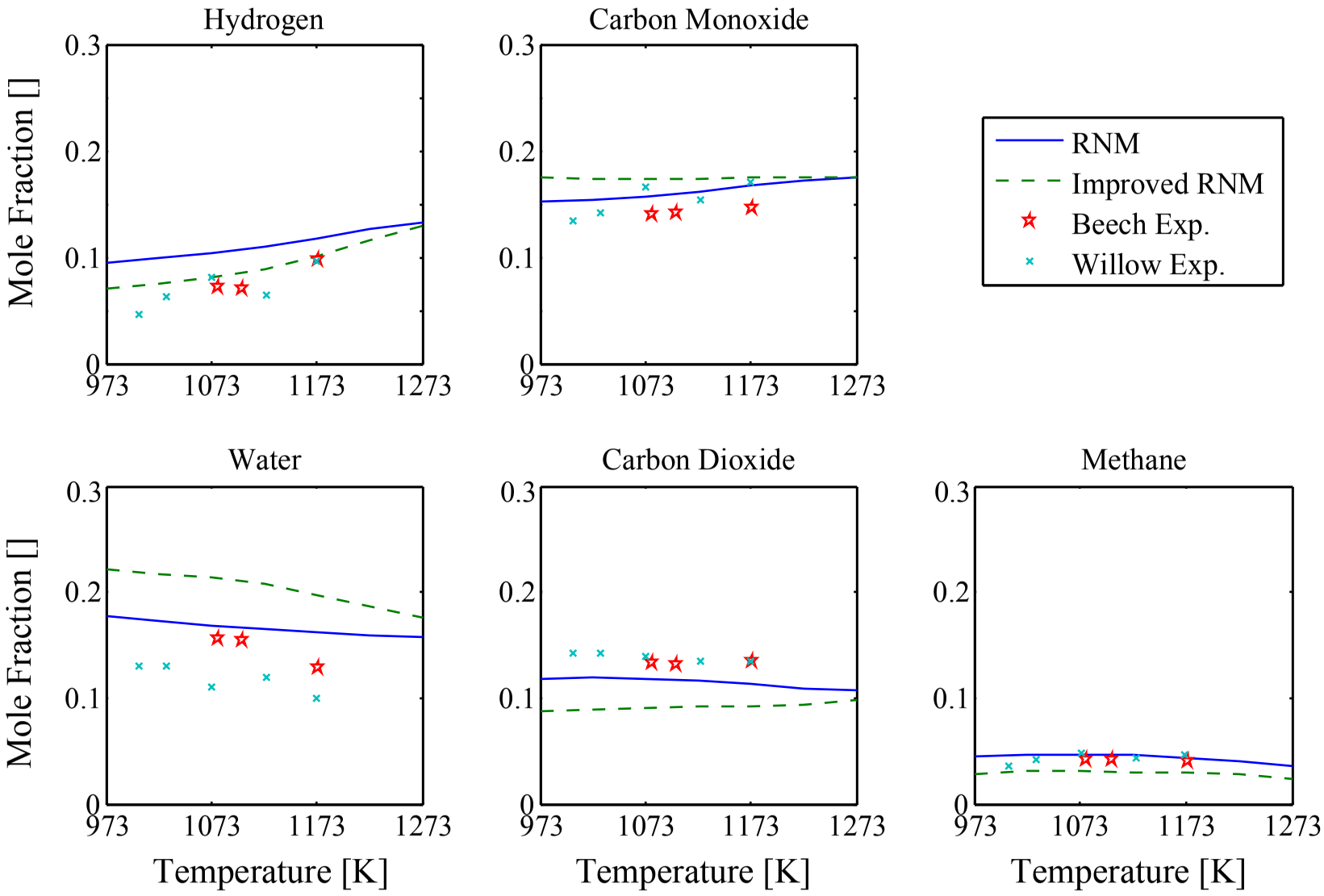


Figure 6-21: Comparison of RNM configuration major species predictions. van Paasen & Kiel reactor conditions ER=0.25, $U_0 = 14.5U_{mf}$.

### 6.7.3 Influence of devolatilization gas and oxidant distribution in the bed on chemistry

Fluidized bed reactors are employed due to their ability to create a large degree of mixing and contact within the bed-zone between the solid phases, the gas and the solid phases as well as within the gas-phase. This is particularly important in FBBG operation since the availability of oxygen plays an important role as to whether primary devolatilization tars are oxidized to smaller target gasses such as CO and $H_2$ or react with other aromatic compounds and unsaturated hydrocarbons and grow into PAHs.

As discussed in section 6.6.1, the solid reactions, in particular drying and devolatilization, occur within the emulsion phase and under these operating conditions this zone is highly concentrated near the fuel inlet. As such, if there is significant gas-bypass through the bubble phase as quantified by the devolatilization gas mass fraction in Figure 6-18, these devolatilization zones operate at relatively rich conditions with air-to-fuel ratios well below the set operating condition (i.e. in a reactor where the global A/F is set to 0.25 these zones could operate at conditions $<<0.25$). Under these extremely rich conditions in the emulsion phase it is expected that PAH growth would occur more freely in the emulsion, increasing the average tar molecular weight and shifting the speciation of the tar up to larger PAHs. Due to the recalcitrance of these species, once they have been formed then they are not likely to be cracked and oxidized in the bed or freeboard zone.

In Figure 6-22 two devolatilization gas and oxidant mixing extremes are compared. At one extreme (blue lines) the devolatilization gas is assumed to be releases solely into the emulsion (the CSTR). Then the gas bypassing in the bubble is comprised solely of the oxidant, and the remainder of the flow through the emulsion. At the other extreme (green lines) the devolatilization gas and the oxidant are assumed to be uniformly mixed at the inlet both to the emulsion (the CSTR) and the bubble phase (PFR). At the inlet to the freeboard (the exit of the bed, solid lines) it is observed that there are very different concentration profiles dependent on these mixing

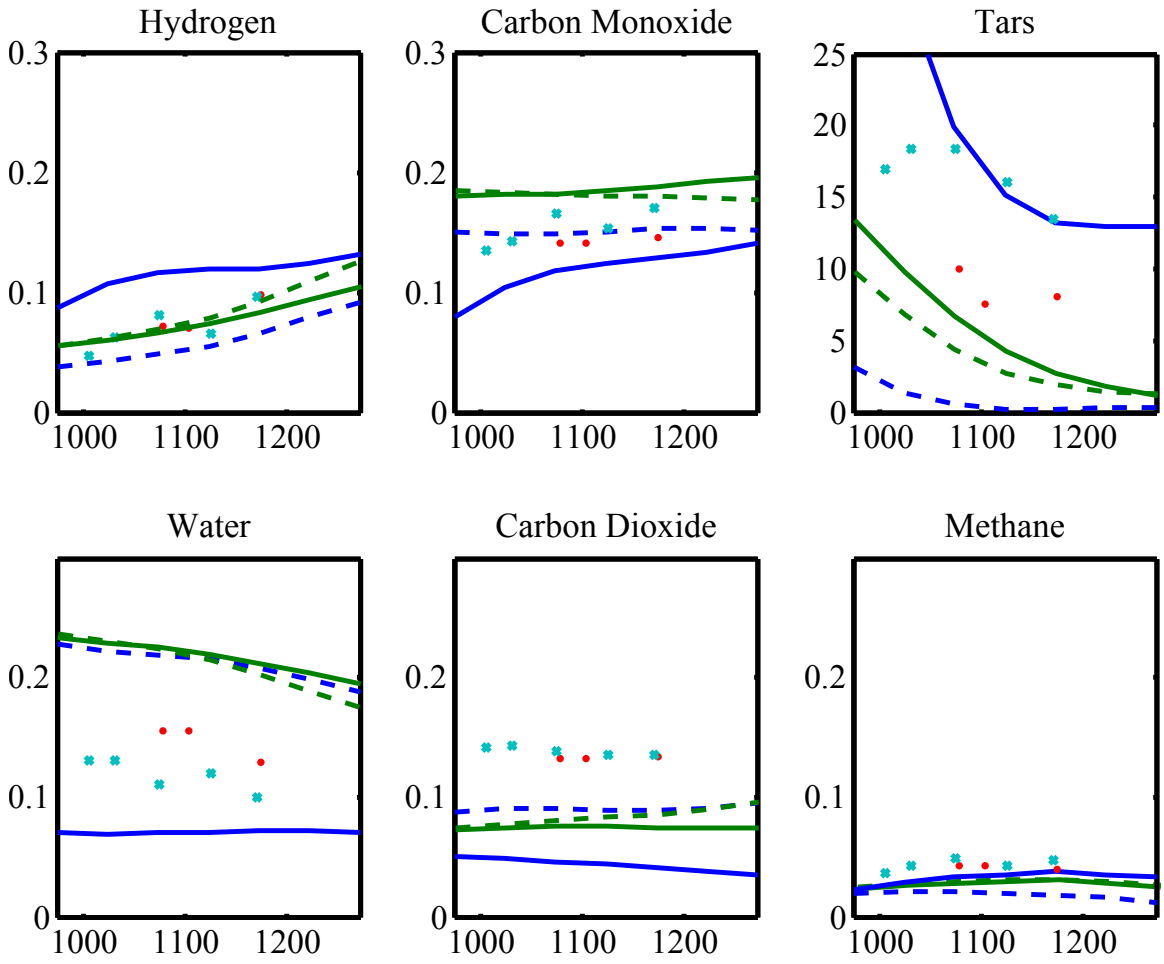


Figure 6-22: Major gas species (mole fraction) and total tars ($g/Nm^3$) are plotted with respect to temperature for the base van Paasen case (Run 6 in Table 6.6). The solid lines are the species concentrations at the exit of bed entering the freeboard, and the dashed lines are the predicted species concentrations at the exit. The green lines are where the devolatilization gases and oxidants are distributed evenly through the emulsion and the bubble reactor, while the blue lines are for the case where the devolatilization gases are assumed to be released solely in the emulsion phase.

assumptions. In particular the influence on the amount of tar entering the freeboard is readily apparent, where devolatilization gasses are released solely in the emulsion it is observed that due to lack of oxygen much more primary tars are evolved and enter the freeboard than when oxygen is present.

Interestingly, however, when the exit of the freeboard is considered (dashed lines) there are more total tars predicted under the uniformly mixed conditions than under the poorly mixed condition. This is likely due to the fact that under the poorly mixed extreme a large amount of oxygen is available through the whole freeboard allowing for additional oxidation reactions to occur to the smaller tars and hydrocarbons. This is evidenced by the decreased amount of methane predicted under these conditions, which shows a high degree of oxidation relative tothe inlet to the freeboard and the exit, while under the well-distributed extreme shows no reduction, but perhaps an indistinguishable increase. This bed then acts like a gasifier allowed to run in a rich condition in the bed with a secondary air injection into the freeboard. Thus, while using the same amount of oxidant, improved exit concentrations are achieved with respect to the total amount of tar and methane present.

In Figure 6-23 the total predicted tar concentrations from the bed are plotted as contours with respect to the bed operating temperature and the bed flow-rates. It is observed that for an even distribution of devolatilization and oxidant gases into the emulsion and the bubble phase the total tar production is nearly uniformly decreasing with respect to temperature with a minor uptick at high temperatures at low flow rates This is due to the growth of larger class 4 and 5 tars given the sufficient residence time and high temperatures necessary for their growth. Additionally, an overall decrease in total tar concentration is observed with decreasing flowrates at temperatures below 1200K. Here, due to the longer residence times there is continued cracking and oxidation of class 2 and 3 tars occuring, however the temperature is too low for significant PAH growth to class 4 and 5 tars.

For the case where the bypassing gas in the bubble phase consists solely of air with no devolatilization gas it is observed that there are uniformly fewer tars predicted at the exit for all operating conditions. This is due to the fact that in this assumption

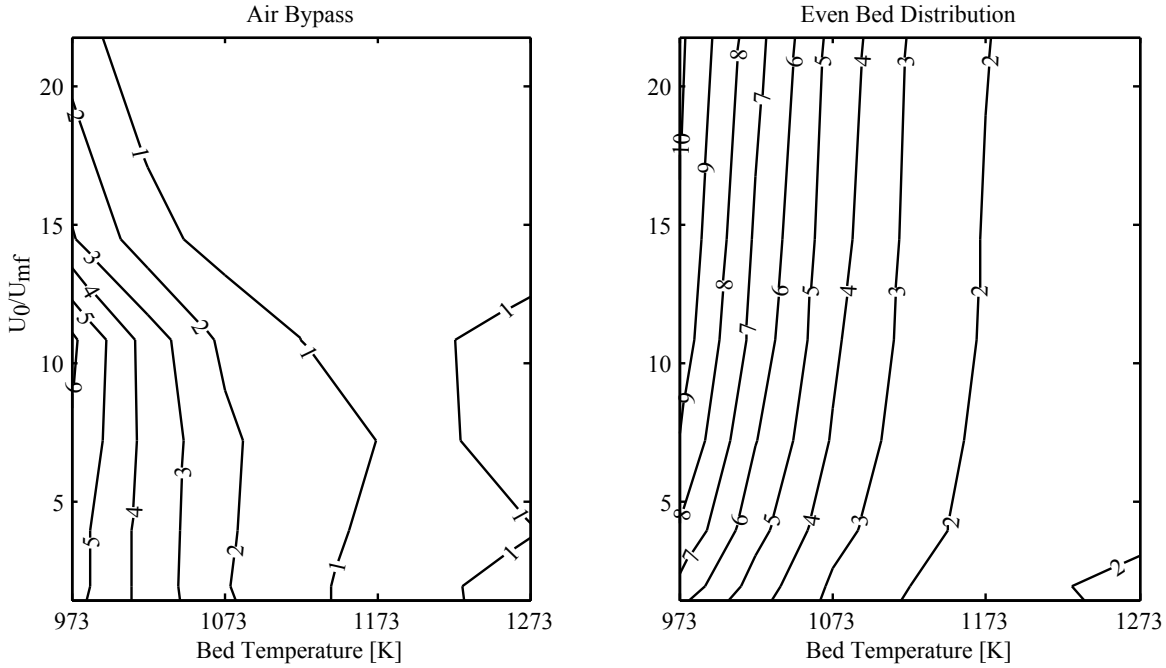


Figure 6-23: Total predicted tar concentration at the outlet $[g/Nm^3]$ of the reactor for two mixing assumptions (1) air by-pass and (2) evenly distributed devolatilization gases in the bed zone.

of lack of mixing much more oxygen is present in the freeboard allowing for an overall reduction of the total tar amount specifically through cracking and oxidation reactions of class 2 and 3 tar compounds through the length of the freeboard. While the temperature trends are similar with decreasing tars at higher temperatures, it is observed that the uptick at higher temperatures is expanded to higher gas flow-rates than for the even bed distribution, this is due to an increased amount of PAH compounds present (class 4 and 5 tars).

It is observed that the overall tar species distribution changes under these different mixing conditions. In Figure 6-24 contours of the mass fraction of the tars at the exit for each tar class proposed by Milne and employed by van Paasen & Kiel (the species in the CRECK mechanism falling into this classification are tabulated in Table 4.3) [101]. For the case of having well distributed devolatilization and oxidant gases at the inlet to the emulsion and the bubble phase we observe the expected temperature trends at each temperature, a decreasing amount of class 2 tars, an increasing, and subsequently decreasing, amount of class 3 tars and exponentially increasing amounts

of class 4 and 5 tars at elevated temperatures.

For the case of pure air by-passing however, the uniform trends observed for the well-distributed mixing case break down. Here it is also observed that class 2 tars show a uniform temperature dependence at all flow conditions it is only at the fastest flow-rates and lowest temperatures where they make up an appreciable fraction of the tars at the exit. This is primarily due to the short residence times where there is insufficient time for the tars to fully oxidize in the freeboard or to grow into PAH compounds. For class 3 tars, it is observed that their peak prevalence is shifted to lower temperatures than is observed in the well distributed case. Additionally, it is seen that from 1100-1200K there is a negative dependence of the predicted fraction of class 3 tars on the overall flow-rate. Increased amounts of PAHs (class 4 and 5 tars) are observed for all operating conditions and especially so for faster flow rates under the air bypass conditions.

This last observation, that larger PAH compound fractions are predicted at higher flow-rates, is likely due to the fact that with increasing flow-rates a larger fraction of the oxygen is bypassing the emulsion due to a larger volume fraction of the bubble phase (as shown in figure 6-17), and as such the local air-fuel ratio in the emulsion is necessarily less than the global operating air-fuel ratio of the bed as a whole. As such, in this relatively rich area the primary tars, in the absence of oxygen, are able to form small PAH compounds (class 4 tars) in relative abundance since the competing oxidation pathways are unavailable with decreased oxygen. Then in the freeboard, while there is then sufficient oxygen to consume much of the excess class 2 and 3 tars as observed in figure 6-22 the light PAHs that were formed in the rich emulsion are able to continue to grow larger since they become relatively recalcitrant to cracking and oxidizing.

## 6.8 Conclusions

In this chapter the influence of superficial gas velocity on the solid and gas mixing rates in the bed zone of a fluidized bed reactor were considered with reactive CFD

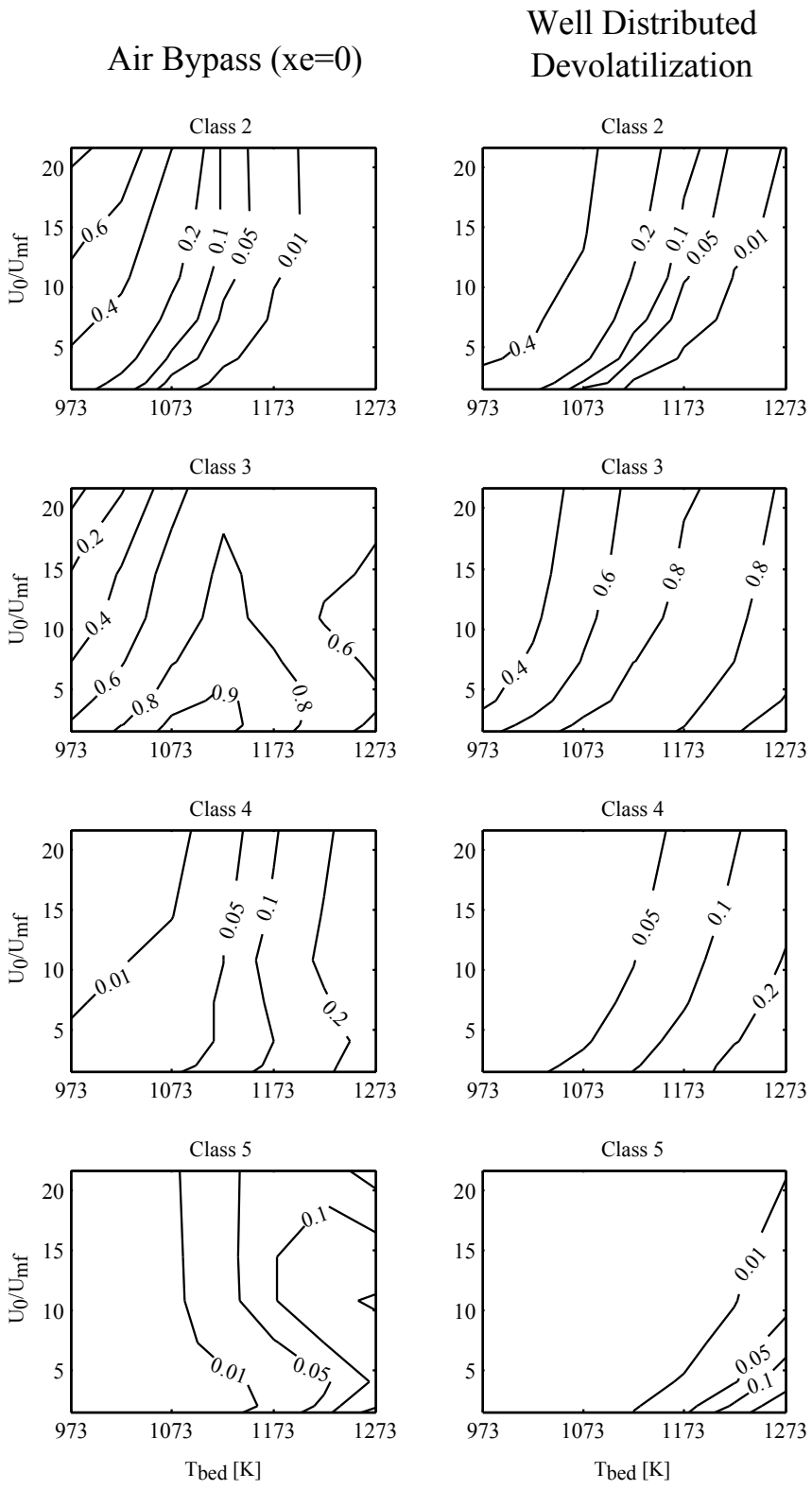


Figure 6-24: The influence of temperature and superficial gas velocity on tar speciation. The mass fractions of each tar class of the total amount of tar is plotted against reactor bed temperatures and flow rates.

simulation of a bench-scale fluidized bed gasifier. Fluidized bed reactors are utilized for solid to gas conversion processes due to their ability to provide a high degree of gas-solid contact, fast solid-solid mixing and fast gas mixing within the bed-zone due to solids-induced turbulent flow. In many reactor models of fluidized bed gasifiers this has lead researchers to assume that the bed zone can be modeled as a CSTR. Here the realistic limitations of this model have been quantified and an improved RNM developed capable of capturing the resulting reactor heterogeneities and resultant transport limitations. It was shown that this improved RNM is able to better capture the formation of large PAH compounds implying that their formation is strongly dependent on the availability of rich zones in the emulsion phase.

The influence of superficial gas velocity on the bed zone was analyzed, and it was found that with increasing superficial gas velocity the bed-zone geometry and flow conditions vary drastically with the gas volume of and gas mass flow-rates through the bubble-zone growing faster than those of the emulsion zone. This shift was shown to occur predominately through the additional flow of oxidant gas through the bubbles, while devolatilization gas grew to dominate the emulsion phase. As such, it was shown that with increasing superficial gas velocity up to $14.5U_{mf}$ the emulsion phase grew richer, and above this this trend leveled off with, perhaps, a slight decrease due to the transition to a turbulent bed with increased mixing and particle entrainment.

It was shown that this inhomogeneous bed condition, with oxidant bypassing in the bubble phase, leads to certain consequences in the predicted chemical species. First, little variation was shown for the major syn-gas species, since their concentrations are largely dictated by the global equilibrium. Second, the bypassing shows strong influence on the predicted tar concentrations both through the total tar concentration, which is decreased with increasing oxidant bypass due to more oxygen being available in the freeboard, and also through the speciation. It was shown that with a high degree of oxidant bypassing, the relative fraction of heavy PAH compounds in the exit tars are shown to increase due to the relatively rich zone in the emulsion phase where their formation is favored.

# Chapter 7

# Influence of Fuel Particle Diameter on Devolatilization Zone Distribution

## 7.1 Introduction

In chapter 6 CFD simulation was employed to investigate the impact of superficial gas velocity on the thermochemical conversion of biomass in an air-blown FBBG. Here, the influence of fuel particle diameter on solids mixing and the devolatilization reaction-zone distribution in the bed is considered using reactive CFD simulations.

## 7.2 Solid-Solid Mixing and Devolatilization Zone Distribution

Solid-Solid mixing is an important process which directly impacts the distribution of devolatilization and the overall contact between gas and reacting solid. In a system where the timescale of fuel mixing through the bed is much longer than the timescale of chemical conversion processes, the assumption of a well-stirred bed is necessarily violated.

A Damköhler number for devolatilization $Da_d$ can be defined as:

$$Da_{devol} = \frac{\tau_{mix}}{\tau_{devol}}, \tag{7.1}$$

where $\tau_{mix}$ is the characteristic time of biomass mixing through the bed, and $\tau_{devol}$ is the characteristic time of devolatilization for the fuel particle. Given this, for $Da_d < 1$ a FBBG will be expected to have devolatilization occurring uniformly throughout the bed, whereas for $Da_d > 1$ a localized devolatilization zone near the injection point is expected. It has been demonstrated that in realistic fluidized beds the rate of lateral mixing is the limiting factor relative to axial mixing [85,92,107,125], and therefore we assume that $\tau_{mix} \approx \tau_{l,mix}$. Lateral mixing has been successfully modeled as a dispersion process in the literature such that the lateral mixing time can be estimated as:

$$\tau_{l,mix} \cong \frac{D_{bed}^2}{\Lambda_l}, \tag{7.2}$$

where $\tau_{l,mix}$ is the lateral mixing time, $\Lambda_l$ is the lateral fuel dispersion coefficient and $D_{bed}$ is the bed diameter. Values of $\Lambda_l$ are dependent on a number of system variables, but reported values are near $10^{-3}[m^2/s]$ for cylindrical beds operating in bubbling to slugging regimes [107].

As demonstrated in Chapters 2 and 3, the devolatilization time of thermally large biomass particles ($d_p > 1mm$) scales as $\tau_{devol} \propto d_p^{\sigma}$, $\sigma \approx 2$. So, it can be established that:

$$Da_{devol} = \frac{\tau_{mix}}{\tau_{devol}} = \frac{D_{bed}^2}{\Lambda \tau_{devol}} \propto \left(\frac{D_{bed}}{d_p}\right)^2. \tag{7.3}$$

So, we expect that the dimensionless ratio of the bed diameter to the biomass particle diameter to play an important role in characterizing the reactor conditions in a fluidized bed system.

In Figure 7-1 the Devolatilization Damköhler Numbers for two different fluidized bed biomass gasifiers ($D_{bed} = 0.074\&0.15[m]$) for van Paasen & Kiel and Kurkela & Stålberg respectively) are plotted against the bed to biomass diameter ratio. It is

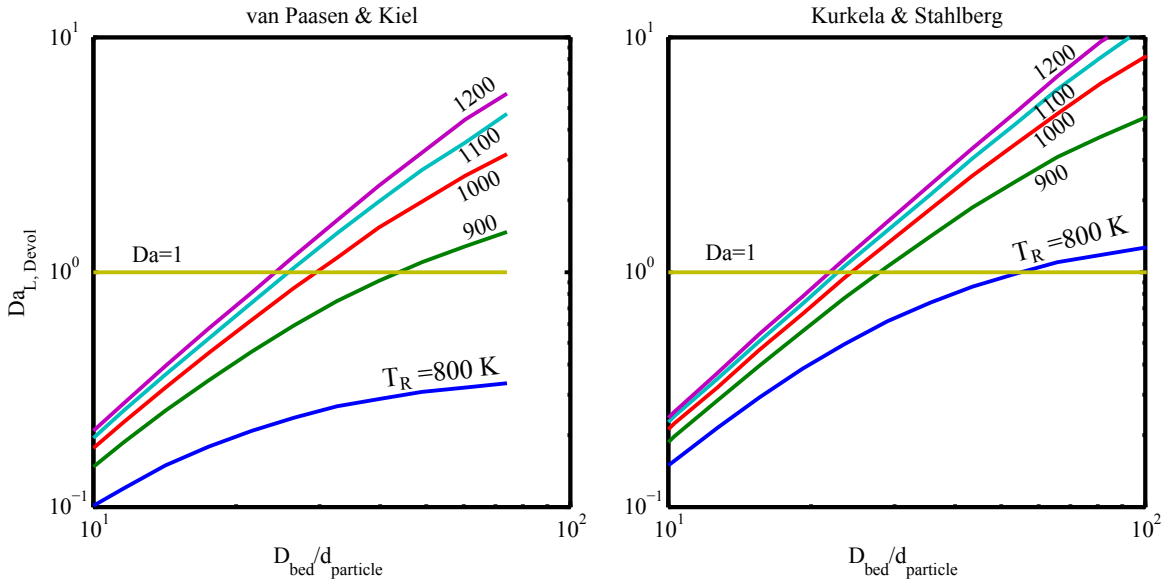


Figure 7-1: Estimated lateral Damköhler numbers are plotted for different bed temperatures and bed-particle ratios. Devolatilization times are calculated using the lagrangian particle model developed in chapter 2, timescale of lateral mixing is estimated as $t_L = \Lambda_l / D_{bed}^2$ where the lateral solids dispersion coefficient is taken to be $\Lambda_l \approx 10^{-3}$ in line with the reported values of Olsson [107].

observed that for sufficiently high temperatures, where internal heat transfer effects play a strong role, the scaling relation derived in equation 7.3 holds, while at lower temperatures the curvature of the line signifies the transition to kinetic control. For moderate bed temperatures ($> 1100K$) it can be determined that for $(D_{bed}/d_p) \geq 20 - 30$ uniform devolatilization does not likely occur. This bed to fuel particle ratio can be calculated for each of the cases to be 74 for dry 1mm particles in the van Paasen & Kiel bed, and 75-150 for dry particles in the Kurkela & Stålberg bed. As such, it is clear that neither of these beds are expected to operate with uniform devolatilization through the bed leading to localized devolatilization zones near the inlet. As such, mixing likely plays an important role in these reactors.

In order to further study the influence of fuel particle diameter on devolatilization and drying zone segregation a parameteric study has been undertaken in the Kurkela & Staålberg reactor. This reactor was chosen due to it's larger bed diameter allowing for a wider range of bed to particle diameter ratios to be studied. A reactive 3D CFD simulation is employed focusing on the bed-zone in the reactor. Drying and

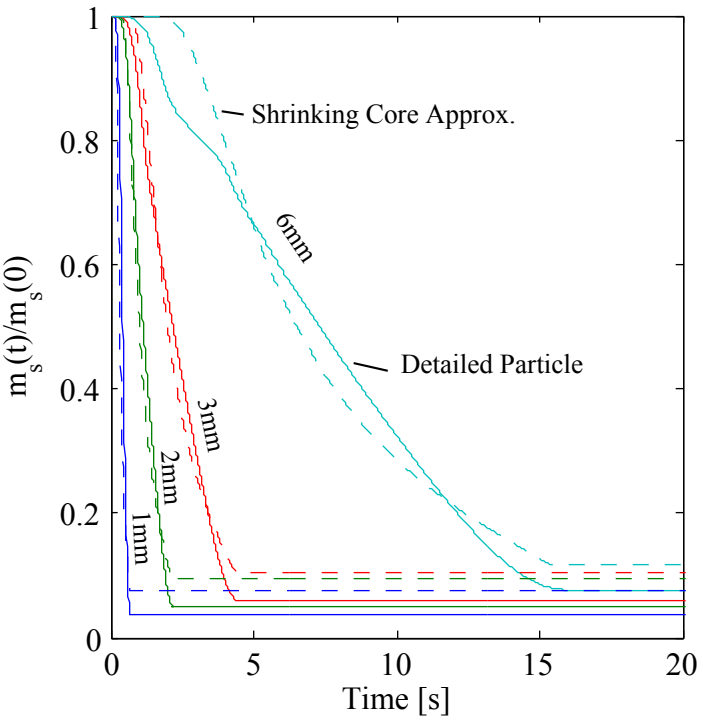


Figure 7-2: Comparison of detailed particle model and shrinking core particle model mass loss curve predictions for 1,2,3 and 6mm particles in the Kurkela & Stålberg reactor conditions.

devolatilization reactions are directly simulated with a shrinking core model employed for the devolatilization reactions. The parameters employed in the CFD simulation are shown in Table 7.1. Reactive CFD simulations are run for 50 seconds and time averaged values are extracted from 30-50 seconds.

Four particle diameters have been selected for this study: 1, 2, 3 and 6 mm. The first three diameters are chosen since they characterize the particle-size distribution in the original published work. A six millimeter particle is also employed since its predicted long devolatilization time allows for sufficient mixing to occur during its conversion. In Figure 7-2 the predicted mass-loss curves of the detailed particle model along with the eulerian shrinking core model are compared showing excellent dynamical agreement even though the only fitting parameter employed was optimized to predict conversion time. In the shrinking core approximation, the drying is allowed to happen uniformly through the particle and this accounts for the early disagreement between the two models early on for the 6mm particle.

Table 7.1: Summary of CFD simulation parameters for Kurkela & Ståhlberg fuel particle diameter parametric study.

| | Parameter | Value(s) |
|---|---|---|
| Gasifier Specifications | Geometry | cylindrical |
| | Diameter [cm] | 15 |
| | Height [cm] | 120 |
| | Bed Material | Silica sand |
| | Bed Material Diameter [$\mu m$] | 600 |
| | Bed Material Density [$kg/m^3$] | 2500 |
| | Total Bed Material [kg] | 4 |
| | Biomass Feed Height [cm] | 10 |
| Operating Conditions | Temperature [$K$] | 1073 |
| | Air-Fuel ER [] | 0.25 |
| | Pressure [bar] | 4 |
| | Feedstock Species | Pine Wood |
| | Fuel Diameter [mm] | Variable, 1,2,3,6 |
| | Fuel Feed Rate [kg/hr] | 40 |
| | Feedstock Moisture [%wt] | 5.9 |
| | Air Feed Rate [kg/hr] | 48.62 |
| | Steam Feed Rate [kg/hr] | 12.8 |
| Simulation | Time [s] | 50 |
| | Time averaged span [s] | 30-50 |
| Initial Conditions | Bed Configuration | packed bed material at bottom |
| | Temperature | uniform |
| Thermal Boundary Conditions | Walls | Isothermal |
| | Distributor Plate (bottom) | Specified gas temperature (1073K) |
| | Biomass inlet | Specified biomass temperature (373K) |
| Chemistry Modeling | Heats of Reaction | 0 (isothermal assumption) |
| | Number of Devolatilization Reactions | 3 + drying |
| | Shrinking Core Model | Devolatilization reactions only |

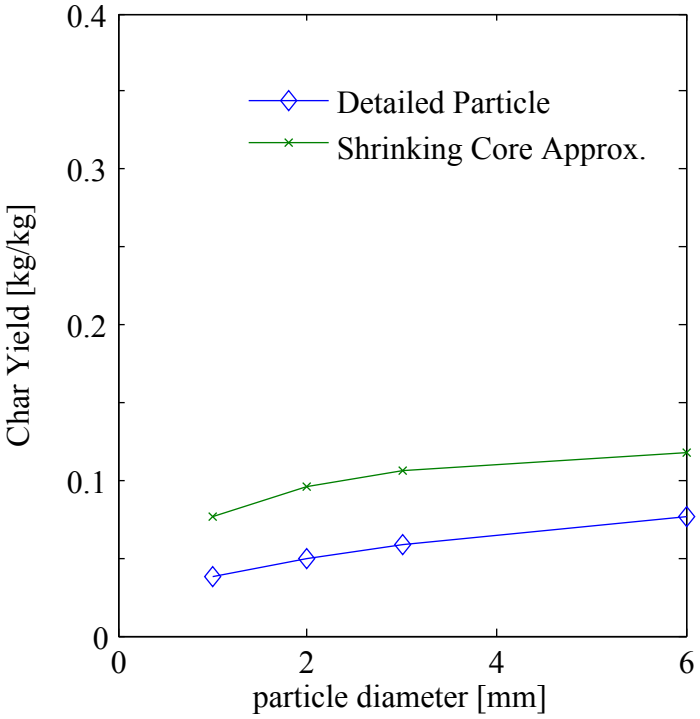


Figure 7-3: Comparison of detailed particle model and shrinking core particle model char yield predictions versus particle diameter in the Kurkela & Stålberg reactor conditions.

Since the shrinking core model was optimized in order to capture the devolatilization time, a certain amount of error is experienced in the chemical conversion predictions as highlighted in Figure 7-3, where predicted char yields are compared. The shrinking core model over-predicts the char yield by 40-50%, however the qualitative trend is preserved. This is due to the fact that the shrinking core modeling framework employs an effective devolatilization rate that is multiplied by each reaction equally in order to 'slow down' the devolatilization by taking into account the finite internal heat transfer rate. However, this has the effect of uniformly decreasing the effective reaction temperature as well, since the temperature employed in calculating the rates is the particle temperature as calculated using the lumped capacitance model of heat transfer. This divergence is not expected to cause any major errors in gaining insight into the distribution of the devolatilization reaction and drying zones, however, since their spatial distribution depends more on the rates, which we have captured with a high degree of accuracy.

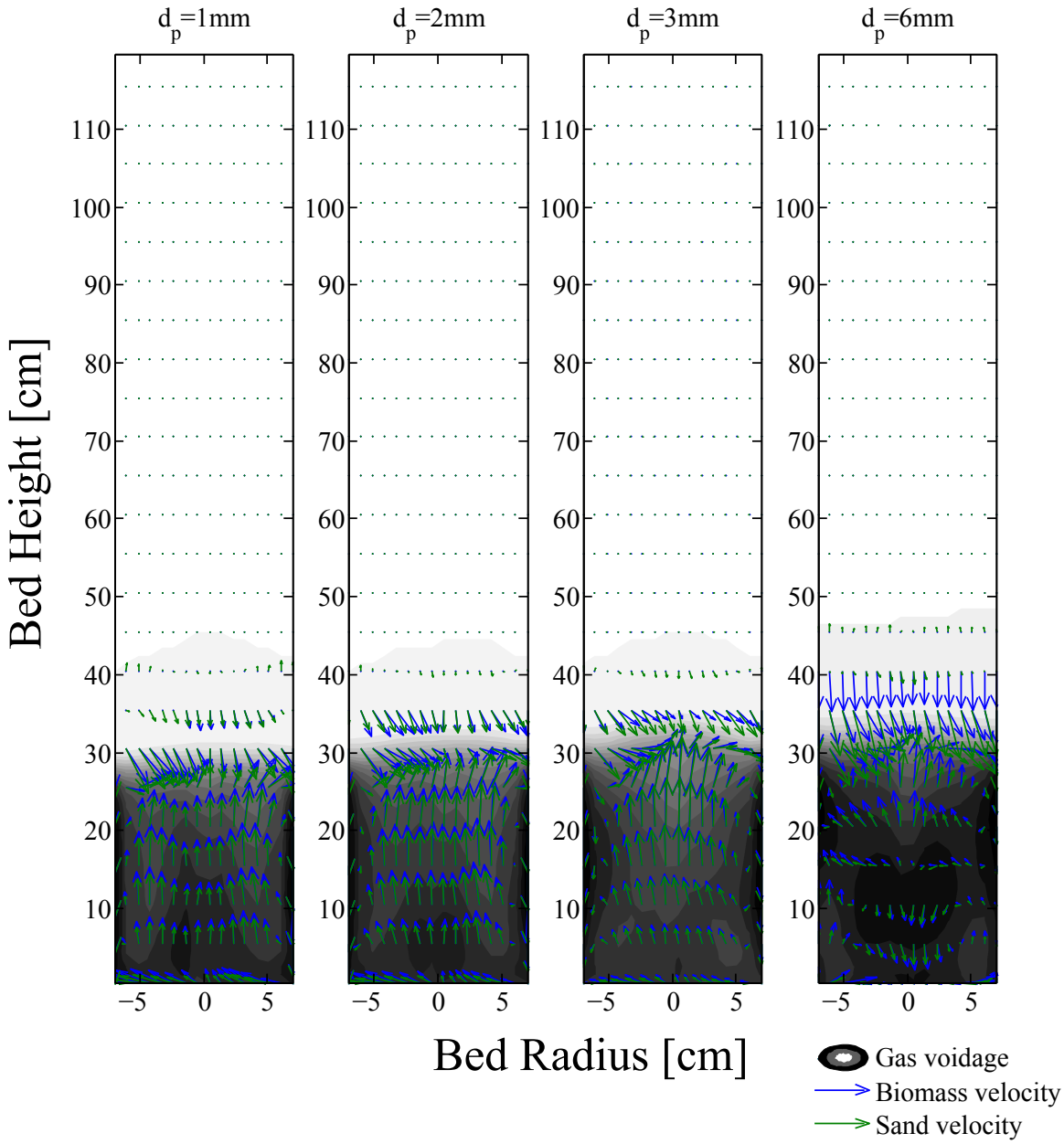


Figure 7-4: Time averaged solids distributions, biomass velocity and sand velocity for 1, 2, 3 and 6mm particles predicted with reactive CFD simulation of the Kurkela & Stålberg reactor.

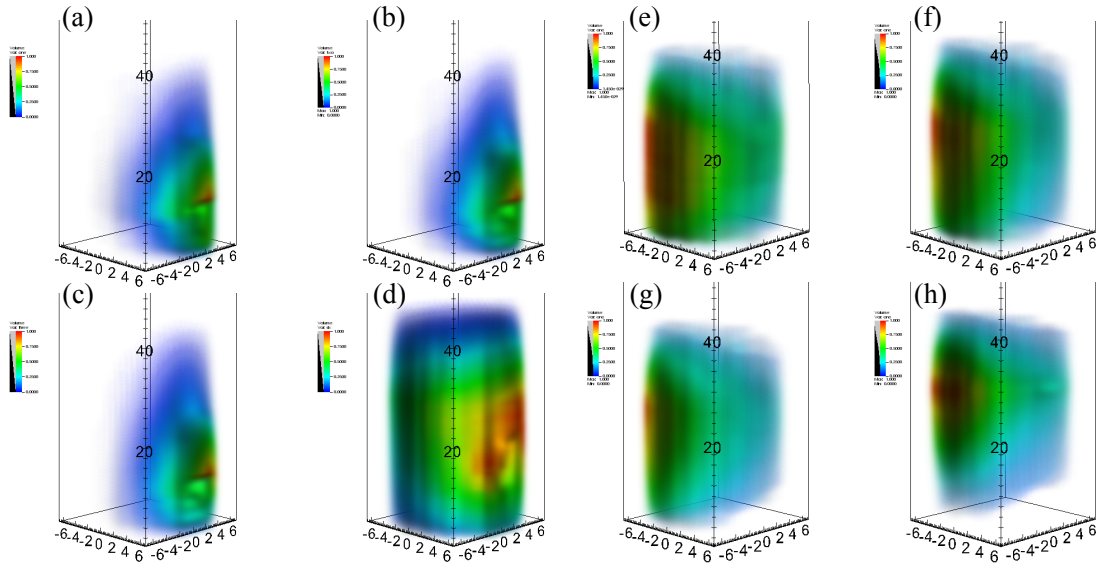


Figure 7-5: CFD prediction of time-averaged normalized drying, (a)-(d), and devolatilization, (e)-(f), rates in the Kurkela & Staålberg bed versus particle diameter. The fuel inlet is on the right-hand size at 10cm above the distributor (the bottom). (a) and (e) are 1mm particles, (b) and (f) are 2mm particles, (c) and (g) are 3mm particles and (d) and (h) are 6mm particles.

It is observed that, even though the gas and solids inlet mass flow-rates were held constant, the fuel particle diameter plays a crucial role in defining the time-averaged flow characteristics within the bed. In Figure 7-4 the biomass and sand velocity vector fields are overlayed onto the time-averaged gas-voidage distributions. For the smallest fuel particle diameter, 1mm, the development of a toroidal preferential bubble path is evident, with a dense center-line and outer recirculation zone along the wall with negative solids velocity. With increasing particle diameter, 2 and 3mm, it is clear that a more central preferential bubble path is established and the densest zone is relegated to the wall recirculation zone. Finally, at the largest particle size, where devolatilization rates are slower on a per particle basis, a bi-layer solids circulation pattern is developed, where the lower half of the bed has a toroidal upward flow and a strong center-line downward solids recirculation and in the upper half of the bed a strong central upward flow is established with downward recirculation occurring at the wall. Additionally it is observed that the lower part of the bed is relatively dense.

Text about Figure 7-5.

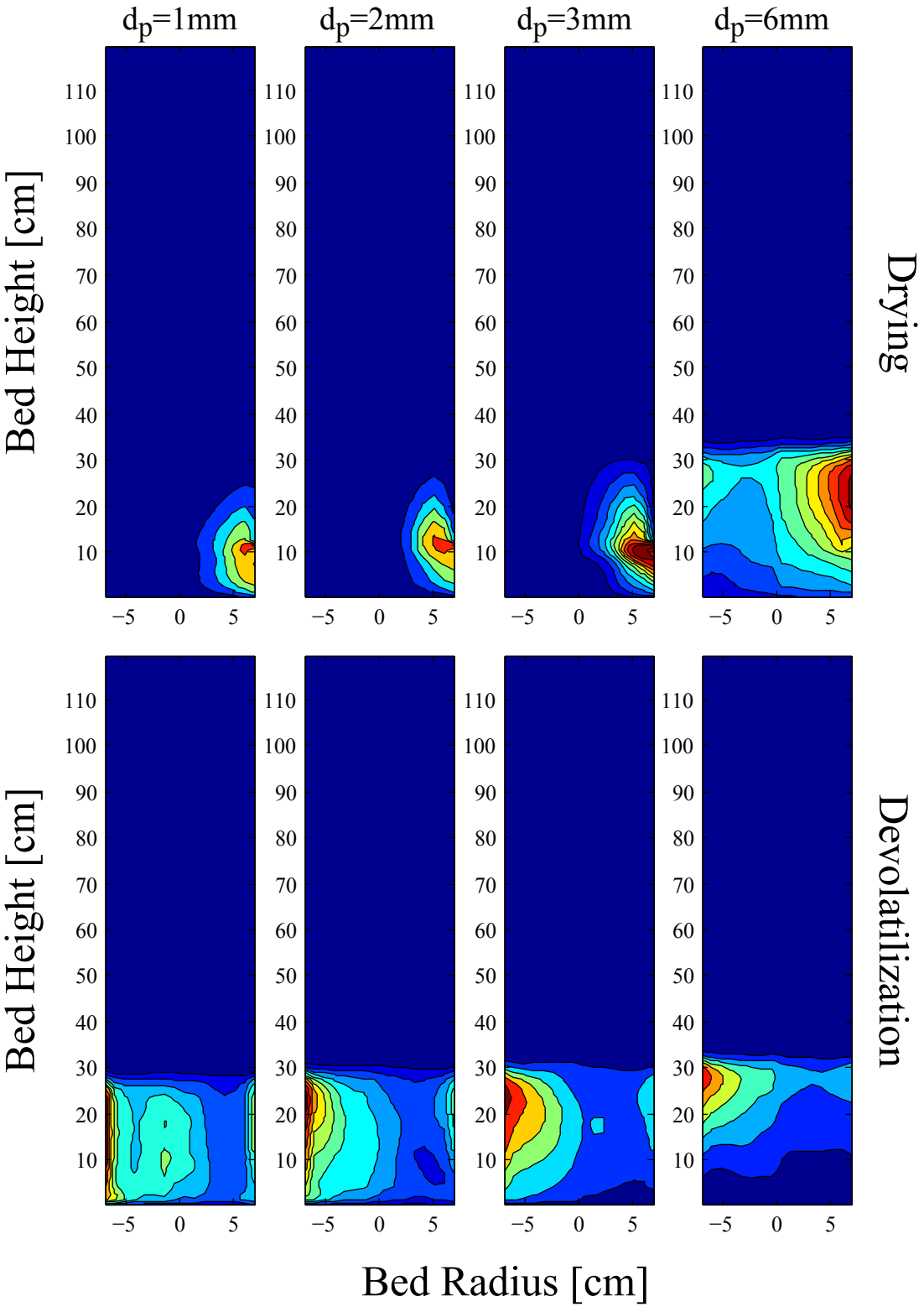


Figure 7-6: The time-averaged normalized drying (top row) and devolatilization (bottom row) reaction rates are plotted for 1, 2, 3 and 6mm particles.

These patterns likely indicate a strong degree of biomass devolatilization zone segregation, both in the axial and the radial directions which are dependent on the biomass particle diameters. In order to better illustrate this segregation, the time averaged locations of the solids drying and devolatilization reactions are plotted in Figure 7-6 for each particle diameter. Here the influence of particle diameter on the location of the drying zone is immediately obvious, in both the radial and axial directions. With increasing particle size the surface are to volume ratio of the particle decreases as $1/d_p$, and therefore more time is required to bring the particle up to drying temperature and to provide sufficient heat to evaporate the total moisture in the particle, this allows for a more distributed drying zone as the drying timescale overtakes the mixing time in the system. Similarly, for devolatilization, the same radial distribution effect is observed where for the smallest particles devolatilization occurs most predominately in the outer solids recirculation zone, while with increasing particle diameter the devolatilization occurs with an increased radial distribution. In the axial direction, however, it is notable that the particle radius has the opposite effect, decreasing the axial distribution of the devolatilization zone. This is due to the increasing particle segregation forces.

In Figure 7-7 the axial distributions of normalized drying and devolatilization reactions are plotted for each particle diameter. For each of the drying and the devolatilization reactions it is clear that axial segregation is occurring. For smaller particles (1-3mm) the maximum drying height is at 11-12 cm above the distributor, just above the solid inlet at 10cm. This is as expected since heat transfer to these particles can occur relatively fast in the fluidized bed and the particle can quickly heat up to drying temperatures. The peak drying location is strongly shifted up for the 6mm particles, however, this is due to the increased time required for particle heat-up and therefore a slower drying time relative to the time of biomass segregation. Additionally, with increasing particle diameter the prevalence of drying below the inlet decreases indicating an increasing prevalence of the particles to be transported upward rather than down. The influence of particle diameter on the axial location of the devolatilization reactions is also evident in Figure 7-7, with larger particle

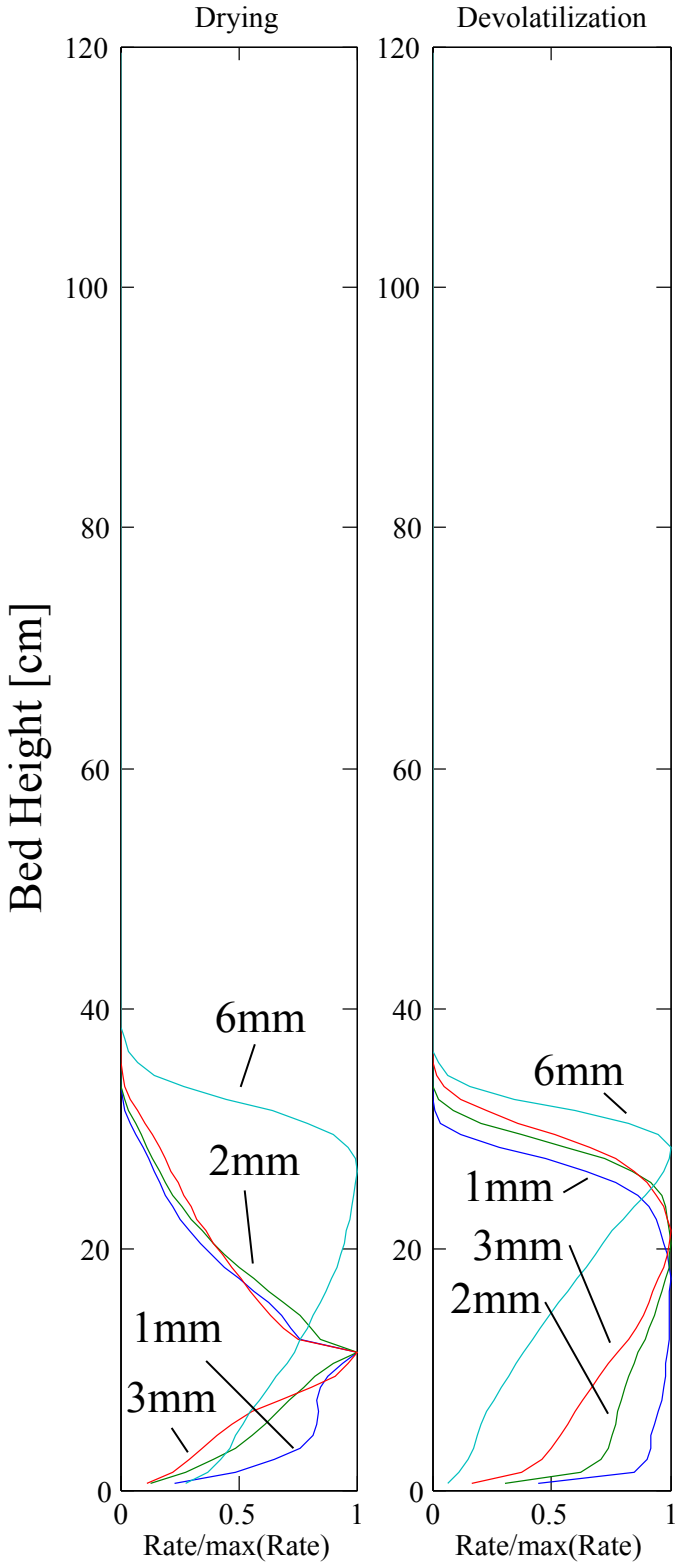


Figure 7-7: Influence of particle diameter on the axial distribution of drying and devolatilization in the Kurkela & Stålberg FBBG.

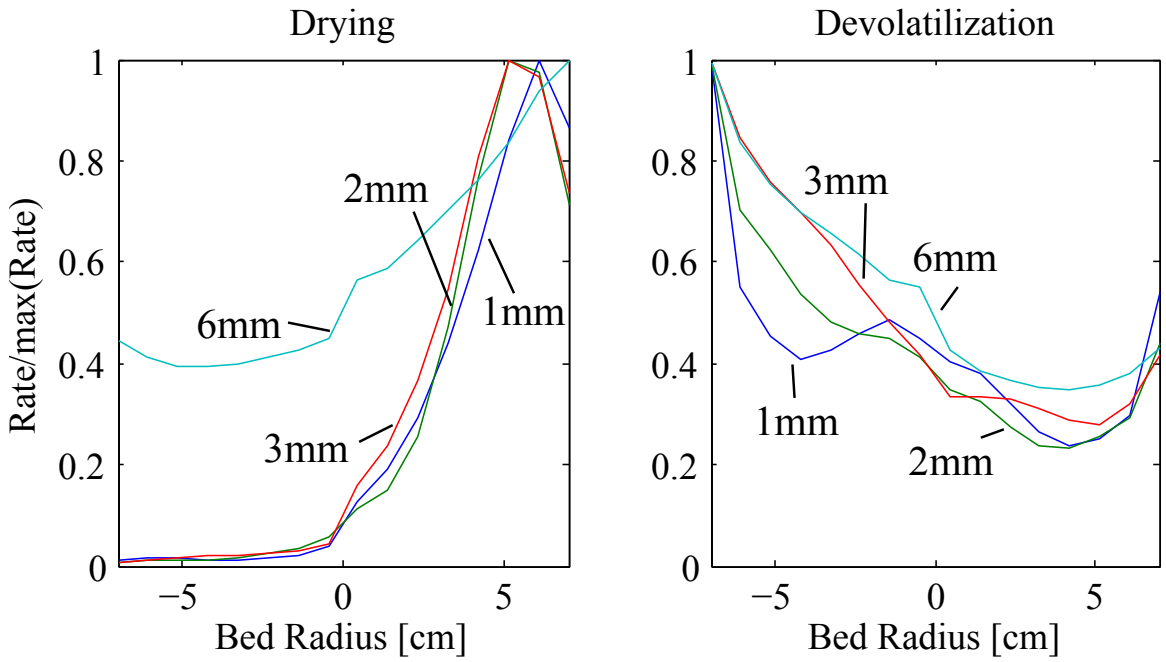


Figure 7-8: Influence of particle diameter on the radial distribution of drying and devolatilization in the Kurkela & Stålberg FBBG.

diameter leading to an increased amount of axial segregation of the devolatilization zone.

In order to assess the lateral distribution of the drying and devolatilization reactions the radial distribution of each of the reactions is considered. In Figure 7-8 the hemisphere-averaged normalized reaction rate distribution is plotted for drying and devolatilization, it is clear that except for the 6mm particle, drying is highly localized near the inlet, and very little drying occurs in the hemisphere opposite of the inlet. Given the slow heating rate of the 6mm particle drying is observed to occur throughout each hemisphere, however there is still a strong preference for the zone nearest the inlet, this is likely due to the tendency of the largest particles to quickly segregate to the top where the out-ward solids circulation has a tendency to push the wet raw biomass to the wall and therefore to slow down the dispersion of the wet biomass throughout the bed.

The mean reaction zone heights are plotted in Figure 7-9, and evidence of axial reaction zone segregation is clear. This is important since it implies that the lower portion of the bed, where little devolatilization is occurring may be underutilized in

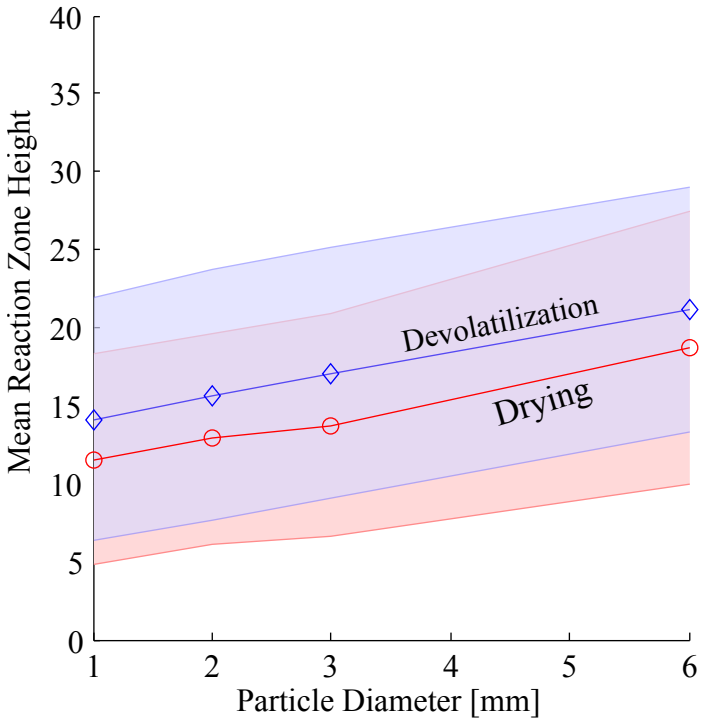


Figure 7-9: Influence of particle diameter on the mean reaction zone height of drying and devolatilization in the Kurkela & Stålberg FBBG. Shaded zones represent the mean ± one standard deviation.

tar reforming, and in the upper part of the bed where devolatilization is occurring, richer conditions are expected, and therefore, the possibility of PAH formation is potentially increased.

Conversely, it is observed that with increasing particle diameter the radial segregation of the drying zone is observed to decrease, while the devolatilization zone is consistently well distributed radially. This is illustrated in Figure 7-10 where the mean reaction zone radius is plotted versus particle diameter. At the largest particle diameter it is notable that the drying and devolatilization zones are co-located with a large variance indicating a high degree of radial uniformity throughout the bed. A slight uptick of the mean reaction zone radius is noted in the devolatilization zone between 1 and 2mm particle diameters which is likely resultant from the shifting flow conditions pushing the devolatilization zone outward.

It is clear that particle diameter plays an important role in determining the distribution and uniformity of the solids drying and devolatilization reactions in the bed

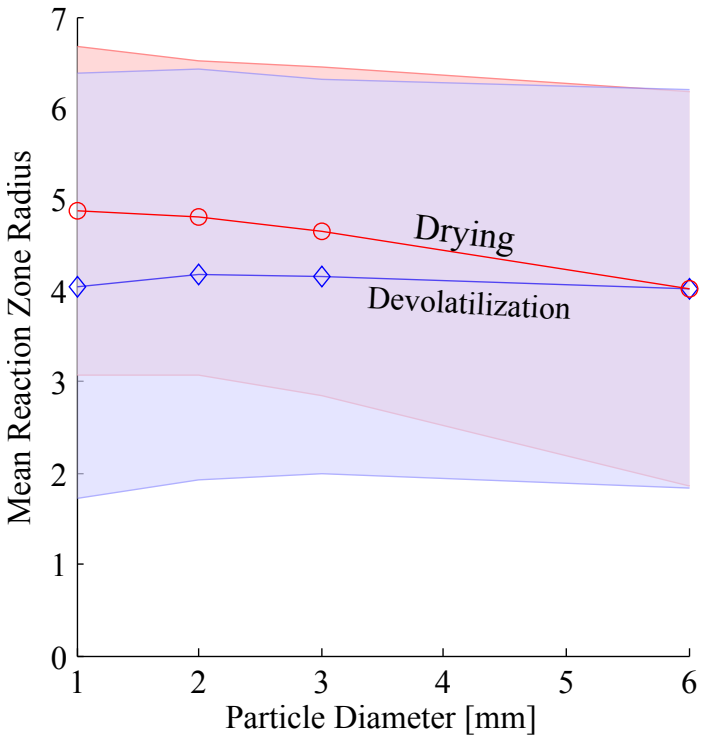


Figure 7-10: Influence of particle diameter on the mean reaction zone radius of drying and devolatilization in the Kurkela & Stålberg FBBG. Shaded zones represent the mean ± one standard deviation.

due to shifting timescales of mixing and reaction as well as a shifting tendency of larger particles to segregate upward in the bed. This segregation ultimately leads to non-uniformity through the bed zone and an under-utilization of the the reactor volume in the bed. In Figure 7-11 the time-averaged normalized distributions of nitrogen and tar are plotted in the bed illustrating the major impact that devolatilization zone segregation has on the spatial distribution in the gas phase. The trend of increasing vertical segregation with increasing particle diameter is clear, with the 6mm particle exhibiting a very lean zone in the lower part of the bed where there have been no tars released from devolatilization. Additionally, with increasing particle diameter, particularly from 1-3, an improved degree of radial uniformity of the gases in the freeboard zone ($y > 40cm$) due to an increasing degree of radial devolatilization zone uniformity in the bed. It is notable that there is a decrease again with the 6mm particles, this is due to the amount of drying occurring on the right hand side of the bed near the solid inlet which both depresses the local temperature of the solids and releases a large amount of steam at the surface which then is not mixed in the radial direction since the particles are segregated to the top of the bed and are not mixed well by the solids since little solids-induced gas mixing occurs after the splash zone and radial non-uniformity can only be resolved through diffusion. Both of these trends indicate a non-linear relationship between the particle diameter and the overall well-mixedness of the solids and uniformity of the gas release zones.

## 7.3 Conclusions

In this chapter reactive CFD simulations in a 3D cylindrical geometry were employed to study the influence of fuel particle diameter on the distribution of solids reactions in an air and steam blown FBBG. It was shown that the particle diameter influences the conversion dynamics through two mechanisms. First, increasing particle diameter leads to a more uniform radial distribution of the reaction zone since the ratio of the characteristic time of devolatilization to lateral mixing becomes larger. Second, increasing particle diameter was shown to result in an increased amount of vertical

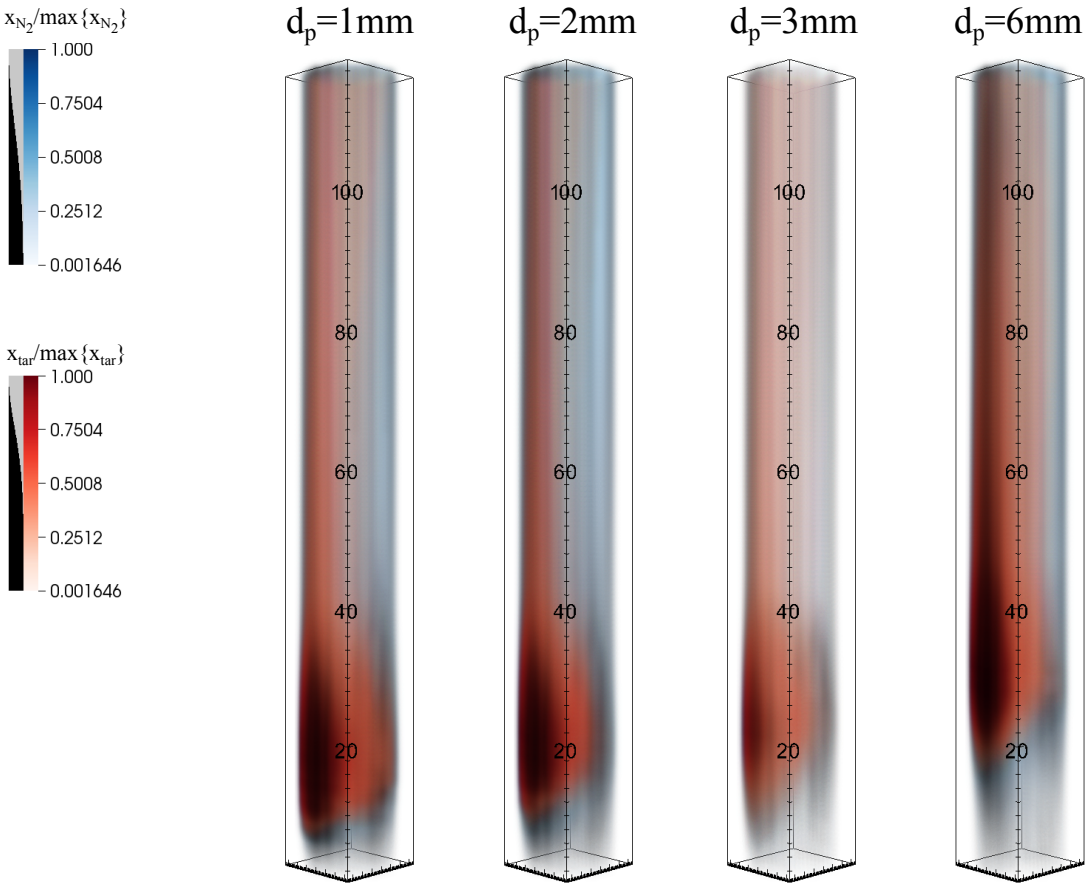


Figure 7-11: CFD prediction of time-averaged normalized concentrations of nitrogen and tar throughout the Kurkela & Staålberg bed versus particle diameter. The fuel inlet is on the right-hand size at 10cm above the distributor (the bottom).

reaction-zone segregation, since the buoyancy force on the larger particles is more pronounced. This can lead to additional radial non-uniformity in the freeboard, especially if non-uniform reaction zones develop on the surface of the bed.

These two dynamics were shown to result in a non-linear influence on the gas-phase mixing of the released volatiles and the oxidizing fluidizing medium, with an increase in particle diameter from 1 to 3mm resulting in a more homogeneous freeboard and a more utilized bed-zone, while for the largest particles, 6mm, significant segregation is observed leading to a severely under-utilized bed-zone. It is concluded that devolatilization and solids mixing times must be considered in order to guarantee a uniform devolatilization distribution throughout the bed, with insufficient mixing rates leading to localized devolatilization gas release and therefore locally rich zones within the bed.

# Chapter 8

# Conclusions

In this work the thermochemical conversion of biomass in fluidized bed reactor systems (both gasification and pyrolysis) has been analyzed with a focus on the interaction of transport and chemical conversion processes. Three modeling frameworks - (1) single particle devolatilization modeling, (2) Reactor network modeling and (3) Reactive 3D Computational Fluid Dynamic modeling - were employed to consider the interaction of transport and chemistry on the thermochemical conversion at each time and length scale. In particular transport has been shown to play an important role in the formation and growth of PAH compounds both at the particle and reactor scales. In Section 8.1 the overarching conclusions of the influence of the major controllable parameters in the thermochemical conversion of biomass are discussed. In Section 8.2 the major contributions of each chapter are highlighted and discussed. Finally in Section 8.3 recommended future work and potential applications of the models developed are presented.

## 8.1 Influence of controllable parameters on the thermochemical conversion of biomass

It has been shown in this thesis that a number of parameters play a role in the thermochemical conversion of biomass. In this work two important scales of conversion

- the particle scale and the reactor scale - have been considered, and a number of important parameters were identified at each scale which play important roles in the overall conversion. Four major metrics of conversion have been identified, the $H_2$:CO ratio of the syngas, the chemical conversion efficiency, $\eta_C$, the tar yield in the syn-gas and the PAH yield in the syn-gas.

### 8.1.1 The Particle Scale

At the particle scale the devolatilization process and resultant primary devolatilization gas distribution is governed primarily by:

1. The chemical composition of the biomass - decreased lignin content directly lowers primary tar precursor production.

2. The particle diameter - decreasing particle diameter decreases tar precursors via lower effective devolatilization temperature.

3. The moisture content - higher moisture content slows down particle heat up resulting in dispersion of devolatilization away from biomass inlet.

4. The initial fuel temperature - increased initial particle temperature decreases primary tar production via higher effective devolatilization temperature.

In table 8.1 the influence of each of these parameters on the four major conversion metrics is summarized.

Table 8.1: Summary of the influence of major controllable particle-scale parameters on important syn-gas characteristics.

| Parameters | H2:CO ratio | $\eta_C$ | Tar Yield | PAH Yield |
|---|---|---|---|---|
| Decrease lignin fraction | ↑ | ↑ | ↓ | ↓ |
| Decrease particle diameter | - | ↓ | ↓ | ↓ |
| Decrease moisture content | - | ↑ | - | - |
| Increased initial fuel temperature | ↑ | ↑ | ↓ | - |

### 8.1.2 The Reactor Scale

At the reactor scale the gas-phase conversion of the devolatilization gases and the gasification and oxidation of the char is governed by:

1. The reactor temperature - higher temperatures lead to increased kinetic rates of tar cracking and char gasification.

2. The oxygen to fuel ratio - higher oxygen concentrations lead to increased oxidation potential of tars and hydrocarbons.

3. The steam to fuel ratio - increased water concentrations pushes forward the water-gas shift reaction as well as increases the concentration of $\cdot OH$ and $\cdot HO_2$ radicals.

4. The superficial gas velocity - at slow flow conditions ($< 4U_m f$) increasing superficial gas velocity will improve bed mixing, however further increase will lead to slugging and gas-phase inhomogeneity.

5. The particle to bed diameter ratio ($d_p : D_b$) - Increased fuel particle diameter increases devolatilization zone uniformity through the bed by increasing the devolatilization time relative to the mixing time of the solid fuel.

In table 8.2 the influence of each of these parameters on the four major conversion metrics is summarized.

Table 8.2: Summary of the influence of major controllable particle-scale parameters on important syn-gas characteristics.

| Parameters | H2:CO Ratio | $\eta_C$ | Tar Yield | PAH Yield |
|---|---|---|---|---|
| Increase Temperature | - | $\uparrow$ | $\downarrow$ | $\uparrow$ |
| Increase oxygen to fuel ratio | $\downarrow$ | $\downarrow$ | $\downarrow$ | $\downarrow$ |
| Increase steam to fuel ratio | $\uparrow$ | $\uparrow$ | $\downarrow$ | $\downarrow$ |
| Increased superficial gas velocity | - | $\downarrow$ | $\downarrow$ | $\uparrow$ |
| Increased $d_p : D_b$ | - | $\uparrow$ | $\downarrow$ | $\downarrow$ |

## 8.2 Summary of Contributions

This primary focus of this thesis is the consideration and development of predictive multi-scale chemistry models of biomass gasification in a fluidized bed reactor. In particular, an effort has been made to capture the effect of transport phenomena on the chemistry of conversion from the particle to the reactor scales.

In Chapter 2 the conversion of solid biomass to reactive gaseous intermediates and char, or the devolatilization step, was analyzed using a detailed Lagrangian particle model which incorporates internal and external heat transfer with a detailed kinetic and thermochemical model of devolatilization. It was was shown that transport properties, in particular the particle diameter, plays an important role in defining the effective temperature of devolatilization at the reaction wave surface, thus directly effecting the predicted devolatilization gas distribution. It was shown that the yields of tar precursors can be decreased by decreasing particle diamter as well as increasing reactor temperatures.

In Chapter 3 a shrinking-core model of biomass devolatilization for use in reactive Eulerian CFD simulations of FBBGs was developed and validated against the Lagrangian particle model developed in Chapter 2. It was shown that the simplified representation of heat transfer, via a shrinking core model, is sufficient to capture particle diameter effects with simple one-step devolatilization chemistry for investigation of particle devolatilization in CFD simulations where the solids are represented as granular eulerian fluids. It was shown that both the influence of particle diameter on conversion time as well as devolatilization chemistry can be captured in a shrinking core model.

In Chapter 4 the thermochemical conversion of the devolatilization gasses to syngas, tars and other byproducts was considered. A 1-D reactor network model of a FBBG was developed which was shown to capture trends in the major syngas species $H_2$, CO, $H_2O$, $CO_2$ and $CH_4$ as well as tar species. It was demonstrated that modified CO oxidation and/or water gas shift kinetics are required in order to reflect the catalytic impact of bed materials, ash and char on conversion kinetics. Additionally, the

conversion mechanism of the major devolatilization products of cellulose, hemicellulose and lignin were elucidated and the important intermediates in PAH formation and growth were identified.

In Chapter 5 the particle and reactor network models developed in Chapters 2 and 4 respectively were applied to a fluidized bed pyrolysis reactor developed at the National Renewable Energy Laboratory (NREL) in order to investigate the impact of particle diameter and temperature on polycyclic aromatic hydrocarbon formation and growth. It was shown that particle diameter has a direct impact on PAH formation through the production of sinapoyl aldehyde as a primary tar precursor.

In Chapter 6 the influence of the fluidization regime, solids-phase mixing and devolatilizing particle segregation on the predicted gas distribution from the gasifier was analyzed utilizing fully reactive CFD simulations of bench-scale gasifiers. The reactor network model developed in Chapter 4 was extended to capture these effects by addition of a PFR in the bed to capture gas bypass of the emulsion through the bubble phase. It is shown that particle diameter plays a role in the overall uniformity of devolatilization distribution due to the trade-off in devolatilization time and mixing times in the fluidized bed. Additionally, variation in the superficial gas velocity is shown to play an important role in predicted gas bypass through the bubble phase. Finally, it is shown that these mixing phenomena play a crucial role in the formation and growth of PAH compounds, while having minimal effect on the predicted trends of the major gas species.

## 8.3 Future Work and Anticipated Applications

Each of the modeling frameworks and tools developed in this thesis likely have broad application potential beyond what was here discussed. In this section liberty is taken to suggest potential future work and applications for each of these models. Further,

### 8.3.1 Particle-Scale Devolatilization

The development of a detailed particle model of the thermochemical conversion of solid biomass is of utmost utility in a number of applications. Of immediate note is in the development of improved simplified particle sub-models for CFD and RNM models of reactors of interest as has been explored in Chapter 3. Further, a particle model with improved chemistry modeling can allow for better prediction of pyrolysis product distributions as well as the locations in the reactor system where certain processes occur and products are released, this type of information can aid in improving reactor designs and this is a goal of this work. Finally, an anticipated application of this work is use of the model to improve experimental design for the kinetic study of biomass pyrolysis. Each of these applications are discussed below.

#### Reactor Design, Analysis and Product Prediction in Fast Pyrolysis and other Processes

The development of a detailed particle model of the thermochemical conversion of solid biomass is of utmost utility in a number of applications. Of immediate note is in the development of improved simplified particle sub-models for CFD and RNM models of reactors of interest. Further, a particle model with improved chemistry modeling can allow for better prediction of pyrolysis product distributions as well as the locations in the reactor system where certain processes occur and products are released, this type of information can aid in improving reactor designs and this is a goal of this work. Finally, an anticipated application of this work is use of the model to improve experimental design for the kinetic study of biomass pyrolysis. Each of these applications are discussed below.

#### Analysis and Improvement of Experimental Design for Pyrolysis Kinetics

Current experimental techniques employed in the study of pyrolysis kinetics of biomass assume that the conversion process at the particle scale is completely kinetically controlled and the external/internal heat transfer limitations are negligible and therefore

do not influence the resultant data. However, simple analysis can show that heat transfer is likely to play a roll in fixed bed reaction schemes (as is the case in many TGA studies) and as such the pyrolysis kinetic parameters are likely skewed due to this systemic bias error. With improved conversion models at the particle scale it should be possible to estimate and decouple this error in current experimental designs and/or design better experimental procedures that take into account the heat transfer effects.

### 8.3.2 RNM Modeling of FB Thermochemical Conversion Technology

The development of reactor network models of FB reactors is of utmost importance to industrial technology deployment. Although there have been great improvements in CFD modeling technology and abilities, the ability to capture complex chemistry in CFD simulations is still severely limited due to the complex hydrodynamics being directly modeled. However, it is was demonstrated in Chapter 6.3 that CFD simulation is an important tool for the development of RNMs capable of capturing fluid-dynamic and mixing dynamics. Due to the limits of experimental investigation of internal flow conditions at high-temperature reactive conditions, CFD simulation is necessary to interrogate the internal reacting-gas dynamics.

#### Further RNM development

In this thesis time-averaged solids distributions calculated using CFD were used in estimating the volumes of the emulsion and bubble phase as well as the gas flowrates through these zones in the bed for the improved RNM developed in Chapter 6.3. However, it was shown that solids also have circulation patterns through the bed which dictate the locations of devolatilization gas release and char distribution. A potential improvement of the RNM is to add a solids RNM capturing the flows and reaction zones of the raw biomass and char. This could then be used to further predict the prediction of rich zones where PAH formation is favored.

### Extention of RNM modeling to other FB reactor technology

Capturing cas by-pass is of particular importance in reactors where solid catalysts are employed, such as fluidized catalytic crackers, or in novel reactor technology such as catalytic pyrolysis reactors. If there is excessive by-passing of the gasses the overall gas-solids contact is expected to be decreased therefore decreasing the overall reactor one-pass efficiency. It is likely that applying the methodology to take CFD simulation data and develop an RNM capable of capturing this bypass would allow for better modeling of these reactors.

# Bibliography


[1] Christos Altantzis, Richard B. Bates, and Ahmed F. Ghoniem. Comparison of simplified 1d models with 2d and 3d cfd simulations of a laboratory-scale bubbling fluidized bed hydrodynamics. In *International Conference on Multiphase Flow*, Jeju, South Korea, 2013.

[2] M. J. Antal. Biomass pyrolysis: A review of the literature part 1 - carbohydrate pyrolysis. *Advances in Solar Energy.*, 1:61–112, 1982.

[3] M. J. Antal. Biomass pyrolysis: A review of the literature part 2 - lignocellulose pyrolysis. *Advances in Solar Energy*, 2:175–255, 1985.

[4] M. J. Antal and G. Varhegyi. Cellulose pyrolysis kinetics - the current state of knowledge. *Industrial and Engineering Chemistry Research*, 34(3):703–717, 1995.

[5] Michael Jerry Antal. Effects of reactor severity on the gas-phase pyrolysis of cellulose- and kraft lignin-derived volatile matter. *Industrial & Engineering Chemistry Product Research and Development*, 22(2):366–375, 1983.

[6] Michael Jerry Antal, Gabor Varhegyi, and Emma Jakab. Cellulose pyrolysis kinetics: Revisited. *Industrial & Engineering Chemistry Research*, 37(4):1267–1275, 1998.

[7] Donald F. Arseneau. Competitive reactions in the thermal decomposition of cellulose. *Canadian Journal of Chemistry*, 49(4):632–638, 1971.

[8] Hamid Asadi-Saghandi, Rahmat Sotudeh-Gharebagh, Amir Motamed Dashliborun, Hossein Kakooei, and Mohammad Hajaghazadeh. Sequential-based process modelling of vocs photodegradation in fluidized beds. *The Canadian Journal of Chemical Engineering*, 92(11):1865–1874, 2014.

[9] G.M. Atri, R.R. Baldwin, D. Jackson, and R.W. Walker. The reaction of {OH} radicals and {HO2} radicals with carbon monoxide. *Combustion and Flame*, 30(0):1 – 12, 1977.

[10] Eitan Avni, Robert W. Coughlin, Peter R. Solomon, and Hsiang Hui King. Mathematical modelling of lignin pyrolysis. *Fuel*, 64(11):1495–1501, 1985.

[11] B. V. Babu and A. S. Chaurasia. Heat transfer and kinetics in the pyrolysis of shrinking biomass particle. *Chemical Engineering Science*, 59(10):1999–2012, 2004.

[12] SP Babu, B Shah, and A Talwalkar. Fluidization correlations for coal gasification materials-minimum fluidization velocity and fluidized bed expansion ratio. In *AIChE Symp. Ser*, volume 74, pages 176–186, 1978.

[13] A Bakshi, C Altantzis, and AF Ghoniem. Towards accurate three-dimensional simulation of dense multi-phase flows using cylindrical coordinates. *Powder Technology*, 2014.

[14] C. H. Bamford, J. Crank, and D. H. Malan. The combustion of wood. part i. *Mathematical Proceedings of the Cambridge Philosophical Society*, 42(2):166, 1946.

[15] M. Barrio, B. Gøbel, H. Rimes, U. Henriksen, J.E. Hustad, and L.H. Sørensen. *Steam Gasification of Wood Char and the Effect of Hydrogen Inhibition on the Chemical Kinetics*, pages 32–46. Blackwell Science Ltd, 2008.

[16] M. Barrio and J.E. Hustad. *CO2 Gasification of Birch Char and the Effect of CO Inhibition on the Calculation of Chemical Kinetics*, pages 47–60. Blackwell Science Ltd, 2008.

[17] Charles W. Bauschlicher and Alessandra Ricca. Mechanisms for polycyclic aromatic hydrocarbon (pah) growth. *Chemical Physics Letters*, 326(34):283 – 287, 2000.

[18] Charles W. Bauschlicher, Alessandra Ricca, and Marzio Rosi. Mechanisms for the growth of polycyclic aromatic hydrocarbon (pah) cations. *Chemical Physics Letters*, 355(12):159 – 163, 2002.

[19] Francesco Berna, Paul Goldberg, Liora Kolska Horwitz, James Brink, Sharon Holt, Marion Bamford, and Michael Chazan. Microstratigraphic evidence of in situ fire in the acheulean strata of wonderwerk cave, northern cape province, south africa. *Proceedings of the National Academy of Sciences*, 2012.

[20] A. Bharadwaj, L. L. Baxter, and A. L. Robinson. Effects of intraparticle heat and mass transfer on biomass devolatilization: Experimental results and model predictions. *Energy & Fuels*, 18(4):1021–1031, 2004.

[21] Václav Bíba, Jiri Macak, Erhard Klose, and Jiri Malecha. Mathematical model for the gasification of coal under pressure. *Industrial & Engineering Chemistry Process Design and Development*, 17(1):92–98, 1978.

[22] Julien Blondeau and Hervé Jeanmart. Biomass pyrolysis at high temperatures: Prediction of gaseous species yields from an anisotropic particle. *Biomass and Bioenergy*, 41:107 – 121, 2012.

[23] R. W. Breault. Gasification processes old and new: A basic review of the major technologies. *Energies*, 3:216–240, 2010.

[24] A. V. Bridgwater, D. Meier, and D. Radlein. An overview of fast pyrolysis of biomass. *Organic Geochemistry*, 30(12):1479–1493, 1999.

[25] Robert Brown. Hybrid thermochemical/biological processing. *Applied Biochemistry and Biotechnology*, 137-140(1):947–956, 2007.

[26] Matteo Calonaci, Roberto Grana, Emma Barker Hemings, Giulia Bozzano, Mario Dente, and Eliseo Ranzi. Comprehensive kinetic modeling study of bio-oil formation from fast pyrolysis of biomass. *Energy Fuels*, 24(10):5727–5734, 2010.

[27] Wai-Chun R. Chan, Marcia Kelbon, and Barbara B. Krieger. Modelling and experimental verification of physical and chemical processes during pyrolysis of a large biomass particle. *Fuel*, 64(11):1505–1513, 1985.

[28] Wai Chun Ricky Chan, Marcia Kelbon, and Barbara Krieger-Brockett. Single-particle biomass pyrolysis: correlations of reaction products with process conditions. *Industrial & Engineering Chemistry Research*, 27(12):2261–2275, 1988.

[29] Wei-Hsin Chen and Po-Chih Kuo. A study on torrefaction of various biomass materials and its impact on lignocellulosic structure simulated by a thermogravimetry. *Energy*, 35(6):2580–2586, 2010.

[30] R. Chirone, P. Salatino, F. Scala, R. Solimene, and M. Urciuolo. Fluidized bed combustion of pelletized biomass and waste-derived fuels. *Combustion and Flame*, 155(1-2):21–36, 2008.

[31] José Corella, José M. Toledo, and Gregorio Molina. A review on dual fluidized-bed biomass gasifiers. *Industrial & Engineering Chemistry Research*, 46(21):6831–6839, 2007.

[32] Lee J. Curtis and Dennis J. Miller. Transport model with radiative heat transfer for rapid cellulose pyrolysis. *Industrial & Engineering Chemistry Research*, 27(10):1775–1783, 1988.

[33] JF Davidson. The two-phase theory of fluidization: successes and opportunities. In *AIChE Symposium Series*, volume 87, pages 1–12, 1991.

[34] John Frank Davidson and David Harrison. *Fluidised particles*, volume 3. Cambridge university press Cambridge, UK, 1963.

[35] ML de Souza-Santos. *Combustion and Gasification of Solid Fuels, Modeling, Simulation, and Equipment Operation*. CRC Press, Taylor & Francis Group, 2010.

[36] A. Demirbaş. Combustion characteristics of different biomass fuels. *Progress in Energy and Combustion Science*, 30(2):219–230, 2004.

[37] Colomba Di Blasi. Modeling and simulation of combustion processes of charring and non-charring solid fuels. *Progress in Energy and Combustion Science*, 19(1):71–104, 1993.

[38] Colomba Di Blasi. Comparison of semi-global mechanisms for primary pyrolysis of lignocellulosic fuels. *Journal of Analytical and Applied Pyrolysis*, 47(1):43–64, 1998.

[39] Colomba Di Blasi. Modeling chemical and physical processes of wood and biomass pyrolysis. *Progress in Energy and Combustion Science*, 34(1):47–90, 2008.

[40] Colomba Di Blasi and Carmen Branca. Kinetics of primary product formation from wood pyrolysis. *Industrial & Engineering Chemistry Research*, 40(23):5547–5556, 2001.

[41] Colomba Di Blasi, Federico Buonanno, and Carmen Branca. Reactivities of some biomass chars in air. *Carbon*, 37(8):1227–1238, 1999.

[42] Capucine Dupont, Li Chen, Julien Cances, Jean-Michel Commandre, Alberto Cuoci, Sauro Pierucci, and Eliseo Ranzi. Biomass pyrolysis: Kinetic modelling and experimental validation under high temperature and flash heating rate conditions. *Journal of Analytical and Applied Pyrolysis*, 85(12):260–267, 2009.

[43] Capucine Dupont, Timothée Nocquet, José Augusto Da Costa Jr., and Christèle Verne-Tournon. Kinetic modelling of steam gasification of various woody biomass chars: Influence of inorganic elements. *Bioresource technology*, 102(20):9743–9748, 2011.

[44] Ali Eslami, Abolhasan Hashemi Sohi, Amir Sheikhi, and Rahmat Sotudeh-Gharebagh. Sequential modeling of coal volatile combustion in fluidized bed reactors. *Energy & Fuels*, 26(8):5199–5209, 2012.

[45] Exxon Mobil Research and Engineering. Methanol to gasoline (mtg): Production of clean gasoline from coal. Technical report, Exxon Mobil, 2009.

[46] Andre Faaij. Modern biomass conversion technologies. *Mitigation and Adaptation Strategies for Global Change*, 11(2):335–367, 2006.

[47] Farm and Dairy News. For first time, corn will supply more ethanol plants than feed farm animals, 2011.

[48] Carolina Font Palma. Model for biomass gasification including tar formation and evolution. *Energy & Fuels*, 27(5):2693–2702, 2013.

[49] Carolina Font Palma. Modelling of tar formation and evolution for biomass gasification: A review. *Applied Energy*, 111(0):129 – 141, 2013.

[50] A. Fourcault, F. Marias, and U. Michon. Modelling of thermal removal of tars in a high temperature stage fed by a plasma torch. *Biomass and Bioenergy*, 34(9):1363 – 1374, 2010.

[51] Michael Frenklach. On the driving force of {PAH} production. *Symposium (International) on Combustion*, 22(1):1075 – 1082, 1989.

[52] Michael Frenklach, David W. Clary, William C. Gardiner Jr., and Stephen E. Stein. Detailed kinetic modeling of soot formation in shock-tube pyrolysis of acetylene. *Symposium (International) on Combustion*, 20(1):887 – 901, 1985. Twentieth Symposium (International) on Combustion.

[53] Michael J. Frost, Paul Sharkey, and Ian W. M. Smith. Reaction between hydroxyl (deuteroxyl) radicals and carbon monoxide at temperatures down to 80 k: experiment and theory. *The Journal of Physical Chemistry*, 97(47):12254–12259, 1993.

[54] L.E. Fryda, K.D. Panopoulos, and E. Kakaras. Agglomeration in fluidised bed gasification of biomass. *Powder Technology*, 181(3):307 – 320, 2008.

[55] N Fuji and T Asaba. Shock-tube study of the reaction of rich mixtures of benzene and oxygen. In *Proceedings of the Fourteenth Symposium (International) on Combustion*, volume 14, page 433, 1973.

[56] Katherine R Gaston, Mark W Jarvis, Perrine Pepiot, Kristin M Smith, William J Frederick Jr, and Mark R Nimlos. Biomass pyrolysis and gasification of varying particle sizes in a fluidized-bed reactor. *Energy & fuels*, 25(8):3747–3757, 2011.

[57] Siddhartha Gaur and Thomas B. Reed. *Thermal data for natural and synthetic fuels*. CRC Press, 1998.

[58] D. Geldart. *Gas Fluidization Technology*. Wiley-Interscience, New York, 1986.

[59] S. Gerber, F. Behrendt, and M. Oevermann. An Eulerian modeling approach of wood gasification in a bubbling fluidized bed reactor using char as bed material. *Fuel*, 89(10):2903–2917, 2010.

[60] A. W. Glazer and H. Nikaido. *Microbial Biotechnology: fundamentals of applied microbiology*. W. H. Freeman, 1995.

[61] A. Gómez-Barea and B. Leckner. Modeling of biomass gasification in fluidized bed. *Progress in Energy and Combustion Science*, 36(4):444–509, 2010.

[62] A. Gómez-Barea and B. Leckner. Estimation of gas composition and char conversion in a fluidized bed biomass gasifier. *Fuel*, 107:419–431, 2013.

[63] David G. Goodwin, Harry K. Moffat, and Raymond L. Speth. Cantera: An object-oriented software toolkit for chemical kinetics, thermodynamics, and transport processes. http://www.cantera.org, 2014. Version 2.1.2.

[64] DJ Gunn. Transfer of heat or mass to particles in fixed and fluidised beds. *International Journal of Heat and Mass Transfer*, 21(4):467–476, 1978.

[65] P. Harris. On charoal. *Interdisciplinary Science Reviews*, 24(4):301–306, 1999.

[66] Y Haseli, JA van Oijen, and LPH de Goey. Predicting the pyrolysis of single biomass particles based on a time and space integral method. *Journal of Analytical and Applied Pyrolysis*, 96:126–138, 2012.

[67] Y Haseli, JA van Oijen, and LPH de Goey. A simplified pyrolysis model of a biomass particle based on infinitesimally thin reaction front approximation. *Energy & Fuels*, 26(6):3230–3243, 2012.

[68] Abolhasan Hashemi Sohi, Ali Eslami, Amir Sheikhi, and Rahmat Sotudeh-Gharebagh. Sequential-based process modeling of natural gas combustion in a fluidized bed reactor. *Energy & Fuels*, 26(4):2058–2067, 2012.

[69] Hilligardt and Werther. Gas flow in and around bubbles in gas fluidized beds–local measurements and modelling considerations. In *Fluidization, World Congress II of Chemical Engineering*, 1986.

[70] S Hulkkonen, A Jahkola, and E Kurkela. The otaniemi pressurized fluidized bed test facility and research project. In *Proc. Int. Conf. Fluid. Bed Combust., 10th, April*, pages 233–237, 1989.

[71] E. Jakab, O. Faix, F. Till, and T. Székely. Thermogravimetry/mass spectrometry study of six lignins within the scope of an international round robin test. *Journal of Analytical and Applied Pyrolysis*, 35(2):167–179, 1995.

[72] R. K. Jalan and V. K. Srivastava. Studies on pyrolysis of a single biomass cylindrical pellet - kinetic and heat transfer effects. *Energ Conv*, 40(5):467–494, 1999.

[73] Harold E. Jegers and Michael T. Klein. Primary and secondary lignin pyrolysis reaction pathways. *Industrial & Engineering Chemistry Process Design and Development*, 24(1):173–183, 1985.

[74] B. M. Jenkins, L. L. Baxter, T. R. Miles, and T. R. Miles. Combustion properties of biomass. *Fuel Processing Technology*, 54(1-3):17–46, 1998.

[75] G. A. Jensen. The kinetics of gasification of carbon contained in coal minerals at atmospheric pressure. *Industrial & Engineering Chemistry Process Design and Development*, 14(3):308–314, 1975.

[76] Andreas Jess. Mechanisms and kinetics of thermal reactions of aromatic hydrocarbons from pyrolysis of solid fuels. *Fuel*, 75(12):1441 – 1448, 1996.

[77] Filip Johnsson, Sven Andersson, and B Leckner. Expansion of a freely bubbling fluidized bed. *Powder Technology*, 68(2):117–123, 1991.

[78] Alan Kéromnès, Wayne K Metcalfe, Karl A Heufer, Nicola Donohoe, Apurba K Das, Chih-Jen Sung, Jürgen Herzler, Clemens Naumann, Peter Griebel, and Olivier Mathieu. An experimental and detailed chemical kinetic modeling study of hydrogen and syngas mixture oxidation at elevated pressures. *Combustion and Flame*, 160(6):995–1011, 2013.

[79] M. T. Klein and P. S. Virk. Model pathways in lignin thermolysis. Technical report, MIT Energy Laboratory, 1981.

[80] C. A. Koufopanos, N. Papayannakos, G. Maschio, and A. Lucchesi. Modelling of the pyrolysis of biomass particles. studies on kinetics, thermal and heat transfer effects. *The Canadian Journal of Chemical Engineering*, 69(4):907–915, 1991.

[81] Daizo Kunii and Octave Levenspiel. Fluidization engineering. 1991.

[82] Kenneth K Kuo. *Principles of combustion*. Wiley New York et al., 2 edition, 2005.

[83] E. Kurkela and P. Stålberg. Air gasification of peat, wood and brown coal in a pressurized fluidized-bed reactor. i. carbon conversion, gas yields and tar formation. *Fuel Process. Technol.*, 31:1–21, 1992.

[84] Luca Laghi. Cellulose strand, 2013.

[85] Bo Leckner and Joachim Werther. Scale-up of circulating fluidized bed combustion. *Energy & fuels*, 14(6):1286–1292, 2000.

[86] Chunshan Li and Kenzi Suzuki. Tar property, analysis, reforming mechanism and model for biomass gasification: An overview. *Renewable and Sustainable Energy Reviews*, 13(3):594 – 604, 2009.

[87] Juan Li, Zhenwei Zhao, Andrei Kazakov, Marcos Chaos, Frederick L. Dryer, and James J. Scire. A comprehensive kinetic mechanism for co, ch2o, and ch3oh combustion. *International Journal of Chemical Kinetics*, 39(3):109–136, 2007.

[88] X. T. Li, J. R. Grace, C. J. Lim, A. P. Watkinson, H. P. Chen, and J. R. Kim. Biomass gasification in a circulating fluidized bed. *Biomass and Bioenergy*, 26(2):171–193, 2004.

[89] R.P. Lindstedt and K.-A. Rizos. The formation and oxidation of aromatics in cyclopentene and methyl-cyclopentadiene mixtures. *Proceedings of the Combustion Institute*, 29(2):2291 – 2298, 2002.

[90] Hong Lu, Elvin Ip, Justin Scott, Paul Foster, Mark Vickers, and Larry L. Baxter. Effects of particle shape and size on devolatilization of biomass particle. *Fuel*, 89(5):1156–1168, 2010.

[91] Hong Lu, Warren Robert, Gregory Peirce, Bryan Ripa, and Larry L. Baxter. Comprehensive study of biomass particle combustion. *Energy & Fuels*, 22(4):2826–2839, 2008.

[92] Karsten Luecke, Ernst-Ulrich Hartge, and Joachim Werther. A 3d model of combustion in large-scale circulating fluidized bed boilers. *International Journal of Chemical Reactor Engineering*, 2(1), 2004.

[93] P. M. Lv, Z. H. Xiong, J. Chang, C. Z. Wu, Y. Chen, and J. X. Zhu. An experimental study on biomass air/steam gasification in a fluidized bed. *Bioresource technology*, 95(1):95–101, 2004.

[94] K Maniatis and A.A.C.M Beenackers. Tar protocols. {IEA} bioenergy gasification task. *Biomass and Bioenergy*, 18(1):1 – 4, 2000.

[95] Keigo Matsumoto, Keiji Takeno, Toshimitsu Ichinose, Tomoko Ogi, and Masakazu Nakanishi. Gasification reaction kinetics on biomass char obtained as a by-product of gasification in an entrained-flow gasifier with steam and oxygen at 900&1000°$c$. *Fuel*, 88(3):519–527, 2009.

[96] Thomas McGrath, Ramesh Sharma, and Mohammad Hajaligol. An experimental investigation into the formation of polycyclic-aromatic hydrocarbons (pah) from pyrolysis of biomass materials. *Fuel*, 80(12):1787 – 1797, 2001.

[97] Thomas E. McGrath, W.Geoffrey Chan, and Mohammad R. Hajaligol. Low temperature mechanism for the formation of polycyclic aromatic hydrocarbons from the pyrolysis of cellulose. *Journal of Analytical and Applied Pyrolysis*, 66(12):51 – 70, 2003.

[98] William Meeks III and Joaquín Pérez. The classical theory of minimal surfaces. *Bulletin of the American Mathematical Society*, 48(3):325–407, 2011.

[99] D. Meier and O. Faix. State of the art of applied fast pyrolysis of lignocellulosic materials - a review. *Bioresource technology*, 68(1):71–77, 1999.

[100] Wayne K Metcalfe, Sinéad M Burke, Syed S Ahmed, and Henry J Curran. A hierarchical and comparative kinetic modeling study of c1- c2 hydrocarbon and oxygenated fuels. *International Journal of Chemical Kinetics*, 45(10):638–675, 2013.

[101] T. Milne, R. J. Evans, and N. Abatzoglou. Biomass gasifier tars: Their nature, formation and conversion. Technical Report TP-570-25357, National Energy Technology Laboratory (NETL), 1998.

[102] Ivan Milosavljevic, Vahur Oja, and Eric M. Suuberg. Thermal effects in cellulose pyrolysis: Relationship to char formation processes. *Industrial & Engineering Chemistry Research*, 35(3):653–662, 1996.

[103] M. A. Mueller, R. A. Yetter, and F. L. Dryer. Flow reactor studies and kinetic modeling of the h2/o2/nox and co/h2o/o2/nox reactions. *International Journal of Chemical Kinetics*, 31(10):705–724, 1999.

[104] Ahindra Nag. *Biosystems Engineering*. McGraw Hill Professional, 2009.

[105] I. Narváez, A. Orío, M. P. Aznar, and J. Corella. Biomass gasification with air in an atmospheric bubbling fluidized bed. effect of six operational variables on the quality of the produced raw gas. *Ind Eng Chem Res*, 35:2110–2120, 1996.

[106] Daniel Neves, Henrik Thunman, Arlindo Matos, Luís Tarelho, and Alberto Gómez-Barea. Characterization and prediction of biomass pyrolysis products. *Progress in Energy and Combustion Science*, 37(5):611–630, 2011.

[107] Johanna Olsson, David Pallarès, and Filip Johnsson. Lateral fuel dispersion in a large-scale bubbling fluidized bed. *Chemical Engineering Science*, 74:148–159, 2012.

[108] CV Ovesen, P Stoltze, JK Nørskov, and CT Campbell. A kinetic model of the water gas shift reaction. *Journal of catalysis*, 134(2):445–468, 1992.

[109] I. A. Pearl. *The Chemistry of Lignin*, volume 157. Marcel Dekker, New York, 1967.

[110] R. D. Perlack, L. L. Wright, A. F. Turhollow, R. L. Graham, B. J. Stoke, and D. C. Erbach. Biomass as feedstock for a bioenergy and bioproducts industry: The technical feasibility of a billion-ton annual supply. Technical report, Oak Ridge National Laboratory, 2005.

[111] Francis P. Petrocelli and Michael T. Klein. Model reaction pathways in kraft lignin pyrolysis. *Macromolecules*, 17(2):161–169, 1984.

[112] R. F. Probstein and R. E. Hicks. *Synthetic Fuels*. McGraw-Hill, New York, New York, 1982.

[113] Maria Puig-Arnavat, Joan Carles Bruno, and Alberto Coronas. Review and analysis of biomass gasification models. *Renewable and Sustainable Energy Reviews*, 14:2841–2851, 2010.

[114] D. L. Pyle and C. A. Zaror. Heat transfer and kinetics in the low temperature pyrolysis of solids. *Chemical Engineering Science*, 39(1):147–158, 1984.

[115] X. Qin, T. Mohan, M. El-Halwagi, G. Cornforth, and B. McCarl. Switchgrass as an alternate feedstock for power generation: an integrated environmental, energy and economic life-cycle assessment. *Clean Technologies and Environmental Policy*, 8(4):233–249, 2006.

[116] Ramin Radmanesh, Jamal Chaouki, and Christophe Guy. Biomass gasification in a bubbling fluidized bed reactor: Experiments and modeling. *AIChE Journal*, 52(12):4258–4272, 2006.

[117] WE Ranz. Friction and transfer coefficients for single particles and packed beds. *Chemical Engineering Progress*, 48(5):247–253, 1952.

[118] Eliseo Ranzi, Michele Corbetta, Flavio Manenti, and Sauro Pierucci. Kinetic modeling of the thermal degradation and combustion of biomass. *Chemical Engineering Science*, 110:2 – 12, 2014.

[119] Eliseo Ranzi, Alberto Cuoci, Tiziano Faravelli, Alessio Frassoldati, Gabriele Migliavacca, Sauro Pierucci, and Samuele Sommariva. Chemical kinetics of biomass pyrolysis. *Energy & Fuels*, 22(6):4292–4300, 2008.

[120] Eliseo Ranzi, Sauro Pierucci, Pier Carlo Aliprandi, and Silvano Stringa. Comprehensive and detailed kinetic model of a traveling grate combustor of biomass. *Energy Fuels*, 25(9):4195–4205, 2011.

[121] S. Rapagnà and G. Mazziotti di Celso. Devolatilization of wood particles in a hot fluidized bed: Product yields and conversion rates. *Biomass and Bioenergy*, 32(12):1123–1129, 2008.

[122] Sergio Rapagnà and Ajmal Latif. Steam gasification of almond shells in a fluidised bed reactor: the influence of temperature and particle size on product yield and distribution. *Biomass and Bioenergy*, 12(4):281–288, 1997.

[123] Reaction Design. *CHEMKIN-PRO 15131.* 2013.

[124] Thomas B. Reed. *Biomass gasification : principles and technology*, volume 67. Noyes Data Corp, Park Ridge, N.J. :, 1981.

[125] P.N. Rowe. Estimation of solids circulation rate in a bubbling fluidised bed. *Chemical Engineering Science*, 28(3):979 – 980, 1973.

[126] R. Rowell. *The Chemistry of Solid Wood*, volume 207. American Chemical Society, Washington, DC, 1984.

[127] M. Ruggiero and G. Manfrida. An equilibrium model for biomass gasification processes. *Renewable Energy*, 16(14):1106–1109, 1999.

[128] Fabrizio Scala, Riccardo Chirone, and Piero Salatino. Combustion and attrition of biomass chars in a fluidized bed. *Energy Fuels*, 20(1):91–102, 2006.

[129] Timothy D. Searchinger, Steven P. Hamburg, Jerry Melillo, William Chameides, Petr Havlik, Daniel M. Kammen, Gene E. Likens, Ruben N. Lubowski, Michael Obersteiner, Michael Oppenheimer, G. Philip Robertson, William H. Schlesinger, and G. David Tilman. Fixing a critical climate accounting error. *Science*, 326(5952):527–528, 2009.

[130] F. Shafizadeh. Introduction to pyrolysis of biomass. *Journal of Analytical and Applied Pyrolysis*, 3(4):283–305, 1982.

[131] E. Sjöström. *Wood Chemistry: Fundamentals and Applications*, volume Second. Academic Press, San Diego, California, 1993.

[132] RJ Smith, Muruganandam Loganathan, Murthy Shekhar Shantha, et al. A review of the water gas shift reaction kinetics. *International Journal of Chemical Reactor Engineering*, 8(1), 2010.

[133] Addison Killean Stark. Multi-criteria lifecycle evaluation of transportation fuels derived from biomass gasification. Master's thesis, Massachusetts Institute of Technology, 2010.

[134] A.P. Steynberg. *Fischer-Tröpsch Technology*, volume 152 of *Studies in Surface Science and Catalysis*. Elsevier, 2004.

[135] Madhava Syamlal, William Rogers, and Thomas J OBrien. Mfix documentation: Theory guide. *Technical Note, DOE/METC-94/1004, NTIS/DE94000087, National Technical Information Service, Springfield, VA*, 1993.

[136] Kok Tat Tan, Keat Teong Lee, and Abdul Rahman Mohamed. Role of energy policy in renewable energy accomplishment: The case of second-generation bioethanol. *Energy Policy*, 36(9):3360–3365, 2008.

[137] R Turton, TJ Fitzgerald, and O Levenspiel. An experimental method to determine the heat transfer coefficient between fine fluidized particles and air via changes in magnetic properties. *International journal of heat and mass transfer*, 32(2):289–296, 1989.

[138] S. V. B. van Paasen and J. H. A. Kiel. Tar formation in a fluidised bed gasifier. Technical Report ECN-C–04-013, Energy Research Center of the Netherlands, 2004.

[139] Jürgen Warnatz, Ulrich Maas, and Robert W Dibble. *Combustion: physical and chemical fundamentals, modeling and simulation, experiments, pollutant formation*. Springer, 2006.

[140] Paul T. Williams and Serpil Besler. The influence of temperature and heating rate on the slow pyrolysis of biomass. *Renewable Energy*, 7(3):233–250, 1996.

[141] Johann C Wurzenberger, Susanne Wallner, Harald Raupenstrauch, and Johannes G Khinast. Thermal conversion of biomass: Comprehensive reactor and particle modeling. *AIChE Journal*, 48(10):2398–2411, 2002.

[142] Q Xue and RO Fox. Reprint of: Multi-fluid cfd modeling of biomass gasification in polydisperse fluidized-bed gasifiers. *Powder Technology*, 2014.

[143] Yao B. Yang, Vida N. Sharifi, Jim Swithenbank, Lin Ma, Leilani I. Darvell, Jenny M. Jones, Mohamed Pourkashanian, and Alan Williams. Combustion of a single particle of biomass. *Energy & Fuels*, 22(1):306–316, 2008.

[144] Heeyoung Yoon, James Wei, and Morton M Denn. A model for moving-bed coal gasification reactors. *AIChE Journal*, 24(5):885–903, 1978.